DENSITY AND BETA LIMITS IN THE MADISON SYMMETRIC TORUS REVERSED-FIELD PINCH

by

KYLE JONATHAN CASPARY

A dissertation submitted in partial fulfillment of

the requirements for the degree of

Doctor of Philosophy

(PHYSICS)

at the

UNIVERSITY OF WISCONSIN-MADISON

2014

Date of final oral examination: March 24th, 2014

The dissertation is under review by the following members of the Final Oral Committee:
Brett Chapman, Senior Scientist, Physics
John Sarff, Professor, Physics
Paul Terry, Professor, Physics
Jan Egedal, Assistant Professor, Physics
David Anderson, Professor, Electrical and Computer Engineering

ABSTRACT

DENSITY AND BETA LIMITS IN THE MADISON SYMMETRIC TORUS REVERSED-FIELD PINCH

Operational limits and the underlying physics are explored on the Madison Symmetric Torus (MST) Reversed-Field Pinch (RFP) using deuterium pellet fueling. The injection of a fast pellet provides a large source of fuel in the plasma edge upon impact with the vessel wall, capable of triggering density limit terminations for the full range of plasma current, up to 600 kA. As the pellet size and plasma density increase, approaching the empirical Greenwald limit, plasma degradation is observed in the form of current decay, increased magnetic activity in the edge and core, increased radiation and plasma cooling. The complete termination of the plasma is consistent with the Greenwald limit; however, a slightly smaller maximum density is observed in discharges without toroidal field reversal.

The plasma beta is the ratio of the plasma pressure to the confining magnetic pressure. Beta limits are known to constrain other magnetic confinement devices, but no beta limit has yet been established on the RFP. On MST, the highest beta values are obtained in improved confinement discharges with pellet fueling. By using pellet injection to scan the plasma density during PPCD, we also achieve a scan of Ohmic input power due to the increase in plasma resistivity. We observe a factor of 3 or more increase in Ohmic power as we increase the density from $1*10^{19}$ to $3*10^{19}$ m^{-3}. Despite this increased Ohmic power, the electron contribution to beta is constant, suggesting a confinement limited beta for the RFP. The electrons and ions are

classically well coupled in these cold, dense pellet fueled plasmas, so the increase in total beta at higher density is primarily due to the increased ion contribution.

The interaction of pellet fueling and NBI heating is explored. Modeling of MST's neutral heating beam suggests an optimal density for beam power deposition of 2-3*10^{19} m^{-3}. Low current, NBI heated discharges show evidence of an increased electron beta in this density range. Additionally, the fast ion population can enhance ablation as well as cause pellet deflection. Other exploratory experiments with the pellet injection system explore additional injection scenarios and expand the injector capabilities.

ACKNOWLEDGEMENTS

Only in graduate school can you finish writing 200 pages on the research you've been working on for so many years… while simultaneously feeling like you know absolutely nothing about anything. I guess that's what happens when you stick your head so far down the rabbit hole, all you see is pellets…

I guess this is the part where I thank all of the people who helped me get to this point. This sort of stuff is not really my specialty. 'You don't seem like much of a hugger', said someone, somewhere. And it's true… I am not, but here it goes.

I would not be studying physics if it weren't for Steven Stevenoski. A man who holds two titles in my book… best high school physic teacher and funniest name… sorry Benedict Cumberbatch. I have heard horror stories about high school physics classes which consisted of nothing but a year long treatise on **F**=m**a**. So thank you for showing me that there was so much more to physics, otherwise I might never have gone looking for it.

Likewise, I would not have gone to grad school were it not for my undergraduate advisors and the physics department at UW - Eau Claire… and for that I hold you all personally responsible. But in all seriousness, I learned an incredible amount from all of you… so thank you for helping to put me on this path, wherever it leads.

To my advisors, Stewart, Dalton, John and most of all Brett, thank you for your guidance and for the opportunity to study fusion. I have often not appreciated how big of an opportunity it was to be able to study plasma physics here at Wisconsin. When I stop to think about it (which admittedly isn't often enough), I am actually stunned by the shear amount I have learned in my time here. I have often joked that while in grad school, I know more than I ever have before, and feel as dumb as I ever will… but the fact remains… I know more now than I ever have. So thank you for helping me learn so much.

Thanks to all of the friends I've had over the years, you make everything better. From the friends I've known since junior high to those I've met in the past year and everyone in between, thank you for the fond memories…

I have seriously considered adding an appendix to this thesis to discuss why Ella Belle is definitively the best cat ever. Who knows, maybe I did, you should check just in case. But if I didn't, it is only because it wouldn't do her justice. Trust me on this one. After a rough day, nothing makes you feel better, faster than having an overly fluffy cat jump up on your lap and start purring in anticipation.

My family has always been there for me and supported me. Collectively, they have had the biggest hand in making me… me. I like the person I have become, so thank you for the part you played in making that happen and thank you for your continued love and support.

Finally, Rachel. I don't know where I would be without you, and I am so happy I get to spend the rest of my life with you. To future…

TABLE OF CONTENTS

CHAPTER 3 DENSITY LIMIT STUDIES ON MST

CHAPTER 4 HIGH β, IMPROVED CONFINEMENT OHMIC DISCHARGES

CHAPTER 5 INVESTIGATION OF PELLET-FAST ION INTERACTION AND HIGH β OPERATION WITH NBI

CHAPTER 6 EXPLORATORY EXPERIMENTS

CHAPTER 7 CONCLUSIONS AND FUTURE WORK

APPENDIX A SUPPLEMENTAL PLOTS FOR CHAPTERS 3-5

APPENDIX B SUPPLEMENTAL PELLET USER'S GUIDE

APPENDIX C 4.0 mm PELLET UPGRADE

LIST OF FIGURES

List of Tables

CHAPTER 1

Introduction

1.1 Motivation

A fictional great man once proclaimed ‘Since the beginning of time, man has yearned to destroy the sun. I shall do the next best thing: block it out.’ Actual great men and women have taken a slightly different approach, spending much of the past century working on the next, next best thing: bringing the power of the Sun a bit closer to home in the form of magnetic confinement fusion energy. The path has been full of obstacles, but every obstacle ultimately leads to an increased understanding which brings us one step closer. In this thesis, we continue to improve our understanding of the limits which govern magnetic confinement fusion experiments, in the hope that we may take one more step toward the ultimate goal of fusion energy.

While the limits we investigate are those that govern density and β in the Reversed Field Pinch (RFP) device, the knowledge gained may very well aid in the understanding of similar limits in other magnetic confinement devices. Operating close to a density limit is beneficial because the fusion reaction rate scales with the square of the density. A large gain in fusion power is obtained by boosting the density a little. β limits represent a cap on the amount of plasma pressure which can be confined by a given magnetic field. Stronger magnets cost more money; therefore higher β leads to more bang for the buck, so to speak. For clarification, the ‘bang’ here is good, unlike most bangs encountered during fusion experiments which range from mundane to terrifying. The RFP device has a naturally high β compared to other devices, and the limits which govern it have not yet been fully explored.

Our primary weapon of choice is pellet injection. An experiment in its own right, we not only expand old and develop new capabilities of the injector, we also utilize it as a tool with which we can probe various aspects of RFP discharges. We also employ Neutral Beam Injection (NBI) for two purposes; to improve our understanding of the pellet-NBI interaction, and to act as a variable heating source.

On the Madison Symmetric Torus (MST) RFP experiment, pellet injection is utilized to study the operational limits of the RFP device; specifically, the limits governing density and β. The RFP shares a common density limit with that of the tokamak, the empirical Greenwald limit, n_{GW}. To study density limit terminations on MST, a means of edge fueling was devised and tested using fast pellet injection. Pellets launched with a velocity greater than 1000 m/s will, if sufficiently large, traverse the plasma rapidly and crash into the vessel wall providing a large source of fuel in the plasma edge. Full termination of the discharge occurs as pellet size increases and the density reaches the Greenwald limit. In order to trigger density limit terminations at the highest available plasma current on MST (600 kA), the pellet injector hardware was modified to accommodate 4.0 mm diameter pellets with a particle content greater than 10^{21}, an approximately 8-fold increase from that of 2.0 mm diameter pellets used in previous work. [1, 2] The study of pellet triggered terminations shows good agreement with the Greenwald limit scaling up to 600 kA. A region exists, starting at roughly 70% of the limiting density, where a partial decay of the plasma current is observed following pellet injection. Electron temperature in the core and edge decrease rapidly, and magnetic mode activity in both the edge and core scale with the increase in plasma density. An investigation of the density limit in discharges without reversed toroidal field reveals a slightly lower limit on the density. Similarly, discharges with larger reversed field appears to behave more robustly to density limit experiments, partially terminating where less reversed discharges would fully terminate. In core fueled high density experiments with improved confinement, record densities of $1.4*n_{GW}$ and $2.0*n_{GW}$ are obtained at 500 kA and 200 kA respectively.

The plasma β is the ratio of the plasma pressure to the confining magnetic pressure. β limits are known to constrain other magnetic confinement devices, but no β limit has yet been established on the RFP. On MST, the highest β values are obtained in improved confinement discharges fueled by pellet injection to high densities, in some cases exceeding n_{GW}. The increase in β is in part due to increased coupling of the electron and ions in the colder, denser pellet fueled plasma. An examination of pellet fueled, improved confinement discharges reveals a fairly constant electron contribution to β as density increases, a consequence of a decrease of the electron temperature. The saturation in the electron β occurs despite a large increase in Ohmic input power at increased density, indicative of a 'soft' β limit, limited by confinement. We observe a factor of 3 or more increase in Ohmic power, based on Spitzer scaling of the resistivity, as we increase the density from $1*10^{19}$ to $3*10^{19}$ m^{-3}. Magnetic mode activity in improved confinement discharges increases with density. At the highest densities, the fluctuations reach a similar level as observed in low density standard RFP discharges where stochastic transport is important. The electron β, however, remains 2-3 times larger in the high density improved confinement case, perhaps partly due to larger shear stabilization of the resonant modes.

The use of NBI heating in conjunction with pellet fueling in improved confinement plasmas was motivated by the prospect of probing the β limit with added non-inductive heating power. Modeling of MST's neutral heating beam suggests an optimal density for beam power deposition of 2-3*10^{19} m^{-3}. 200 kA improved confinement experiments with NBI heating show evidence of an electron temperature enhancement, and corresponding increase in electron β, in this density range. Additionally, the fast ion population was observed to enhance pellet ablation as well as cause a deflection of the pellet. By modeling the asymmetric ablation and tracking the pellet deflection with a high speed camera, an estimate of the fast ion density profile was obtained.

Other exploratory experiments with the pellet injection system investigate additional pellet injection scenarios such as injection into SHAx discharges which promote the growth of a single large dominant mode in the core, injection of alternative fuels (methane), and injection of a pellet during plasma startup. Injection into SHAx discharges results in a briefly sustained dominant mode with increased density, or an immediate relaxation of the dominant mode. Small pellets can also trigger the growth of the dominant mode and early injection allowed access higher density discharges with a large dominant mode. Modifications to the pellet hardware enabled the use of methane as a pellet fuel. Methane pellet injection was able to significantly increase the core carbon density and was used to aid the study impurity transport in the plasma core. The startup pellet fueling experiments were an attempt to gauge the impact that an ablating pellet would have on the current ramp up and other relevant quantities. A comparison shows little change in the plasma startup despite the actively ablating pellet in the plasma.

1.2 Thesis Overview

The remainder of chapter 1 will outline the thesis, discuss the nature of the RFP, and offer a brief review of the density and β limits in magnetic confinement devices. This will also include a comparison between the RFP, tokamak, and stellarator, since it is suspected that there may be some common physics linking the devices and that some insight can be gained by comparing and contrasting the theory and understanding for each device. There will also be a summary of previous pellet fueling results on MST.

Chapter 2 will discuss in more detail the RFP and the MST device specifically, focusing on the three relevant modes of operation: standard RFP discharges, improved confinement achieved with inductive current profile control, and the self organized QSH/SHAx state. Then there will be an overview of the hardware details of the pellet injector, including information about the hardware modifications made during the author's tenure with the pellet injector system. Finally, a discussion of the important diagnostics will wrap up the experimental setup chapter.

Chapter 3 will focus on the density limit experiments performed using excessive edge pellet fueling to routinely trigger terminations of the plasma. These experiments were performed utilizing the full suite of plasma diagnostics on MST, including edge inserted probes. Observations from these diagnostics will be discussed along with the phenomenology of the density limit. Finally we will discuss the highest density obtained on MST, core fueled plasmas with improved confinement.

Using inductive current profile control and pellet injection to obtain high β plasmas will be discussed in chapter 4. An examination of a density scan and corresponding scan of the

Ohmic power will be discussed. An observed saturation of the electron β along with an increase in magnetic fluctuations is indicative of a confinement limited β.

The interactions between the pellet and NBI are explored in chapter 5. A simple model of the NBI beam deposition is used to estimate the optimal density to maximize the deposited power for β limit experiments. Additionally, an observed deflection is attributed to enhance ablation due to the fast ion population and an estimate of the population is obtained by tracking the pellet deflection and modeling the asymmetric ablation.

A number of additional experiments performed with the pellet injector are discussed in chapter 6. First, pellet injection experiments into QSH/SHAx plasmas with a large dominant mode structure are discussed. Next, a look at the development of a means to inject alternative fuels (specifically methane) is included. Finally, attempts were made to fuel with pellets during plasma startup and the results suggest the pellet ablation has little impact on the current ramp, while modestly increasing the startup density.

Finally, chapter 7 will discuss the current state of theory and experimental understanding of the density and beta limits in the RFP. Also included will be several key pieces of information which would help to shed light on the subject and motivate future experiments.

1.3 The Reversed Field Pinch

The Reversed Field Pinch (RFP) is a toroidal magnetic confinement device which has a signature topology where the toroidal component of the magnetic field decreases and reverses direction from the core to the plasma edge. The radial location where the toroidal field is zero is the reversal surface. The RFP geometry is a magnetic topology closely related to Taylor relaxation theory. [3]

An important parameter for plasma stability is the magnetic curvature κ given by

$$\vec{\kappa} = \vec{b} \cdot \vec{\nabla}\vec{b} \tag{1.1}$$

With finite plasma pressure, good or bad curvature are determined by

$$\vec{\kappa} \cdot \vec{\nabla}\vec{P} < 0 \tag{1.2}$$

where P is the plasma pressure. While the tokamak confines the plasma primarily with a strong toroidal field ($B_\varphi >> B_\theta$) and overall good magnetic curvature, the magnetic fields of the RFP are of comparable amplitude ($B_\varphi \sim B_\theta$) and the curvature is everywhere bad.

A primary feature of the RFP is the large magnetic shear length L_s defined by

$$\frac{1}{L_s} = \frac{-R_0}{r}\frac{B_\theta^2}{B^2}\frac{dq}{dr} \tag{1.3}$$

where R_0 is the major radius and q is the safety factor given by

$$q = \frac{rB_\theta}{RB_\varphi} \tag{1.4}$$

with r and R representing the major and minor radius and B_θ, B_φ representing the poloidal and toroidal components of the magnetic field, respectively. The large magnetic shear allows for naturally high β operation on the RFP. A comparison of the q profiles for the tokamak, RFP and stellarator are shown in figure 1.1. [4]

A key feature for the RFP is the reversed toroidal field at the edge as shown in figure 1.2. The edge reversal is generated and sustained in part by a process known as the plasma dynamo. This is a means by which the plasma converts toroidal and poloidal flux. Magnetic reconnection events involving tearing instabilities are a key component of the dynamo process. Tearing modes can be unstable at locations in the plasma where the fluctuation is everywhere perpendicular to the magnetic field.

$$\vec{k} \cdot \vec{B} = 0 \tag{1.5}$$

Put another way, if we define toroidal and poloidal mode numbers n and m respectively, we can write this relation as

$$m\frac{B_\theta}{r} + n\frac{B_\varphi}{R} = 0 \tag{1.6}$$

This defines the location of rational surfaces in the plasma where q = m/n is a rational number. In a tokamak, q > 1 everywhere primarily to avoid the m/n = 1/1 tearing mode being resonant in the plasma. Since q < 1 everywhere in the RFP, the plasma can be susceptible to a number of m = 1 modes in the plasma core and m = 0 modes at the reversal surface where q = 0. A closer look at the RFP q profile and the resonant modes is shown in figure 1.3 for the MST experiment.

These modes individually can be thought to have an island structure resonant in the plasma with a spatial width corresponding in part to the amplitude of the resonant mode. However, when these islands overlap with each other, the result is a stochastic field typical of the standard RFP discharge. The host of unstable modes and the stochastic nature of the RFP help to define many aspects including confinement and transport. [5, 6] Electron thermal transport in the core is dependent on the square of these mode amplitudes. [7] On MST the global energy and particle confinement times are ~1 ms and are governed primarily by the edge plasma region. The innermost resonant mode is governed by the value of q on axis and strongly depends on the aspect ratio of the experiment. For MST, the innermost resonant mode is typically n = 6, but for some modes of operation the n = 5 will be resonant in the core.

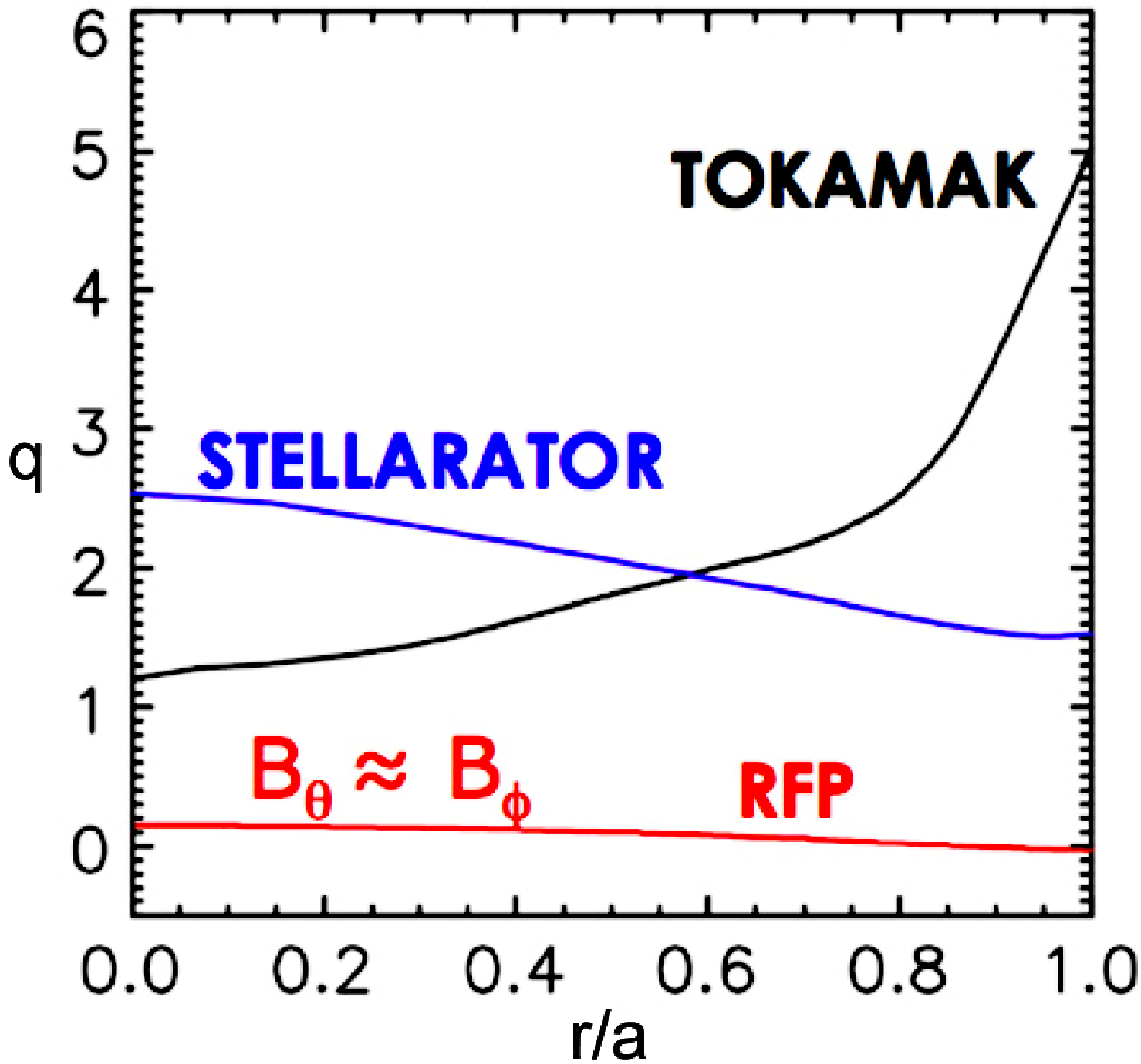

Figure 1.1: Shown is the q profile for the tokamak, stellarator and RFP. An appropriately scaled plot of the RFP q profile can be seen in figure 1.3. Figure from Reference 4.

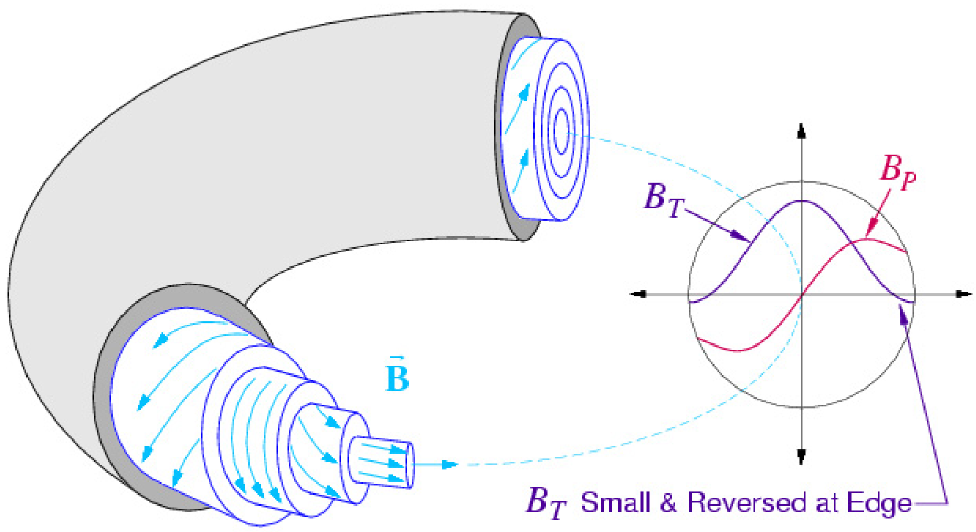

Figure 1.2: Diagram of the RFP magnetic topology. The magnetic field is purely toroidal at the magnetic axis and toroidal component decreases radially outward, eventually reversing direction in the edge.

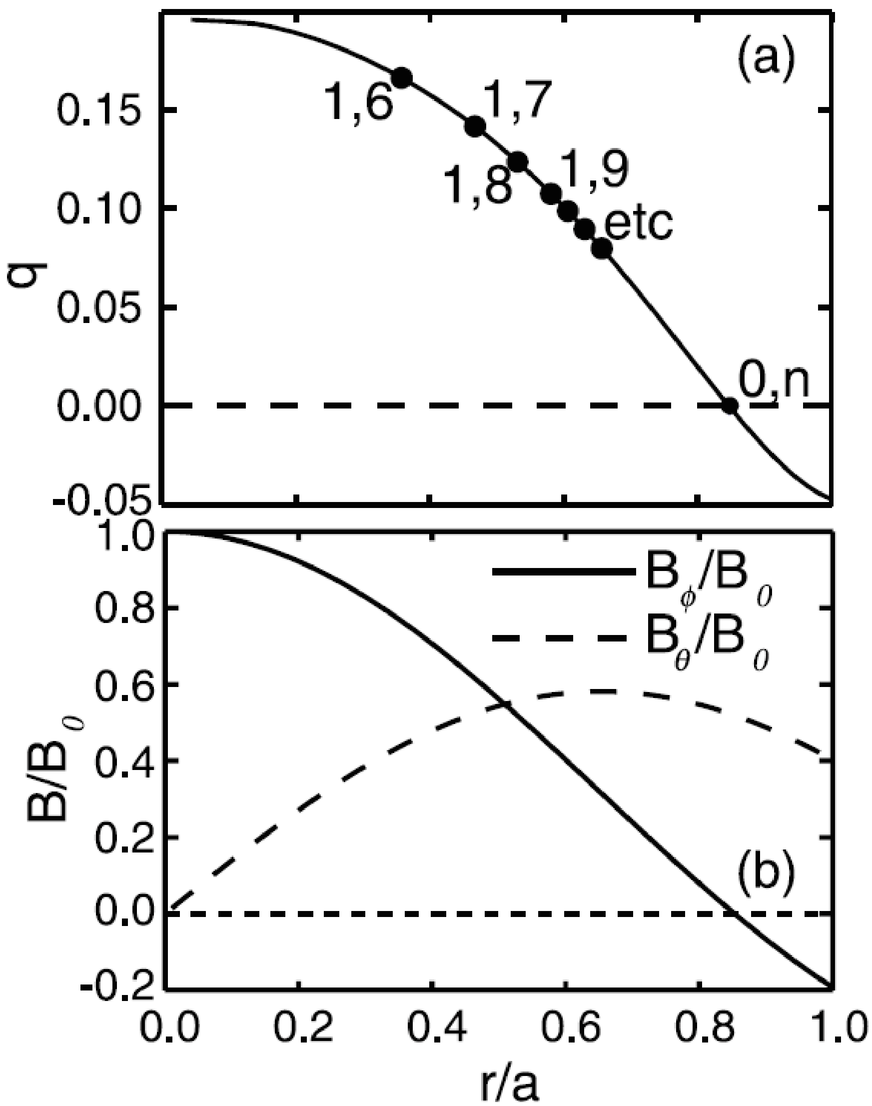

Figure 1.3: (a) The q profile for the RFP showing the location of the relevant resonant modes in the core (m=1) and edge (m=0). (b) Normalized magnetic field profiles for a typical RFP. Figure from Reference 1.

1.4 Limits in Magnetic Confinement Experiments

Understanding the various stability limits for magnetically confined plasmas is important for the future of magnetic confinement fusion research. What follows is a brief discussion of two relevant limits, the density and β limits, for three magnetic confinement devices; the tokamak, the stellarator and the RFP. By comparing and contrasting the work among the devices, we hope to help motivate the experiments in this thesis.

1.4.1 Density Limits

The upper density limit for magnetic confinement devices is extremely important due to the fusion reaction rate scaling as the square of the density. The empirical Greenwald density is known to define the limit on line averaged density in edge fueled tokamak experiments and is also found to match well the scaling of the RFP 'I/N' limit (defined later). [8] For a device with a circular cross section, the Greenwald limit on line averaged density is

$$n_{GW} = \frac{I_p}{\pi a^2} \qquad (1.7)$$

where I_p is the plasma current in MA, a is the minor radius in m and the limiting density (n_{GW}) is in units of 10^{20} m^{-3}.

We start with a discussion of the tokamak density limit from a historical context as it was the first of the three devices to explore density limits in detail. As highlighted in reference 8, the list of symptoms which occur at the Greenwald density limit include but are not limited to; excess radiation, current decay, current channel shrinking, edge cooling, thermal collapse of the plasma, MHD activity and many more, ultimately resulting in a disruption.

The MARFE (Multifaceted Asymmetric Radiation From the Edge) was observed as density increased in the tokamak and was determined to be a precursor to high density disruptions. The MARFE structure is a zone of toroidally symmetric radiation, typically located on the inboard side of an experiment. [9] The initial model deemed the MARFE an instability dependent on impurity radiation. It was modeled well as a form of radiative condensation, as increases in local plasma density lead to increased radiative power. The subsequent decrease in temperature requires a further increase in density to maintain pressure balance. The Greenwald density limit was connected to rapid radial MARFE expansion, followed by mode locking leading to mode growth and to disruption, marking the MARFE as a precursor to the density limit on tokamak experiments. [10, 11]

As already stated, the ultimate consequence of the tokamak density limit is a disruption, which can be damaging to the experiment due to large electromagnetic forces on the structures or due to the generation of runaway electrons. Experiments on mitigating the impact of a density limit disruption included work on JT-60U. By softening the current quench (slowing the rate of current decay) during disruption, they were able to achieve plasma shutdown with a current decay rate of 6 MA/s without runaway electron generation. [12] This was done through a combination of wall conditioning to reduce impurity influx from the edge along with NBI core heating during the disruption which combined to reduce the loop voltages which drive runaways. More recently, the use of impurity gas puffing has been successful at impeding the generation of runaways during a density limit disruption and is capable of achieving acceptable current decay rates of 20 MA/s over 5 ms. [13]

Experiments with pellet fueling on JT-60U show that plasmas with peaked density profiles are able to exceed the density limit suggesting the edge density is important. [14] Observed MHD modes also play a primary role. MHD simulations of density limit disruptions suggest radiation destabilizes the q = 1 kink mode and leads to the thermal quench, current decay and disruption of the plasma. [15] TEXTOR-94 experiments noted a large increase in radiated power at the density limit suggesting an edge radiation instability resulting from a power imbalance caused by excessive radiation. At this point, it is clear that the control of impurities, radiative power and edge recycling are key factors that impact the density limit. [16] Further highlighting the importance of the edge parameters, densities above the Greenwald limit are achieved on DIII-D by peaking the density profile through pellet injection and enhanced edge pumping. [17]

Extensive experimental work has been done to diagnose the nature of the limit, both the symptoms and the causes. Density and temperature measurements during a density limit energy quench show the onset of T_e decay near the m/n = 2/1 O-point prior to decay of the core temperature. [18] Density limit experiments with helium plasmas again highlight the importance of radiation. The density limit was found to be twice that of deuterium for L-mode helium discharges, coinciding with the balance of heating and radiated power, but no significant difference was observed in H-mode plasmas. [19]

A more recent look at the density limit scaling on FTU shows a dependence of the density limit on the toroidal magnetic field instead of directly on the plasma current (poloidal magnetic field). However, a Greenwald like scaling with the current is still observed for edge density measurements. [20, 21]

The most recent picture of the density limit mechanism involves radiation driven MHD modes in the edge, leading to the myriad of other symptoms associated with the density limit. [22, 23] The balance of heating power and radiated power from a resonant surface matches well the Greenwald limit scaling.

We now shift to focus on the state of the RFP density limit. Historically, the RFP has been limited by I/N [24] where I is the plasma current and the particle content N is commonly given by

$$N = \langle n \rangle \pi a^2 \tag{1.8}$$

It is again noted that the I/N limit leads to the same scaling as the Greenwald limit, begging the question of whether the shared limit also implies shared physics. Indeed the connection between the physics in the tokamak and RFP has been a question for some time. [25] The RFP exhibits many of the same symptoms at the Greenwald limit. Figure 1.4 shows the shared nature of the upper density limit for several tokamak experiments as well as for the RFX-Mod RFP device. In RFX-Mod, experiments operating near the density limit show evidence of edge density accumulation, radiation condensation as well as radiation structures reminiscent of MARFEs in tokamaks. [26] The radiating structures are toroidally localized and poloidally symmetric, due to the differing nature of the magnetic field profiles in the RFP where the edge field is predominantly poloidal, in contrast to the tokamak edge field, which is toroidal. While the RFP density limit displays many of the same symptoms as the tokamak limit, the resulting terminations do not yet display any of the potentially damaging features of tokamak disruptions such as runaway electrons or halo currents. The end of the discharge appears to be due to the highly resistive edge plasma. A radiating edge region corresponds to the presence of m = 0 island structures detached from the wall, suggesting a possible link between the density limit and the edge resonant tearing modes. [27] The most recent model attributes the density limit to the growth of this m = 0 island chain resonant in the plasma edge. [28, 29] Previous experiments on MST show that the density limit can be exceeded through the use of pellet fueling to achieve peaked density profiles, again highlighting the importance of the edge plasma on the density limit. [1]

Finally, we will discuss the density limit on stellarator experiments. While the density limit for the stellarator does not follow the Greenwald scaling, many of the symptoms observed seem to share a common element with both the tokamak and RFP experiments. The stellarator limit, the Sudo limit, [30] is given by

$$\langle n \rangle \propto \left(\frac{PB}{V} \right)^{.5} \tag{1.9}$$

where P, B and V are the heating power, field strength and plasma volume respectively. The stellarator limit scales with the square root of the heating power. An effective value for the Greenwald limit can be calculated and is comparatively higher in the stellarator. It has been modeled as a balance between the power absorbed by the plasma and the power lost due to radiative cooling much like the early tokamak models. [31, 32, 33] Density limit experiments on LHD observe asymmetric radiative collapse as the density limit is approached, very similar to the MARFEs observed in tokamaks. [34] On W7-AS, detachment of the plasma is observed as the density limit is approached, yet another example of shared symptoms between devices. [35]

Some work has already been done to compare helical structures in the RFP to those of tokamaks and stellarators, searching for common ground among the devices. [36] The prospect of shared physics across these different magnetic confinement devices and the study of the limit across all three could prove useful in determining the way towards maximizing density in each device. One thing is clear: a better understanding of the edge physics is key to understanding the physics of the density limit. This was one of the motivations for using internal probe measurements to better understand the edge plasma dynamics at the density limit in MST.

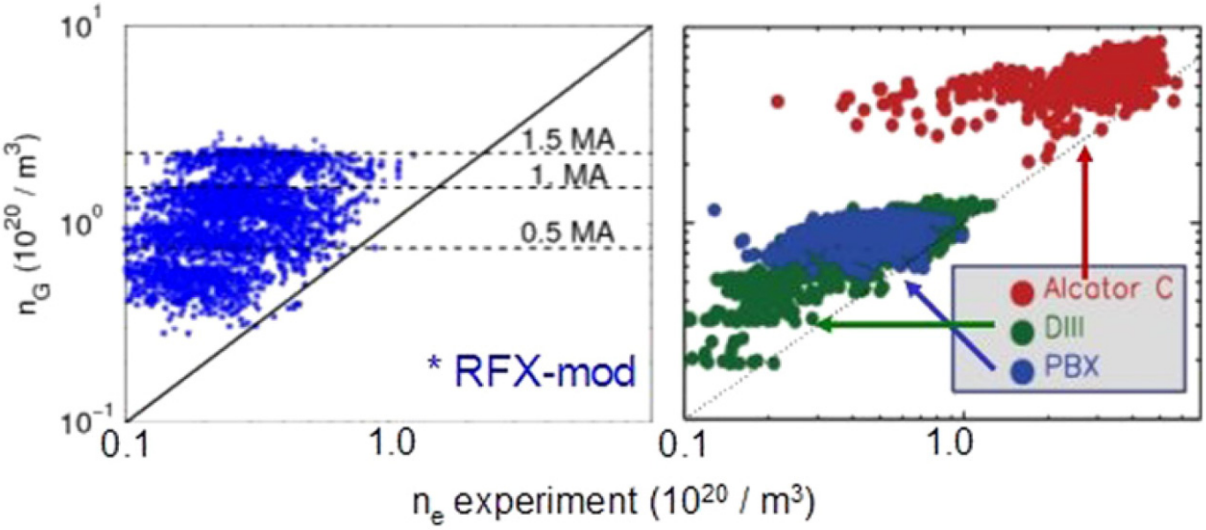

Figure 1.4: The density limit operating space for the RFX-mod experiment is compared with that of several tokamaks. The qualitative agreement with the Greenwald density limit is evident. Figure from Reference 26.

1.4.2 β Limits

The plasma β is the ratio of the plasma pressure to the confining magnetic pressure and is a useful metric for fusion performance. The plasma β is given by

$$\beta = \frac{\int_V p dV}{\frac{B^2(a)}{2\mu_0}\int_V dV} \tag{1.10}$$

The toroidal and poloidal β, represented by β_φ and β_θ, are obtained in the same manner by substituting the toroidal or poloidal magnetic field at the wall into equation 1.10. Tokamak β limits against ideal MHD depend on the aspect ratio of the experiment. [37, 38, 39] The tokamak β limit is given by

$$\beta_\varphi = \frac{\varepsilon}{q_*^2} \tag{1.11}$$

where ε is the inverse aspect ratio and q_* is a modification of the safety factor. The maximum β_φ established by the limit is fairly low (~5%) and is a disruptive limit that has been experimentally verified. [40] As such, a number of shaping parameters have been shown to have an effect on the observed β limit and have shed light on the nature of the limit which is to first order based on ideal stability, an advantage for initial understanding. [37, 41] Changes to the tokamak q profile have a direct impact on the mode stability which governs the β limit; specifically the value of q on axis has a strong impact on the β limit. [42] More recently, the importance of neoclassical tearing modes (NTM) on the β limit have been established. [43, 44] Changing the q profile on axis and changing shaping parameters also impacts the NTM β limit on DIII-D.

Like the tokamak, the stellarator has an ideal MHD β limit which also depends on the inverse aspect ratio; ε. [39] Unlike the tokamak, the stellarator does not appear to have a disruptive β limit. [45] High β experiments have been observed to be limited by the available heating power with no evidence of a disruptive stability limit. Increases in low m/n MHD activity is observed as β is increased and even coincides with predicted β limit values, however, the increased activity does not limit access to higher β. [46, 47] Often this is referred to as a 'soft' β limit, where only weak degradation of the plasma is observed, even in regimes predicted to be linearly unstable to pressure driven modes. [48] For the stellarator it seems ideal stability is a predictor of instability, but not a barrier for higher β.

In more recent LHD experiments, a high β of 5% was obtained with NBI heating and pellet injection. The growth rates of the observed mode activity were close to that of resistive interchange. [49] The stellarator is also able to achieve pressures which exceed the Mercier criterion (for interchange instability) which balances pressure gradients against magnetic shear.

One of the primary benefits of the RFP from a fusion standpoint is its naturally high β when compared to tokamaks and stellarators. For the RFP, the highest experimental β of 26%, achieved in improved confinement pellet fueled plasmas on MST, corresponds to a β_θ of 40%. [1, 2] Similar to the results on MST, improved confinement plasmas on TPE-RX show an increase in β_θ from 5 to 30%. Though in contrast to MST, a similar value for β_θ is observed with and without pellet fueling. [50] For comparison, the achieved β for modern tokamaks and stellarators is ~5% and coincides with predicted stability limits. However, despite the RFP β being high, it is still well below the ideal stability threshold. The ideal MHD limit for m = 0 instabilities is $\beta_\theta < 50\%$ and even less restrictive for m = 1 instabilities with $\beta_\theta < 100\%$ marking ideal stability. [51] Furthermore, recent looks at high β RFPs suggest the limit on β_θ may be even higher, with the modified m = 0 stability criterion given by equation 1.12. [52]

$$\beta_\theta < \frac{r_0^2}{a^2}\frac{B_\theta^2(r_0)}{B_\theta^2(a)}\left[\frac{1}{2}+\frac{2\mu_0 p(r_0)}{B_\theta^2(r_0)}+\frac{4\mu_0}{r_0^2 B_\theta^2(r_0)}\int_{r_0}^{a} rp\,dr\right] \tag{1.12}$$

It is clear from the additional terms in equation 1.12 that the ideal limit will be higher under this equation, and if we use experimental profiles from low current PPCD pellet experiments, we find that $\beta_\theta < 106\%$ is the resulting limit.

High β plasmas on MST can also have pressure gradients in the core which exceed the Mercier criterion that governs ideal interchange stability, given by equation 1.13. [53]

$$-\frac{2\mu_0 p'}{rB_\varphi^2}\left(\frac{q}{q'}\right)^2\left(1-q^2\right)\geq\frac{1}{4} \tag{1.13}$$

The Mercier limited β can be inferred by setting the plasma pressure gradient equal to the Mercier criterion for the entire plasma volume and forcing the pressure to go to zero at the boundary. This establishes a more constraining limit on β with β < 25% in standard discharges with normal magnetic shear and β < 50% in improved confinement discharges with significantly higher shear, as shown in figure 1.5. This poses the most restrictive constraint on RFP β. While linear stability calculations of high β discharges suggest pressure driven modes might be unstable, it is noted here that the transition from resistive to ideal interchange occurs at several times the Suydam limit (the cylindrical version of the Mercier Limit). [54] So ideal stability is likely not the largest concern at this point, which leaves resistive instabilities.

The most likely candidate for β limiting instabilities are resistive interchange and resistive tearing modes, which are commonly unstable in the RFP. Another look at MHD the stability of pressure driven RFP modes in the plasma edge shows tearing parity dominant for moderate β with a transition to ideal interchange at only very high β. [55] Evidence of resistive interchange in the edge of the RFX-Mod experiment has been found and is supported by linear stability analysis. The pressure gradient at the reversal surface appears to play a large role. [56]

Understanding the nature of the magnetic instabilities has been an important aspect of RFP research. [5, 6] A look at shaping effects on RFP β limits shows little impact of changing the various shaping parameters. [57, 58] This is in contrast to the tokamak where shaping can have a significant impact on the maximum achievable β. [40]

A key aspect of establishing a limit on the plasma β is observing a saturation of β with additional heating power and serves as a motivation for the high β experiments explored in this thesis.

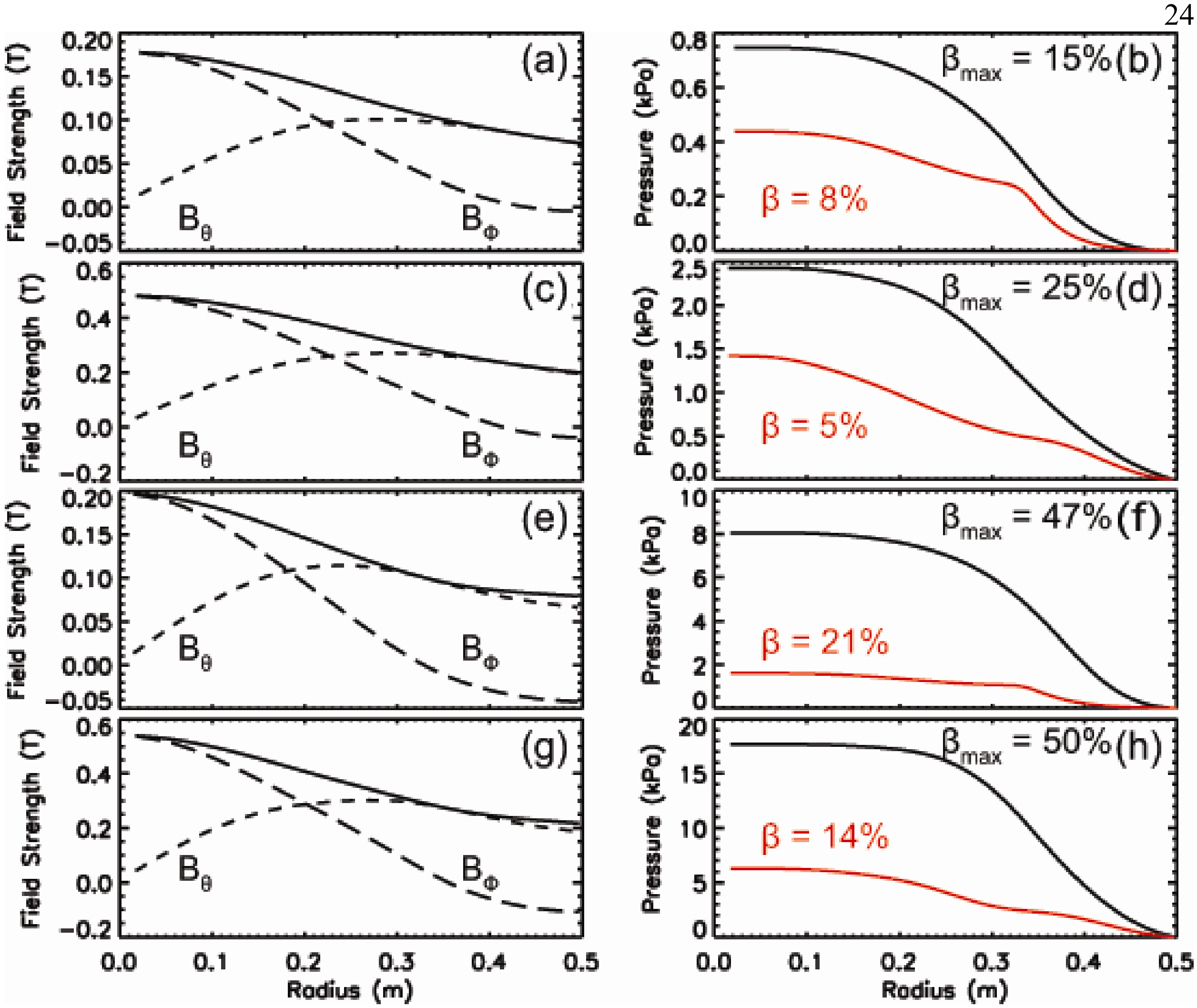

Figure 1.5: Magnetic field profiles (left) and experimental pressure (red) and 'maximum' pressure (black) profiles (right) for 4 plasma conditions on MST; (a,b) 200 kA standard discharge, (c,d) 500 kA standard discharge, (e,f) 200 kA PPCD discharge, and (g,h) 500 kA PPCD discharge. Experimental β (red) and 'maximum' β (black) values associated with Mercier limit on pressure driven interchange modes are shown.

1.5 Summary of Previous Results with Pellet Injection on MST

In this section we highlight a number of key results from previous pellet fueling experiments on MST. [1, 2] Discharges with inductive current profile control technique known as Pulsed Parallel Current Drive (PPCD) were typically limited to a density < $1*10^{19}$ m^{-3} and it was thought that pellet fueling might be a means to achieving a higher density PPCD discharge. Experiments were successful, with high density discharges obtained by injecting a pellet prior to the onset of improved confinement. A record value for β in an RFP of 26% was obtained in pellet fueled improved confinement plasmas at low current. Additionally, an ion temperature increase was observed at high density, but not at low density in these plasmas. This is in part explained by the increased collisional coupling between the electrons and ions in the cold, dense plasmas which result from pellet injection fueling. While confinement is overall improved in high density PPCD experiments, compared to standard discharges, the degree of improvement is less than that of low density PPCD. An increase in tearing mode activity was observed in high density discharges. They were also host to a large pressure gradient exceeding the Mercier criterion in the core of the plasma. Linear stability calculations using the cylindrical DEBS code predicted that pressure driven tearing and interchange instabilities were linearly unstable in the core. Growth rates are plotted in figure 1.6 at their resonant location. The results summarized above come from a close examination of the best case shots for 200 kA and 500 kA PPCD experiments.

Previous density limit experiments on MST utilized pellet injection as well as high throughput gas valve fueling to test agreement with the Greenwald limit for low currents.

Standard discharges fueled from the edge were observed to terminate as density reached the Greenwald limit. The single modified valve was capable of fueling to the limit for plasma currents up to 300 kA. By fueling the core with slow pellets, the density limit was exceeded briefly, though discharges were observed to collapse after a few ms if the density remained high. In PPCD experiments, a density 1.2 times the density limit was achieved at a plasma current of 200 kA without any deleterious effects. Densities of 0.7 times the Greenwald limit were obtained in 500 kA PPCD discharges, limited by the available pellet size.

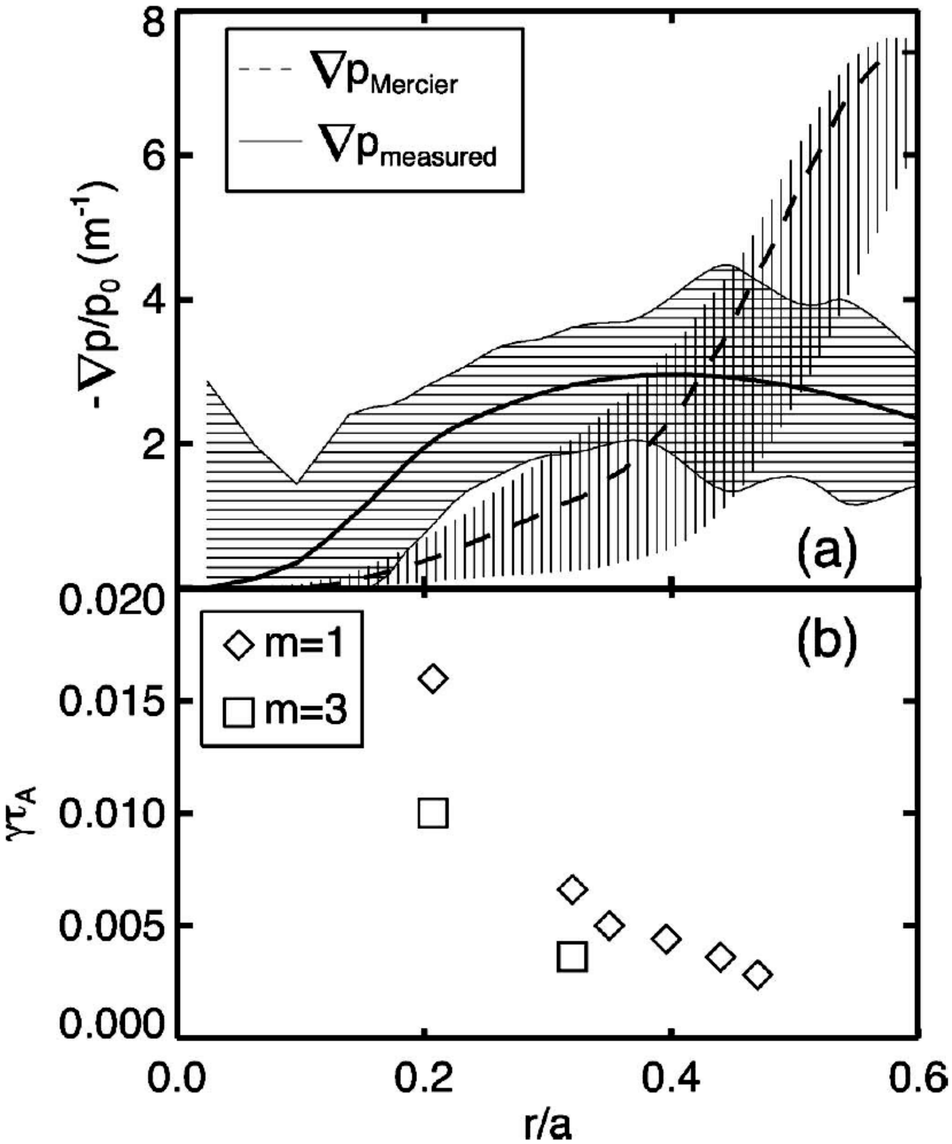

Figure 1.6: (a) Measured (solid) and critical (dashed) pressure gradients for a pellet fueled discharge with improved confinement. Pressure exceeds the critical gradient in the core. (b) Linear growth rate for resistive pressure driven tearing (diamonds) and interchange (square) like modes. Growth rates are plotted at their resonant location. Figure from Reference 2.

1.6 References

1) M.D. Wyman, B.E. Chapman, J.W. Ahn, A.F. Almagri, J.K. Anderson, F. Bonomo, D.L. Brower, S.K. Combs, D. Craig, D.J. Den Hartog, B.H. Deng, W.X. Ding, F. Ebrahimi, D.A. Ennis, G. Fiksel, C.R. Foust, P. Franz, S. Gangadhara, J.A. Goetz, R. O'Connell, S.P. Oliva, S.C. Prager, J.A. Reusch, J.S. Sarff, H.D. Stephens, and T. Yates, Nucl. Fusion **49**, 015003 (2009).

2) M.D. Wyman, B.E. Chapman, J.W. Ahn, A.F. Almagri, J.K. Anderson, F. Bonomo, D.L. Brower, S.K. Combs, D. Craig, D.J. Den Hartog, B.H. Deng, W.X. Ding, F. Ebrahimi, D.A. Ennis, G. Fiksel, C.R. Foust, P. Franz, S. Gangadhara, J. a. Goetz, R. O'Connell, S.P. Oliva, S.C. Prager, J.A. Reusch, J.S. Sarff, H.D. Stephens, and T. Yates, Phys. Plasmas **15**, 010701 (2008).

3) J.B. Taylor, Rev. Mod. Phys. **58**, 741–763 (1986).

4) P. Martin, J. Adamek, P. Agostinetti, M. Agostini, A. Alfier, C. Angioni, V. Antoni, L. Apolloni, F. Auriemma, O. Barana, S. Barison, M. Baruzzo, P. Bettini, M. Boldrin, T. Bolzonella, D. Bonfiglio, F. Bonomo, A.H. Boozer, M. Brombin, J. Brotankova, A. Buffa, A. Canton, S. Cappello, L. Carraro, R. Cavazzana, M. Cavinato, L. Chacon, G. Chitarin, W.A. Cooper, S.D. Bello, M. Dalla Palma, R. Delogu, A. De Lorenzi, G. De Masi, J.Q. Dong, M. Drevlak, D.F. Escande, F. Fantini, A. Fassina, F. Fellin, A. Ferro, S. Fiameni, A. Fiorentin, P. Franz, E. Gaio, X. Garbet, E. Gazza, L. Giudicotti, F. Gnesotto, M. Gobbin, L. Grando, S.C. Guo, Y. Hirano, S.P. Hirshman, S. Ide, V. Igochine, Y. In, P. Innocente, S. Kiyama, S.F. Liu, Y.Q. Liu, D. Lòpez Bruna, R. Lorenzini, A. Luchetta, G. Manduchi, D.K. Mansfield, G. Marchiori, D. Marcuzzi, L. Marrelli, S. Martini, G. Matsunaga, E. Martines, G. Mazzitelli, K. McCollam, S. Menmuir, F. Milani, B. Momo, M. Moresco, S. Munaretto, L. Novello, M. Okabayashi, S. Ortolani, R. Paccagnella, R. Pasqualotto, M. Pavei, G.V. Perverezev, S. Peruzzo, R. Piovan, P. Piovesan, L. Piron, A. Pizzimenti, N. Pomaro, N. Pomphrey, I. Predebon, M.E. Puiatti, V. Rigato, A. Rizzolo, G. Rostagni, G. Rubinacci, A. Ruzzon, H. Sakakita, R. Sanchez, J.S. Sarff, F. Sattin, A. Scaggion, P. Scarin, W. Schneider, G. Serianni, P. Sonato, E. Spada, A. Soppelsa, S. Spagnolo, M. Spolaore, D.A. Spong, G. Spizzo, M. Takechi, C. Taliercio, D. Terranova, V. Toigo, M. Valisa, M. Veranda, N. Vianello, F. Villone, Z. Wang, R.B. White, D. Yadikin, P. Zaccaria, A. Zamengo, P. Zanca, B. Zaniol, L. Zanotto, E. Zilli, G. Zollino, and M. Zuin, Nucl. Fusion **51**, 094023 (2011).

5) H.A.B. Bodin and A.A. Newton, Nucl. Fusion **20**, 1255–1324 (1980).

6) H.A.B. Bodin, Nucl. Fusion **30**, 1717–1737 (1990).

7) A.B. Rechester and M.N. Rosenbluth, Phys. Rev. Lett. **40**, 38–41 (1978).

8) M. Greenwald, Plasma Phys. Control. Fusion **44**, R27–R53 (2002).

9) J.F. Drake, Phys. Fluids **30**, 2429 (1987).

10) M. Persson and A. Bondeson, Nucl. Fusion **29**, 989–998 (1989).

11) V. Mertens, W. Junker, M. Laux, M. Schittenhelm, K. Buchl, F. Mast, A. Carlsont, A. Field, C. Fuchs, O. Gehre, O. Gruber, A. Hermann, G. Haas, A. Kallenbach, M. Kaufmann, W. Koppendorfer, K. Lackner, G. Lieder, S. Pitcher, J. Neuhauser, F. Ryter, H. Salzmann, W. Sandmann, K.-H. Steuer, M. Weinlich, U. Wenzel, H. Zohm, and A.U. Team, Plasma Phys. Control. Fusion **36**, 1307 (1994).

12) R. Yoshino, Y. Neyatani, N. Hosogane, S.W. Wolfe, M. Matsukawa, and H. Ninomiya, Nucl. Fusion **33**, 1599 (1993).

13) M. Bakhtiari, H. Tamai, Y. Kawano, G.J. Kramer, A. Isayama, T. Nakano, Y. Kamiya, R. Yoshino, Y. Miura, Y. Kusama, and Y. Nishida, Nucl. Fusion **45**, 318 (2005).

14) Y. Kamada, N. Hosogane, R. Yoshino, T. Hirayama, and T. Tsunematsu, Nucl. Fusion **31**, 1827–1833 (1991).

15) R.G. Kleva and J.F. Drake, Phys. Fluids B Plasma Phys. **3**, 372–383 (1991).

16) P. de Vries, J. Rapp, F. Schüller, and M. Tokar', Phys. Rev. Lett. **80**, 3519–3522 (1998).

17) R. Maingi, M.A. Mahdavi, T.W. Petrie, L.R. Baylor, T.C. Jernigan, R.J. La Haye, A.W. Hyatt, M.R. Wade, J.G. Watkins, and D.G. Whyte, J. Nucl. Mater. **266–269**, 598–603 (1999).

18) F. Salzedas, S. Hokin, F.C. Schüller, and A. a. M. Oomens, Phys. Plasmas **9**, 3402 (2002).

19) J. Rapp, A. Huber, L.C. Ingesson, S. Jachmich, G.F. Matthews, V. Philipps, and R. Pitts, J. Nucl. Mater. **313–316**, 524–529 (2003).

20) G. Pucella, O. Tudisco, M.L. Apicella, G. Apruzzese, G. Artaserse, F. Belli, W. Bin, L. Boncagni, A. Botrugno, P. Buratti, G. Calabrò, C. Castaldo, C. Cianfarani, V. Cocilovo, L. Dimatteo, B. Esposito, D. Frigione, L. Gabellieri, E. Giovannozzi, G. Granucci, M. Marinucci, D. Marocco, E. Martines, G. Mazzitelli, C. Mazzotta, S. Nowak, G. Ramogida, A. Romano, A.A. Tuccillo, L. Zeng, and M. Zuin, Nucl. Fusion **53**, 083002 (2013).

21) G. Pucella, O. Tudisco, M.L. Apicella, G. Apruzzese, G. Artaserse, F. Belli, W. Bin, L. Boncagni, A. Botrugno, P. Buratti, G. Calabrò, C. Castaldo, C. Cianfarani, V. Cocilovo, L. Dimatteo, B. Esposito, D. Frigione, L. Gabellieri, E. Giovannozzi, G. Granucci, M. Marinucci, D. Marocco, E. Martines, G. Mazzitelli, C. Mazzotta, S. Nowak, G. Ramogida, A. Romano, A.A. Tuccillo, L. Zeng, and M. Zuin, Nucl. Fusion **53**, 023007 (2013).

22) D.A. Gates and L. Delgado-Aparicio, Phys. Rev. Lett. **108**, 165004 (2012).

23) D.A. Gates, L. Delgado-Aparicio, and R.B. White, Nucl. Fusion **53**, 063008 (2013).

24) F.W. Perkins and R.A. Hulse, Phys. Fluids **28**, 1837–1844 (1985).

25) S. Ortolani and G. Rostagni, Nucl. Instruments Methods Phys. Res. **207**, 35–48 (1983).

26) M.E. Puiatti, P. Scarin, G. Spizzo, M. Valisa, M. Agostini, A. Alfier, A. Canton, L. Carraro, E. Gazza, R. Lorenzini, R. Paccagnella, I. Predebon, D. Terranova, D. Bonfiglio, S. Cappello, R. Cavazzana, S. Dal Bello, P. Innocente, L. Marrelli, R. Piovan, P. Piovesan, F. Sattin, and P. Zanca, Nucl. Fusion **49**, 045012 (2009).

27) M.E. Puiatti, P. Scarin, G. Spizzo, M. Valisa, R. Paccagnella, I. Predebon, M. Agostini, A. Alfier, A. Canton, S. Cappello, L. Carraro, E. Gazza, P. Innocente, R. Lorenzini, L. Marrelli, and D. Terranova, Phys. Plasmas **16**, 012505 (2009).

28) G. Spizzo, P. Scarin, M. Agostini, A. Alfier, F. Auriemma, D. Bonfiglio, S. Cappello, A. Fassina, P. Franz, L. Piron, P. Piovesan, M.E. Puiatti, M. Valisa, and N. Vianello, Plasma Phys. Control. Fusion **52**, 095011 (2010).

29) P. Scarin, M. Agostini, L. Carraro, A. Scaggion, G. Spizzo, M. Spolaore, and N. Vianello, J. Nucl. Mater. **438, Suppl**, S550–S553 (2013).

30) S. Sudo, Y. Takeiri, H. Zushi, F. Sano, K. Itoh, K. Kondo, and A. Iiyoshi, Nucl. Fusion **30**, 11–21 (1990).

31) L. Giannone, J. Baldzuhn, R. Burhenn, P. Grigull, U. Stroth, F. Wagner, R. Brakel, C. Fuchs, H.J. Hartfuss, K. McCormick, A. Weller, C. Wendland, NBI Team, ECRH Team, W7-AS Team, K. Itoh, and S.-I. Itoh, Plasma Phys. Control. Fusion **42**, 603–627 (2000).

32) J. Miyazawa, R. Sakamoto, S. Masuzaki, B.J. Peterson, N. Tamura, M. Goto, I. Yamada, K. Narihara, K. Tanaka, T. Tokuzawa, M. Shoji, M. Kobayashi, H. Arimoto, K. Kondo, S. Murakami, H. Funaba, S. Sakakibara, M. Osakabe, S. Morita, Y. Nagayama, N. Ohyabu, H. Yamada, A. Komori, O. Motojima, and the L.E. Group, Nucl. Fusion **48**, 015003 (2008).

33) B.J. Peterson, J. Miyazawa, K. Nishimura, S. Masuzaki, Y. Nagayama, N. Ohyabu, H. Yamada, K. Yamazaki, T. Kato, I. Murakami, N. Ashikawa, Y. Xu, A.Y. Kostrioukov, Y. Liu, R. Sakamoto, M. Goto, K. Narihara, M. Osakabe, K. Tanaka, T. Tokuzawa, M. Shoji, H. Funaba, S. Morita, T. Morisaki, O. Kaneko, K. Kawahata, A. Komori, S. Sudo, O. Motojima, and the L.E. Group, Plasma Fusion Res. **1**, 045–045 (2006).

34) B.J. Peterson, Y. Xu, S. Sudo, T. Tokuzawa, K. Tanaka, M. Osakabe, S. Morita, M. Goto, S. Sakakibara, J. Miyazawa, K. Kawahata, N. Ohyabu, H. Yamada, O. Kaneko, A. Komori, and L.E. Group, Phys. Plasmas **8**, 3861–3864 (2001).

35) L. Giannone, R. Brakel, R. Burhenn, H. Ehmler, Y. Feng, P. Grigull, K. McCormick, F. Wagner, J. Baldzuhn, Y. Igitkhanov, J. Knauer, K. Nishimura, E. Pasch, B.J. Peterson, N. Ramasubramanian, N. Rust, A. Weller, A. Werner, and the W.-A. Team, Plasma Phys. Control. Fusion **45**, 1713–1731 (2003).

36) R. Lorenzini, E. Martines, P. Piovesan, D. Terranova, P. Zanca, M. Zuin, A. Alfier, D. Bonfiglio, F. Bonomo, A. Canton, S. Cappello, L. Carraro, R. Cavazzana, D.F. Escande, A. Fassina, P. Franz, M. Gobbin, P. Innocente, L. Marrelli, R. Pasqualotto, M.E. Puiatti, M. Spolaore, M. Valisa, N. Vianello, P. Martin, L. Apolloni, J. Adamek, M. Agostini, S. V. Annibaldi, V. Antoni, F. Auriemma, O. Barana, M. Baruzzo, P. Bettini, T. Bolzonella, M. Brombin, J. Brotankova, A. Buffa, P. Buratti, M. Cavinato, B.E. Chapman, G. Chitarin, S.D. Bello, A. De Lorenzi, G. De Masi, A. Ferro, E. Gaio, E. Gazza, L. Giudicotti, F. Gnesotto, L. Grando, L. Guazzotto, S.C. Guo, V. Igochine, Y.Q. Liu, A. Luchetta, G. Manduchi, G. Marchiori, D. Marcuzzi, S. Martini, K. McCollam, F. Milani, M. Moresco, L. Novello, S. Ortolani, R. Paccagnella, S. Peruzzo, R. Piovan, L. Piron, A. Pizzimenti, N. Pomaro, I. Predebon, J.A. Reusch, G. Rostagni, G. Rubinacci, J.S. Sarff, F. Sattin, P. Scarin, G. Serianni, P. Sonato, E. Spada, A. Soppelsa, S. Spagnolo, G. Spizzo, C. Taliercio, V. Toigo, F. Villone, R.B. White, D. Yadikin, P. Zaccaria, A. Zamengo, B. Zaniol, L. Zanotto, E. Zilli, and H. Zohm, Nat. Phys. **5**, 570–574 (2009).

37) J.A. Wesson and A. Sykes, Nucl. Fusion **25**, 85 (1985).

38) J.J. Ramos, Phys. Fluids B Plasma Phys. **3**, 2247–2250 (1991).

39) J.P. Freidberg, *Ideal Magnetohydrodynamics* (1987), p. 489.

40) L.C. Bernard, F.J. Helton, R.W. Moore, and T.N. Todd, Nucl. Fusion **23**, 1475 (1983).

41) H.R. Koslowski, G. Fuchs, R. Jaspers, A. Krämer-Flecken, A.M. Messiaen, J. Ongena, J. Rapp, F.C. Schüller, and M.Z. Tokar', Nucl. Fusion **40**, 821 (2000).

42) Y. Ishii, T. Ozeki, S. Tokuda, T. Fujita, Y. Kamada, S. Ishida, and S. Takeji, Plasma Phys. Control. Fusion **40**, 1607 (1998).

43) D.A. Kislov, Y. V. Esipchuk, N.A. Kirneva, I. V. Klimanov, Y.D. Pavlov, A.A. Subbotin, V. V. Alikaev, A.A. Borshegovskiy, Y. V. Gott, A.M. Kakurin, S. V. Krilov, T.B. Myalton, I.N. Roy, E. V. Trukhina, V. V. Volkov, and T.-10 Team, Nucl. Fusion **41**, 1619 (2001).

44) R.J. La Haye, B.W. Rice, and E.J. Strait, Nucl. Fusion **40**, 53 (2000).

45) M. Hirsch, J. Baldzuhn, C. Beidler, R. Brakel, R. Burhenn, A. Dinklage, H. Ehmler, M. Endler, V. Erckmann, Y. Feng, J. Geiger, L. Giannone, G. Grieger, P. Grigull, H.-J. Hartfuß, D. Hartmann, R. Jaenicke, R. König, H.P. Laqua, H. Maaßberg, K. McCormick, F. Sardei, E. Speth, U. Stroth, F. Wagner, A. Weller, A. Werner, H. Wobig, S. Zoletnik, and for the W.-A. Team, Plasma Phys. Control. Fusion **50**, 053001 (2008).

46) A.H. Boozer, Plasma Phys. Control. Fusion **50**, 124005 (2008).

47) A. Weller, J. Geiger, A. Werner, M.C. Zarnstorff, C. Nührenberg, E. Sallander, J. Baldzuhn, R. Brakel, R. Burhenn, A. Dinklage, E. Fredrickson, F. Gadelmeier, L. Giannone, P. Grigull, D. Hartmann, R. Jaenicke, S. Klose, J.P. Knauer, A. Könies, Y.I. Kolesnichenko, H.P. Laqua, V. V. Lutsenko, K. McCormick, D. Monticello, M. Osakabe, E. Pasch, A. Reiman, N. Rust, D.A. Spong, F. Wagner, Y. V. Yakovenko, W.-A. Team, and NBI-Group, Plasma Phys. Control. Fusion **45**, A285 (2003).

48) A. Weller, M.C. Zarnstorff, and S. Ohdachi, **50**, (2006).

49) S. Sakakibara, K.Y. Watanabe, Y. Suzuki, Y. Narushima, S. Ohdachi, N. Nakajima, F. Watanabe, L. Garcia, A. Weller, K. Toi, I. Yamada, K. Tanaka, T. Tokuzawa, K. Ida, H. Yamada, A. Komori, O. Motojima, and the L.E. Group, Plasma Phys. Control. Fusion **50**, 124014 (2008).

50) H. Koguchi, H. Sakakita, S. Kiyama, K. Yambe, T. Asai, Y. Hirano, F. Auriemma, D. Terranova, and P. Innocente, Plasma Fusion Res. **4**, 022–022 (2009).

51) D.C. Robinson, Plasma Phys. **13**, 439–462 (1971).

52) J.-E. Dahlin and J. Scheffel, Nucl. Fusion **47**, 1184–1188 (2007).

53) C. Mercier, Nucl. Fusion **1**, 47–53 (1960).

54) F. Ebrahimi, S.C. Prager, and C.R. Sovinec, Phys. Plasmas **9**, 2470–2473 (2002).

55) R. Paccagnella, Phys. Plasmas **20**, 012119 (2013).

56) M. Zuin, S. Spagnolo, R. Paccagnella, E. Martines, R. Cavazzana, G. Serianni, M. Spolaore, and N. Vianello, Nucl. Fusion **50**, 052001 (2010).

57) R. Paccagnella, A. Bondeson, and H. Lütjens, Nucl. Fusion **31**, 1899–1907 (1991).

58) S. C. Guo, X. Y. Xu, Z. R. Wang, and Y. Q. Liu, Nucl. Fusion **53**, 113035 (2013)

CHAPTER 2

Experimental Setup and Hardware Information

2.1 Introduction

The details of the Madison Symmetric Torus (MST) plasma experiment as well as the pellet injector system and the relevant diagnostics will be discussed in this chapter. Highlights include a look at the injector upgrade to accommodate 4.0 mm diameter pellets along with an overview of the pellet formation process and other aspects of injector operation. Some additional material pertaining to the pellet injector is available in the appendices.

2.2 The Madison Symmetric Torus

As far as RFP's are concerned, MST is one of the largest currently in operation with a major radius of 1.5 m and a minor radius of 0.52 m. [1] MST utilizes a large number and variety of diagnostics which usually obscure the view of the vessel, however, figure 2.1 shows an atypically bare view of the experiment including the four gate valves through which pellets are injected. The plasma current in MST ranges from 200 to 600 kA with magnetic fields of 0.2 to 0.6 Tesla on the magnetic axis. Pulse lengths up to 80 ms with 20 ms current flat tops can be obtained with a shot cycle time of 2-5 minutes depending on the desired plasma current. The typical MST discharge is edge fueled through a combination of wall recycling and gas puffing from 6 valves separated toroidally around the machine as shown in figure 2.2 along with the location of the pellet injector. For the purposes of this thesis, all experiments are fueled with deuterium gas puffing, although hydrogen and helium are also used as fuel gasses on MST. The typical plasma density is $1*10^{19}$ m^{-3} when fueled only by edge gas puffing and wall recycling. Electron temperatures of up to 2 keV are obtained in the hottest plasmas. The plasma current in MST is generated through transformer action with the wound iron core acting as the primary and the plasma acting as the secondary circuit of the transformer. With little exception, the portholes on MST are intentionally small in order to limit the impact of error fields on the plasma operation. MST's vacuum vessel, a 5 cm thick shell of aluminum, also doubles as a single turn toroidal field winding. The close fitting conducting shell is also important for wall stabilization of instabilities.

As an experimental fueling technique, pellet fueling has been used in a variety of ways to fuel several different modes of operation. The relevant modes of operation will be discussed further.

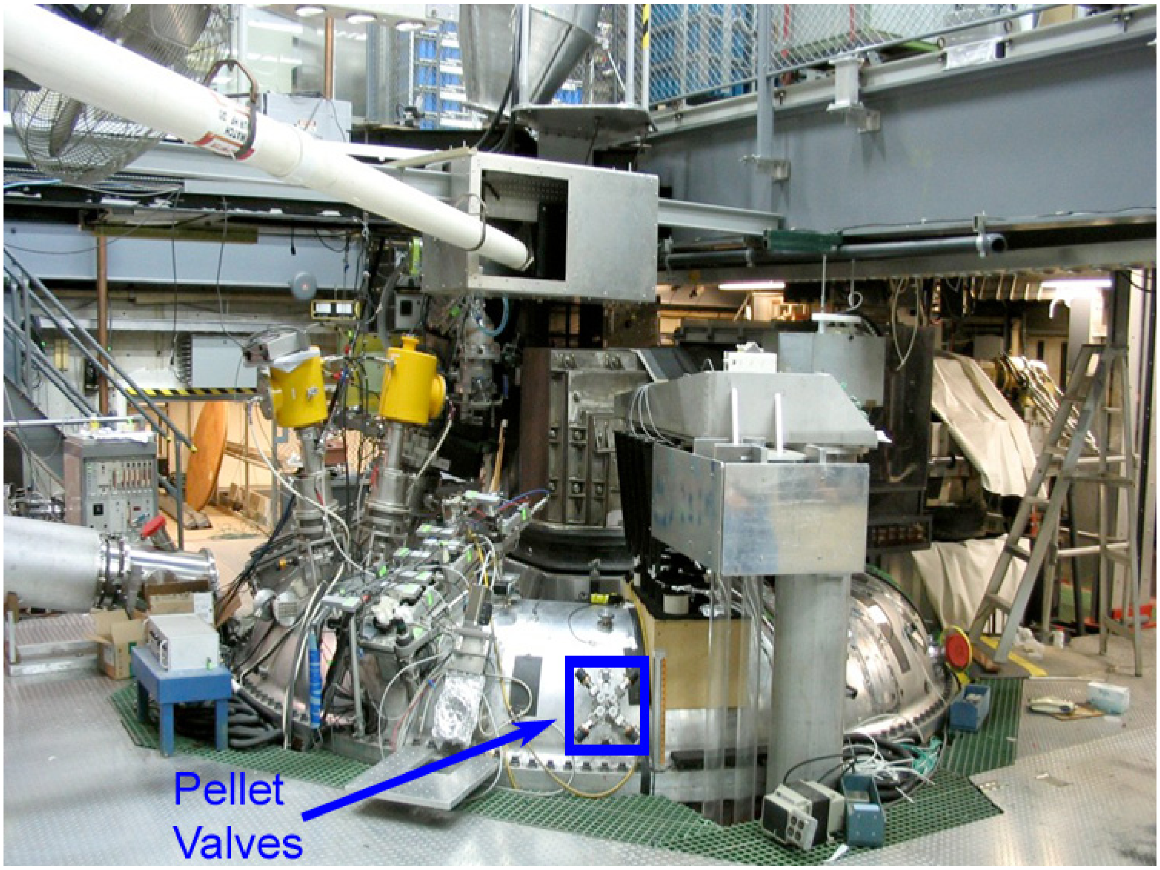

Figure 2.1: A rare picture of the Madison Symmetric Torus (MST) experiment with much of the vessel visible. The four pellet gate valves where pellets enter the vessel are highlighted.

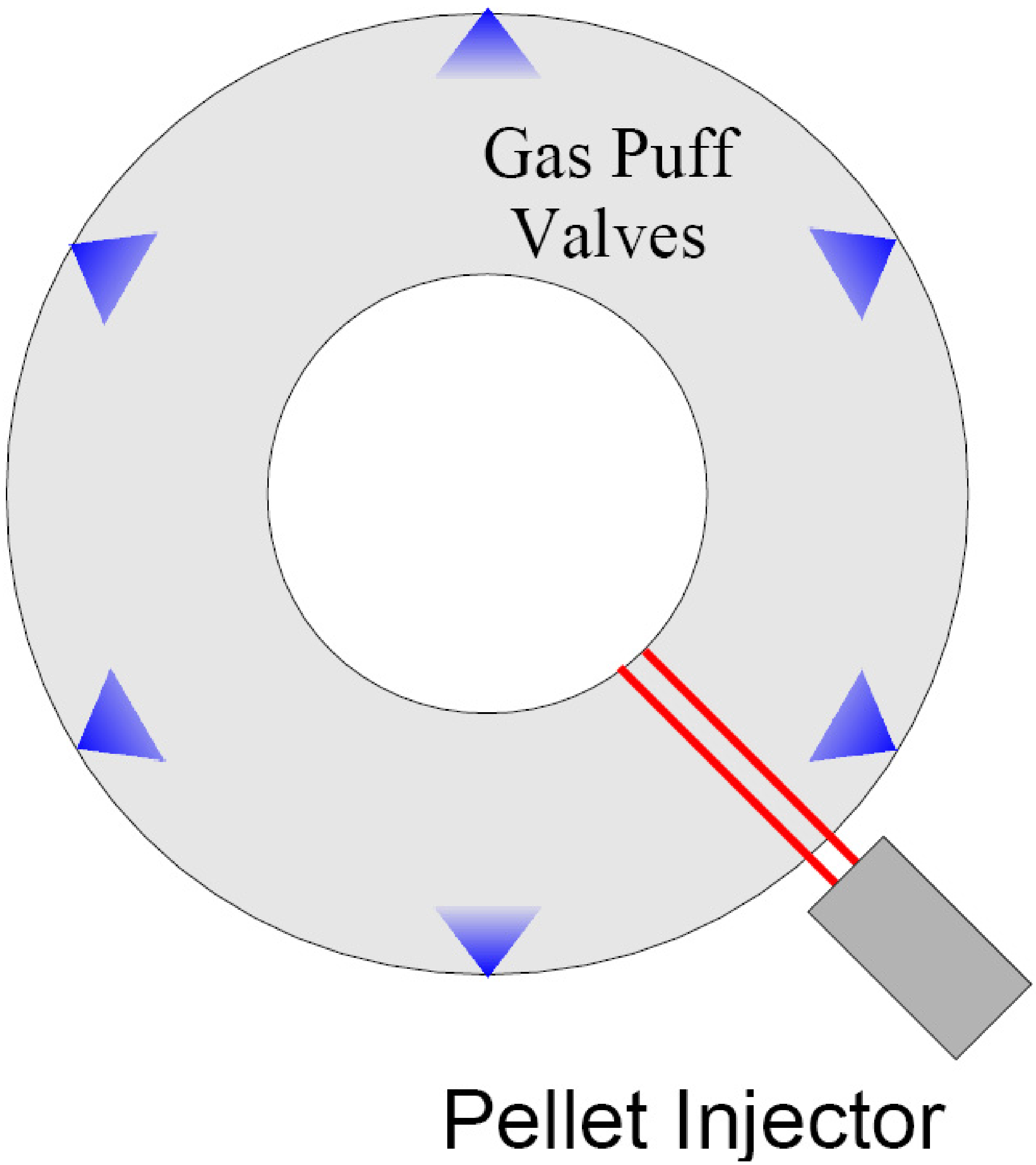

Figure 2.2: A topside cartoon of MST is shown, highlighting the location of the gas puff valves as well as the location of the pellet injector and pellet injection lines.

2.2.1 The Standard MST Discharge

The goal of studying standard MST discharges was primarily to explore the nature of the plasma density limit on MST as described in chapter 3. In figure 2.3, operational signals from a standard reversed discharge are shown. After the initial current ramp up, the current is sustained for a maximum of 20 ms. Two important parameters for characterizing an RFP discharge are the reversal and pinch parameters F and Θ defined by

$$F \equiv \frac{B_\varphi(a)}{\left\langle B_\varphi \right\rangle} \tag{2.1}$$

$$\Theta \equiv \frac{B_\theta(a)}{\left\langle B_\varphi \right\rangle} \tag{2.2}$$

where B(a) refers to the field strength at the wall (r = a), $\left\langle B_\varphi \right\rangle$ refers to the average field strength and φ, θ refer to the toroidal and poloidal components of the field respectively. Typical values for F and Θ are -0.2 and 1.6 during the current flat top, though both values can be varied through the adjustment of capacitor bank voltages. As discussed in chapter 1, the tearing modes resonant in the edge and the core have sufficient overlap in the standard discharge to produce a stochastic field which limits confinement in the core of the plasma, but the global confinement times are approximately 1 ms in the standard RFP discharge governed primarily by transport in the edge. [2] The puncture plot in figure 2.4 shows the nature of this stochasticity using experimentally measured mode amplitudes.

MST can also be operated without reversal at the edge, forcing the toroidal field to go to zero at the conducting wall. This has a subtle but important impact on the q profile. The on axis q value is slightly larger, enough so that in these non-reversed discharges the m = 1, n = 5 tearing mode tends to be the innermost resonant mode instead of the m = 1, n = 6 mode normally resonant in reversed discharges. The m = 0 resonant surface is also removed from the plasma resulting in a decrease in m = 0 activity.

The standard reversed discharge has periodic bursts of activity associated with reconnection events known as sawtooth crashes. [4] During these events, a process known as the plasma dynamo generates toroidal flux. Non-reversed discharges tend to have a weakened sawtooth cycle if any at all.

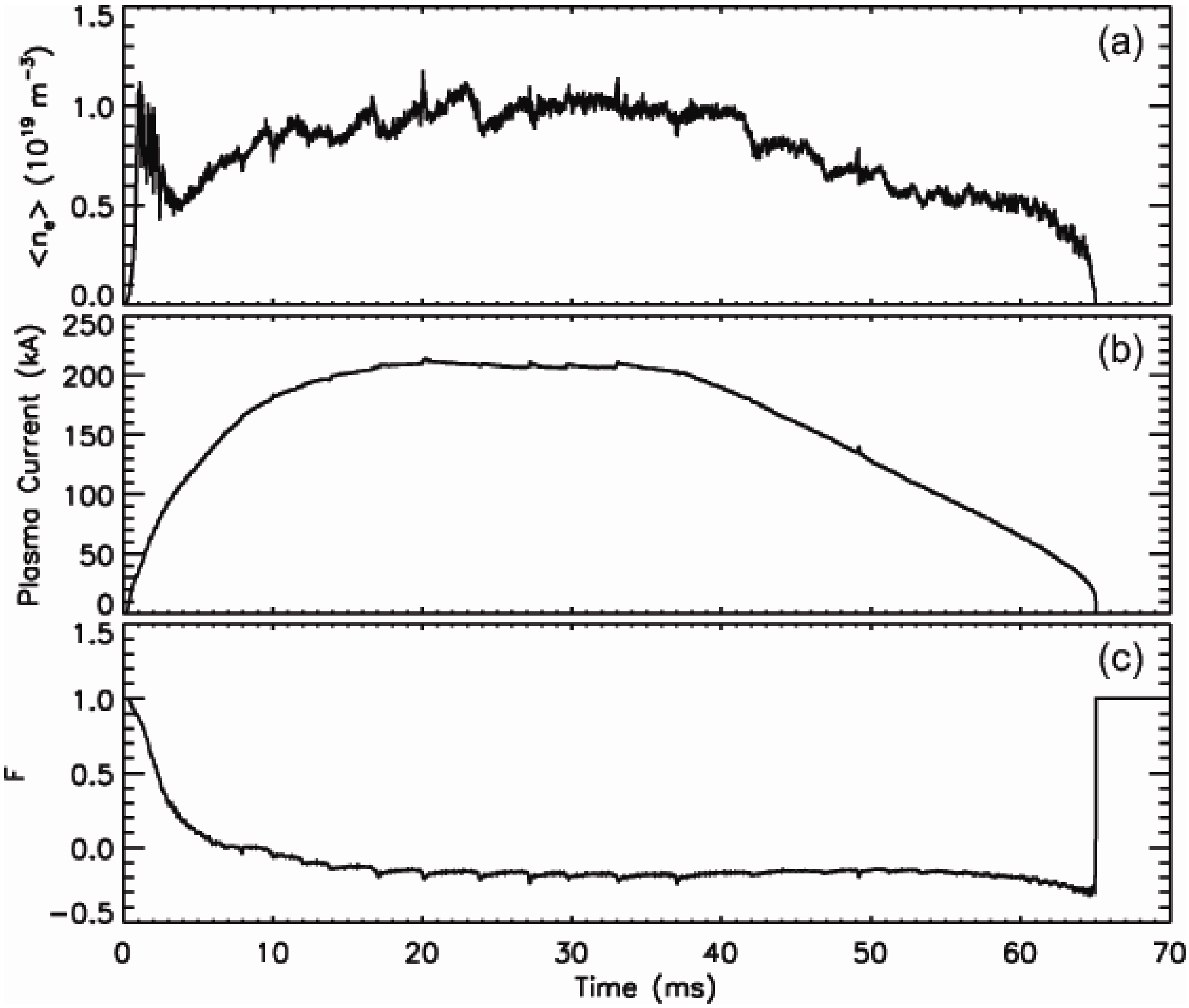

Figure 2.3: Representative signals for the (a) line averaged plasma density, (b) plasma current and (c) reversal parameter are shown for a standard MST discharge. [Shot 1130318040]

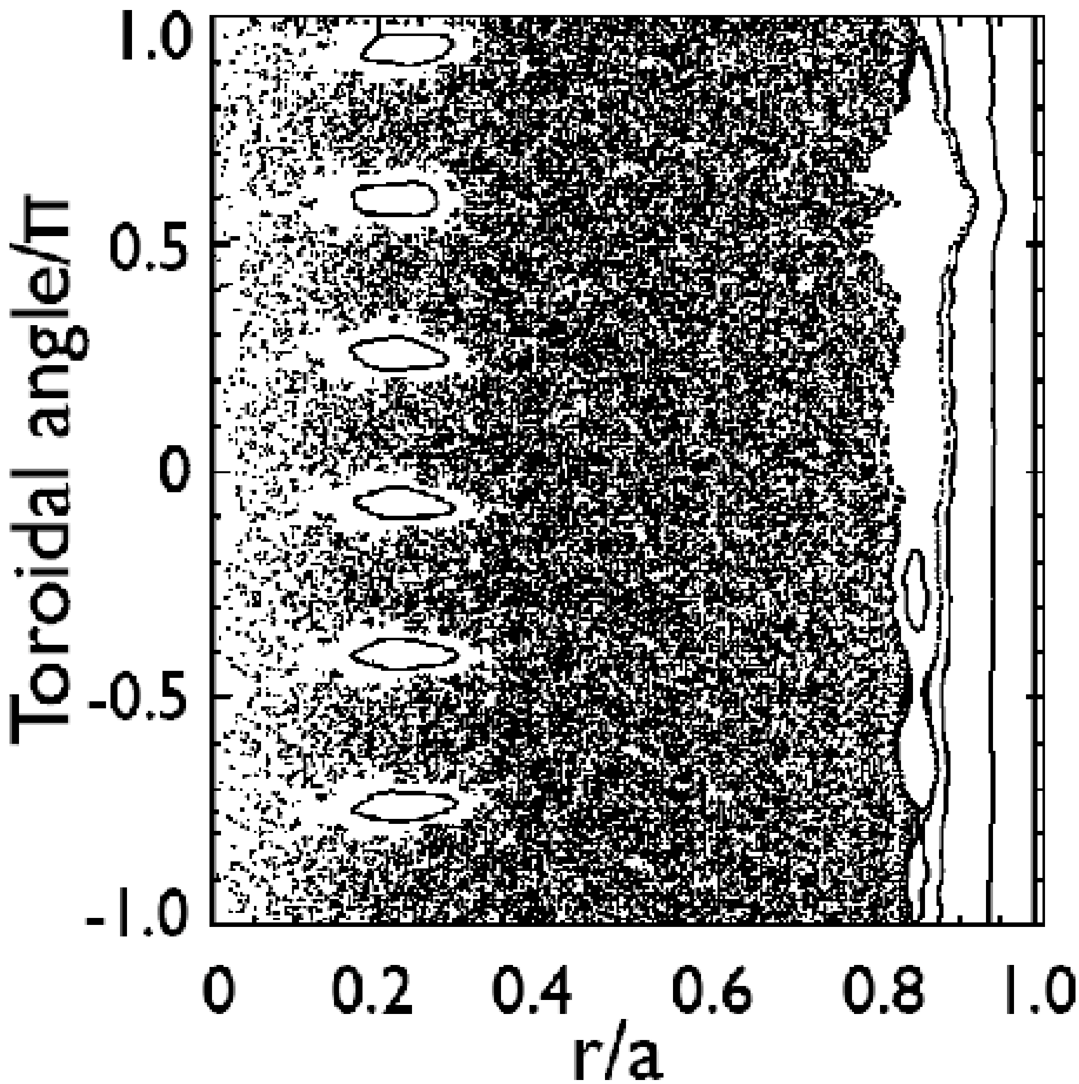

Figure 2.4: A puncture plot of a standard MST discharge with significant island overlap. The n = 6 structure is visible in the core. The resulting stochastic field contributes to particle and energy transport in the core. From Reference 3.

2.2.2 Pulsed Parallel Current Drive (PPCD)

The tearing instabilities responsible for the poor confinement of the standard RFP are driven primarily by current gradients in the plasma. Pulsed Parallel Current Drive (PPCD) is a transient method of current profile control that inductively drives current in the edge, decreasing the drive for magnetic fluctuations in both the edge (m = 0) and the core (m = 1) which leads to an improvement in confinement. [5] This is done by driving a poloidal current in the shell (also the toroidal field winding). This produces a poloidal electric field at the edge driving poloidal current in such a way as to increase the reversed magnetic field in the edge. The response to this increasing field in the edge of the plasma is an increase in parallel plasma current, flattening the overall current profile, reducing the instability drive. A diagram of the PPCD circuit is shown in figure 2.5 and the applied edge electric field along with the core and edge modes are shown in the signals of figure 2.6. The edge parallel electric field is driven positively, and the m = 0 and m = 1 instabilities are both reduced shortly thereafter. The improved confinement period following application of PPCD typically lasts approximately 10 ms.

Improved confinement with PPCD is limited to low density ($n_e < 1*10^{19}$ m^{-3}) with only edge fueling due to the gas puffing and recycling destabilizing the m = 0 modes which ultimately limit the confinement. For this reason, PPCD discharges are a prime target for high density fueling with the pellet injector, as the fuel can be deposited directly in the core with limited perturbation of the plasma. While the pellet does perturb the plasma during ablation, more fuel can be deposited much more rapidly than other fueling methods. PPCD experiments with pellet fueling and NBI heating are the focus of chapters 4 and 5.

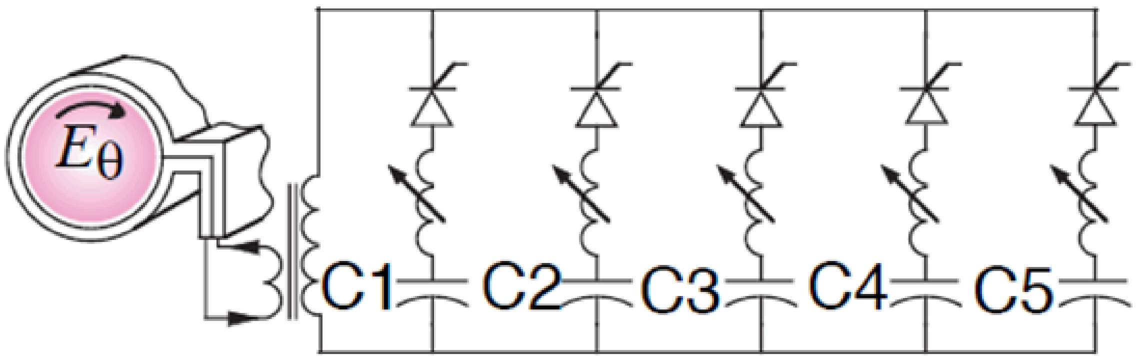

Figure 2.5: The diagram for the PPCD circuit shows the 5 capacitor bank stages which are discharged sequentially to inductively drive current in the shell. The plasma responds with an edge current drive, flattening the current profile and reducing the instability drive.

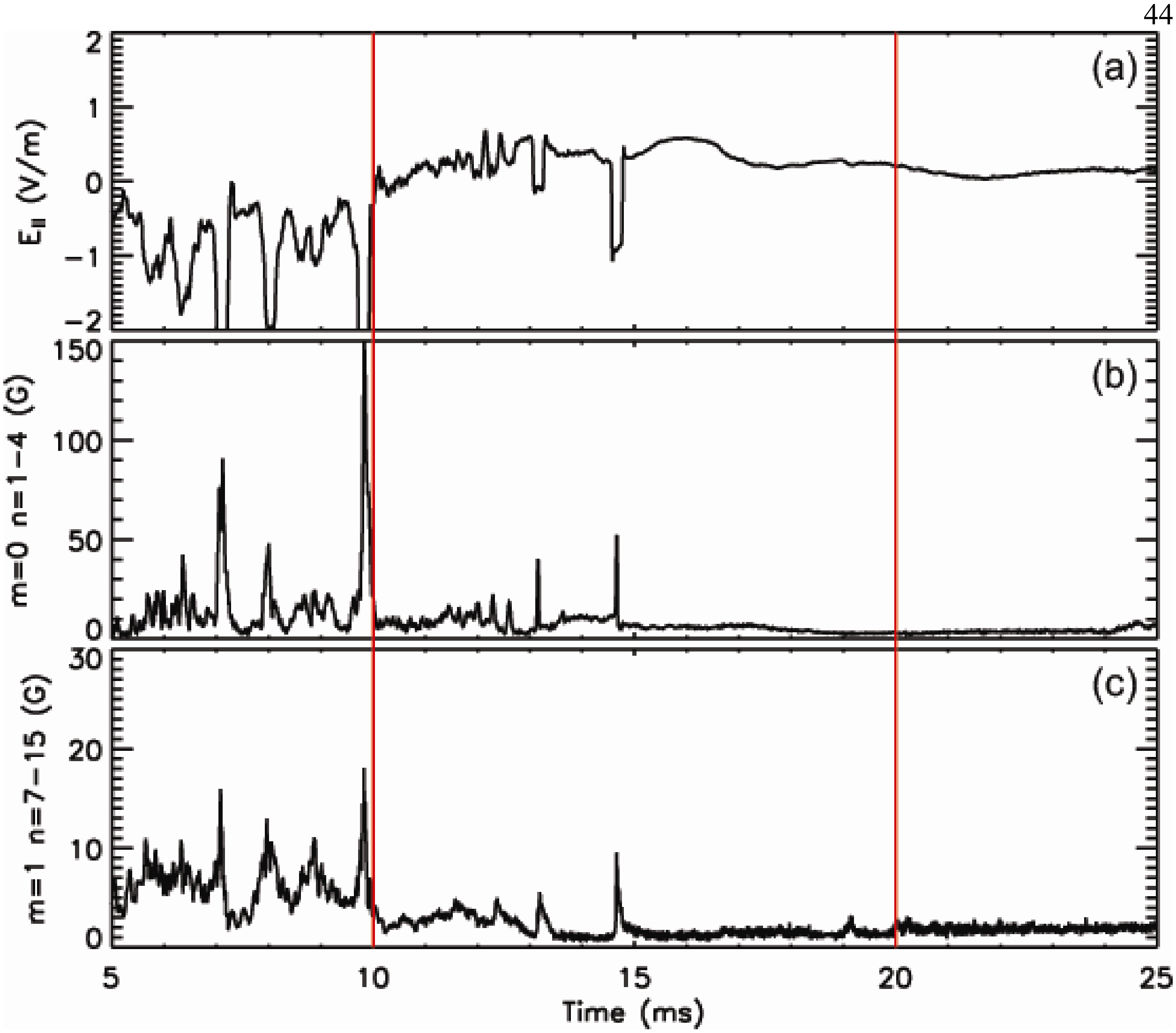

Figure 2.6: (a) parallel electric field at the wall, (b) RMS edge mode fluctuations and (c) RMS core mode fluctuations for a representative PPCD discharge on MST. The application of PPCD from 10-20 ms is marked by the vertical red lines. [Shot 1130305058]

2.2.3 Quasi-Single-Helicity and Single-Helical-Axis Plasmas (QSH/SHAx)

Recently, a new plasma regime has become a primary focus for RFP research. In this regime, the plasma spontaneously transitions to a state with a single large magnetic structure (the inner most resonant m = 1 mode) while the secondary modes are observed to decrease in amplitude. This Quasi Single Helicity (QSH) state is in contrast to the Multiple Helicity (MH) state of the standard RFP where all of the modes have comparable amplitudes. In some cases, the dominant mode grows sufficiently large and can encompass the original Shafranov-shifted magnetic axis, transitioning to a plasma with a Single Helical Axis (SHAx). [6] An improvement in confinement has been observed in such regimes and their spontaneous and self-organized nature makes them an intriguing avenue of research for the RFP.

The conditions which promote the growth of the dominant mode in MST are shallow reversal (F = 0 for this Thesis), high current (> 500kA) and low density (0.5 - 0.7e19 m^{-3}). Typical operational signals for a SHAx discharge on MST are shown in figure 2.7.

Similar to the PPCD pellet experiments, the SHAx plasmas are an attractive target for pellet fueling in part because they appear to be inherently limited to low density. These experiments will be discussed further in chapter 6.

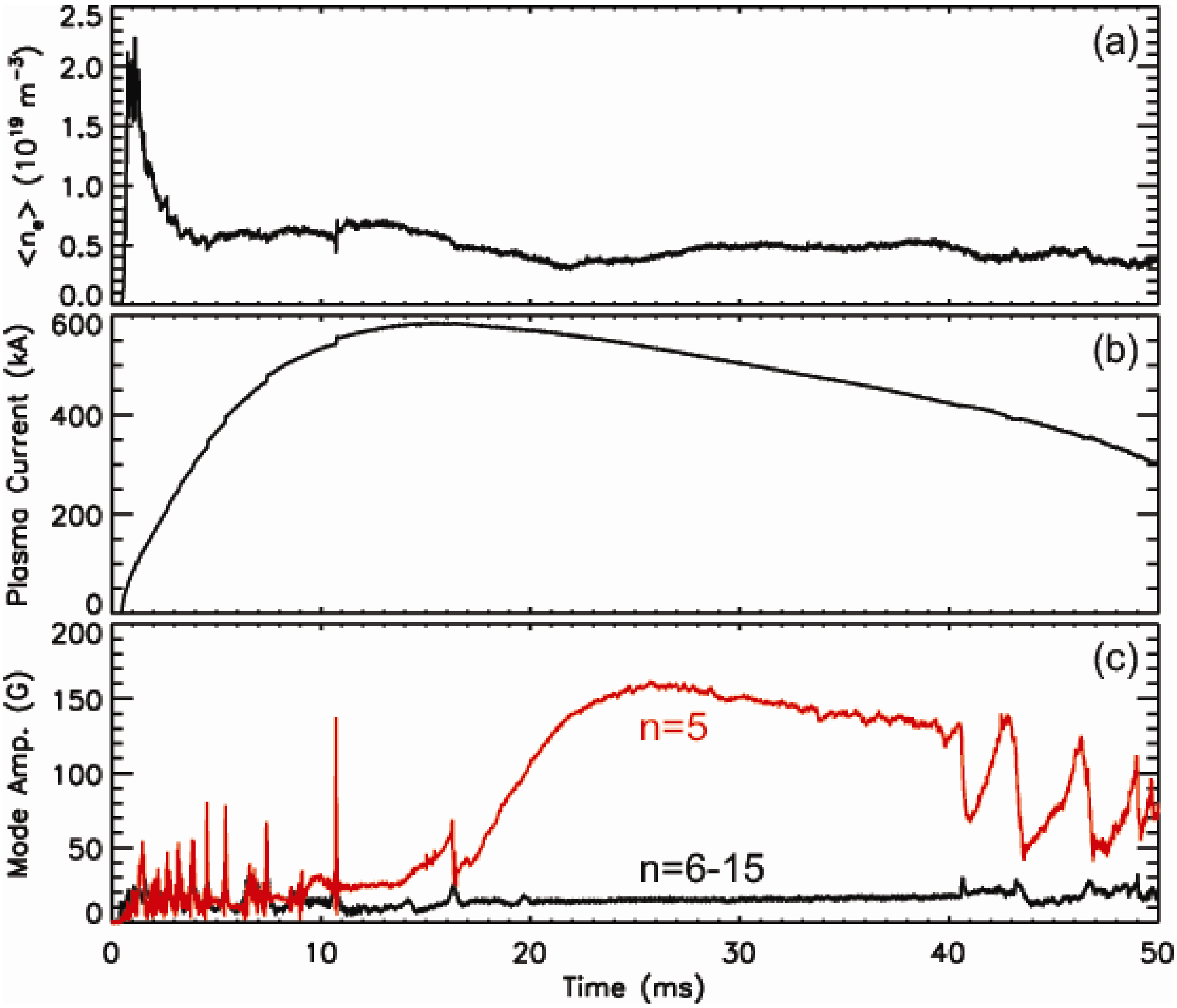

Figure 2.7: (a) Plasma density, (b) current (c) and dominant (red) and secondary (black) mode amplitudes for a representative QSH/SHAx discharge on MST. The amplitudes for the dominant m = 1, n = 5 mode (red) and secondary modes (black) are plotted. The value for the secondary modes is an RMS average of m = 1, n = 6-15. [Shot 1110412037]

2.3 Pellet Injection System

The combination of gas puffing and wall recycling is sufficient for the majority of experiments on MST; however, these edge based fueling techniques have their limitations when it comes to high density operation as they lead to hollow density profiles when used excessively. Pellet injection fueling allows us to explore various aspects of high density operation on MST as well as giving some limited control over the density profile. Pellet fueling provides the capability for peaked, flat or hollow density profiles depending on the ablation of the pellet.

2.3.1 Hardware details

MST's pellet injector is part of an ongoing collaboration with Oak Ridge National Labs (ORNL). [7] It is a four-barrel pipe-gun [8] injector originally designed to inject deuterium pellets with diameters of 1.0-2.0 mm and a length-to-diameter ratio (L/D) of 1-3. After a recent upgrade of the pellet guide tubes, which constrain the pellet flight into the MST vessel, the injector can now support pellets with a diameter up to 4.0 mm. This upgrade will be discussed in detail later in this chapter. The injector is capable of launching pellets at a variety of velocities. The primary methods of pellet propulsion are high pressure gas and mechanical punch. The gas valves and punches are both solenoid driven. Figure 2.8 shows a schematic drawing of the injector from the MST vessel to the gas manifold which houses the fuel and propellant gas lines. Pellets are injected radially from the outboard side, at an angle 30 degrees above the midplane. Also shown are a few relevant diagnostics, the light gate and microwave cavity used to measure pellet speed and mass in flight. The surge tanks which limit the amount of propellant gas that makes it downstream to the MST gate valves are also shown. Figure 2.9 shows a photo of the pellet injection system.

The typical velocity for pellets fired with the close-coupled gas valves is 1000 - 1200m/s. Mechanical punch driven pellets are propelled at speeds of 100 - 200 m/s. When combined with a gas valve, combination (both punch and gas) driven pellets reach speeds of 300 - 400 m/s. The light gate measurement triggers as the pellet crosses that location and the microwave cavity registers a pulse whose amplitude is proportional to the pellet mass. These diagnostics are separated by 0.93 m, shown in figure 2.10, and together they are used to measure the speed and in turn estimate the time the pellet will arrive at the plasma. Further details of pellet hardware can be found in [9] as well as the appendix of this thesis.

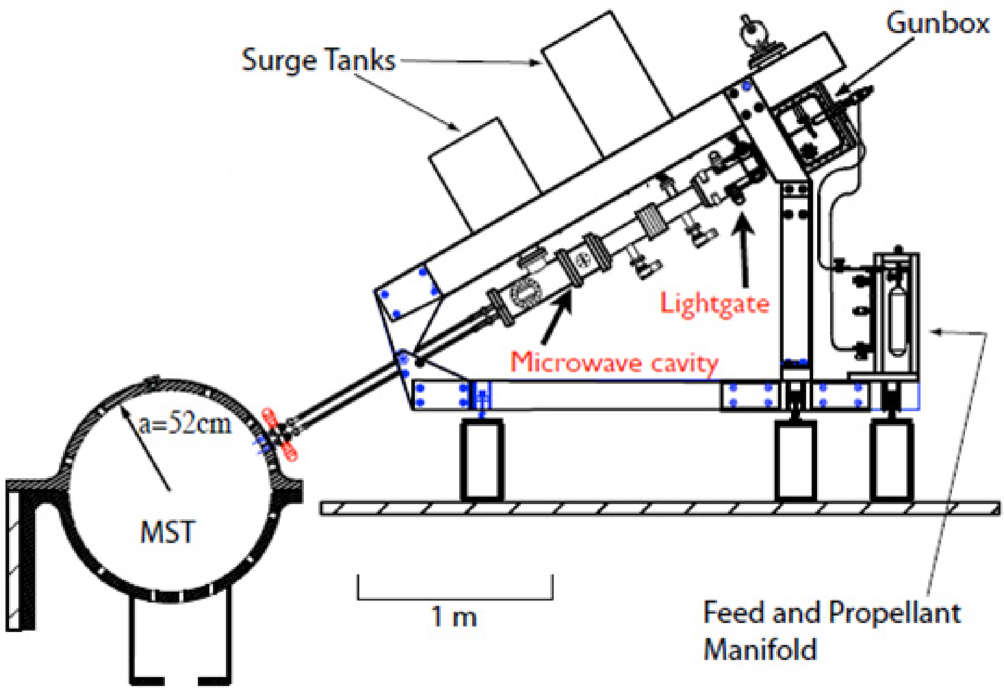

Figure 2.8: A schematic drawing of the pellet injector showing the gunbox, where the pellet barrels are located and where the pellets are formed. A cross section of the MST vacuum vessel shows the injection geometry. The two surge tanks limit the amount of residual pellet fuel and propellant gas which reach the MST vessel.

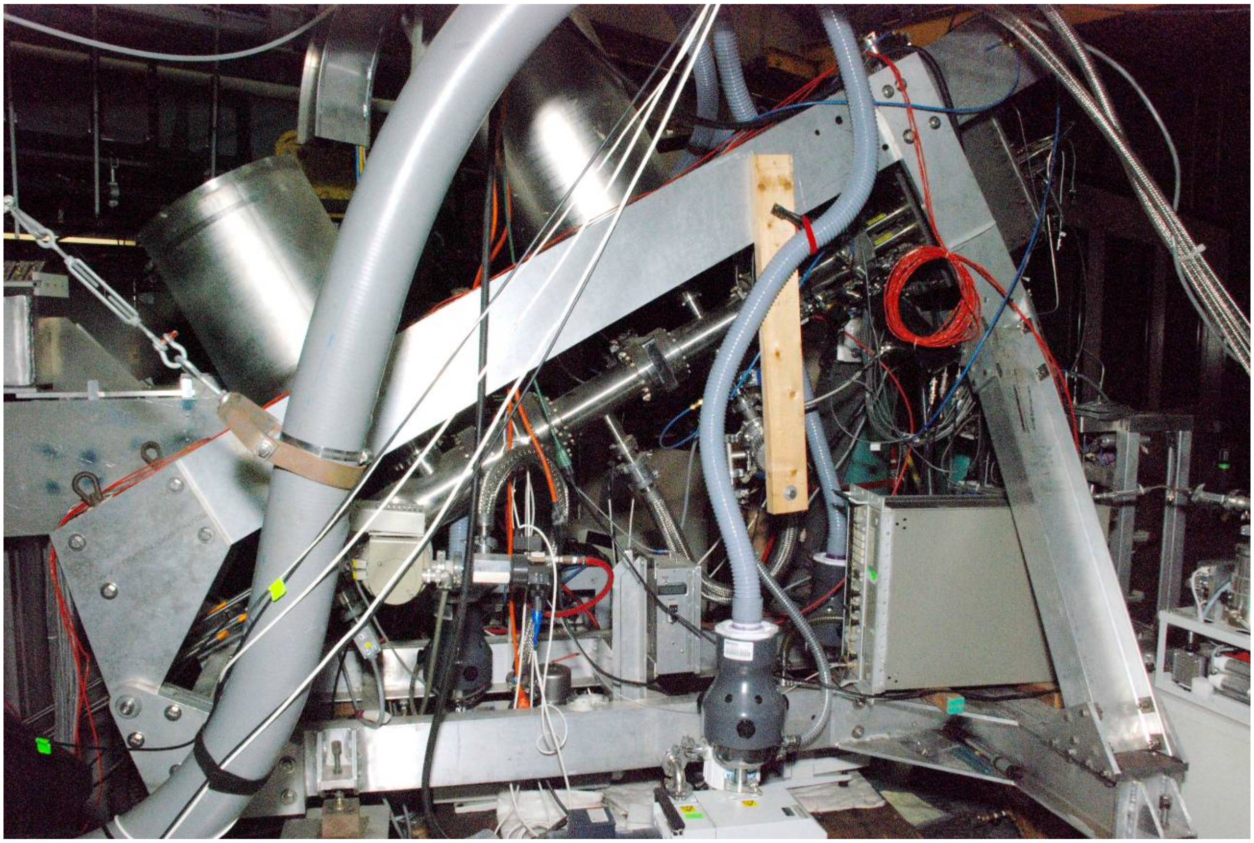

Figure 2.9: The pellet injector system on MST.

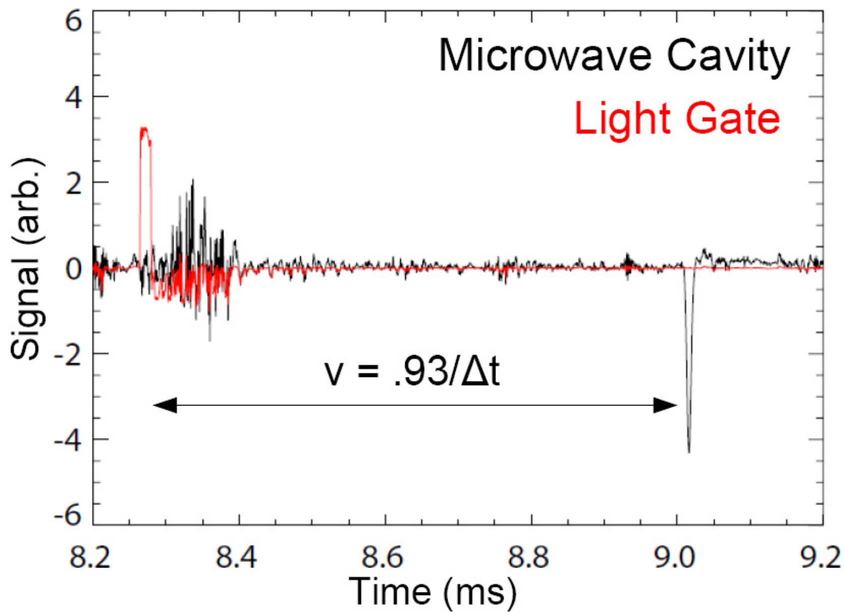

Figure 2.10: Signals for the microwave cavity and light gate measurements which are used to calculate the pellet velocity as well as to estimate the pellet arrival time at the plasma. They are separated by 0.93 m on the pellet injection line.

2.3.2 Pellet Formation

For a pipe gun injector, the pellet is formed inside the already cooled barrel. For deuterium pellets, the barrel is cooled to ~10 K. The triple point temperature for deuterium gas is 18 K. An important step in the pellet formation process is the removal of residual pellet (or other) material from the barrel. Prior to pellet formation, the barrels are heated to > 25K while under vacuum to remove evaporated pellet material. If that is insufficient, the 'dry-fire' method of actuating the high pressure gas propellant valve can aid the removal of stubborn material and assuage any doubts the pelleteer might be having about the forthcoming pellet. This can also be done to clear a pellet that did not break away initially though occasionally several attempts must be made to successfully clear a stubborn barrel.

After the pre-pellet heating, the barrel is allowed to cool to < 12 K before the fuel gas is introduced. A cartoon of the pellet formation process is shown in figure 2.11. The fuel pressure is kept at 30-100 Torr and is varied based on the size of the desired pellet, with a higher fuel pressure required for a larger pellet. The downstream barrel valve is closed, isolating the barrel from the vacuum pumps downstream. Then the upstream valve to the fuel reservoir is opened while the fuel pressure is monitored. Based on the desired pellet diameter and length, when the pressure in the reservoir has decreased enough to form a pellet of the desired size, the upstream barrel valve is closed. At this point, all of the pellet gas is in the barrel and we wait for it to condense in the pellet freezing zone. The pellet freezing zone is determined by the barrel contact to the copper block inside the gunbox as well as by mechanical heat shorts (metal braids) attached (zip tied) to the barrel. The location of these heat shorts is important to properly define the cooling zone and form a solid pellet rather than a hollow ice tube (which is not ideal). Careful measurement of the heat short location is critical for pellets < 2.0mm in diameter. The larger pellets have proven much more forgiving to the location of the heat shorts to the point that the 4.0 mm pellet barrel in fact has no heat shorts to define the freezing zone with the normal hardware connections being sufficient to establish an appropriate freezing zone. Shown in Table 2.1 are desired pellet diameters and the approximate spacing of the heat shorts.

The fuel freezes in the aptly named freezing zone and continues to freeze inward until it can no longer do so at which point a pellet is formed. Typically 1-3 minutes is allowed, often referred to as the soak time for the pellet. In practice, the soak time can coincide with the charge time for the MST capacitor banks or some fraction thereof. It is often beneficial for pellet reproducibility to use the same soak time for each formed pellet as it is one of the many variables which can impact a successful pellet launch.

Prior to launch, the downstream barrel gate valve must be opened. In automated operation, this comes immediately after the soak time has finished (though it takes about 5s for the Labview program to run through those steps). Depending on the barrel characteristics, the best time to trigger the launch of the pellet can be anywhere from a few seconds to a minute or more after this valve is opened. Once triggered, the power supply actuates the solenoid for the desired propulsion method and the pellet is launched by a burst of ~1200 psi hydrogen and/or by a mechanical punch.

Pellet Diameter (mm)	Heat Short Spacing (In.)
1.0	~1/4
1.3	~5/16
1.6	~3/8
2.0	~1/2
4.0	Not Attached

Table 2.1: Shows the approximate distance to place the heat shorts for the desired pellet diameter. For the largest pellets, the best results were obtained with the heat shorts removed meaning the pellet freezing zone was established by the barrel hardware connections alone.

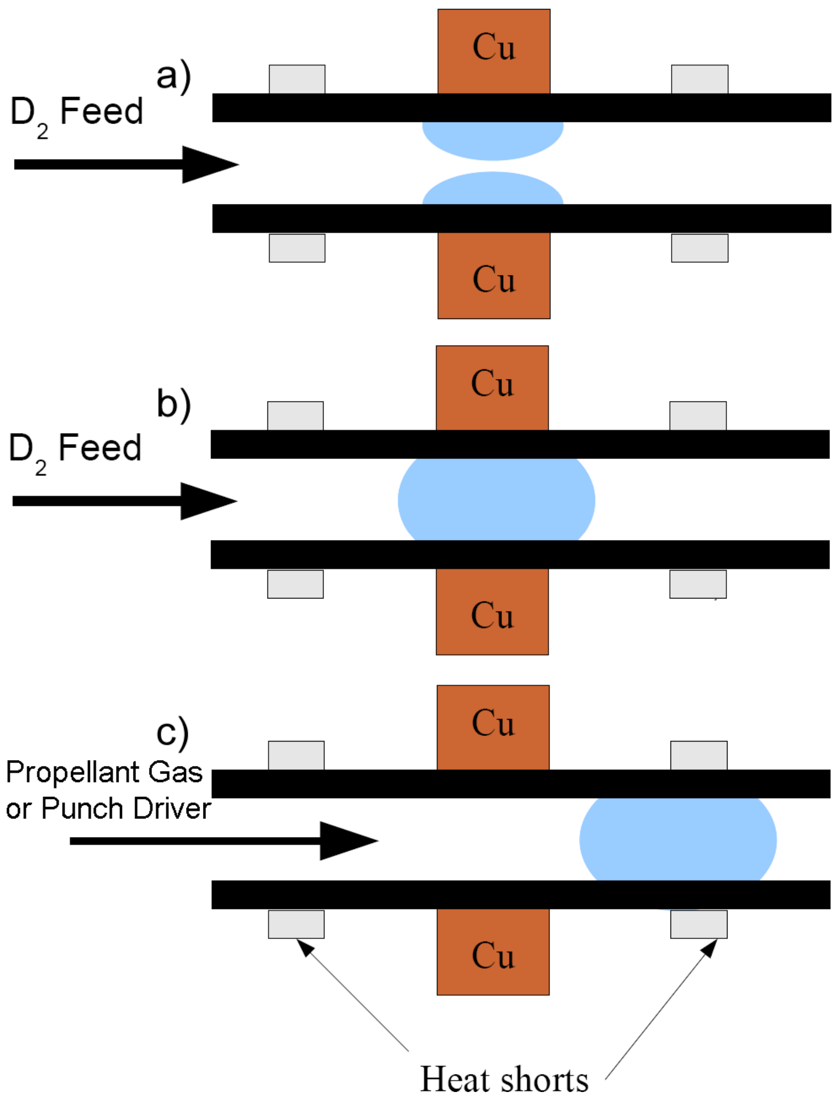

Figure 2.11: (a) With the downstream valve closed, the upstream valve opens and fuel gas at a pressure of 30-100 Torr fills the barrel volume. It freezes selectively in the freezing zone defined by the copper contacts on the barrel which are attached to the coldhead of the cryocooler. (b) The pellet formation zone is defined in part by the placement of heat shorts, metal braids which connect the barrel to the metal vacuum chamber. This allows the pellet to freeze inward to form a solid pellet rather than freezing only on the barrel surface, leaving the pellet hollow. (c) After the soak time, the downstream valve is opened and the pellet is launched with a mechanical punch and/or a burst of high pressure gas.

As the pellet travels toward the plasma, it passes through the light gate and microwave cavity diagnostics discussed previously. The light gate station records a pulse as the pellet blocks the signal. The first pulse typically indicates the front of the pellet, but other pulses can be observed, usually for high speed pellets indicating a cloud of pellet material ablating off of the rear end of the pellet. As such, this can sometimes be used to determine the quality of the pellet, but the microwave cavity diagnostic is a better measure of that.

Located 0.93 m past the light gate, the microwave cavity gives a response proportional to the pellet mass (when tuned properly). Due to the very large variation in pellet mass from the available pellet barrels, the microwave cavity frequency generator does require some adjustment to tune it for the desired mass. The light gates and microwave cavity signals provide a measure of the velocity of the pellet in flight and can then be used to estimate the arrival time to the plasma. By observing the neutral pressure rise in MST after a pellet hits the far wall in the absence of plasma, a means of calibrating the pellet mass measurements was devised. Pressure signals for a variety of pellets are shown in figure 2.12. One readily notes that pellets with approximately the same mass produce drastically different neutral pressure measurements. Indeed it is observed that there is a relation between the pellet velocity and the neutral pressure rise. Further, the dynamics of the neutral pressure after injection also change as indicated by the linear fits in figure 2.12. For slow pellets, the pressure continues to rise, suggesting pellet fragments are still ablating. For sufficient velocity, the pressure is observed to drop following the initial peak as one would expect from a vacuum vessel being continuously pumped out.

Several assumptions are made to estimate the pellet particle content based on the neutral pressure measurements. First, the amount of gas released upon pellet impact is assumed to be proportional to the total kinetic energy of the pellet. This would explain the neutral pressure measurements as well as the subsequent dynamics. Next, that released gas is assumed to fill the volume of the MST vessel in an adiabatic process. With these assumptions, a relation between the neutral pressure and the pellet particle content is devised

$$N_p \propto \frac{2Q\Delta P V_f^{\gamma}}{v^2 k T_f V_i^{(1-\gamma)}} \tag{2.3}$$

Where P, V and T are the pressure volume and temperature. The subscripts i and f refer to the initial and final state of the pellet material, γ is the ratio of specific heats for deuterium and v is the pellet velocity. Q is the heat required to ablate frozen deuterium and raise it to the final temperature.

By calibrating this estimate with the known particle content of some fully ablated pellets, the estimated pellet content scaling in fact holds for even the largest pellets as shown in figure 2.13. As will be discussed in chapter 3, large 4.0 mm pellets are capable of achieving densities of nearly 10^{20} m^{-3}, consistent with the scaling predictions presented here.

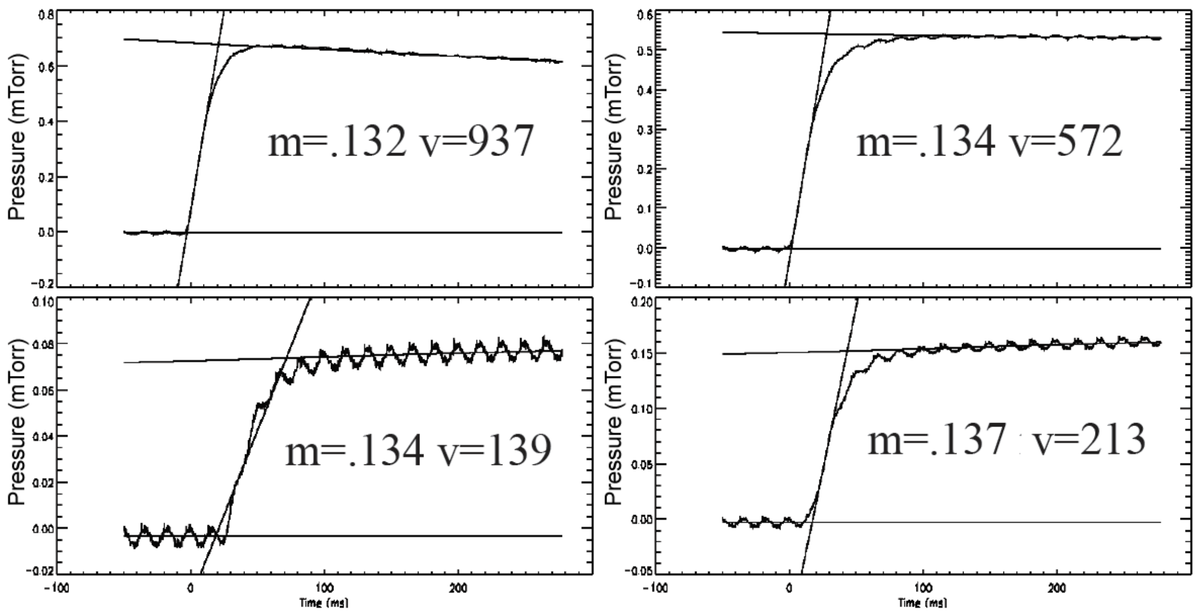

Figure 2.12: Neutral pressure measurements used for pellet mass calibration. Pellet mass measurement (arb.) and velocity (m/s) are shown. A strong dependence on the neutral pressure change with the pellet velocity was observed, leading to a model to estimate the relation between particle content and neutral pressure, related to the kinetic energy of the pellet. The fitted lines indicate the general trend of the neutral pressure during and after the pellet hits the wall.

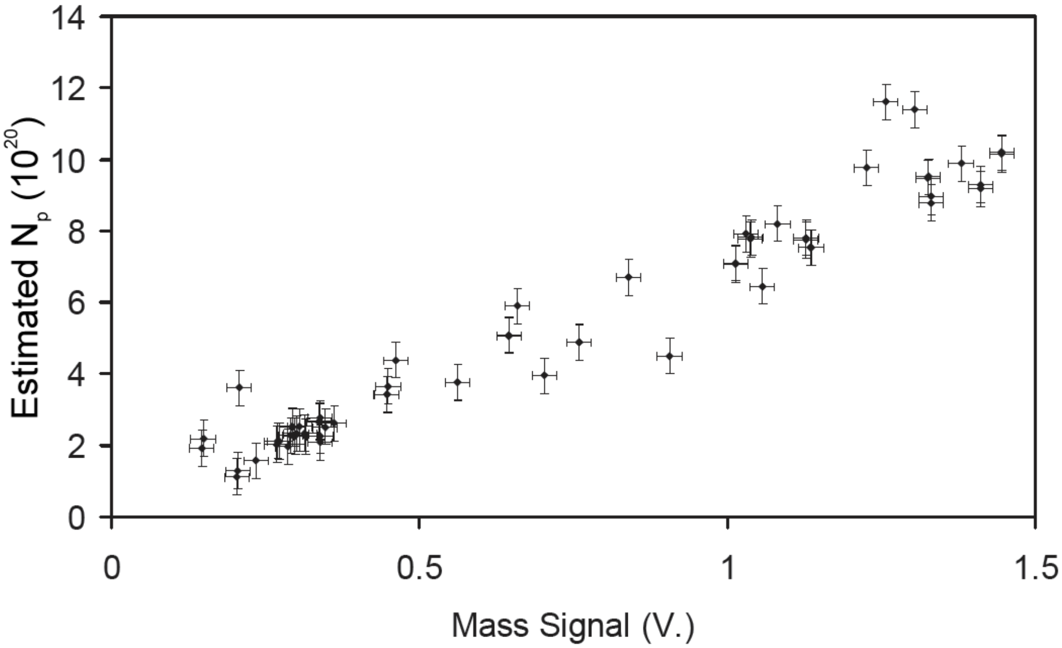

Figure 2.13: Pellet particle content estimates based on equation 2.3, which shows a scaling consistent with the observed impact of the largest 4.0 mm pellet reaching densities close to 10^{20} m^{-3}.

2.3.3 Key Hardware Changes

During the author's time with the pellet injector, a number of modifications and upgrades have been performed which will be discussed in this section, with additional details in the appendices.

One of the most limiting aspects of experimental operation with the pellet injection system is reliability and consistency in the pellets. Previously, the low pellet reliability and lack of reproducibility was thought to be caused by residual material remaining in the barrel after pellet launch. An operational technique was devised to remove excess material by administering a puff of propellant gas into the pellet-less barrel. This 'dry-fire' technique was successful in improving the reliability of pellet formation, but suggested the possibility of impurity contamination in the pellets. To this end, several key changes to the manifold system were implemented in order to reduce the potential impurity content of the pellets. First, the fuel source was changed from a high purity deuterium gas cylinder to the same fuel source used in the puff valve fueling system for MST which goes through a purification stage. A gas line was constructed and connected from the MST gas manifold to the pellet injector manifold. Second, the pellet manifold roughing pump was swapped for a portable turbo pump. The baseline pressure dropped from a few mTorr with the roughing pump to ~1e-6 Torr with the turbo pump. In true scientific brilliance of course (sarcasm intended), both modifications were implemented simultaneously, however the results were very stark. During injector tests following these upgrades, it was discovered that the 'dry-fire' technique was no longer required for reliable pellet formation. Indeed, the pellet reliability seemed to be entirely independent of the 'dry-fire' technique. The practice is still administered at times, but primarily as a symbolic gesture to appease the pellet gods. However, this was not entirely the end of the apparent pellet formation problems.

During pellet fueling experiments with 2.0 mm and 2.5 mm pellets, a significant number of pellets were observed to reach the plasma in pieces despite appearing nominally well formed based on observed light gate and microwave cavity signals. This was in stark contrast to previous observations of pellet inconsistencies where evidence of pellet breakup was observed in the light gate and/or the microwave cavity signals. In our attempts to push the limits of pellet size, we had in fact encroached upon the designed upper limits for pellet diameter which were suspected to be constrained by the inner diameter of several guide tube sections. The purpose of the guide tubes is to constrain the pellet in flight. However, deuterium pellets are rather non-aerodynamic and tend to tumble in flight. The guide tubes, it seemed, had become obstacles for the larger tumbling pellets. With the desire to push pellet size even larger, a substantial upgrade to the injector was performed to allow pellets with a diameter up to 4.0 mm, sufficient for any possible future experiment with the pellet injector. This 4.0 mm value came from estimates of pellet particle content for various pellet sizes.

$$D_{max}^3 = D_{pellet}^3 \frac{N_{max}}{N_{pellet}} \tag{2.4}$$

By setting the maximum particle content to that required to fuel with a single pellet up to a Greenwald fraction of 2 for a plasma current of 800 kA, the 4.0 mm pellet diameter was obtained as the maximum useful size for MST plasmas.

Additional details of the injector removal, dis-assembly, upgrade, re-assembly, re-installation and recommissioning are included in Appendix C, but an overview of the modifications will be discussed here. The essence of the upgrade was to replace guide tube pieces with pieces capable of accommodating 4.0 mm pellets. The major hurdle was the lack of detailed information for the inner hardware of the injector. Step one was the removal and tear down of the entire injector. This revealed the exact extent of the hardware changes required. Indeed nearly every part of the guide tube sections required at least some minor modifications while many required the fabrication of new parts to replace the originals.

A diagram of the guide tube sections is shown in figure 2.14 and the changes to the spatial constraints are outlined in table 2.2. First, new barrels were fabricated with 3.0 and 4.0 mm diameters. Next, the inner diameters of guide tube stages 1 - 4 were all increased to accommodate a tumbling 4.0 mm diameter pellet with L/D of 1 - 2. The microwave cavity was replaced with one more appropriate to measurement of larger pellet masses. A weld bead was removed from the barrel 1 section of guide tube 6 (a likely culprit for some of the unexplained pellet losses. The stage 7 guide tubes were replaced with newly cut pieces with a larger increase in ID. Some of the old tubes also had significant bends which may have prohibited the launch of fast pellets (even though I tried anyway). Finally, the compression fittings attached to the MST gate valves had their ID's significantly increased in order to increase the ID at every break between guide tube sections. These ID's had previously been fractionally smaller than the old stage 7 guide tubes marking them as a prime candidate for pellet assassinations. The key requirement for these modifications was to ensure ID's large enough to accommodate the size of a tumbling 4.0 mm pellet and to step up the ID at each guide tube break a sufficient amount based on the length of the break. One bug (a literal bug) was also removed from a surge tank. Fortunately, he was found to not be a critical component.

A funny thing happened after the recent installation of the 4.0 mm barrel. It was discovered that the close coupled propellant valve was capable of tremendous velocity control when used with this larger diameter pellet/barrel merely by changing the pulse width sent to drive the solenoid valve. The range of possible pellet mass and speed combinations is shown in figure 2.15. A full range of pellets masses is available, from those with a mass comparable to an average sized 2.0 mm diameter, up to the plasma crushing pellets with an estimated particle content of over 10^{21}. More remarkable is the range of speed available, from 100 m/s all the way to the normal 1200 m/s.

While a number of changes had been made to the pellet hardware when this improved control was observed, there are two key changes which would help to explain the result. First, with the installation of 3.0 and 4.0 mm pellet barrels, the heat load on the cryocooler was increased. This was immediately observed in a rise of the baseline barrel temperature from 11 K to 13 K. This initially impeded the formation of pellets. After removing the barrel heat shorts from these two barrels, the temperature dropped to 12 K, still higher than before, but sufficient to form pellets successfully. Prior to this, the sensitivity of pellet formation to the barrel temperature had not been explored at all. The increase in barrel temperature can have an effect on the required pressure for pellet breakaway[10]. Second, the pressure at the propellant facing pellet surface as a function of time will change with modifications to the hardware. Shown in figure 2.16 is a model of the propellant valve and the barrel volume V including the connecting volume with a flow conductance C. Two of these connecting volumes had previously been modified to accommodate punches for 2.0 mm pellets. The pressure at the face of the pellet for the simplified system is given by equation 2.5.

$$P(t) = P_0 \frac{\left(e^{t/\tau} - 1\right)}{\left(e^{t/\tau} + 1\right)}; \tau = \frac{V}{CP_0} \tag{2.5}$$

This simple model for the pressure at the pellet surface P(t) while the propellant valve is opened shows that for a larger barrel volume, the expected pressure rise is slowed as shown in figure 2.17 for 3 cases; 1.0 mm diameter barrel with 1.6 mm diameter connecting tube, 2.0 mm diameter barrel with 2.0 mm diameter connecting tube, and 4.0 mm diameter barrel with 2.0 mm diameter connecting tube. The pressure in the barrel has a strong impact on the pellet velocity as shown via the ideal gun equation for a pipe gun.[8] While the propellant gas reservoir is kept at ~1200 psi, the breakaway pressure is closer to 300-400 psi. Traditionally, a pulse width of 2.5-3.0 ms was used for fast pellet propulsion, with a minimum pulse of ~1.0 ms required to actuate the valve. For smaller barrels (case 1 of figure 2.17), there is no control over the pressure with pulse width. Even a 1.0 ms pulse would result in a nearly maximized pressure behind the pellet. As the barrel volume increases, the pressure rises more slowly, allowing some control over the accelerating pressure behind the pellet after it breaks away.

Guide Tube Stage	Old ID (mm)	New ID (mm)
1	3.1	6.4
2	4.0	6.7
3	4.9	7.1
4	6.1	7.5
5	7.9	7.9
6	8.3	8.3
7	8.3	9.3
8	8.3	9.4

Table 2.2: Guide tube sizes before and after upgrade with stage numbers corresponding to those shown/discussed in figure 2.14.

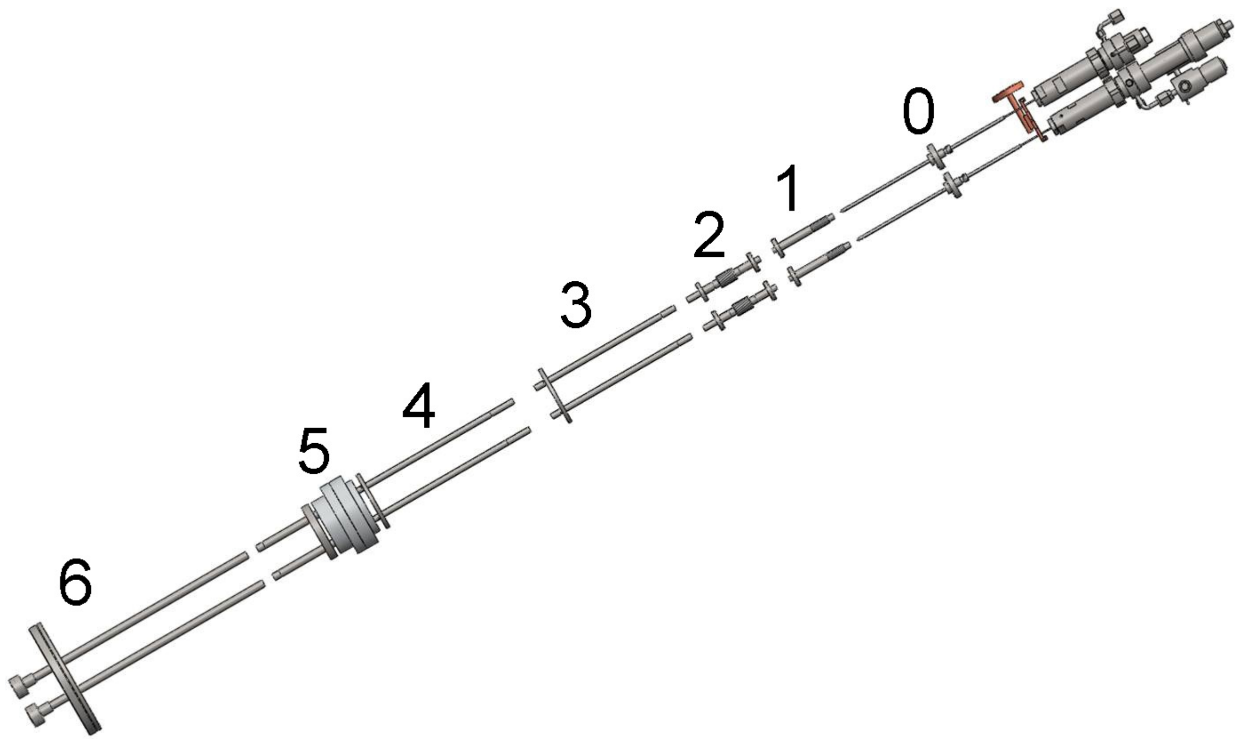

Figure 2.14: This Solidworks drawing of the injector upgrade shows the modified hardware required to upgrade the injector. The list of necessary modifications to allow 4.0mm pellet injection included; new barrels (0), new hardware (1-4), swap of microwave cavity (5), removal of obstruction (6), new guide tube pieces (7-not shown), and the enlargement of the connecting valve to MST gate valve (8-not shown)

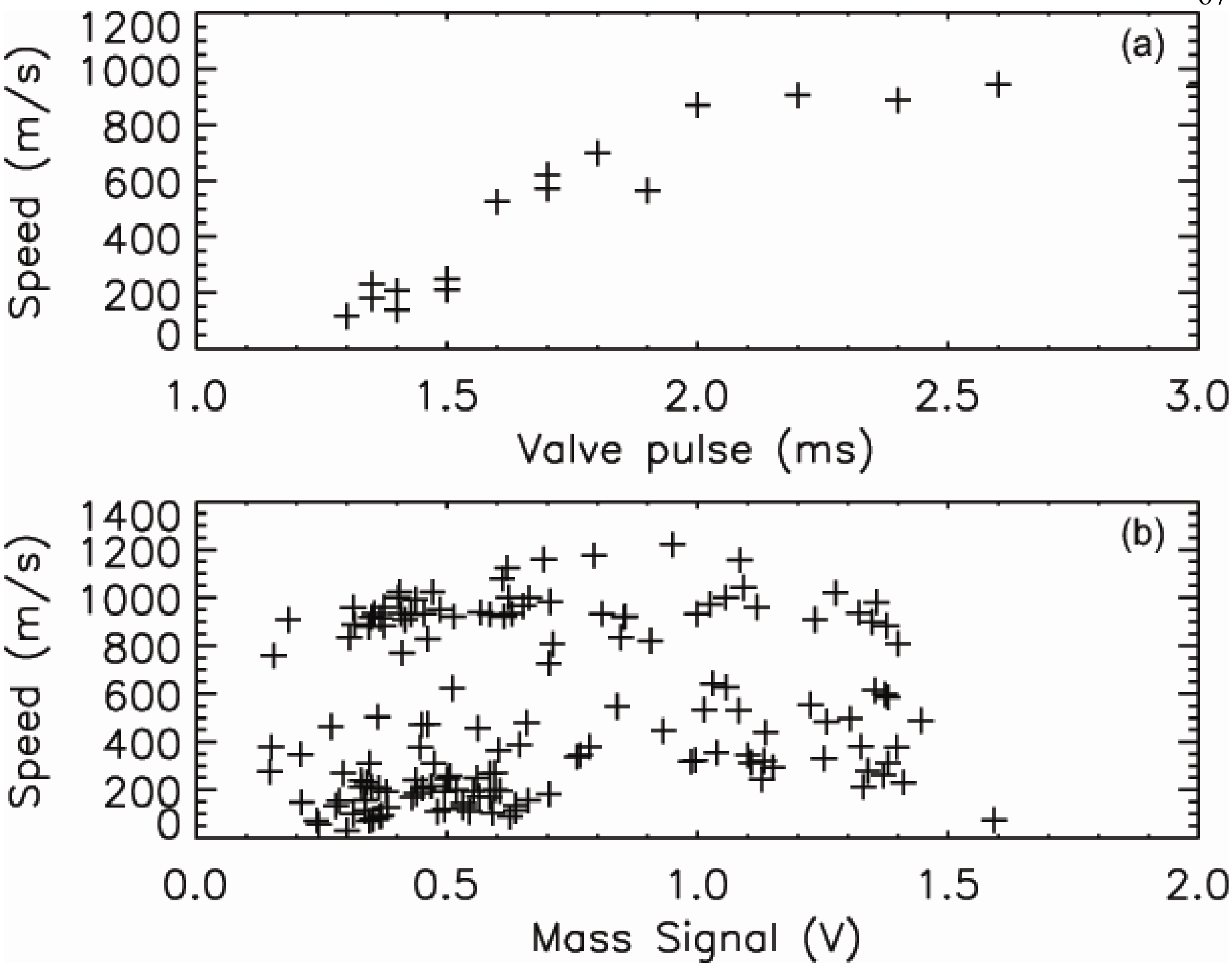

Figure 2.15: (a) Velocity of 4.0 mm pellet for a given valve pulse widthshowing the improved velocity control. (b) Observed pellet velocity vs microwave signal for the post upgrade 4.0 mm pellets. Pellet size can be inferred from particle estimates in figure 2.13.

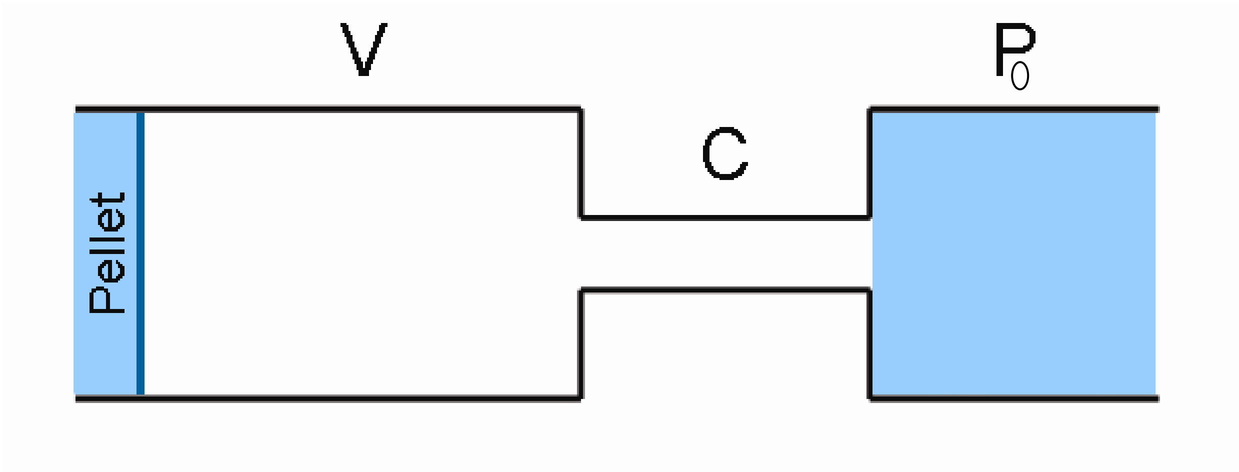

Figure 2.16: A diagram of the relevant parameters used to model the improvement in velocity control. V represents the barrel volume with the pellet being at the far left in this diagram. The connecting volume has a gas conductance C which depends on its diameter. The upstream pressure P_0 is held constant.

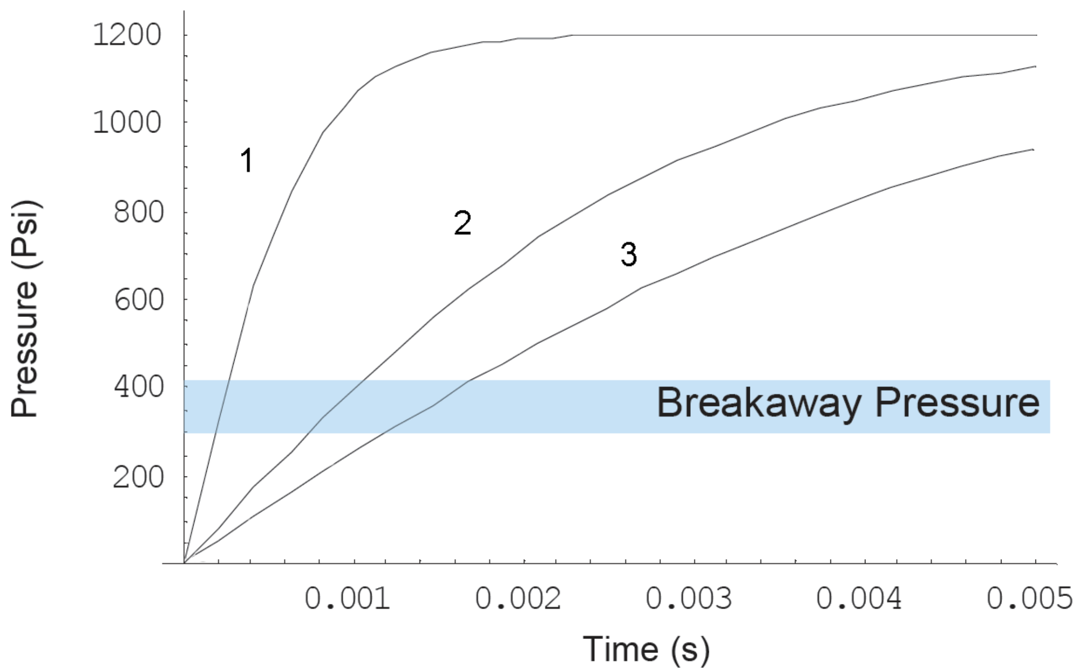

Figure 2.17: Modeled pressure at the pellet face as a function of the valve opening duration for experimental cases based on the model in figure 2.16. In case 1, a 1.0 mm diameter barrel with 1.6 mm diameter connecting volume. In case 2, a 2.0 mm diameter barrel with 2.0 mm diameter connecting volume. In case 3, a 4.0 mm diameter barrel with a 2.0 mm diameter connecting volume. A slower pressure rise allows adjustments to the valve opening duration to impact the accelerating pressure and the pellet speed.

2.4 Relevant Hardware and Diagnostics of Note

A number of other diagnostics have been utilized during pellet fueling experiments for various measurements. What follows is a brief discussion of the capabilities of the relevant hardware. The various diagnostics and locations are noted in figures 2.18 and 2.19.

2.4.1 CO_2 Interferometer

The CO_2 interferometer is located at 40 degrees toroidal compared to the injector at 240 degrees as measured from the poloidal gap of the machine. Used for measurements of central line averaged density, the CO_2 interferometer has one key benefit over the FIR interferometry system in that it does see a loss of signal due to ablating pellets. The robust nature has made it key for much of the density limit experiments. Due to its distance from the injector, the density rise observed after pellet injection can lag by as much as a few ms, depending on the ablation profile of the pellet. The upside is that this density is more likely to represent an equilibrated value without any local fueling effects based on fueling asymmetry.

2.4.2 FIR Interferometer and Polarimeter

The far infrared (FIR) interferometry and polarimetry system consists of 11 chord measurements of line averaged density and Faraday rotation throughout the plasma. The array of density measurements can also be inverted to provide information about the density profile. Polarimetry measurements are an important constraint during equilibrium reconstructions. In addition, fluctuation measurements and density gradient measurements are also possible depending on the mode of operation employed. Unfortunately, due to its proximal location, only 15 degrees of separation, pellet ablation often causes temporary losses of signal which is problematic for many pellet fueling experiments. The rapid changes in density can also cause fringe skips which muddle the dynamics of the density changes. For pellet fueled PPCD where the goal is to maximize the core density, the loss of signal is brief (~2-3ms) and generally not at the time of interest for the study of high beta plasmas. However density limit experiments with substantial edge fueling and hollow profiles have proved to be even more difficult to deal with. Density inversion for hollow profiles is very insensitive to the core density. Even for central chords, that region provides a comparatively small portion of the measurement. This makes the profile information weakly constrained in the core.

2.4.3 Thomson Scattering

Located at 210 degrees toroidal, the Thomson scattering system measures the outboard electron temperature at a number of radial locations. Unlike many of the diagnostics, the high density tends to result in an increase in signal and reduced error bars. Observed temperatures during density limit terminations do push the lower limits of reliable measurements, fitting with the theme that the pellet injector pushes the limits of all hardware. During density limit experiments, s the cold plasmas are constrained to only the lowest channels limiting the fitting routine success.

2.4.4 CHERS, Rutherford Scattering and CNPA

The Charge Exchange and Recombination Spectroscopy (CHERS) system is primarily used for core impurity T_i measurements. It is also capable of measuring the impurity ion temperature at other radial locations. The diagnostic neutral beam suffers from increased attenuation at higher density. Rutherford scattering, when available, provides an off axis measurement of the bulk ion temperature. The Compact Neutral Particle Analyzer (CNPA) also provides an ion temperature measurement associated with the plasma core.

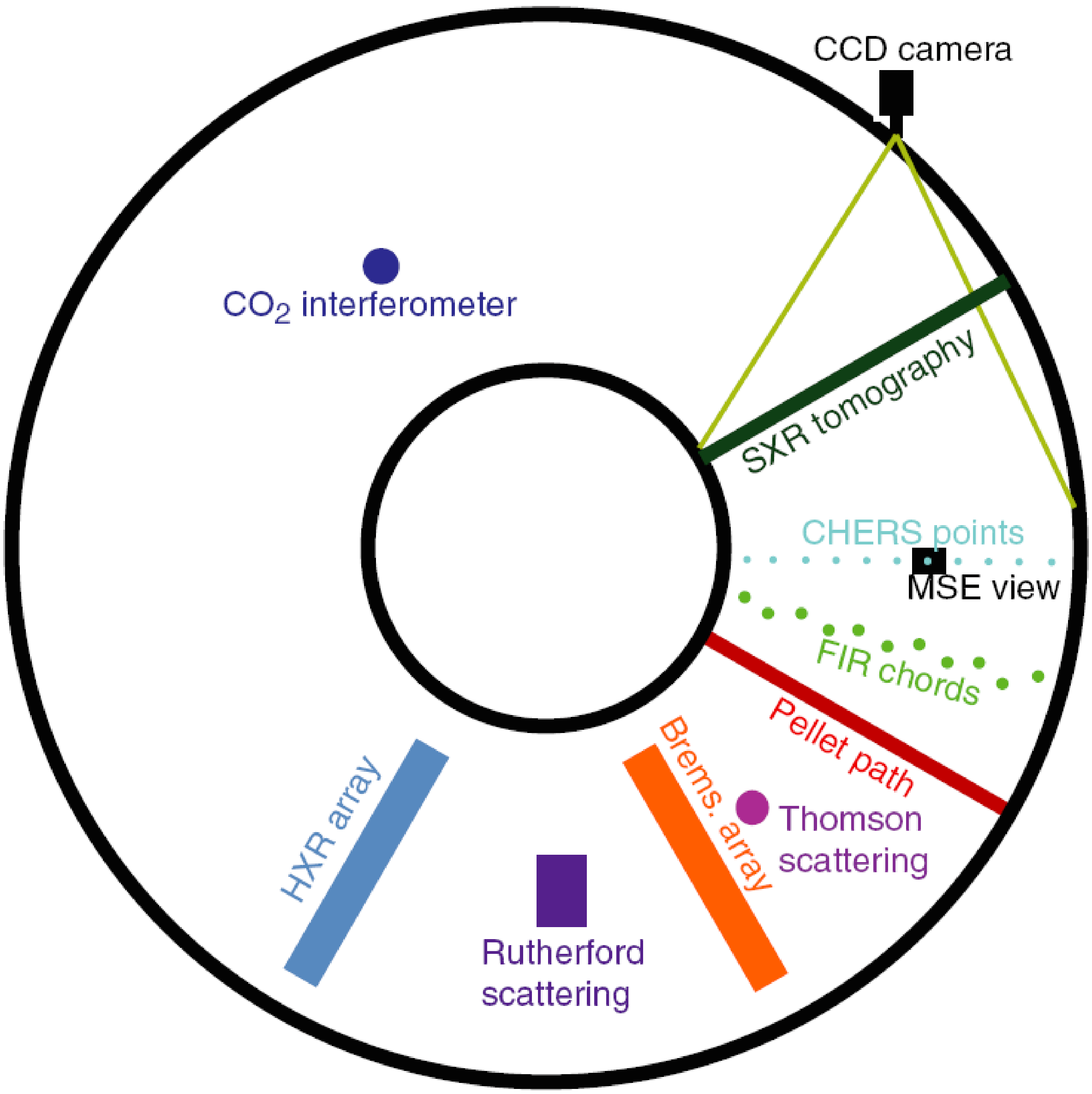

Figure 2.18: Top down view of the diagnostic layout on MST

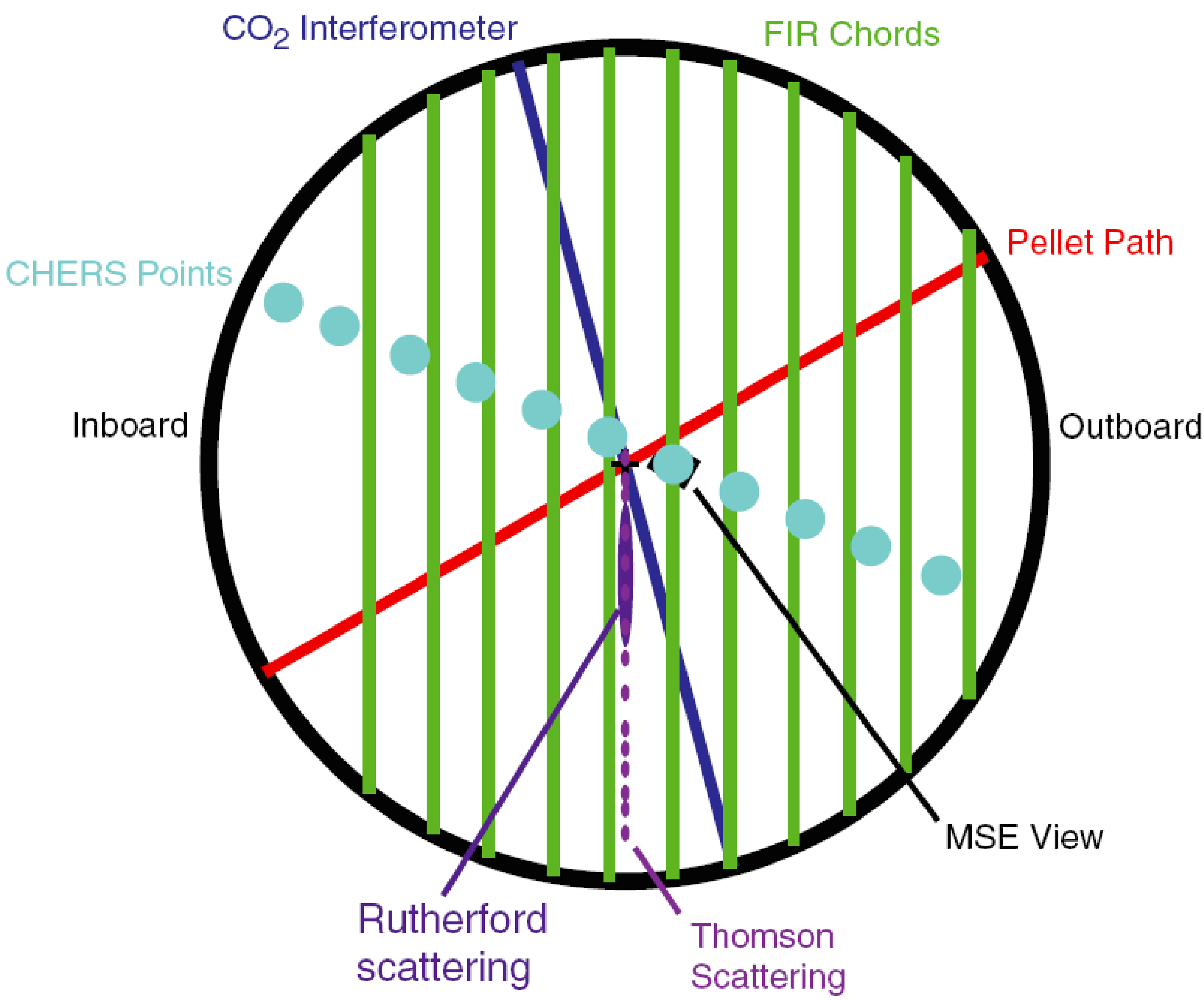

Figure 2.19: Cross sectional poloidal view of the diagnostic coverage on MST

2.5 References

1) R.N. Dexter, D.W. Kerst, T.W. Lovell, S.C. Prager, and J.C. Sprott, Fusion Technol. 19, 131–139 (1991).

2) T.M. Biewer, C.B. Forest, J.K. Anderson, G. Fiksel, B. Hudson, S.C. Prager, J.S. Sarff, J.C. Wright, D.L. Brower, W.X. Ding, S.D. Terry, Phys. Rev. Lett. 91, 045004 (2003).

3) B. Hudson, Fast Ion Confinement in the Reversed Field Pinch, University of Wisconsin, 2006.

4) S. Ortolani, D.D. Schnack, Magnetohydrodynamics of Plasma Relaxation (1993) World Scientific

5) J.S. Sarff, S.A. Hokin, H. Ji, S.C. Prager, and C.R. Sovinec, Phys. Rev. Lett. 72, 3670–3673 (1994).

6) R. Lorenzini, D. Terranova, A. Alfier, P. Innocente, E. Martines, R. Pasqualotto, and P. Zanca, Phys. Rev. Lett. 101, 025005 (2008)

7) S.K. Combs, L.R. Baylor, D.T. Fehling, D.L. Brower, and W.X. Ding, Fusion Sci. Technol. 44, 513–517 (2003).

8) S.L. Milora, W.A. Houlberg, L.L. Lengyel, and V. Mertens, Nucl. Fusion 35, 657–754 (1995).

9) M.D. Wyman, The Physics of High-Density, High-Beta Reversed-Field Pinch Plasmas, University of Wisconsin, (2007)

10) S.K. Combs, Private Communication

CHAPTER 3

Density Limit Studies on MST

3.1 Introduction

Maximizing plasma density is important from a fusion perspective as the fusion reaction rate scales with the square of the plasma density, and operation near the density limit is desirable in a fusion reactor. In addition, the underlying physics which governs the limit in tokamak and RFP experiments is not yet fully understood. Thus, we have continued with the exploration of the RFP density limit on MST. As discussed in chapter 1, the RFP was historically constrained by the 'I/N' limit [1], which matches the Greenwald density limit [2]; an empirical restriction on the line averaged density, $\langle n_e \rangle$, for edge fueled tokamak experiments. For an axisymmetric device such as MST, the Greenwald limit on $\langle n_e \rangle$ is given by

$$n_{GW} = \frac{I_p}{\pi a^2} \tag{3.1}$$

where I_p is the toroidal plasma current in MA and a is the minor radius of the plasma current channel in meters. The normalized density, the ratio of the line averaged electron density to the Greenwald density, will be used here and is represented by N_{GW}.

$$N_{GW} = \frac{\langle n_e \rangle}{n_{GW}} \tag{3.2}$$

As the density limit is approached and exceeded in standard RFP plasmas, a rapid decay of the current is observed along with increased radiation and magnetic activity. The density operational space for the RFX-mod experiment is plotted in figure 3.1, with the upper bound constrained by the Greenwald limit. In tokamak density limit disruptions, MARFES [3] are observed as the limiting density is approached. Analogous radiating structures are observed in the RFX-mod experiment [4]. The increased radiation coincides with the formation of a chain of m = 0 islands resonant at the reversal surface. This island chain is believed to contribute to the rapid resistive decay of the plasma current during a density limit termination.

Previous high density fueling experiments on MST [5, 6] used a high throughput gas valve or pellet fueling to attain plasmas with densities exceeding the Greenwald density for a limited range of plasma current up to 300 kA. Exceeding the limit with edge fueling resulted in the early termination of the plasma. The limit was briefly exceeded without termination in plasmas with a peaked density profile achieved via core fueling with deuterium pellets. This suggested that the edge region of the plasma is important in the density limiting physics in MST and the RFP.

In this chapter, we will utilize a new method of triggering density limit termination using the pellet injection system on MST. By firing a fast pellet such that it collides with the wall, we are able to provide a controllable edge fueling source. The goals of these experiments were first, to use this pellet edge fueling technique to trigger density limit terminations of the plasma in a controllable manner for the full range of available plasma currents on MST (up to 600 kA) and second, to study the density limit termination using the full complement of diagnostics on MST, in order to better understand the underlying physics. This included the insertion of Langmuir probes for the purpose of measuring edge equilibrium and fluctuating quantities during a density limit termination. Measurements of the plasma parameters during a density limit termination show hollow density profiles, rapid cooling in the edge and core, and increases in radiation. A possible toroidal asymmetry is observed in $\langle n_e \rangle$ measurements. The magnetic activity in the edge and the core scales with the density as well. After establishing the density limit at all currents, a closer examination of the collection of density limit experiments reveals that the maximum density is slightly lower in discharges with the m=0 resonant surface removed from the plasma. These experiments were motivated by the RFX-mod model which attributes the density limit to the formation of m=0 islands resonant at the reversal surface. Many of the same symptoms are observed in these non-reversed discharges, including the growth of edge m=0 magnetic modes despite there being no resonant surface in the plasma. Discharges with deeper reversal appear have a higher limit for full plasma termination, suggesting a dependence of the density limit on the degree of reversal. Probe measurements suggest an overall increase in density fluctuations as the density limit is exceeded, a possible indicator of increased electrostatic transport in the edge.

In discharges with improved confinement, the density limit can be exceeded by core pellet fueling. In this way we have exceeded the Greenwald density in PPCD experiments, reaching 2.0 times the limit for 200 kA PPCD experiments and 1.4 times the limit for 500 kA PPCD experiments, the latter corresponding to an absolute density of nearly 10^{20} m^{-3}. While no clear explanation for the RFP density limit is suggested here, we provide a comprehensive discussion of the density limit phenomenology on MST and a significant amount of additional information is obtained to build on the current knowledge base, including an initial test of the RFX-mod model. This stands as an important step toward gaining an understanding of the underlying physics of the RFP density limit.

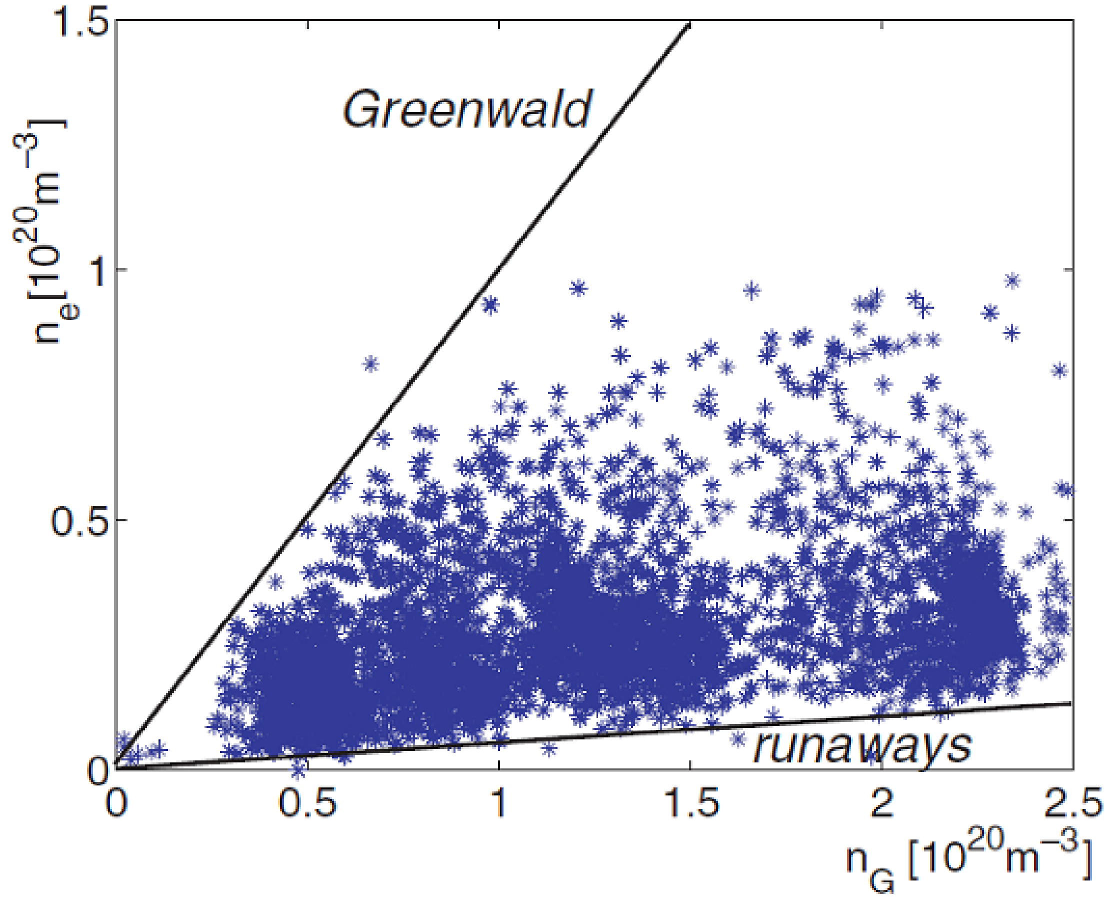

Figure 3.1: The density operating space for the RFX-mod experiment. An upper bound on the density is constrained by the empirical Greenwald density limit. (Plot taken from [4])

3.2 Experimental Technique and Observations

3.2.1 Pellet Triggered Terminations and Confirming Density Limit Scaling

To further explore what occurs as the density limit is approached and exceeded in standard plasmas on MST, a means of triggering a density limit collapse was devised using pellet injection fueling. This is counter to the normal goal of pellet fueling experiments where a centrally peaked density profile is desired. As the density limit is believed to be largely dependent on edge parameters, we note that a fast (v > 1000 m/s) pellet of sufficient size will cross the 1 m diameter plasma in less than 1 ms and impact the inboard vessel wall, providing a large amount of localized edge fuel. A previous look at pellet particle content (see Section 2.3.2) suggested that the amount of gas initially released when a pellet hits the vessel wall increases with pellet velocity and that a pellet traveling at sufficient speed will fully ablate upon impact with the vessel wall. Additionally, as pellet speed increases, pellet ablation in the plasma core will decrease due to the brief transit time and we would expect the plasma to aid in the ablation of any remnant pellet material.

The efficacy of this pellet fueling method of terminating the plasma is shown in figure 3.2 where a set of consecutive discharges shows the onset of a density limit termination by only slightly increasing the mass of the injected pellet, highlighting the level of control available for these experiments. The first pellet had a speed of 989 m/s and a mass signal of .127 V (as measured by the microwave cavity diagnostic) while the subsequent pellet had a comparable speed of 1019 m/s and a mass signal of .154 V, ~20% larger. An observed increase in $\langle n_e \rangle$ of ~10-20% is measured by the CO_2 interferometer. This incremental change is sufficiently large to result in a full termination of the plasma current, in contrast to the smaller pellet case where the plasma current collapse ceases at 130 kA. We note that the CO_2 interferometer is located on the opposite side of the machine, so $\langle n_e \rangle$ measurements are representative of the equilibrated density and likely represent a lower bound. The arrival time of the fast pellet (i.e., the time the pellet smashes into the far wall) is consistently within a 1 ms time window for fast pellet injection and is well controlled by the timing of the high pressure propellant valves. During the pellet triggered termination, we observe a drop in plasma current after injection and observe full terminations of the discharge at $\langle n_e \rangle \sim n_{GW}$. In pellet triggered density limit termination, the current decay rate can reach > 40 MA/s for 200kA discharges, comparable to that observed during tokamak density limit disruptions [7]. During the plasma current decay, we observe an increase in both the edge (m = 0, n = 1-4) and core (m = 1, n = 7-15) magnetic mode activity.

In figure 3.3, the phenomenology of a pellet-triggered density limit termination is compared with two other forms of density limit terminations observed on MST; termination caused by excessive edge fueling from a high throughput gas valve during previous density limit experiments [6], and termination caused by an excessive edge recycling event often observed during conditioning of the plasma-facing wall. In all three cases we make similar observations. The current decays rapidly after the instigating event causes the density to rise. The toroidal field reversal parameter

$$F \equiv \frac{B_\varphi(a)}{\langle B_\varphi \rangle} \tag{3.3}$$

also becomes less negative, eventually slightly exceeding zero, an unstable regime for the RFP. Here $B_\varphi(a)$ is the toroidal field component at the wall, and $\langle B_\varphi \rangle$ is the volume averaged toroidal field. During the current decay, magnetic activity is observed to increase for both the edge and core modes in all cases. The similar nature of these three density limit terminations gives a reasonable expectation that the pellet triggered terminations are in fact a consequence of density limiting physics. The method of using pellet fueling to trigger density limit terminations provided a number of advantages compared to gas valve fueling. First, the timing of the pellet is well controlled as is the amount of fuel deposited. Second, the pellet fueling had little impact on the edge recycling in subsequent shots, as highlighted by the consecutive discharges shown in figure 3.2.

The next step for density limit studies was to establish the limit for the full range of plasma current available to MST. The upgrade to 4.0 mm diameter pellets (see Section 2.3) made possible pellet triggered terminations for the highest current discharges on MST, 600 kA, as shown in figure 3.4. For I_p up to 500 kA, all four capacitor banks in the pulse forming network (generating a flat-topped I_p waveform) were used and pellet triggered terminations were obtained by gradually increasing the pellet size. For I_p up to 300 kA, the plasma is observed to terminate fully at densities consistent with the Greenwald limit. In the highest current discharges, the density limit is exceeded by as much as 20% before the plasma is observed to terminate. This is possibly a result of a decrease in edge fuel, a result of increased core pellet ablation due to the higher electron temperature. For 600 kA plasmas, only two capacitor banks were used, resulting in a shorter current flat top. Regardless, early termination of the plasma is still observed for sufficiently high density. Large 4.0 mm pellets were required for density limit experiments above 300 kA with pellet particle content approaching 10^{21} in 500 kA and 600 kA experiments. Both 2.0 mm and 4.0 mm pellets were used for 200-300 kA density limit experiments.

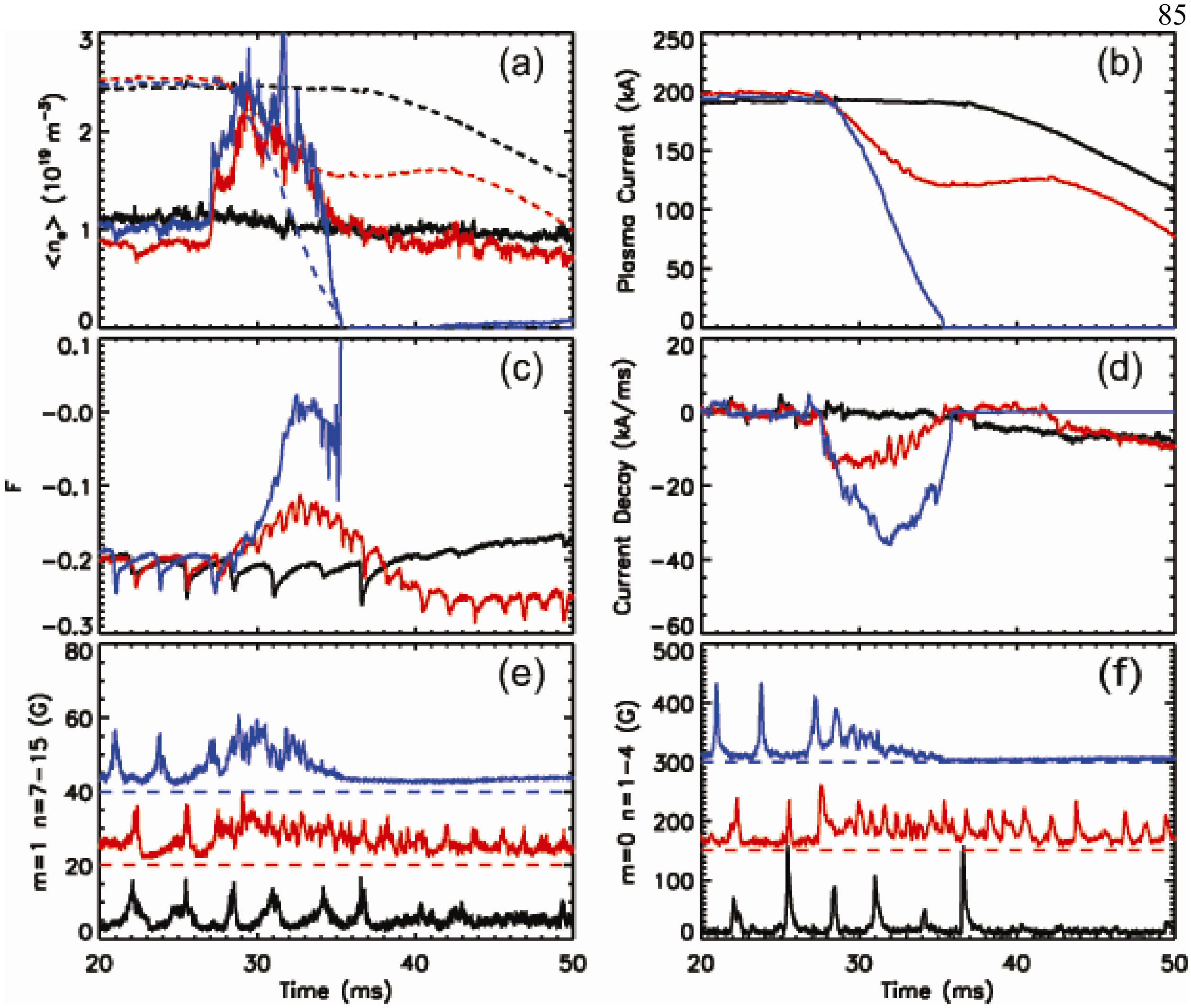

Figure 3.2: A sequence of 3 consecutive shots showing the onset of density limit termination through the use of fast pellet injection for reversed discharges. Plotted signals are (a) $\langle n_e \rangle$ and nGW (dashed), (b) plasma current, (c) reversal parameter F, (d) current decay rate, (e) core mode activity (m=1 n=7-15) and (f) edge mode activity (m=0, n=1-4). Mode activity is artificially shifted with zero values corresponding to horizontal dashed lines. The shots in red and blue are pellet fueled with the pellet for the blue shot having ~20% more mass than that of the red shot resulting in a full termination of the plasma. The shot in black has no pellet. [Shots: 1130312040(red), 1130312041(black), 1130312042(blue)]

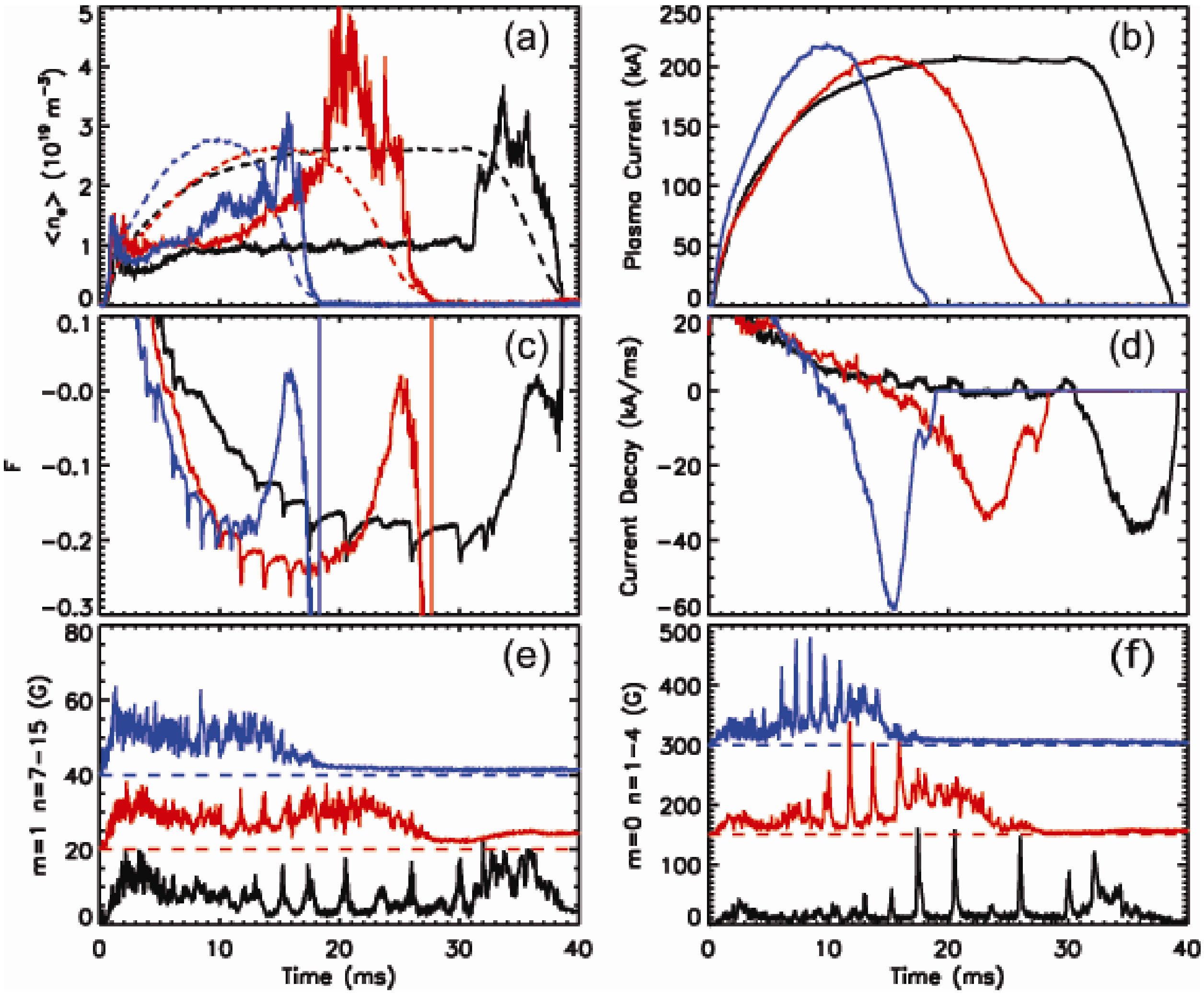

Figure 3.3: A comparison of three means of encountering a density limit termination on MST. Plotted signals are (a) $\langle n_e \rangle$ and n_{GW} (dashed), (b) Plasma Current, (c) reversal parameter F, (d) current decay, (e) core mode activity (m=1 n=7-15) and (f) edge mode activity (m=0, n=1-4). Mode activity is artificially shifted with zero values corresponding to horizontal dashed lines. In black is a pellet fueled discharge where a large fast pellet is used to fuel the edge excessively. In red is a density limit termination caused by over-fueling with a high throughput gas valve. In blue is a density limit termination caused by an over-recycling event during machine wall conditioning. All display the same phenomenological behavior including an increase in magnetic activity and a loss of reversal along with a rapid current decay. [Shots: 1130224028(black), 1050924125(red), 1100623016(blue)]

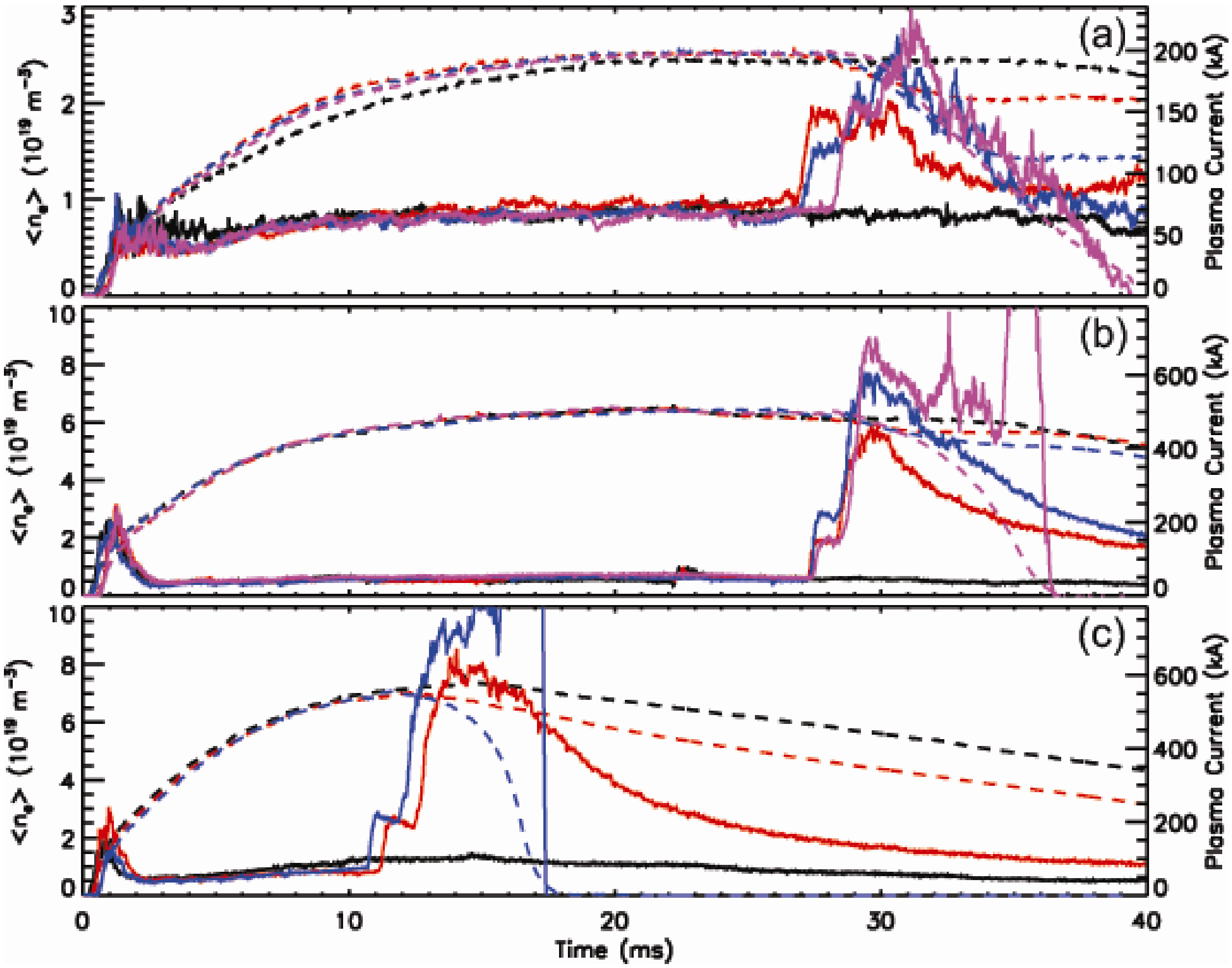

Figure 3.4: Plotted are the CO_2 interferometer measurements of $\langle n_e \rangle$ (solid) and the n_{GW} (dashed) for a series of shots highlighting the onset of full plasma termination by pellet fueling. The dashed line also corresponds with the plasma current in the right-hand axis. (a) The first case consists of 200 kA plasmas with all four capacitor banks in the pulse forming network. (b) The second case for 500 kA plasmas with four capacitor banks and (c) the final case for 600kA plasmas formed with two capacitor banks, resulting in a shorter current flat top. The upgraded 4.0mm pellet capability allows for pellet triggered plasma terminations for the maximum available current in MST and establishes the density limit terminations for all available plasma currents. [Shots (a) 1130312024(black), 1130312044(red), 1130312036(blue), 1130312023(magenta), (b) 11303130241(black), 1130313042(red), 1130313052(blue), 1130313054(magenta), (c) 1130310080(black), 1130310073(red), and 1130310081(blue)]

3.2.2 Dependence of Density Limit on Reversal

The initial density limit experiments were performed in reversed discharges ($F = -0.2$). The density limit model devised by the RFX-mod team highlights the appearance of a radiative chain of $m = 0$ islands at the resonant surface as a key component of the density limit termination. [4] RFX-mod experiments were performed primarily for F of -0.05. These previous results motivated density limit experiments on MST comparing reversed ($F < 0$) and non-reversed ($F = 0$) discharges. RFX-mod is unable to run with $F = 0$ thus representing a unique capability for RFP density limit experiments on MST. Non-reversal removes the $m = 0$ resonant surface from the plasma and so should shed some insight on the RFX-mod model. Pellet-triggered discharge terminations are obtained for plasmas without reversal as shown in figure 3.5. The onset of the limit occurs in the same manner as the reversed discharge, with small changes in pellet mass and the associated increase in $\langle n_e \rangle$ leading to increased I_p decay, ultimately resulting in a full termination of the plasma for sufficiently high density. As the toroidal field circuit approximately clamps F to zero, it no longer approaches zero as in the reversed case, although it is observed to fluctuate during rapid decay of the plasma current. The magnetic activity shows a similar behavior as well, including an increase in core ($m = 1$) and edge ($m = 0$) activity. The increase in edge activity occurs despite the lack of a resonant surface in the plasma, however it should also be noted that the activity is significantly smaller than in the reversed experiments. In figure 3.6, we look at a comparison of reversed and non-reversed terminations. The degree to which the plasma current decays for a given pellet size (and associated density increase) is larger for the non-reversed discharges. This suggests the density limit is slightly lower in the F = 0 case, prompting a look at a third case, F = -0.3. Three pellets of approximately the same size were injected into 200 kA discharges with F = 0, -0.2, and -0.3. Comparison of three discharges is shown in figure 3.7. The F = -0.3 case does not fully terminate, while the other two cases do. This comparison clearly shows that the discharge with deeper reversal is more robust to the high density pellet fueling.

The lower density limit for F =0 experiments is also observed if we look at a collection of pellet fueled density limit experiments. We plot the density operating space for MST in a similar fashion to figure 3.1. The density operating space for reversed and non-reversed discharges is shown in figure 3.8 for plasma currents up to 500 kA using the full set of four capacitor banks. Pellets are injected at ~ 25 ms and the scatter plot represents the range of 20-40 ms, with each point shown representing a 0.5 ms time averaged measurement of $\langle n_e \rangle$ and n_{GW} where there is little observed degradation of the plasma current (1/Ip [dIp/dt] > -5 %/ms). Reversed discharges are shown in red while non-reversed discharges are plotted in blue. Again, we confirm a slightly larger limit before significant current decay is observed for the reversed discharges compared to the non-reversed discharges for all plasma currents. In both cases, the limit still approximately corresponds to the Greenwald limit, though a higher limiting density is again observed at the highest plasma currents, consistent with previous observations.

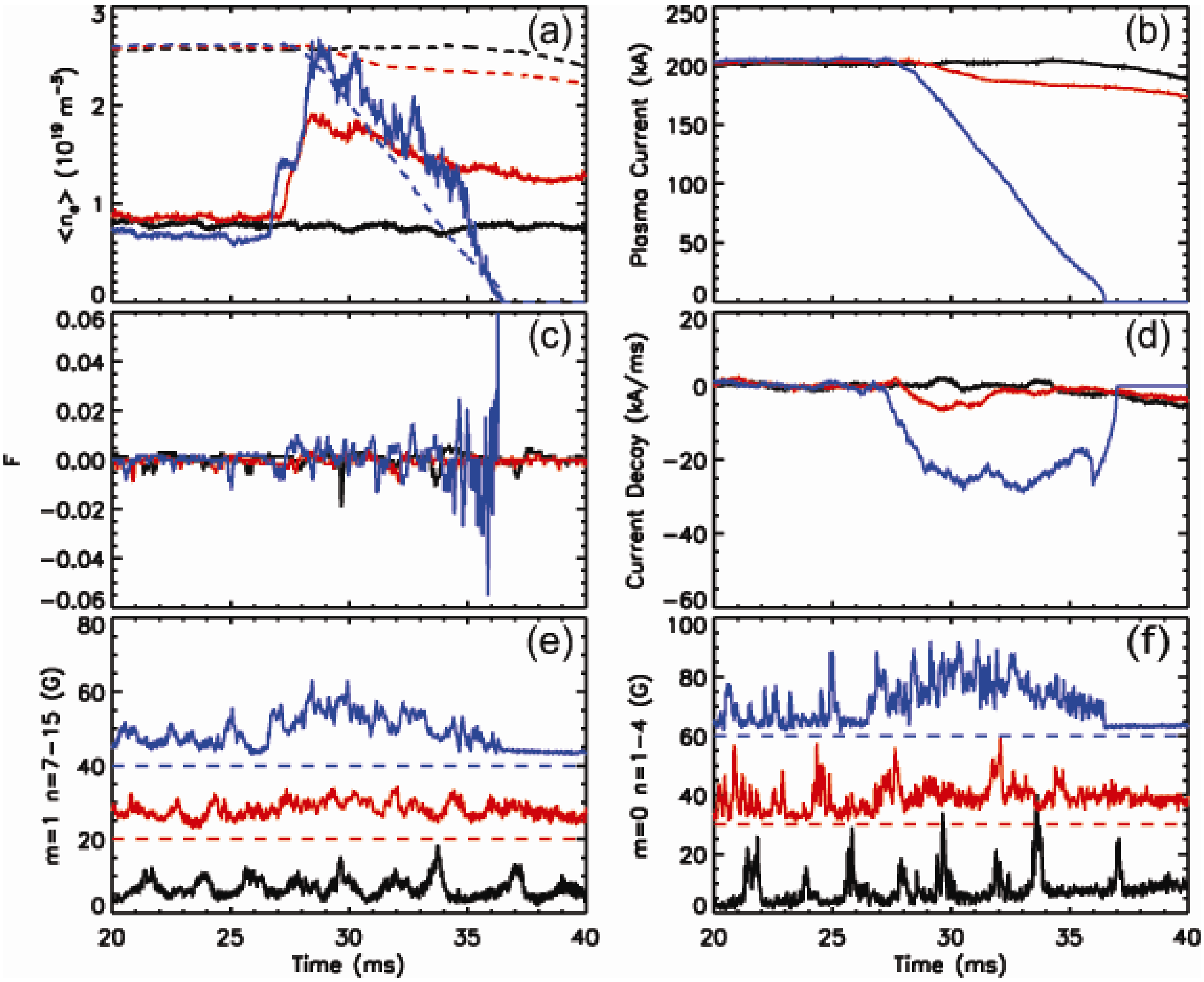

Figure 3.5: A sequence of 3 consecutive shots showing the onset of density limit termination through the use of fast pellet injection for a non-reversed discharges. Plotted signals are (a) $\langle n_e \rangle$ and n_{GW} (dashed), (b) plasma current, (c) reversal parameter F, (d) current decay rate, (e) core mode activity (m=1 n=7-15) and (f) edge mode activity (m=0, n=1-4). Mode activity is artificially shifted with zero values corresponding to horizontal dashed lines. The shot in red shows only a slight current decay despite fueling to a Greenwald fraction of ~75%. The shot shown in black has no pellet. The shot in blue fuels up to the Greenwald limit and results in a full termination of the plasma. [Shots: 1130312089(red), 1130312090(black), 1130312091(blue)]

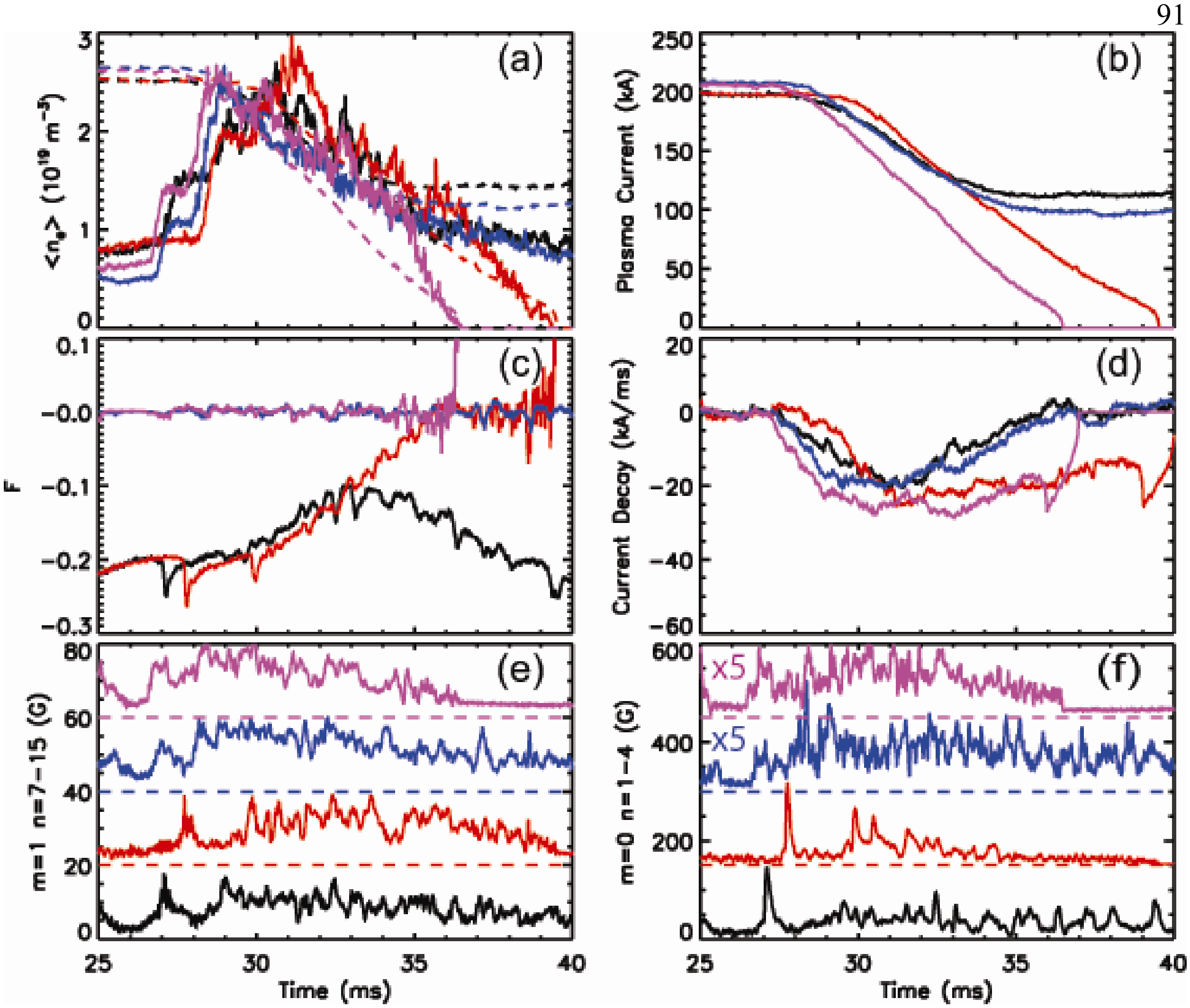

Figure 3.6: A comparison of reversed (red and black) and non-reversed (blue and magenta) pellet fueled discharges. Plotted signals are (a) $\langle n_e \rangle$ and n_{GW} (dashed), (b) plasma current, (c) reversal parameter F, (d) current decay, (e) core mode activity (m=1 n=6-15) and (f) edge mode activity (m=0, n=1-4). Mode activity is artificially shifted with zero values corresponding to horizontal dashed lines and the m = 0 activity for F = 0 discharges is multiplied by 5. The comparison shows a slightly more robust response to the density limit for reversed discharges. [Shots 1130312024(black), 1130312044(blue), 113031036(red), 1130312023(magenta)]

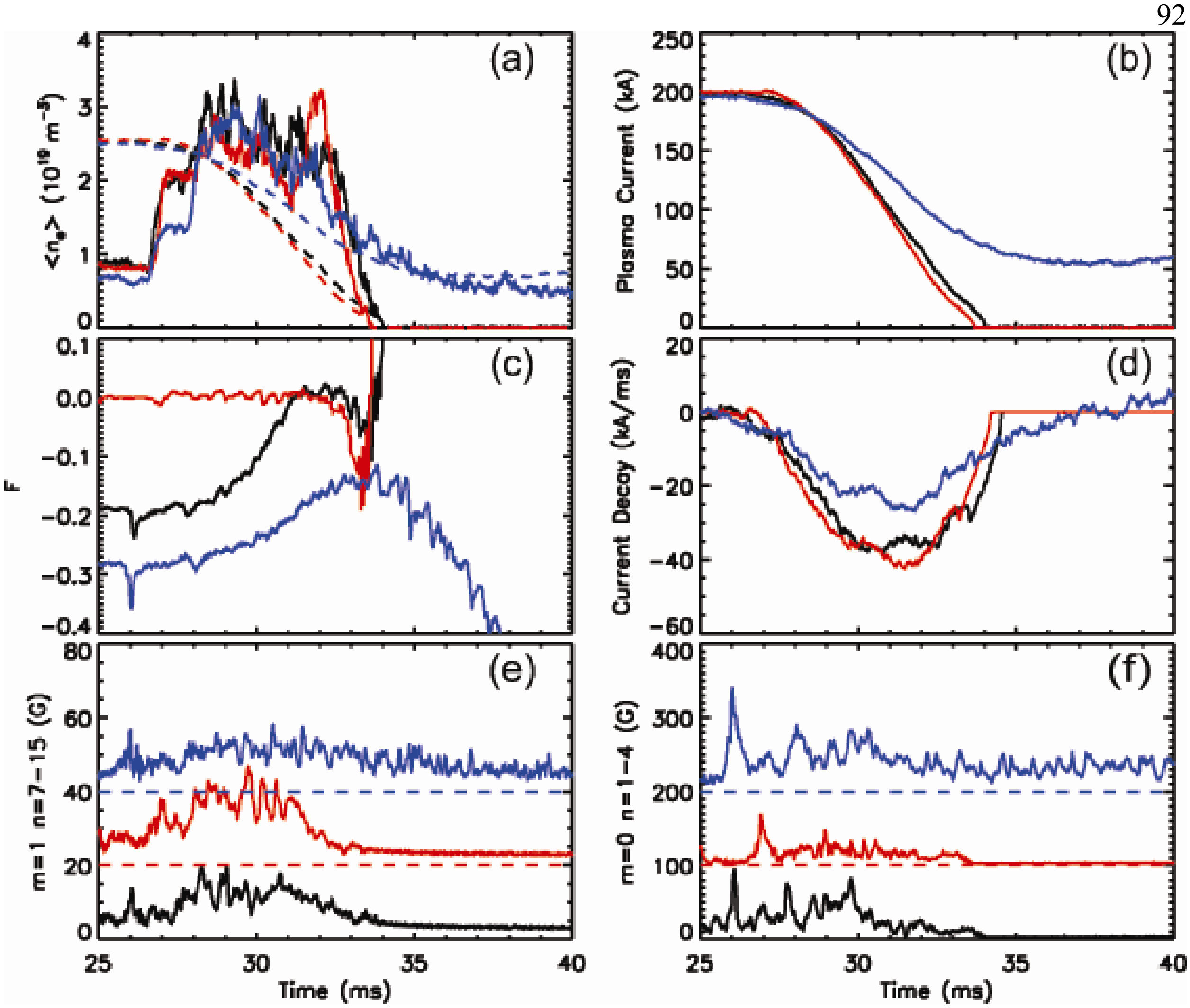

Figure 3.7: A comparison of 3 pellet fueled density limit experiments with similar sized pellets but varying degrees of reversal. Plotted signals are (a) $\langle n_e \rangle$ and n_{GW} (dashed), (b) plasma current, (c) reversal parameter F, (d) current decay rate, (e) core mode activity (m=1 n=7-15) and (f) edge mode activity (m=0, n=1-4). Mode activity is artificially shifted with zero values corresponding to horizontal dashed lines. The discharge with deeper reversal appears to have a more robust nature with respect to the plasma density limit.

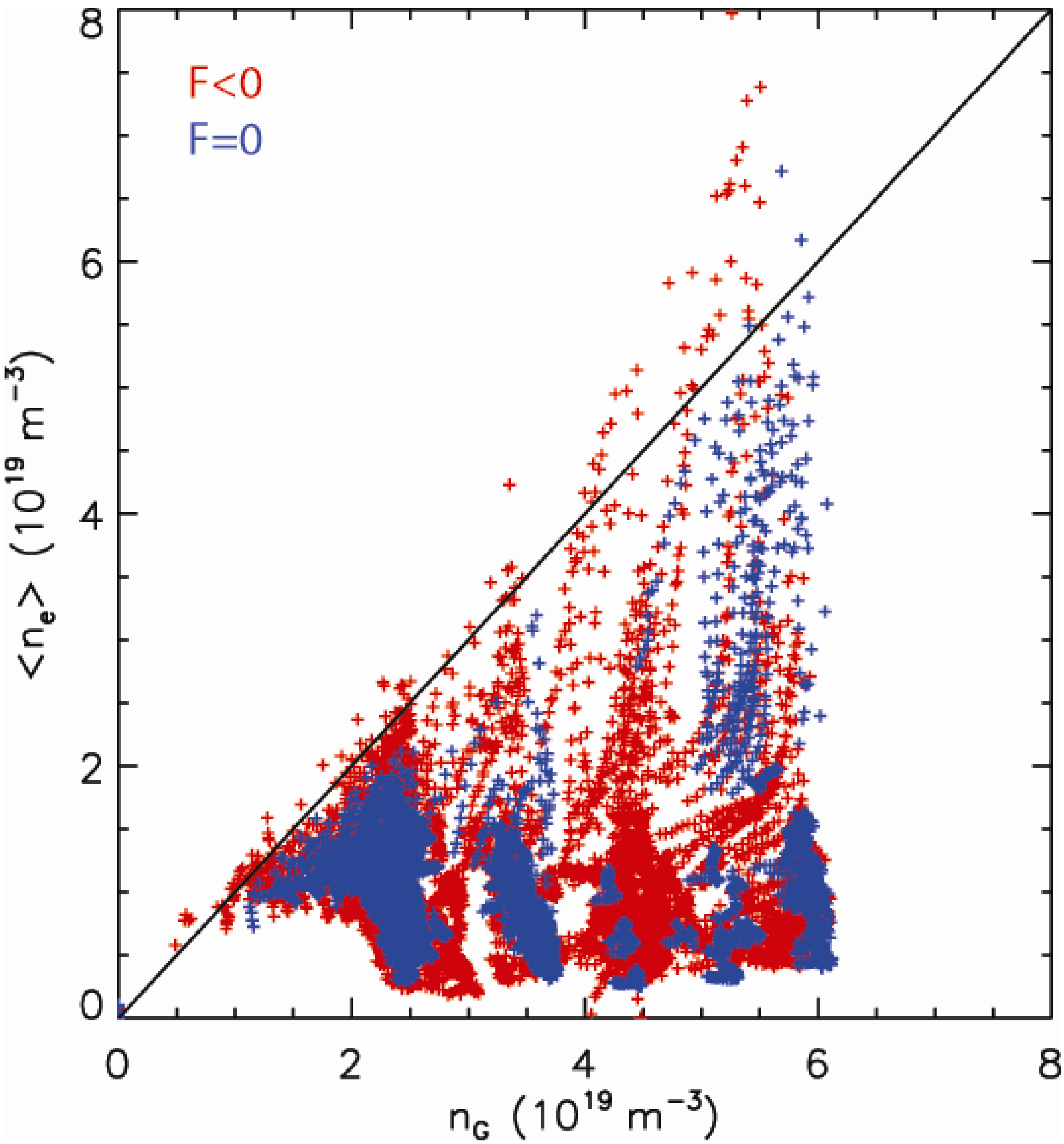

Figure 3.8: The density coverage for a collection of full PFN density limit experiments on MST where the normalized current decay rate is small (1/I*dI/dt > -5%/ms). Each point represents a 0.5 ms time window in time comparing the line averaged density and the Greenwald density. A comparison of reversed (red) and non-reversed (blue) discharges shows a slight difference in the onset of current decay for the two regimes with the reversed discharges extending up to and slightly above the Greenwald limit before showing signs of significant current decay.

3.2.3 Probe Measurements

The full complement of available diagnostics is utilized to investigate the pellet triggered terminations including two triple Langmuir probes inserted into the plasma for measurement of edge equilibrium and fluctuating quantities. Electrostatic fluctuations are known to influence particle transport in the plasma edge[8]. Several radial insertions (2.5cm, 5cm, 7.0 cm and 10.0 cm) were used. One probe was at the toroidal location of the pellet injector and the other 180 degrees away toroidally in order to compare the local and global nature of the density limiting physics. The two probes were located at the same poloidal angle (75 degrees above the outboard midplane). Unfortunately, measurements from the probe located on the other side of the machine were unusable except to estimate the density transit time delay between the two probes, shown in figure 3.9. The delay of ~1 ms is consistent with the estimated particle transit time and is similar to the time delay observed on the CO_2 density measurement compared to the FIR system (see figure 3.12 for comparison). Following the pellet impact on the vessel wall, we observe an increase in the edge n_e at all radii as well as a cooling of the edge to less than 10 eV, shown for a set of discharges in figure 3.10 for a probe insertion of 7 cm. The decrease in edge temperature also coincides with a greater decay of the plasma current.

A fluctuation power spectrum analysis of the probe measurements of density and temperature is effected using a scanning FFT method and shows an increase in the fluctuation power at lower frequencies and a decrease in power at high frequencies for both quantities. In figure 3.11, we compare the density fluctuation power spectrum for 4 cases; no pellet, partial current decay (~25%), half current decay (~50%), and full current decay (100%). These are the same four discharges shown in figure 3.10. Consistently, we observe an increase in the low frequency region of the power spectrum and a general decrease in high frequency activity. One possible explanation is that the activity is associated with the m = 0 edge modes which grow in amplitude as the plasma current decays. While a more comprehensive analysis of the fluctuations would require a significantly larger set of data, the increase in fluctuations could be indicative of increased transport in the edge during a density limit collapse.

3.2.4 Density Profile Evolution

In this section we compare the results of the two interferometer systems which measure $\langle n_e \rangle$ on MST. The FIR system is located close to the pellet injection line while the CO_2 is on the opposite side of the machine. The FIR system suffers some reduction in signal at large densities due to its proximity to the ablating pellet, particularly when set up for simultaneous interferometry and polarimetry measurements. Indeed, full termination discharges offer almost no reliable measurements of the density profile due to the loss of signal caused by the extreme local densities. Partial termination discharges lose signal briefly, but otherwise show an increase in $\langle n_e \rangle$ consistent with CO_2 measurements. As we approach the region in time where signal is lost, there is an apparent asymmetry in the core line averaged density measurements as shown in figure 3.12. The asymmetry also coincides with the region of current decay. The post pellet density profile appears hollow as the edge chords measure a higher $\langle n_e \rangle$, in contrast to the pre pellet measurements. The data in 3.12(c) is shown almost entirely, even though it is of suspect quality due to the decreased signal. The system is more robust when set to solely measure the density. An inverted density profile was obtained for a partial current termination (~25%) discharge and shows an extremely hollow density, figure 3.13. This is consistent with probe measurements as well as $\langle n_e \rangle$ comparisons of core and edge chords.

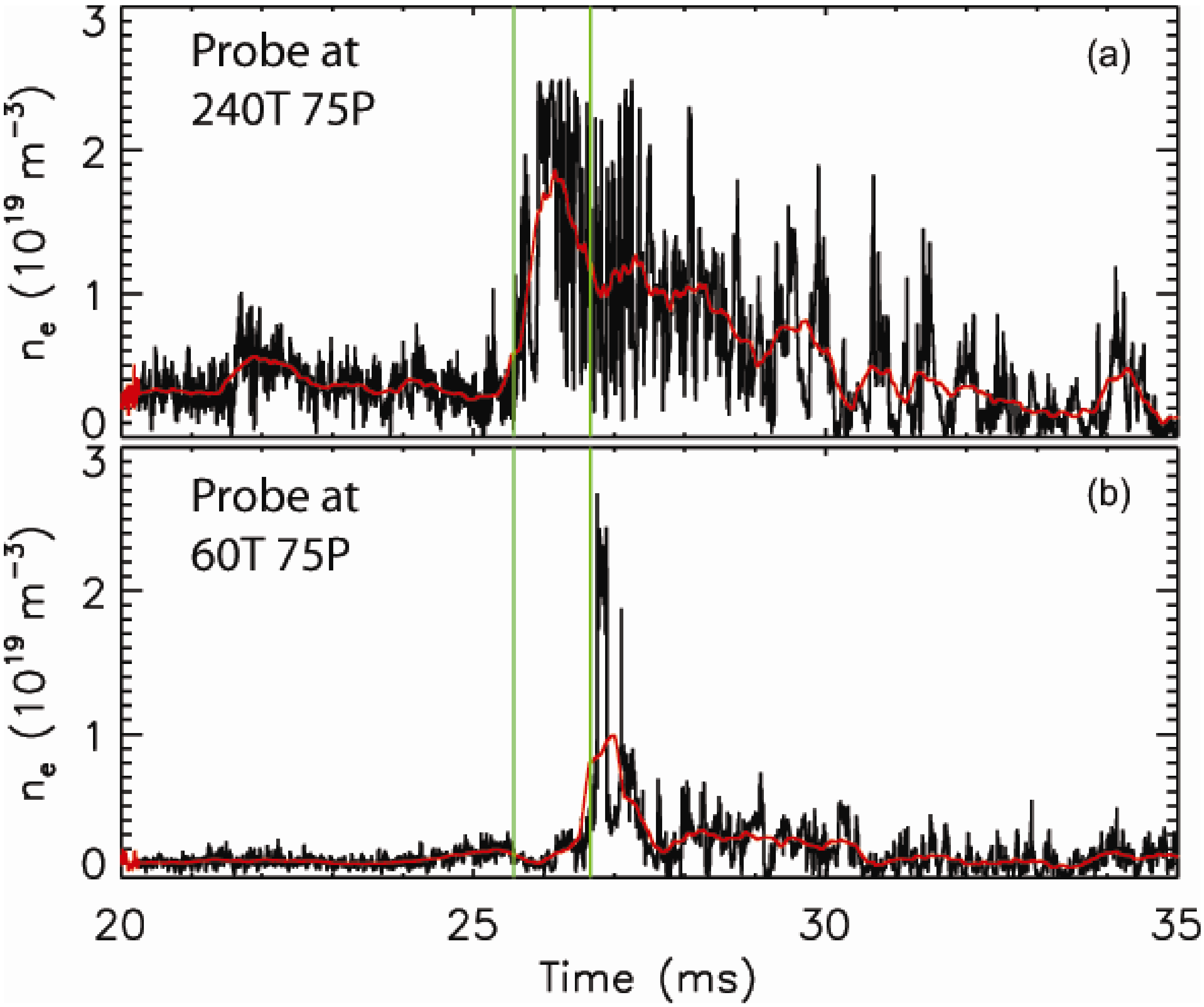

Figure 3.9: The probe density measurement and smoothed average (red) for two inserted Langmuir probes is plotted along with the approximate duration of pellet ablation is indicated by the vertical green lines. (a) The probe at the location of the pellet injector. (b) The probe located on the opposite side of the machine. A small delay in the density signal is consistent with particle transit times. The density data in (b) was consistently low making the pellet timing the only measurement available from that probe. [Shot 1130319042]

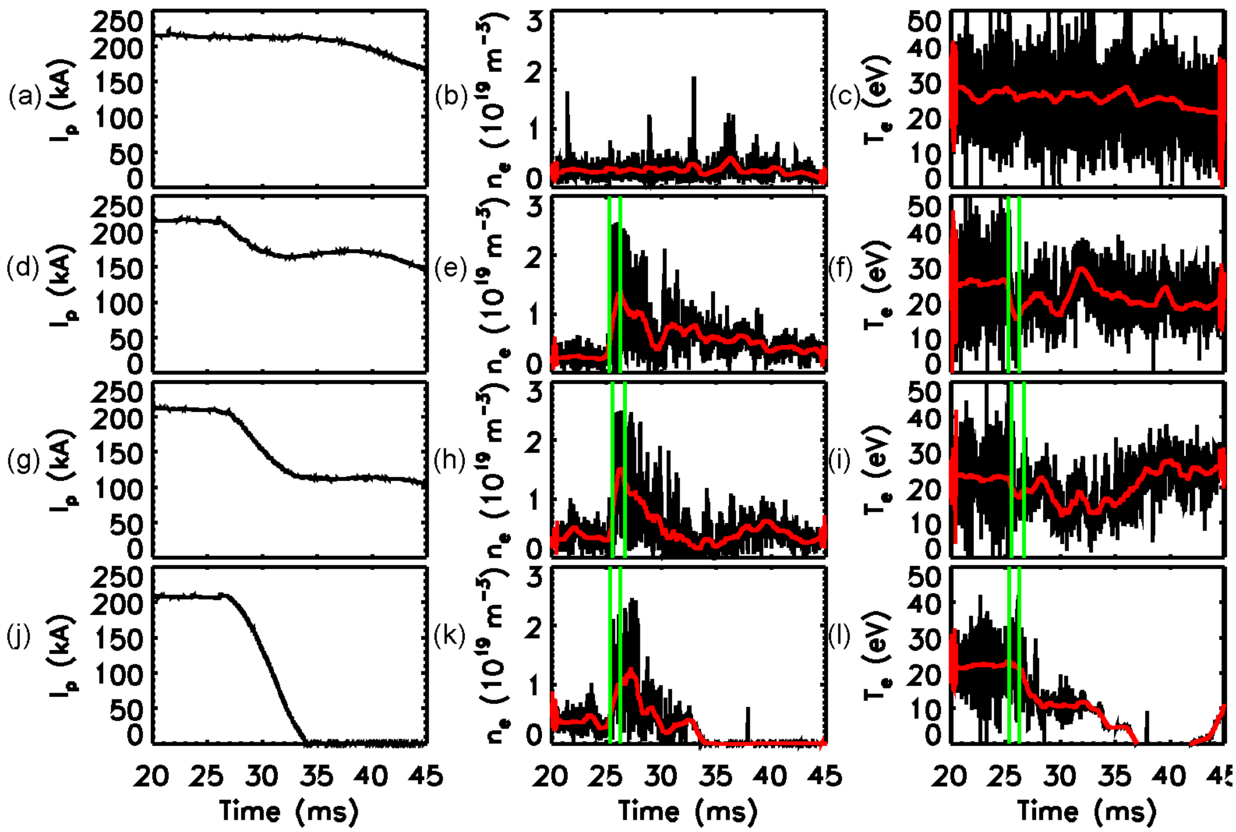

Figure 3.10: Plasma current, probe density and temperature measurements (and smoothed average in red) at the toroidal location of the pellet injector during pellet triggered terminations for four cases: (a, b, c) no pellet, (d, e, f) ~25% current decay, (g, h, i) ~50% current decay, (j, k, l) full current decay of the plasma. Approximate pellet ablation durations are shown by the vertical lines. Probe was inserted 7 cm into the plasma for this set of discharges. [Shots 1130309031(a, b, c), 1130309044(d, e, f), 1130309042(g, h, i), 1130309038(j, k, l)]

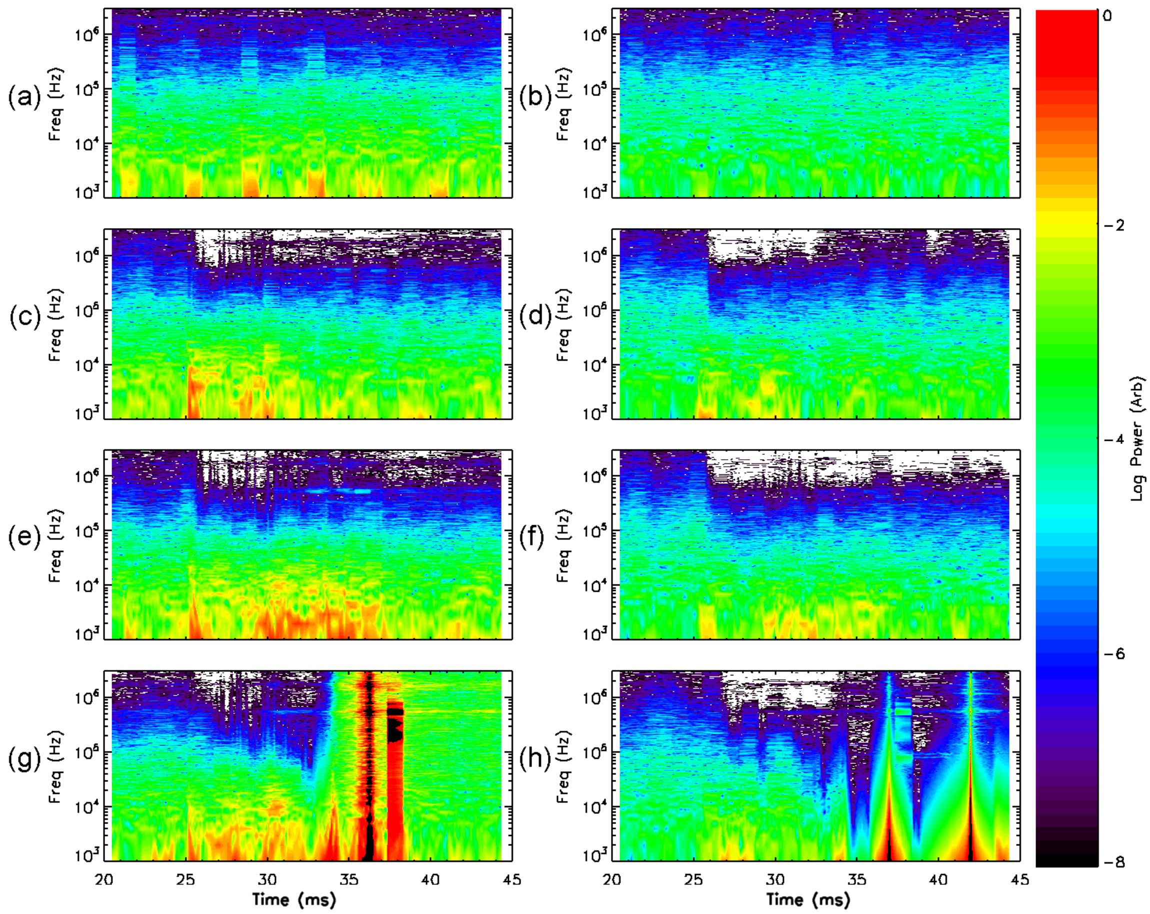

Figure 3.11: Fluctuation power spectrum for the probe density (left) and temperature (right) data shown in figure 3.10. (a, b) no pellet, (c, d) ~25% current decay, (e, f) ~50% current decay, (g, h) full current decay of the plasma. Pellet hits at ~25 ms in plots (c - h) as indicated in figure 3.10. [Shots 1130309031(a, b), 1130309044(c, d), 1130309042(e, f), 1130309038(g, h)]

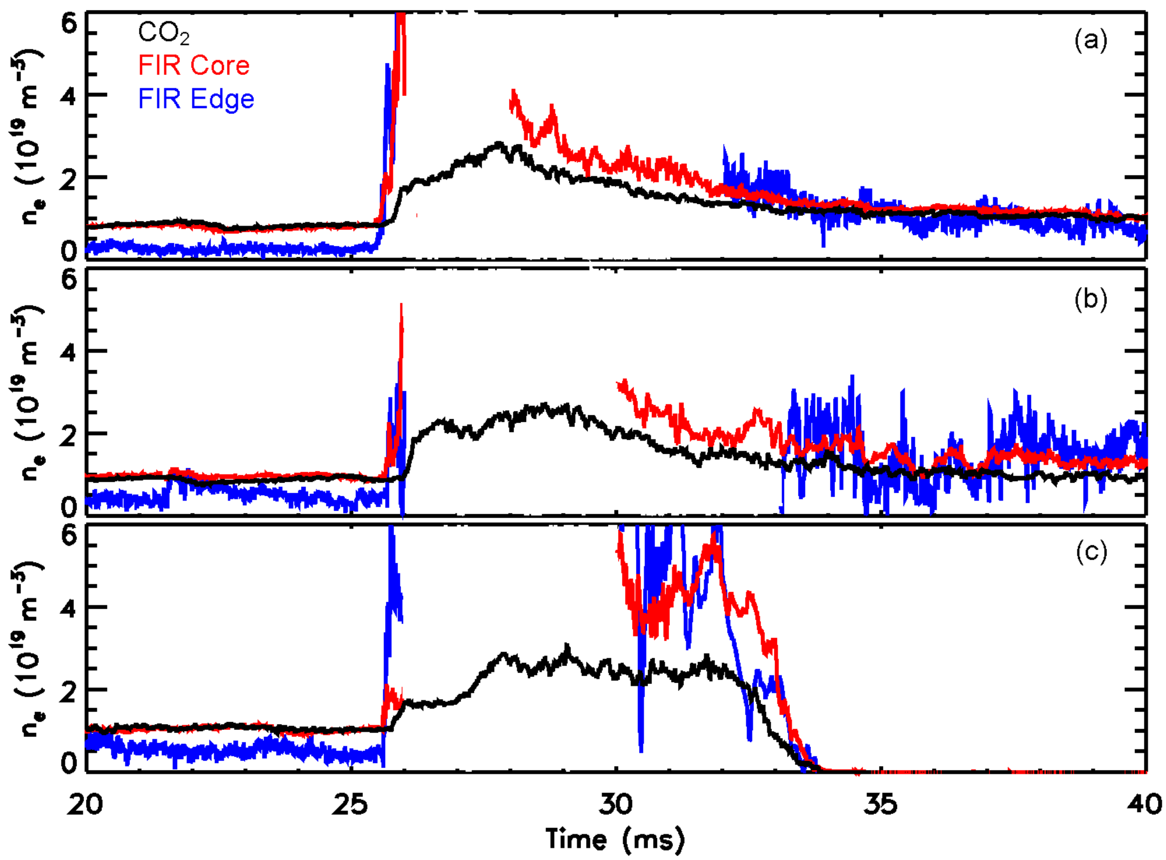

Figure 3.12: Measured $\langle n_e \rangle$ from the CO_2 (black), core (p06) FIR (red) and edge (p43) FIR (blue) for three pellet triggered termination discharges from figure 3.10. (a) is a partial current decay, (b) is a half current decay and (c) is a full termination of the plasma. A toroidal asymmetry is observed in regions of time where current decays. Density after pellet injection is very hollow, as indicated by the larger measurements for the edge $\langle n_e \rangle$ compared to the core. Both core and edge FIR measurements lose signal during pellet ablation and in (c), the entire data is suspect due to the low signal. [Shots 1130309044(a), 1130309042(b), 1130309038(c)]

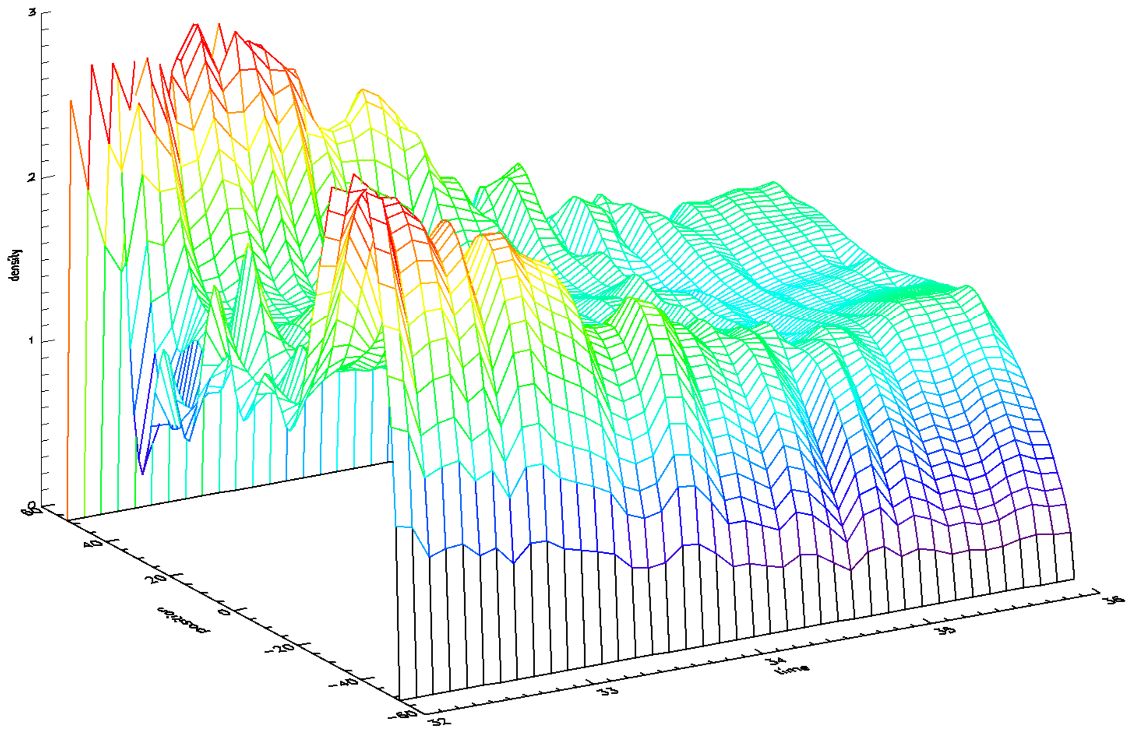

Figure 3.13: Inverted density profile for partial termination discharge showing extremely hollow profile immediately following pellet fueling. [Shot 1130309044]

3.2.5 Observed Increase in Radiation

The role of radiation in the physics of the density limit is well established, prompting a look at the available radiation-based diagnostics on MST. Impurity line radiation, measured by the Impurity Monochromator Array (IMA), is observed to increase by orders of magnitude for some elements. The dominant impurity in MST plasmas is carbon. This is due to the ~10% coverage of the interior of the vessel with graphite tiles. Plasma-wall interaction plays a large role in the impurity influx on MST. IMA radiation signals for CIII, CV, BIV, OIV and NIV are shown for several pellet fueled discharges in figure 3.14. The increase in the CIII, OIV and NIV signals indicate a highly radiative and cold plasma edge region. The decrease in CV and BIV indicate a cooling of the core. Excessive radiation leads to cooling of the electrons, consistent with measurements of plasma edge region with $T_e < 10$ eV. The impact of bremsstrahlung is not considered here, though we do not observe a broadband increase on all detectors, indicating at the very least, that the signal is not dominated by an increase in bremsstrahlung. CCD camera images also show a radiative edge during some plasma terminations as shown in figure 3.15. The camera, normally used for tracking the pellet in flight, shows an inward creep of visible light, suggesting a shrinking of the current channel as the discharge ends.

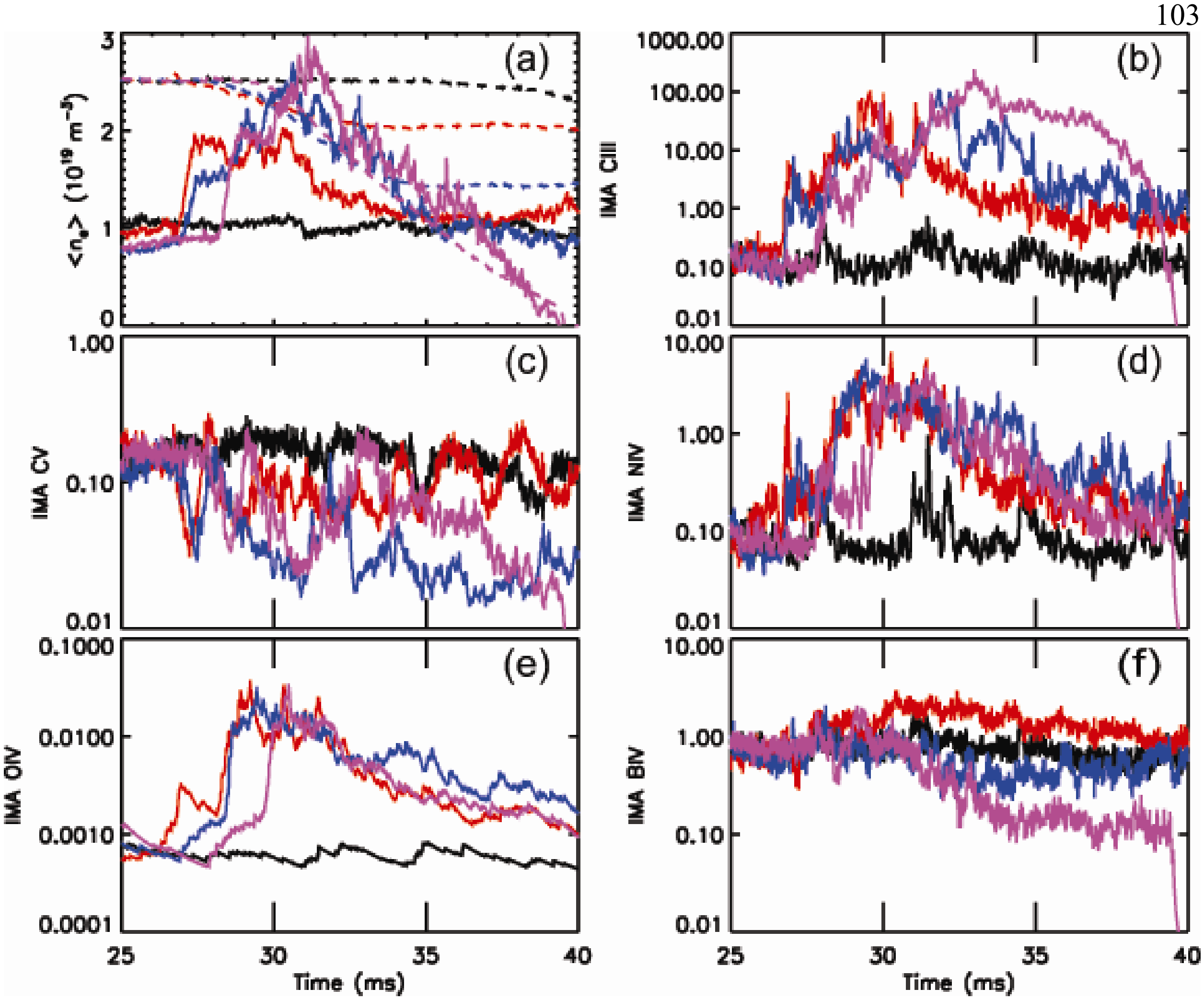

Figure 3.14: A series of pellet fueled discharges with increasing pellet mass results in an increase in the current decay after fueling for a set of reversed discharges. Plotted signals are (a) the $\langle n_e \rangle$ and n_{GW}, IMA radiation measurements for (b) CIII, (c) CV, (d) NIV, (e) OIV and (f) BIV. The observed line radiation for IMA measurements is consistent with core cooling (lower CV, BIV) and edge cooling (CIII, NIV, OIV). The large increase in impurity radiation is consistent with many observations during the density limit. [Shots 1130312026(black), 1130312044(red), 1130312036(red), 1130312023(gray)]

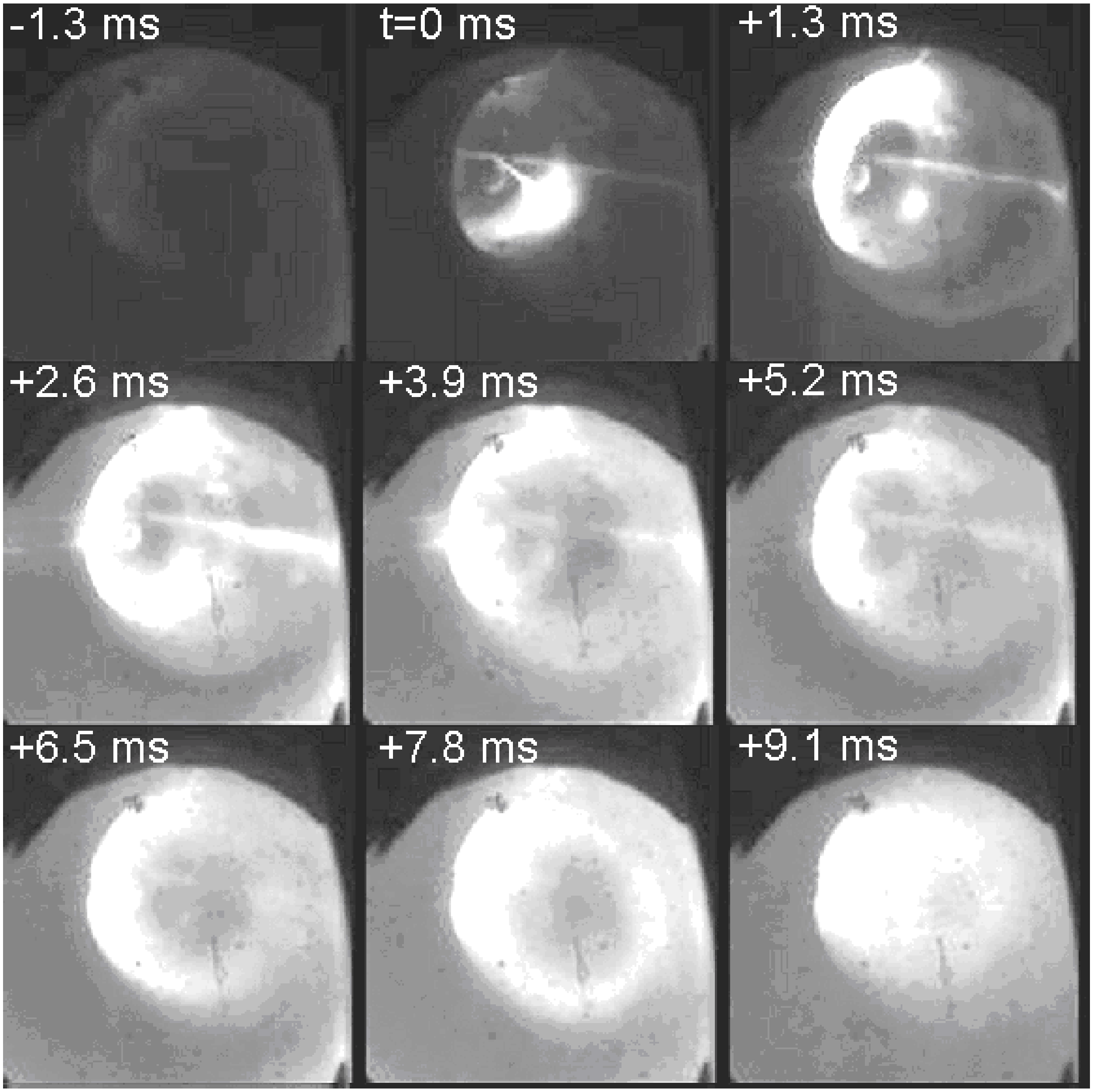

Figure 3.15: Sequence of CCD images in visible spectrum during a density limit termination. An increasing amount of edge radiation is observed during the termination of a discharge. Pellet is injected at ~25 ms and time is recorded relative to the pellet entering the plasma. Framerate is ~770 Hz. (shot 1130312091)

3.3 Phenomenology of the Density Limit Termination

3.3.1 Time evolution of the termination

In contrast to the tokamak disruptive density limit, the experiments on MST show a robust nature of RFP plasmas as density approaches the Greenwald limit. At fueling densities close to the Greenwald limit, the plasma current can decay by 50% or more and ultimately recover, as is observed in the evolution of the plasma current in figures 3.2, 3.4, and 3.5. As a means of further exploring the nature of the limit, we categorize and ensemble the collection of discharges. The ensemble depicts the temporal evolution of the density limit for reversed (figure 3.16) and non-reversed (figure 3.17) experiments. We categorized based upon the fractional loss of plasma current after the pellet fueling as follows; less than 5% (Black), 5% to 15% (Red), 15% to 25% (Green), 25% to 50% (Blue), 50% to 75% (Cyan), and 75% to 100% (Magenta). As opposed to single shot comparison, categorizing the discharges in this manner provides an understanding of how various quantities vary in time as well as how they scale with increased density. We note that the number of non-reversed discharges is smaller for all categories, resulting in a somewhat less clear comparison.

As expected, discharges with a larger density lead to a larger drop in plasma current as well as a larger rate of current decay in both reversed and non-reversed discharges. In reversed discharges, the reversal parameter trends closer to zero as previously observed. The edge and core mode activity increases, but there appears to be saturation in the mode activity with approximately equal levels of activity observed for fractional current decays of 30 – 100% for edge modes and from 50 – 100% for the core mode activity. Similar observations are made for non-reversed discharges, although the saturation in mode activity is not observed in this case, though this could be due to the small number of discharges with large current decay.

Figure 3.18 combines the Thomson scattering and probe measured temperatures to show the evolution of the temperature profile for a partial plasma termination (corresponding to the green curve of figure 3.16). The outermost Thomson measurement is at r/a = ~0.8, while the innermost probe insertion was 10 cm (r/a ~ 0.81), with the majority of probe data at an insertion of 7 cm or less (r/a > 0.87). Thomson scattering temperature measurements show a rapid cooling of the plasma after pellet injection. The core T_e drops to ~100 eV before the plasma recovers and T_e subsequently increases. The edge temperature evolves consistently, with temperatures decreasing for all radii and subsequently recovering slightly along with the core T_e.

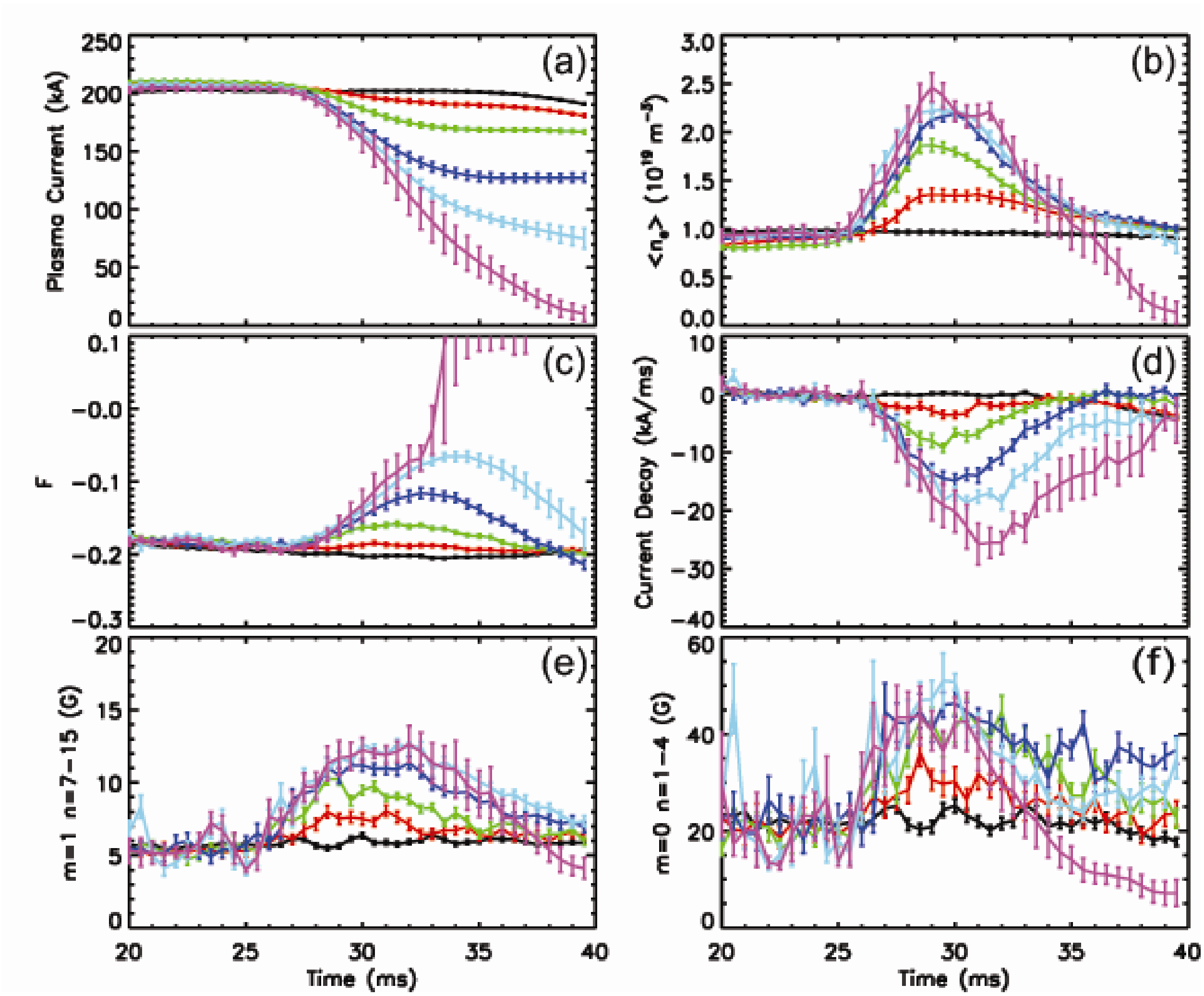

Figure 3.16: Ensemble averages for pellet triggered termination plasmas categorized by the fractional decay of plasma current for reversed discharges. Plotted are (a) plasma current, (b) density, (c) reversal parameter F, (d) current decay rate, (e) edge mode activity and (f) core mode activity. Pellet injected at ~25 ms.

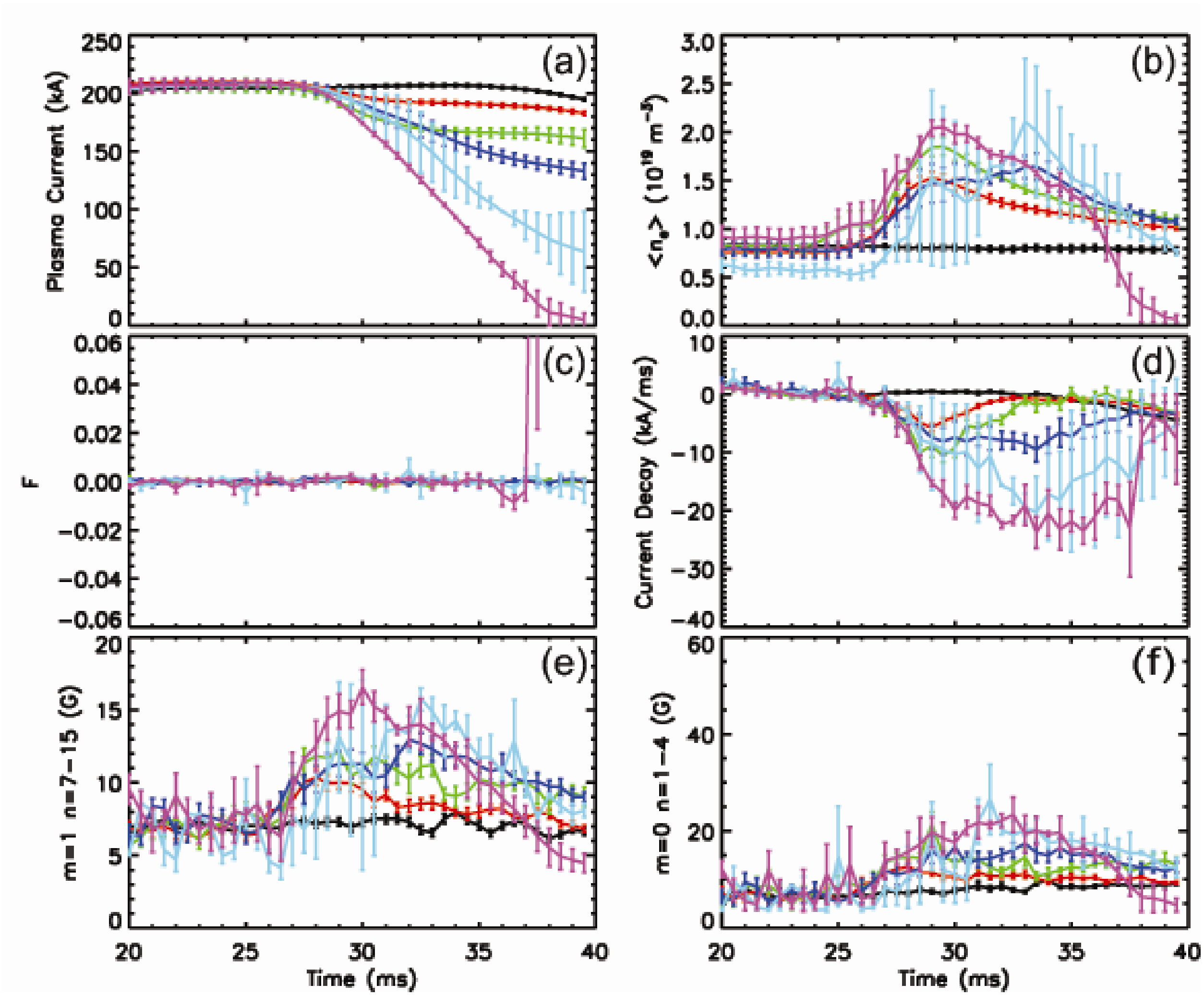

Figure 3.17: Ensemble averages for pellet triggered termination plasmas categorized by the fractional decay of plasma current for non-reversed discharges. Plotted are (a) plasma current, (b) density, (c) reversal parameter F, (d) current decay rate, (e) edge mode activity and (f) core mode activity. Pellet injected at ~25 ms.

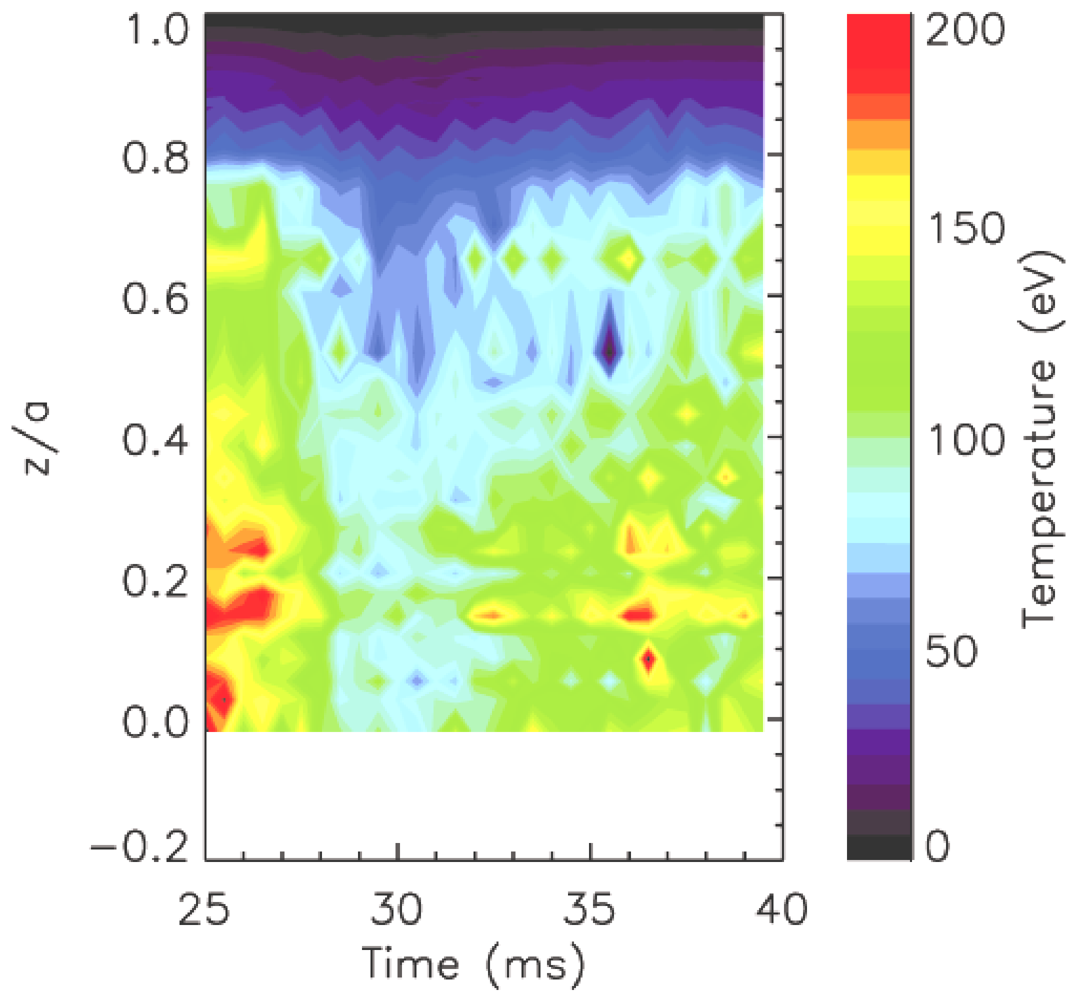

Figure 3.18: Thomson scattering and probe temperature measurements for the green curve in figure 3.16. Pellet injected at ~25 ms.

3.3.2 Density Scaling of measured quantities

We now shift focus to look at how various quantities scale with the density during the collapse. We ensemble the full collection of 200 kA density limit experiments with and without plasma reversal based on the normalized density N_{GW}. Pellets are injected at ~25 ms and the region of interest is the period of current decay following pellet injection from 25-35 ms. For each discharge, this time region is subdivided and averaged at 2 kHz (0.5 ms time windows) to match the rate of Thomson scattering data collection. In figure 3.19 we look at the (a) ensemble size, (b) measured density, (c) plasma current, (d) normalized current decay rate, (e) reversal parameter F, and (f) pinch parameter Θ dependence on the N_{GW}. These parameters serve to characterize the plasma as N_{GW} increases. There are two factors which contribute to the increase in N_{GW}, the measured $\langle n_e \rangle$ and the plasma current ($n_{GW} \sim I_p$). The increase in $\langle n_e \rangle$ is observed up to $N_{GW} \sim 1$, where the ensembled I_p starts to decrease more rapidly with increased N_{GW}. Little difference exists between $\langle n_e \rangle$ and I_p for the reversed and non-reversed ensembles. The normalized current decay rate remains larger for non-reversed discharges, consistent with previous observations of a lower density limit. At $N_{GW} = 1$, the non-reversed discharge is decaying almost twice as fast with a normalized decay rate of 9% compared to 5% for the reversed case. We start to notice a change in both F and Θ starting at N_{GW} ~0.5 – 0.6. In the reversed case, both parameters evolve continuously as N_{GW} increases. In the non-reversed case, F remains zero, while Θ drops from 1.5 to 1.45 at $N_{GW} = 1$, where it remains for further increases in the normalized density.

In figure 3.20 we look at the scaling of (a) core mode activity and (b) edge mode activity, Thomson scattering measurements of T_e in the (c) core (r/a < 0.2), and (d) edge (r/a 0.7-0.8). The normalized core mode activity is observed to increase continuously with increases in N_{GW} for both reversed and non-reversed discharges. In the RFP, stochastic transport scales as the square of the m = 1 fluctuations. The higher amplitude of the core modes in non-reversed discharges could contribute to the earlier onset of plasma termination if stochastic transport plays an important role in the density limit. However, the presence of m = 0 islands is noted in density limit experiments on RFX-mod and we also observe an increase in normalized m = 0 activity as N_{GW} increases. While the edge activity is lower in non-reversed discharges at all densities, it does scale with N_{GW}, increasing in amplitude despite there being no m = 0 resonant surface in the plasma itself.

As we move on to discuss the temperature scaling, we first note that the ensemble size is significantly smaller for both the Thomson scattering and probe measurements due to limited availability. The results are still significant and merit discussion. A strong cooling is observed in Thomson scattering measurements of Te in the core (r/a < 0.2) as well as the edge (r/a = 0.7 – 0.8) as N_{GW} increases. Additionally, the non-reversed discharges appear slightly colder for all values of N_{GW}. Ignoring any changes in Z_{eff} and neoclassical trapped electrons, the change in the classical resistivity scales as $T_e^{-3/2}$, so the colder plasma is more resistive which could account for the difference in the current decay rate for reversed and non-reversed discharges. As N_{GW} approaches and exceeds 1, edge Te (r/a =0.7 - 0.8) drops to 10-20 eV approaching diagnostic limits for Thomson scattering. Figure 3.21 shows the measured n_e and T_e for all four probe insertions of (a, b) 10 cm, (c, d) 7 cm, (e, f) 5 cm, and (g, h) 2.5 cm. For 7 cm insertion, the probe density in non-reversed discharges increases steadily until N_{GW} ~ 0.7, when it stabilizes at ~$0.7*10^{19}$ m^{-3}. In reversed discharges probe density exceeds that of the non-reversed discharges briefly, reaching ~$1.0*10^{19}$ m^{-3} at N_{GW} = 0.7 before again matching the non-reversed case at N_{GW} = 0.9. Though the coverage of the data is limited, we observe similar trends for an insertion of 5 cm and the additional radial insertions of 2.5 and 10 cm are consistent, though lacking. If the edge density is a factor, we do observe a higher maximum value in reversed discharges, compared to non-reversed discharges, though our ensembles are very limited in size. More interesting is that we observe a limit on the edge measured density for all radial insertions, even as N_{GW} continues to increase.

Though the collection of discharges is less for density limit experiments at higher currents, plots identical to 3.19 and 3.20 (except for probe measurements) are available for 300 kA, 400 kA and 500 kA density limit experiments in an appendix.

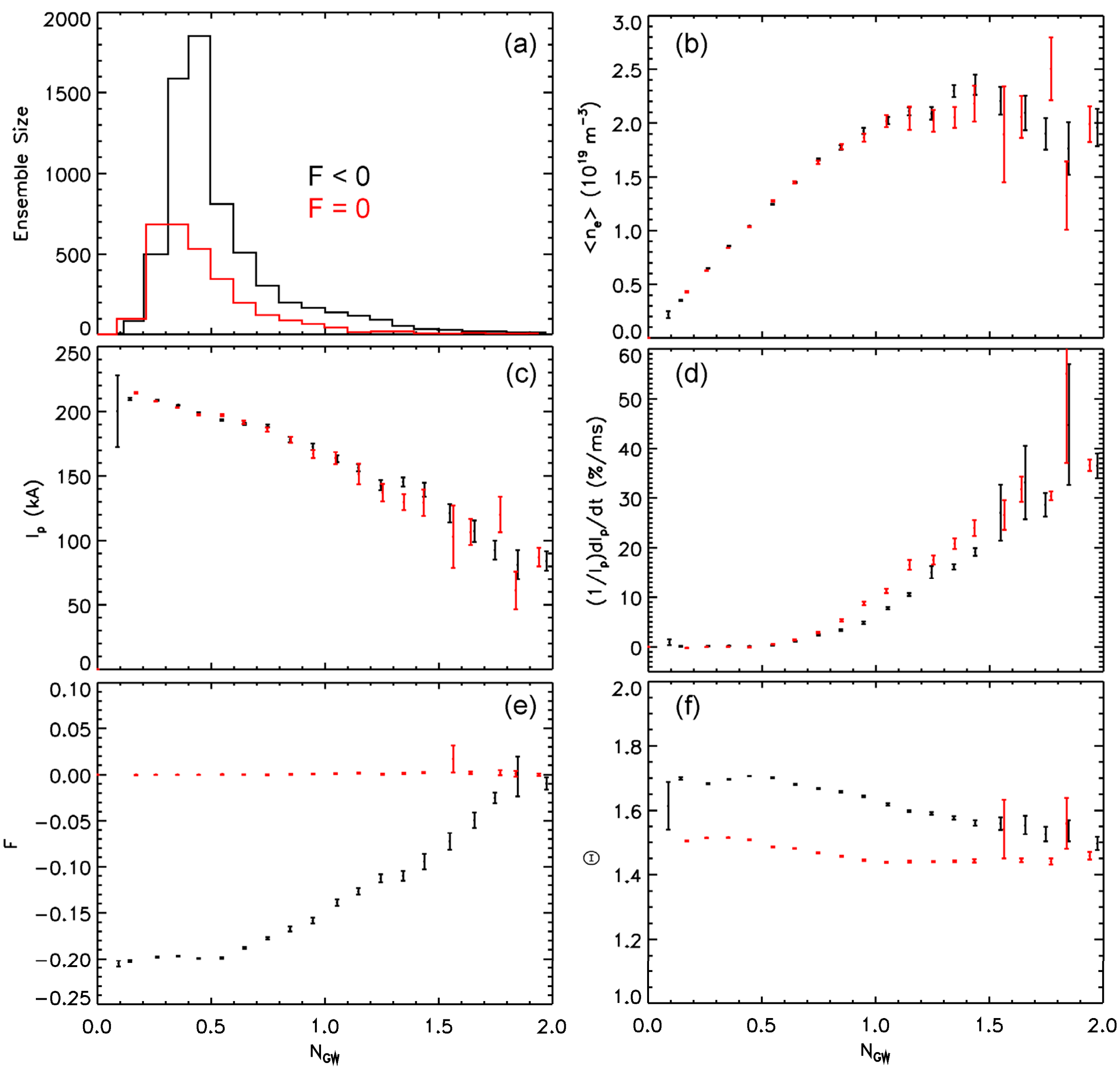

Figure 3.19: (a) Ensemble size, (b) $\langle n_e \rangle$, (c) plasma current, (d) normalized current decay rate, (e) F, and (f) Θ dependence on normalized density for reversed (black) and non-reversed (red) density limit experiments on MST. Error bars are statistical.

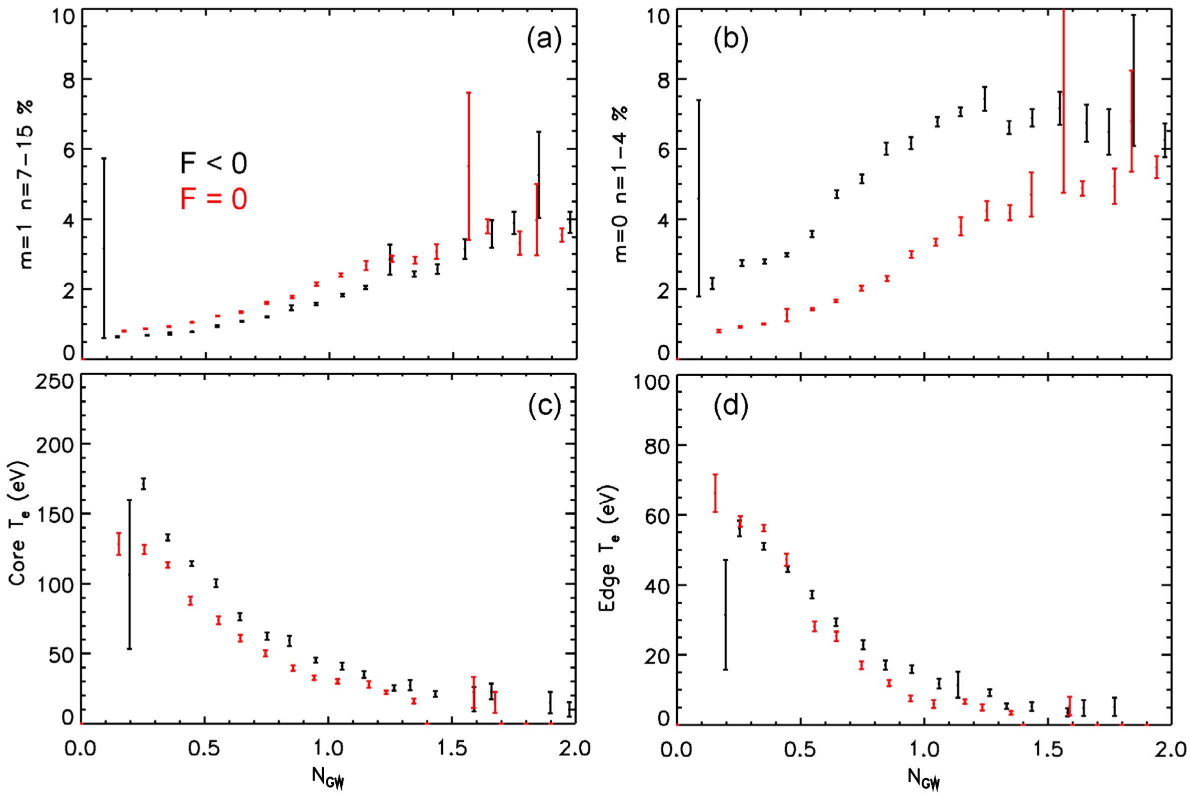

Figure 3.20: (a) Normalized RMS core mode activity, (b) normalized RMS edge mode activity, (c) Thomson scattering core Te (r/a < 0.2), and (d) Thomson scattering edge Te (r/a = 0.7 – 0.8) dependence on N_{GW} for reversed (black) and non-reversed (red) density limit experiments on MST. Error bars are statistical.

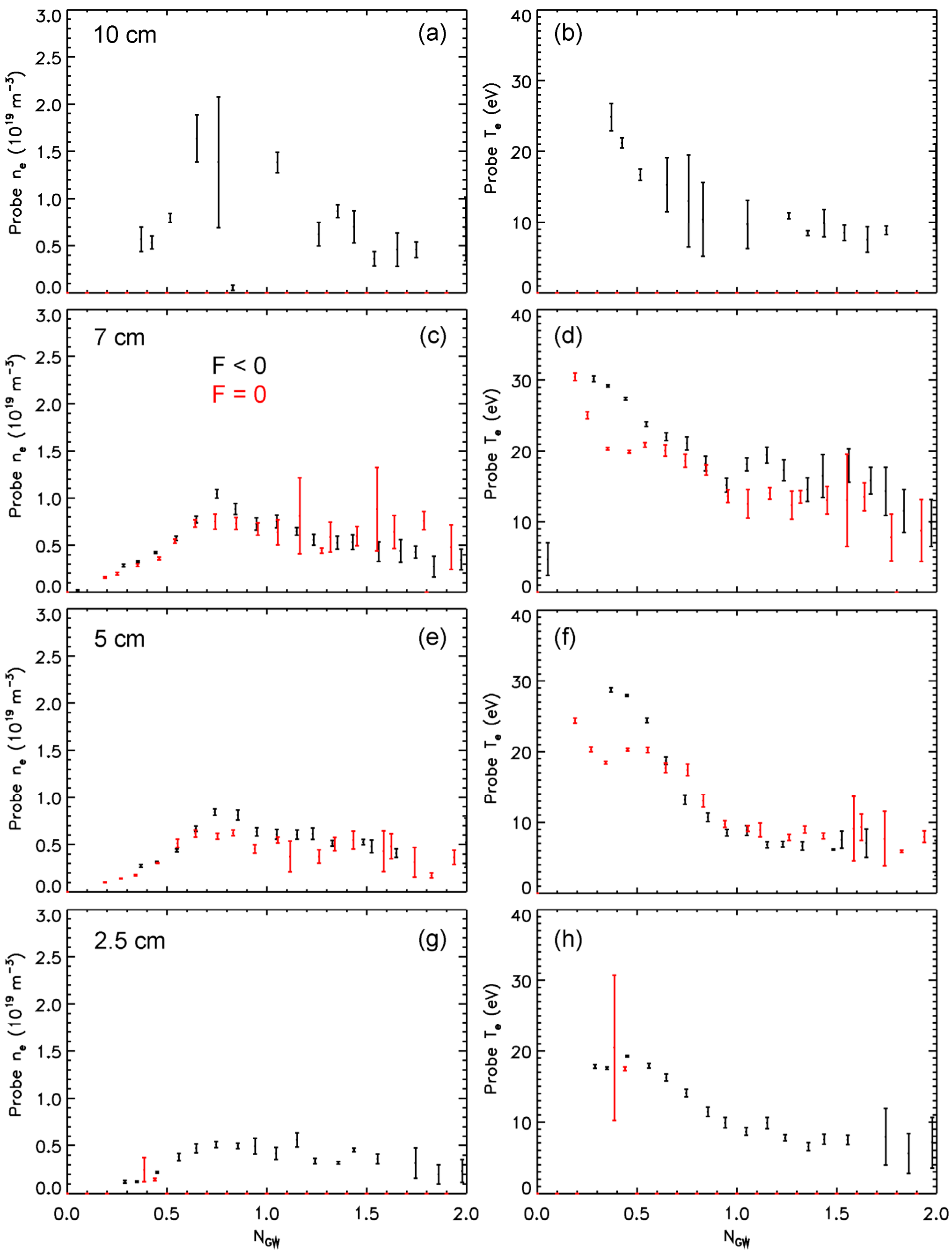

Figure 3.21: Ensemble measurements of probe n_e (left) and T_e (right) for radial insertions of (a, b) 10 cm, (c, d) 7 cm, (e, f) 5 cm, and (g, h) 2.5 cm showing dependence on normalized density for reversed (black) and non-reversed (red) density limit experiments on MST. Error bars are statistical.

3.4 Maximizing Density in PPCD

Although much of the focus of the PPCD discharges with pellet fueling centers on exploring high β (the subject of chapters 4 and 5), maximizing the density during improved confinement by using pellet injection has been an important secondary goal. As these are the plasmas with the best confinement on MST, we wish to understand how/if the density limit differs in these conditions relative to that in standard plasmas. We will briefly discuss the best recorded cases for pellet fueling into these plasmas and leave the discussion of other aspects of these experiments for later chapters. While edge fueling is the goal for density limit experiments in standard discharges, optimizing the core fueling is the primary goal of the high density PPCD experiments discussed here.

As has been shown in the past on MST and in other non-RFP devices, the Greenwald limit can be exceeded with pellet fueling of the plasma core. The primary reason for this is the peaked nature of the pellet fueled density profiles coupled with the improved confinement in PPCD discharges. The highest density discharges obtained in MST are shown in figure 3.22. Greenwald fractions of 2.0 have been achieved in 200 kA PPCD plasmas, currently the largest observed Greenwald fraction in MST and the RFP. It is observed that this high density, even in improved confinement discharges, challenges the plasma sustainment as the observed magnetic activity increases. The density limit is also exceeded in 500 kA PPCD with Greenwald fractions reaching 1.4 during the PPCD period. This corresponds to an absolute density of 9e19 m^{-3}, a record for controlled fueling in MST. Again, an increase in magnetic activity is also observed which is believed to have an impact on the confinement. We note here that in the 200 kA case, the plasma ends prematurely about 10 ms after the density increase, and the current decay is comparable to some of the slower density limit terminations in standard discharges. However, PPCD experiments are also not sustained, unlike the density limit experiments in standard discharges. Matters are further complicated by the core pellet ablation and the significantly different magnetic shear profile associated with PPCD discharges. While not yet attempted, density limit experiments with pellet edge fueling in PPCD discharges would provide a better comparison between the PPCD and standard cases.

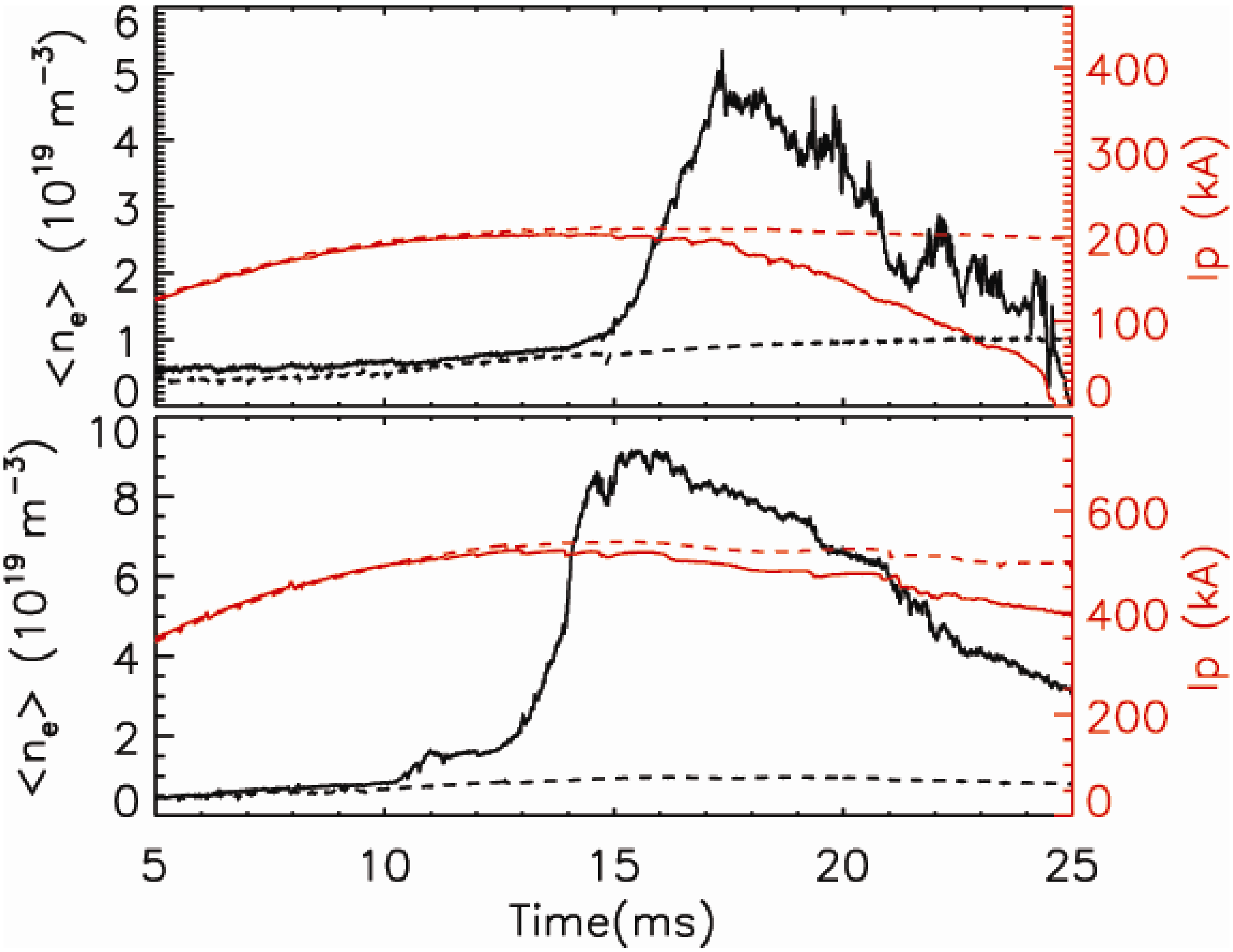

Figure 3.22: The highest density cases obtained in improved confinement discharges in MST at 200 kA (top) and 500 kA (bottom) PPCD discharges. The dashed lines represent PPCD discharges with no pellet fueling for comparison. [Shots 1130305034(top solid), 1130305092 (top dashed), 1131011045 (bottom solid), 1131011040 (bottom dashed)]

3.5 Discussion of Results

A substantial amount of information has been added toward the goal of understanding the density limit on MST and the RFP. By injecting fast pellets into MST discharges, we reliably and reproducibly triggered density limiting terminations and studied them using the full suite of MST's diagnostics. The Greenwald scaling has now been established for the full range of available plasma current on MST, up to 600 kA. A higher terminating limit is observed at high current. One possible explanation for this is an increase in core ablation during pellet transit due to the increased plasma temperature, resulting in a larger pellet required to trigger the density limit collapse upon impact with the wall. The nature of the plasma current response to the RFP density limit also appears rather robust. As the density limit is approached, the plasma current is observed to decay, but not fully terminate. Further increases in density lead to larger current decay, eventually resulting in a full termination of the plasma. Toroidally separated density measurements suggest the possibility of a toroidal density asymmetry during periods of current decay triggered by edge pellet fueling, and inverted density profiles confirm a hollow density in discharges which exhibit a partial (~20%) loss of plasma current.

More intriguing is the apparent change in the density limit with changes in the plasma reversal. In an attempt to test the RFX-mod density limit model for the RFP, which attributes the density limit to the formation of an m = 0 island chain, density limit experiments were performed in discharges without field reversal (F = 0), effectively removing the m = 0 resonant surface from the plasma. While the density limit is in agreement with Greenwald limit in these discharges, a consistently lower density limit is observed in F = 0. Despite the lack of a resonant surface in the plasma, m = 0 activity is observed to increase as the density approaches the limit. A comparison of the collection of density limit experiments with and without reversal highlights several potentially important differences in the discharges. Reversed discharges have consistently higher T_e in core and often in the edge as well. The amplitude of core resonant m = 1 modes is consistently larger in non-reversed discharges, while edge resonant m = 0 modes are consistently larger in reversed discharges. Stochastic transport in the core scales as the square of the m = 1 amplitude, but the m = 0 modes certainly are important in the edge region, though their role is unclear. The maximum probe-measured edge density is consistently higher for reversed discharges and would benefit from further examination. In the end, we can offer no clear explanation for the density limiting physics on the RFP, but we have greatly expanded the pool of knowledge for what occurs during a density limit termination on MST.

3.5.1 Future Work

The impact of toroidal field reversal on the density limit certainly merits further investigation. Recent results from the Frascati Tokamak Upgrade (FTU) show that the density limit scales with the toroidal component of the magnetic field (B_φ), rather than the plasma current (B_θ)[9]. Perhaps the RFP also shares some dependence on the toroidal field as well. Furthermore, PPCD experiments represent an extreme case of toroidal reversal in the RFP. Core fueled densities significantly above the Greenwald limit are obtained regularly in PPCD discharges, but an open question remains as to the nature of the edge fueled density limit in those experiments. This would serve as a motivation for a density limit study of edge fueling in PPCD as well as a closer look at the F dependence.

In addition, several key measurements would be very beneficial for future density limit experiments. Highest on the list would be a measurement of the radiated power. Both the Tokamak and Stellarator limit have been well modeled by a balance of heating and radiated power. A working second probe would help to resolve any local differences in density or temperature during the density limit collapse. Internal measurements of the magnetic field, from the Motional Stark Effect could prove informative as well as the internal dynamics of the magnetic field are currently unknown.

3.6 References

1) S. Ortolani and G. Rostagni, Nucl. Instruments Methods Phys. Res. **207**, 35–48 (1983).

2) M. Greenwald, Plasma Phys. Control. Fusion **44**, R27–R53 (2002).

3) J.F. Drake, Phys. Fluids **30**, 2429 (1987).

4) G. Spizzo, P. Scarin, M. Agostini, A. Alfier, F. Auriemma, D. Bonfiglio, S. Cappello, A. Fassina, P. Franz, L. Piron, P. Piovesan, M.E. Puiatti, M. Valisa, and N. Vianello, Plasma Phys. Control. Fusion **52**, 095011 (2010).

5) M.D. Wyman, B.E. Chapman, J.W. Ahn, A.F. Almagri, J.K. Anderson, F. Bonomo, D.L. Brower, S.K. Combs, D. Craig, D.J. Den Hartog, B.H. Deng, W.X. Ding, F. Ebrahimi, D.A. Ennis, G. Fiksel, C.R. Foust, P. Franz, S. Gangadhara, J.A. Goetz, R. O'Connell, S.P. Oliva, S.C. Prager, J.A. Reusch, J.S. Sarff, H.D. Stephens, and T. Yates, Nucl. Fusion **49**, 015003 (2009).

6) M.D. Wyman, The Physics of High-Density, High-Beta Reversed-Field Pinch Plasmas, University of Wisconsin, 2007.

7) ITER Team. Nucl. Fusion **39,** 2137 (1999)

8) T. D. Rempel, C. W. Spragins, S. C. Prager, S. Assadi, D. J. Den Hartog, and S. Hokin, Phys. Rev. Lett. **67**, 1438 (1991).

9) G. Pucella, O. Tudisco, M.L. Apicella, G. Apruzzese, G. Artaserse, F. Belli, W. Bin, L. Boncagni, A. Botrugno, P. Buratti, G. Calabrò, C. Castaldo, C. Cianfarani, V. Cocilovo, L. Dimatteo, B. Esposito, D. Frigione, L. Gabellieri, E. Giovannozzi, G. Granucci, M. Marinucci, D. Marocco, E. Martines, G. Mazzitelli, C. Mazzotta, S. Nowak, G.

Ramogida, A. Romano, A.A. Tuccillo, L. Zeng, and M. Zuin, Nucl. Fusion **53**, 023007 (2013).

CHAPTER 4

High β, Improved Confinement Ohmic Discharges

4.1 Introduction and Motivation

Improved confinement discharges on MST are obtained through the use of a current profile control technique known as Pulsed Parallel Current Drive (PPCD). Magnetic fluctuations are reduced in PPCD discharges. Particle and energy confinement improves, electron temperature increases and plasma β increases, reaching 15% in 200 kA PPCD discharges and 12% in 500 kA PPCD discharges at low density. [1, 2] As PPCD discharges are normally limited to $n_e < 1*10^{19}$ m^{-3}, they provide an attractive target for pellet fueling experiments. In pellet fueled high density PPCD experiments we again observe improvements in confinement compared to the standard discharge. Magnetic fluctuations are reduced and T_e increases. In contrast to low density PPCD, T_i increases as well, due in part to the increased coupling between the species. A further increase in plasma β is observed, with an RFP record β of 26% achieved in 200 kA PPCD, and β up to 18% obtained in 500 kA PPCD experiments. Though confinement is improved, a pressure gradient exceeding the Mercier criterion for interchange instability is observed and an increase in magnetic activity suggests a transition to a regime where pressure driven instabilities are dominant. [3, 4]

The continuation of pellet fueled PPCD experiments has been aided by the improvements to the pellet injector highlighted in chapter 2. Improvements to pellet reliability and reproducibility have resulted in more consistent high density fueling. Additionally, the upgrade to 4.0 mm diameter pellets resulted in improved control over pellet velocity which aids in achieving the desired core fuel deposition.

The primary goal of the pellet fueled PPCD experiments described here has been to search for evidence of a β limit in the RFP device by continuous attempts to achieve the highest possible β value. As discussed in section 3.3, a secondary goal was to maximize the density in these discharges. The combination of these two goals has resulted in a scan of the plasma density in PPCD discharges, with high β ($\beta > 20\%$) achieved routinely due in part to improved injector operation. The scan of density has additional implications as T_e is naturally lower in high density discharges. By assuming a Spitzer like scaling of the plasma resistivity as discussed in Chapter 3, the scan of plasma density provides a scan of the Ohmic heating power, from ≈ 1 MW at low density to 3 MW or more in high density 200kA discharges. Though β is often larger at higher density, little change is observed in the electron contribution over a large range of density and estimated Ohmic heating power. The constant electron β as density increases suggests a confinement driven ‘soft’ β limit. Density scaling of the core and edge magnetic activity could provide an explanation. Electron thermal transport in the core scales as the square of the core mode activity. Increased transport in the core could provide a loss mechanism to balance the increased heating power.

4.2 High Density, High β Operation

The recipe for obtaining pellet fueled high β plasmas is to inject a pellet just prior to the onset of improved confinement such that it fully ablates in the core prior to the reduction of magnetic activity. The goal is to lock in the increased density for the duration of the improved confinement period. While pellet fueling does perturb the plasma during pellet ablation, reflected by an increase in magnetic activity, the impact is comparable to that normally observed during the first 2-3 ms following the application of PPCD without pellet injection. By adjusting the speed and timing of the pellet, we can fuel such that the pellet perturbation falls in this time to limit the impact of the pellet. The result is high density plasmas with an overall reduction in magnetic activity as shown for a 500 kA PPCD discharge in figure 4.1. In this case, density increases 3 fold, as measured by the CO_2 interferometer, and both the edge (m = 0) and core (m = 1) magnetic activity decreases compared to that of the low density case. The increasing soft x-ray signal is indicative of increasing T_e, though the amplitude depends in part on n_e^2. T_i is also observed to increase on multiple diagnostics. The T_i evolution during improved confinement is shown in figure 4.2 along with the corresponding T_e evolution at a similar radial location. The CHERS measurement of the impurity temperature is made in the core. Rutherford scattering measurements of the bulk ion temperature are made at r/a ~ 0.34. The T_i measurements are paired with corresponding T_e measurements from Thomson scattering. A recent addition, the Compact Neutral Particle Analyzer (CNPA), also confirms an increasing ion temperature for PPCD experiments at high density, but not at low density, shown in figure 4.3. All ion temperature measurements shown here are for 500 kA PPCD experiments, though ion temperature increases are also observed in 200 kA PPCD discharges.

The increase in electron temperature is primarily due to the decrease in χ_e due to the reduced magnetic activity. The Ohmic input power also decreases in these low density plasmas. [2] In high density improved confinement discharges, the increase in the ion temperature is partially explained by the increased coupling between the electrons and ions due to the shorter equilibration time which scales classically as $T_e^{3/2}/n_e$.

The primary quantity of interest here is the plasma β, the ratio of the plasma pressure to the confining magnetic pressure

$$\beta = \frac{\int_V p dV}{\frac{B^2(a)}{2\mu_0}\int_V dV} \tag{4.1}$$

where p is the thermal plasma pressure, and B(a) is the total field at the wall. The terms β_e and β_i will be used to represent the electron and ion contributions to the total β. During PPCD experiments on MST, β reaches its maximum value near the end of the improved confinement period. This is when T_e (and T_i) tends to be highest. It is this region which will be the focus of further analysis.

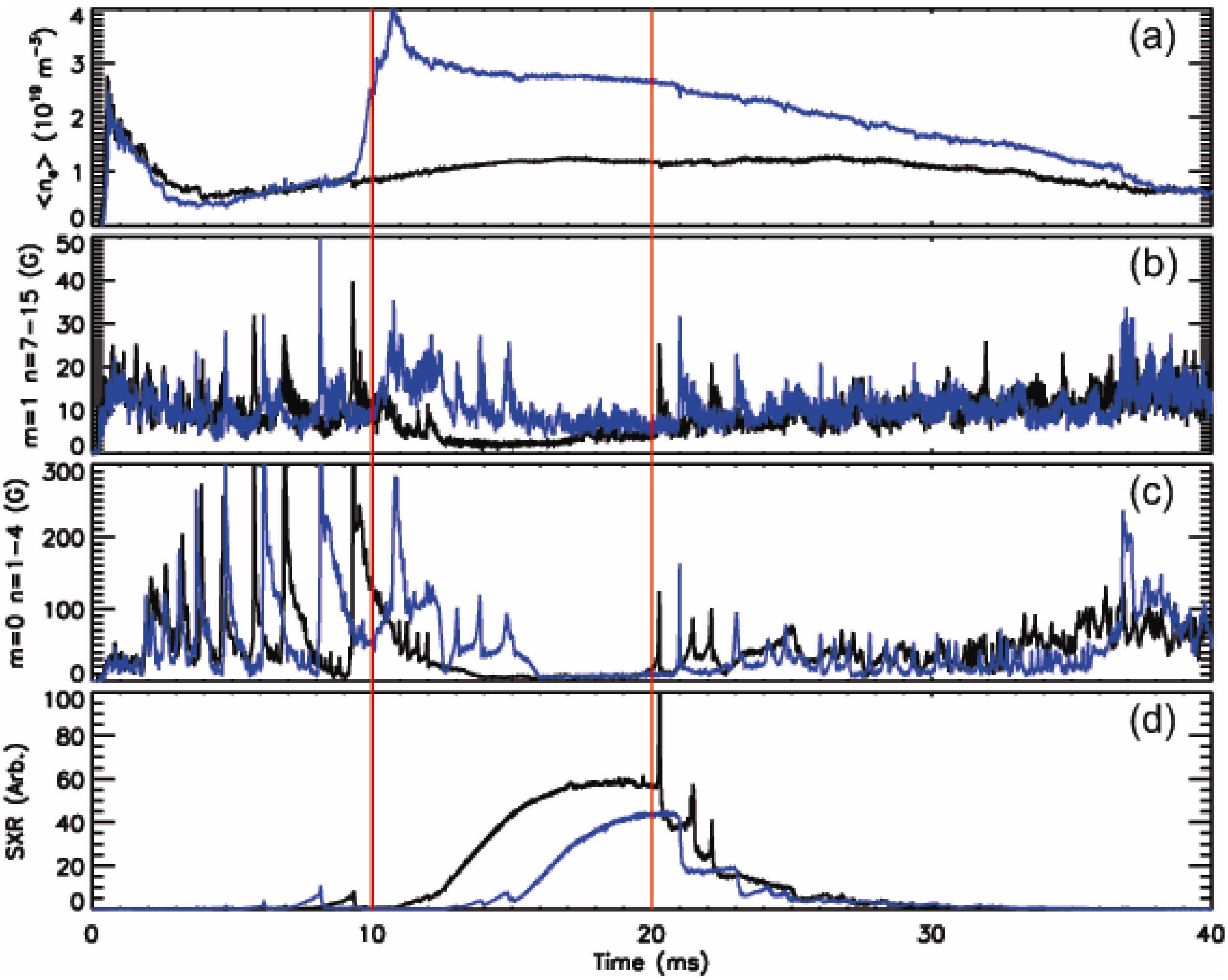

Figure 4.1: Operational signals for a 500 kA pellet fueled PPCD discharge, (a) $\langle n_e \rangle$, (b) the RMS core mode activity, (c) the RMS edge mode activity, and (d) SXR emission. The pellet is injected within a few ms of the start of PPCD at 10ms. The PPCD duration is marked by vertical red lines. The pellet ablates within a few ms and the increase in density is sustained throughout PPCD. The magnetic activity both in the edge and the core is decreased, leading to an improvement in confinement comparable to that observed in low density PPCD experiments. [Shot 1131010087(black) 1131010084(blue)]

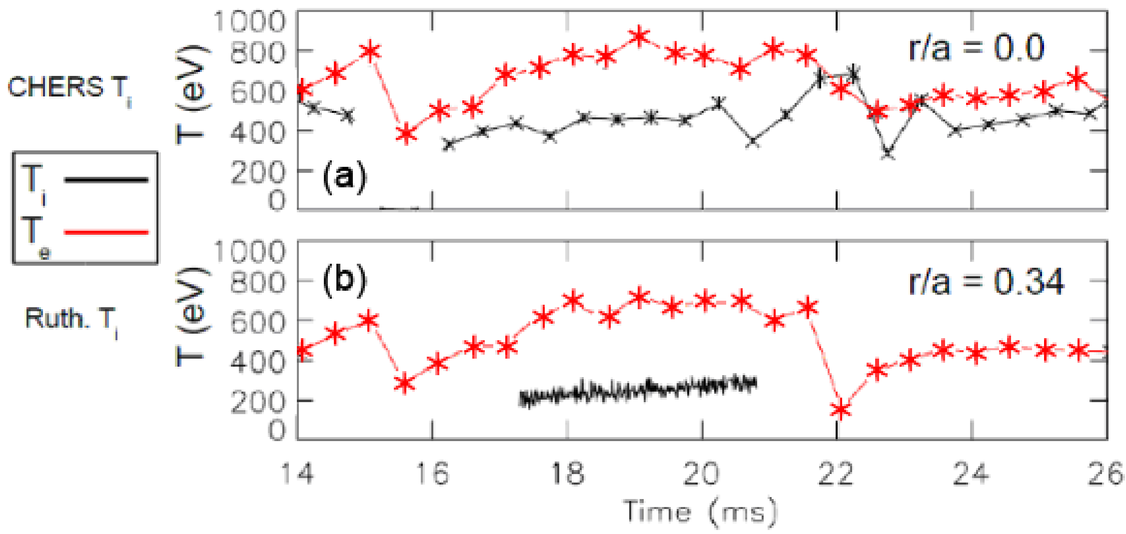

Figure 4.2: A comparison of electron and ion temperature evolution in high density PPCD. (a) Shows increase in both ion and electron temperature in the core measured by CHERS and Thomson scattering respectively. (b) Rutherford scattering and Thomson measurements show ion and electron temperature increases in the mid radius as well.

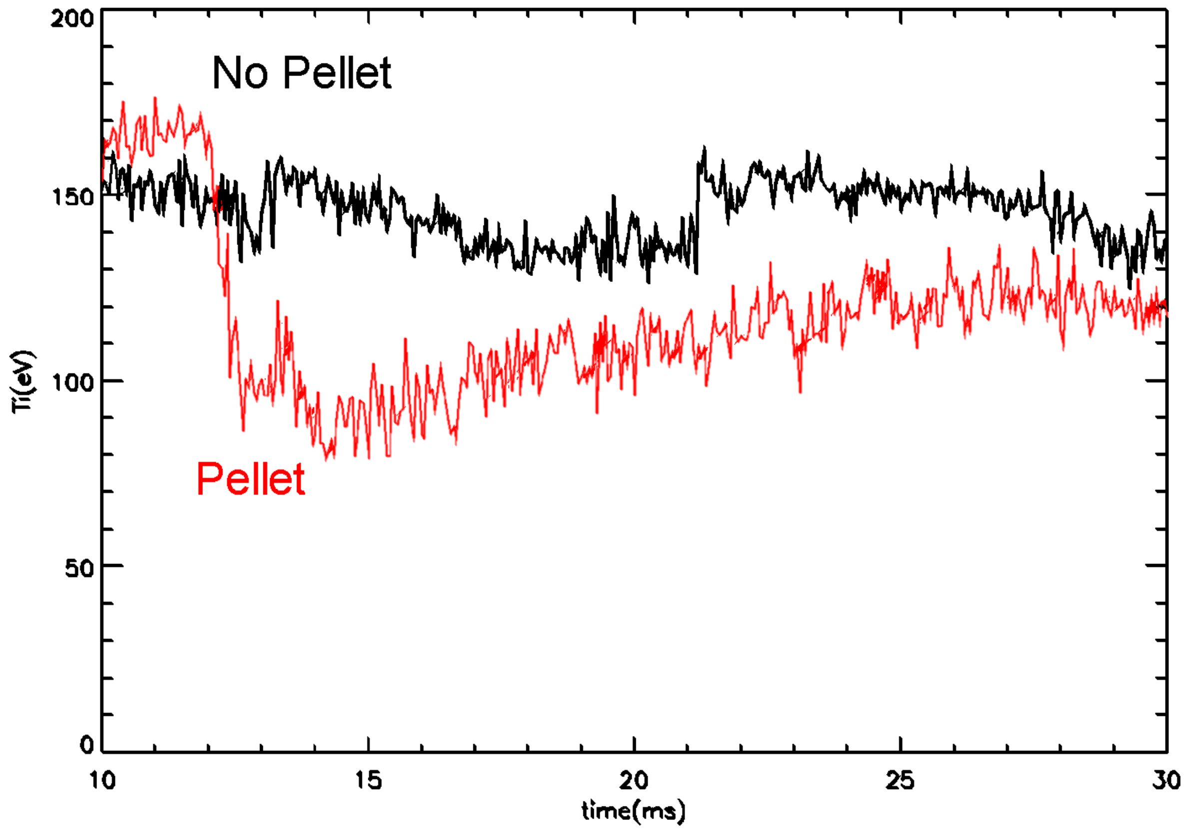

Figure 4.3: Ion temperature evolution from the CNPA for low (black) and high (red) density 500 kA PPCD discharges.

4.2.1 Pressure Driven Modes and Pressure Relaxation

Recently, experiments on RFX-Mod have shown that edge fluctuations consistent with pressure driven instabilities are observed. [5, 6] Equilibrium reconstructed profiles for pellet fueled PPCD experiments on MST have shown pressure gradients in the core that significantly exceed the Mercier criterion [7], given by

$$\frac{1}{4}+\frac{2\mu_0 p'}{rB_\varphi^2}\left(\frac{q}{q'}\right)^2(1-q^2)\geq 0 \tag{4.2}$$

Previous computational results used the cylindrical DEBS code to calculate linear growth rates of pressure driven modes for a discharge with β of 26% and a core pressure gradient exceeding Mercier by a significant margin[3]. We build on those results by looking at a linear stability analysis using the NIMROD code in toroidal geometry. For this analysis, we compare the results for two high β discharges, in figure 4.4. The first is the same discharge discussed in the DEBS analysis with a pressure gradient greatly exceeding Mercier in the core and a β of 26%. The second is a shot which marginally exceeds the Mercier criterion in the core with a β of ~21%. In the marginal case, there is no significant pressure drive, and the calculated linear growth rates are small for all modes. For the other case, both the m=1 modes with tearing parity and the m > 1 interchange like modes have large linear growth rates. The modes with the largest growth rates are associated with the m/n = 1/7 resonant surface. The results are consistent, howoever, the growth rates from NIMROD are a bit larger than the DEBS results for the 26% β case.

Experimentally, a subset of pellet fueled discharges show periodic bursts of magnetic activity. The exact trigger for these bursts is not fully understood, but they are observed more often in discharges at higher density with flat or hollow density profiles ($n_e > 3*10^{19}$ m^{-3} for 200 kA and $n_e > 5*10^{19}$ m^{-3} for 500 kA PPCD). Time resolved equilibrium reconstructions of the pressure profile show pressure relaxation in the core associated with these bursts, as shown in figure 4.5. The core relaxation occurs even though the magnetic activity is dominantly m = 0, localized at the reversal surface. The cases shown have a β of 17-21%, equal or greater than that observed at low density, despite the increased magnetic activity.

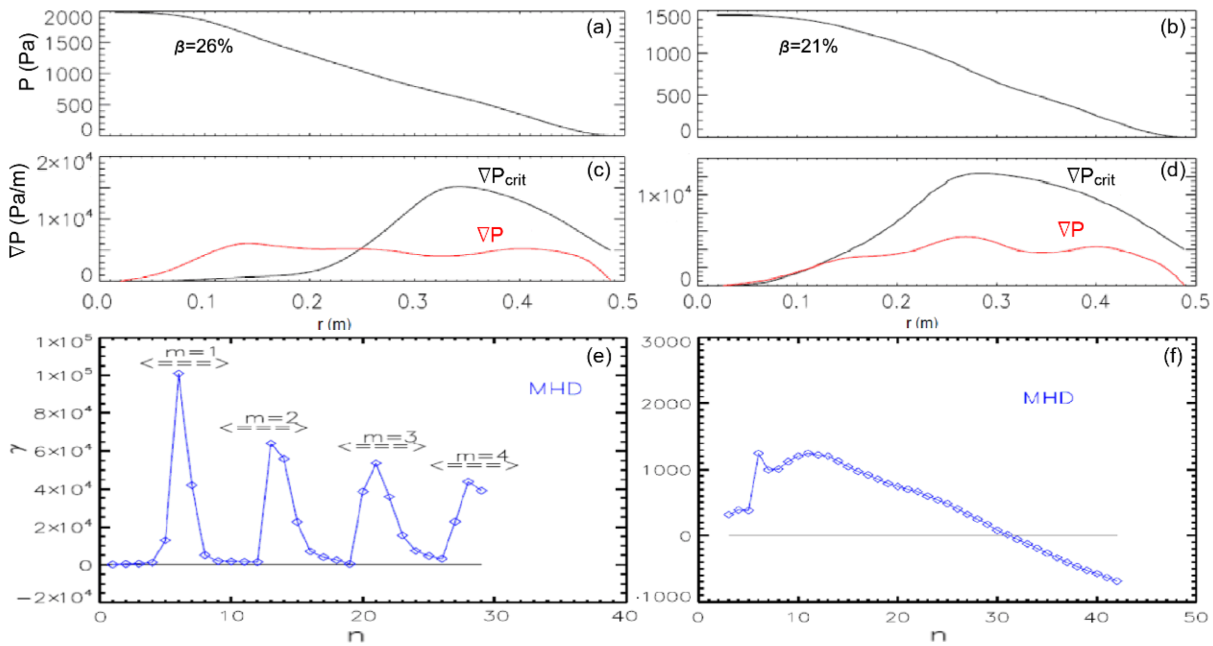

Figure 4.4: (a, b) Plasma pressure, (c, d) experimental and critical pressure gradients and (e, f) associated linear growth rates for pressure driven modes. Both are 200 kA pellet fueled PPCD discharges.

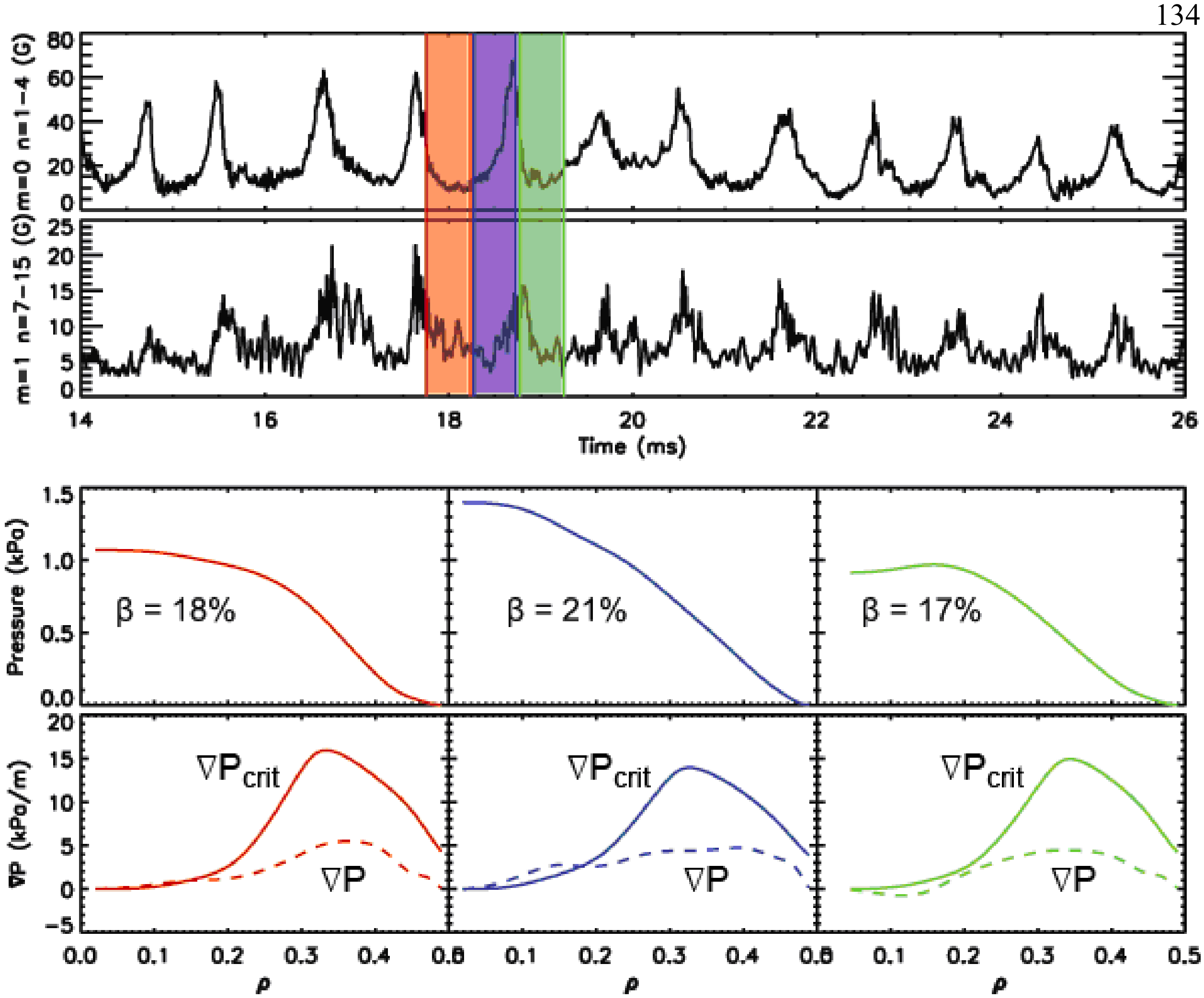

Figure 4.5: (Top) RMS fluctuations of edge and core modes for a high density PPCD discharge with periodic bursts of magnetic activity. (Bottom) Pressure, measured gradient and critical gradient for three reconstructed equilibria corresponding to the shaded time regions. Evolving pressure and pressure gradients along with mode activity showing pressure relaxation in the plasma core.

4.2.2 Broader View of High β Experiments

The previous study of pellet fueled PPCD experiments looked closely at a few high β discharges. One problem with comparing pellet fueled PPCD discharges to one another is that, more so than the average discharge, each pellet fueled discharge is unique due to the variations in pellet size, pellet speed, PPCD quality, plasma density and plasma temperature. Each of those factors has an impact on the ablation characteristics for a given discharge often making a shot to shot comparison an exercise in futility. The reconstruction of the density profile is also challenging for pellet fueled discharges. Instead, we take a broader, statistical look at the collection of pellet fueled discharges.

The normal means of obtaining a value for β comes from combining Thomson scattering T_e measurements with inverted density profiles from the FIR interferometer system. As complete T_i profiles require many similar discharges, the T_i profile is often assumed to match the shape of the T_e profile, with limited local measurements setting the fraction T_i/T_e. As noted previously, the loss of signal observed during pellet ablation complicates the FIR analysis to the point of being far too time consuming for use on a large number of pellet fueled PPCD discharges. Instead, we make use of the more robust $\langle n_e \rangle$ measurement from the CO_2 interferometer system. Then, by transforming the Thomson scattering data to a pseudo line-averaged measurement, $\langle T_e \rangle$, we create an experimentally based estimate of β_e denoted here as $\langle \beta_e \rangle$.

$$\langle \beta_e \rangle = \frac{2\mu_0 \langle n_e \rangle \langle T_e \rangle}{|B(a)|^2} \tag{4.4}$$

The total field at the wall B(a) is used instead just the poloidal component due to the significant toroidal component of the field in PPCD discharges. A similar method of calculating $\langle\beta_i\rangle$ could be done, however the measurement of T_i has proven problematic, especially in 200 kA PPCD. The colder temperature and increased density significantly reduce the signal from CHERS measurements of the impurity T_i. Rutherford scattering was unavailable for the majority of these experiments and the CNPA also had difficulty with measuring T_i for 200kA PPCD.

Originally, $\langle\beta_e\rangle$ was to serve as a useful means of characterizing the collection of high density discharges and selecting the most promising-looking shots for further analysis. For example, the high β cases of 26% and 21% discussed in the previous section correspond to $\langle\beta_e\rangle$ values of 10.5% and 9.2 %, respectively, and the sequence of reconstructions in figure 4.5 with total β of 18%, 21% and 17% correspond to $\langle\beta_e\rangle$ of 7.2%, 8.7% and 7.1%. A simple look at the scaling of $\langle\beta_e\rangle$ with density in figure 4.6 reveals a saturation in the maximum achieved $\langle\beta_e\rangle$ as density increases. This implies that the previously observed increases in β are primarily a result of the increased ion contributions due to the higher ion temperature. We also note that $\langle\beta_e\rangle$ exhibits no obvious dependence on the Greenwald limit and we are able to achieve a comparable $\langle\beta_e\rangle$ value for densities significantly exceeding the Greenwald limit. It is noted that the $\langle\beta_e\rangle$ value ignores profile effects for both the density and temperature.

As the ions and electrons become more tightly coupled at higher density, the observed $\langle\beta_e\rangle$ saturation establishes an effective limit on β in these plasmas of ~2β_e, the idealized case where the species fully equilibrate with $T_i \sim T_e$ ($\beta_i \sim \beta_e$). Each point in figure 4.6 corresponds to a Thomson scattering measurement of the T_e profile, typically captured at 2 kHz. Other relevant quantities are averaged over a 0.5 ms window around the Thomson collection time. The relevant time shown is at the end of the improved confinement period from 17-20 ms. Again, while $\langle\beta_e\rangle$ is not a direct measurement of β_e, which depends on the relevant profiles, it does in fact provide a good relative measure of β_e. $\langle\beta_e\rangle$ values above ~8.5% typically correspond to a 'high β' discharge with total β greater than 20% for density above $2*10^{19}$ m^{-3}. The $\langle\beta_e\rangle$ parameter is key in allowing a statistical look at the collection of high β discharges, discussed in the following section. It should also be noted that the represented data has not been filtered, though unphysical measurements (i.e., 1 keV Te) have been omitted.

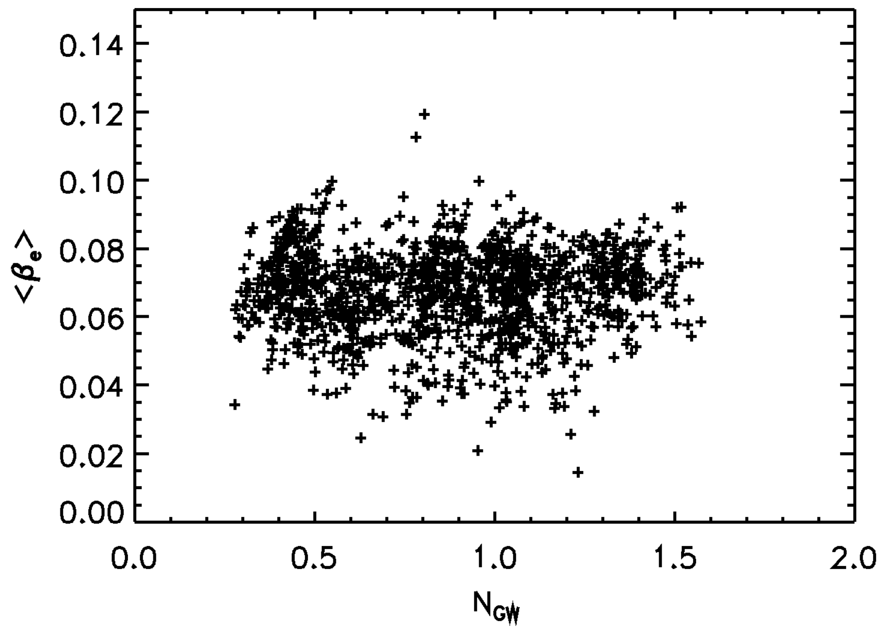

Figure 4.6: A scatterplot of $\langle \beta_e \rangle$ values for a range of densities in 200 kA PPCD discharges. An approximately constant value of $\langle \beta_e \rangle$ is observed, and the there is little observed difference in the best cases as $\langle n_e \rangle$ increases. Each point represents a single measurement of the electron temperature at 2 kHz and a 0.5 ms average of other experimental quantities.

4.3 A Broader Look at Density Scalings at High β

Before we consider fully the implications of the saturated $\langle\beta_e\rangle$ discussed in the previous section, we will use a similar method to look at how several relevant quantities scale with increased density in PPCD discharges. For the rest of this chapter, we will focus on the 200kA PPCD case as it has the largest collection of discharges. The 500kA PPCD cases show similar trends, but with smaller sample sizes. Those plots are provided in appendix A.

4.3.1 Mode Activity Scaling

As has been previously discussed, there is an increase in the overall tearing mode spectrum in high density PPCD experiments. It was proposed that pressure driven tearing or interchange modes might play a role. Again by looking at the collection of data we can see the scaling with the normalized density N_{GW} of both the m = 0 and m = 1 tearing modes in figure 4.7. In the best cases (defined by the lower edge of the scatterplot) with the lowest fluctuations, both the edge and core tearing modes scale with increasing N_{GW}. An important caveat for discussing the increase in core magnetic activity is the potential for edge resonant m=1 modes in 200 kA PPCD discharges. The value of q at the wall is such that the m = 1, n = -5, -6, etc. modes are resonant, meaning the measured increase in m = 1 activity is a combination of both the core and edge mode contributions.

4.3.2 S Scaling

If we follow the formalism in [9] we can estimate the Lundquist number S for these discharges with some assumptions,

$$S = \frac{30 I_p T_{e0}^{3/2} (1 - f_t)}{(.4 + .6 Z_{eff}) \ln\Lambda \sqrt{\mu_i \bar{n}}} \tag{4.5}$$

The assumptions made here are Z_{eff} = 2.0, and trapped particle fraction f_t = 0.25. These assumptions are in line with results from previous pellet fueling experiments, but there are not direct measurements of these quantities available for all of the discharges. At this point, we are assuming constant values for Z_{eff} and f_t, despite the fact that they do vary with density. From figure 4.8, we can see again little to no scaling in $\langle \beta_e \rangle$, but there does appear to be a scaling in the magnetic modes. A simple linear fit to the plotted data yields a scaling for the magnetic fluctuations of $\tilde{b}_{m=1} = S^{-0.80}$ and $\tilde{b}_{m=0} = S^{-0.75}$. This is a significantly stronger scaling than previously observed in standard discharges. [9] This is the first look at S scaling in PPCD experiments where the dynamo is suppressed.

4.4 β Limit Discussion

In a means similar to that outlined in section 3.4, we ensemble the collection of discharges over the normalized density and discuss the trends in more detail. The shots again represent 0.5 ms time averages (to match the 2 kHz Thomson data rate). The region of interest here is 17-20 ms near the end of the PPCD improved confinement period, the same data represented by figures 4.6-4.8. A collection of plots is shown in figures 4.9 and 4.10.

Figure 4.9 shows dependence on the normalized density (N_{GW}) for (a) the ensemble size, (b) $\langle n_e \rangle$, (c) the plasma current, (d) reversal parameter F, (e) core mode activity, and (f) edge mode activity. The density scales as expected, and a small drop in the plasma current is observed during the transition to higher N_{GW}. Again we observe a mostly constant value for $\langle \beta_e \rangle$ with increasing N_{GW}. The magnetic activity in the edge and the core both increase with N_{GW}.

Figure 4.10 shows the N_{GW} dependence for (a) ensemble size, (b) $\langle \beta_e \rangle$, (c) Thomson T_e measured in the core (r/a < 0.2), (d) the edge (r/a = 0.7 – 0.8), (e) $T_e^{-3/2}$, and (f) S. This ensemble size represents the number available T_e measurements; the total collection for more general measurements is larger. A look at T_e in the edge and the core shows an inverse relation with N_{GW} consistent with expectations. If we assume a Spitzer like resistivity (a good assumption for pellet fueled discharges), we can also look at how the ohmic power scales with density by looking at the scaling of $T_e^{-3/2}$ with N_{GW}. We observed a factor of ~5 increase in $T_e^{-3/2}$ as we increase N_{GW} from .5 to 1.5, corresponding to a $\langle n_e \rangle$ of $1*10^{19}$ and $3*10^{19}$ m^{-3} respectively. Meanwhile, the plasma current drops by approximately 10-15% over that range, a crude estimate for the degree of Ohmic power increase would be close to a factor of 3-4. Estimates of the Ohmic power from reconstructed profiles for a pair of discharges are given by

$$P_{Ohmic} = \eta \cdot j^2 \tag{4.6}$$

where η is the resistivity and j the current density. In this way we find P_{Ohmic} to be less than 1 MW at a density of $1*10^{19}$ and 3 MW or more for a density of $3*10^{19}$, consistent with the scaling predictions. In our attempts to maximize density in PPCD experiments and probe for a β limit, we have also scanned the Ohmic power for a variety of PPCD discharges and have observed very little variation in $\langle \beta_e \rangle$ over a significant range of Ohmic heating power.

Meanwhile, the edge and core mode activity increases with N_{GW}. The increase starts at N_{GW} = 0.3 and continues increasing at a fairly linear rate. It has long been observed that fluctuations rise rapidly as density exceeds $1*10^{19}$ m^{-3} in PPCD discharges, corresponding to N_{GW} ~ 0.5 at 200 kA. The core fluctuations are particularly important as it is known that they play a strong role in stochastic transport in the core. We make use of the work done in chapter 3 to compare the mode activity in high density PPCD experiments (figure 4.9 and 4.10) to that observed in low density standard discharges in figure 4.11. The data from figure 4.11 is a reprint of figure 3.20. At higher N_{GW} with PPCD, Both edge and core activity approach and exceed the levels observed in low density standard discharges, however, the observed $\langle\beta_e\rangle$ value remains significantly higher in the PPCD case. The increased fluctuations contribute to an increase in stochastic transport. As previously discussed, edge m = 1 modes are resonant in these PPCD discharges, meaning the core m = 1 modes are in fact not reaching the levels incated due to the contamination from edge mode contributions. We observe an approximately 4-6 fold increase in m = 1 fluctuation amplitude as we increase N_{GW} from 0.5 to 1.5. However, if stochastic transport is indeed playing an important role in the core, then an increase by a factor of 2 would be sufficient to balance the estimated increase in ohmic heating power.

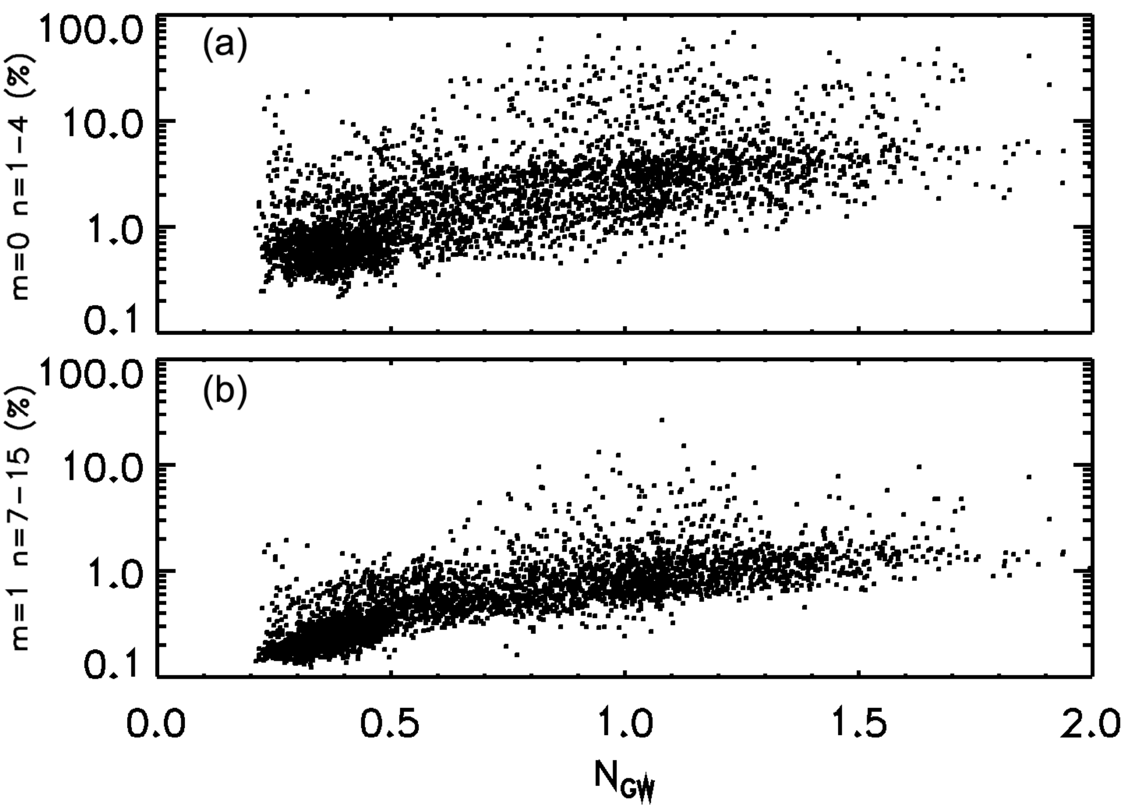

Figure 4.7: Scatterplot showing a scaling of the (a) edge magnetic activity and (b) core magnetic activity with N_{GW} in 200 kA PPCD discharges.

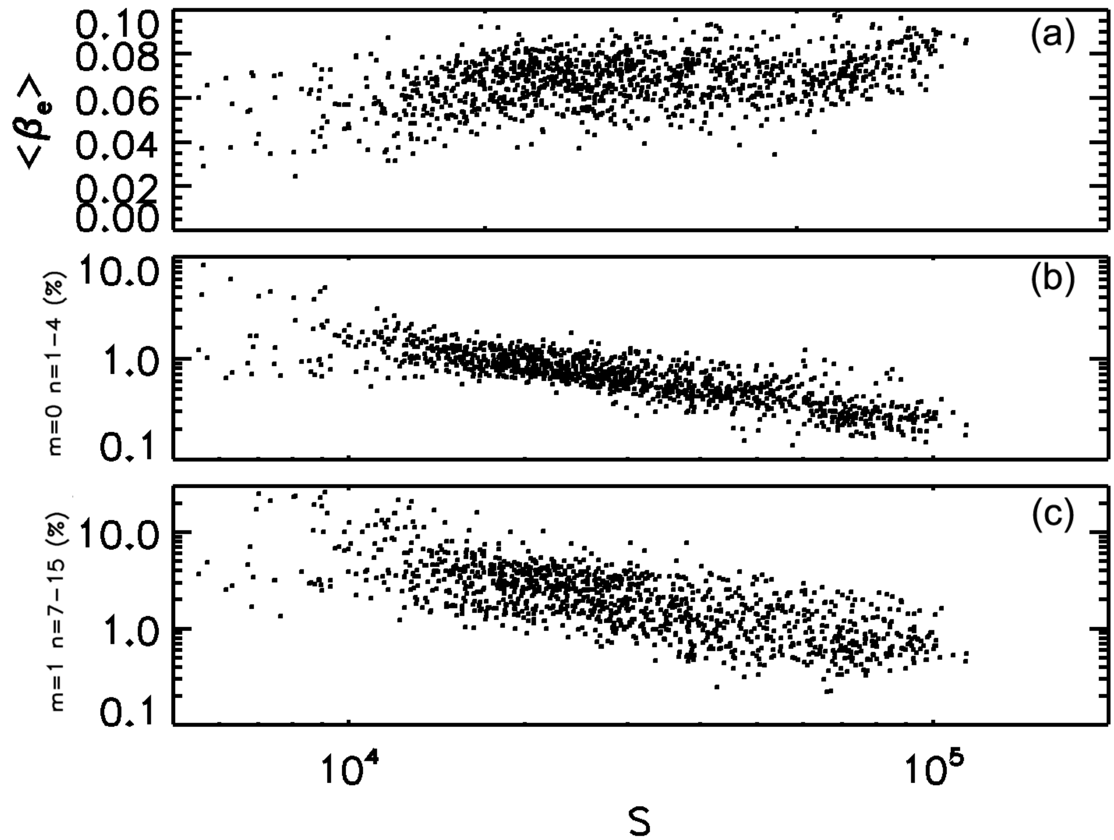

Figure 4.8: Scatterplot showing S scaling of various quantities for 200 kA PPCD discharges with pellet fueling; a weak scaling of (a) $\langle \beta_e \rangle$, and strong linear scaling for (b) the edge magnetic fluctuations and (c) core magnetic fluctuations.

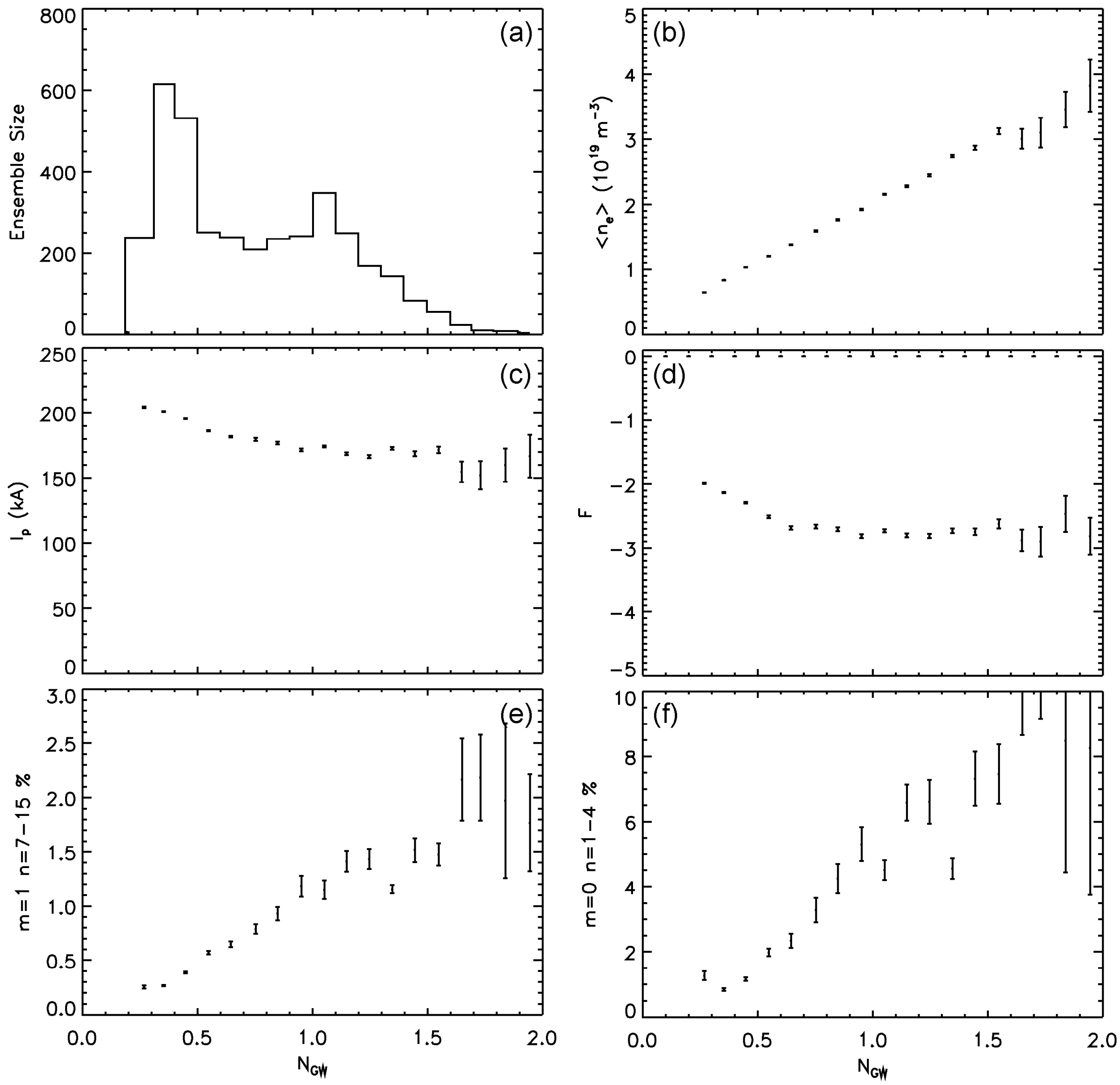

Figure 4.9: Ensemble analysis for 200 kA PPCD discharges with pellet fueling. A series of plots represent (a) ensemble size, (b) $\langle n_e \rangle$, (c) plasma current, and (d) reversal parameter F, (e) normalized core mode activity, and (f) normalized edge mode activity. Error bars are statistical.

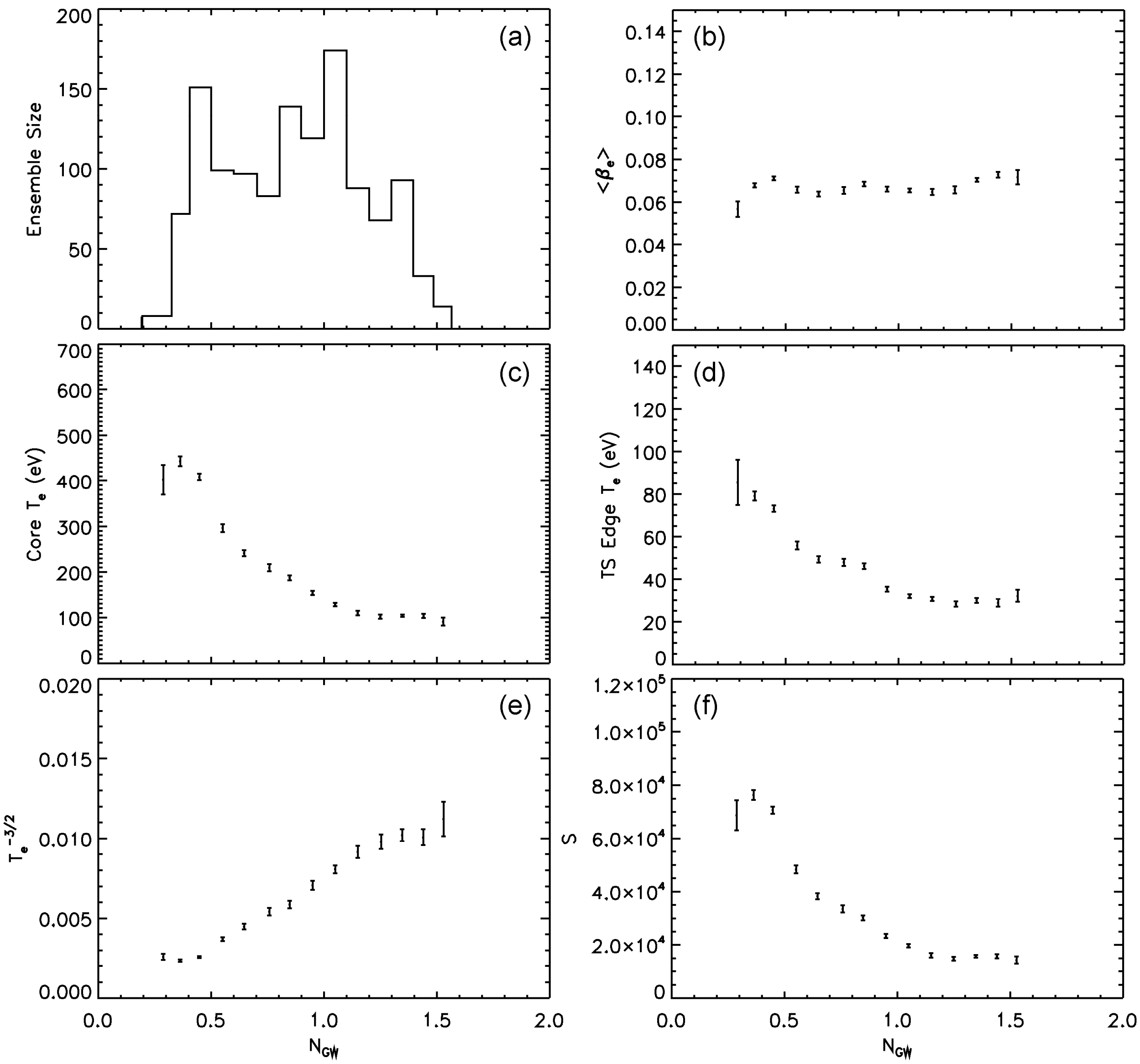

Figure 4.10: Scaling with N_{GW} for the 200 kA PPCD ensemble of figure 4.9. Plotted quantities are (a) ensemble size, (b) $\langle \beta_e \rangle$, (c) core (r/a < 0.2) Thomson scattering T_e, (d) edge (r/a = 0.7 – 0.8) Thomson scattering T_e, (e) core $T_e^{-3/2}$ and (f) S. . Error bars are statistical.

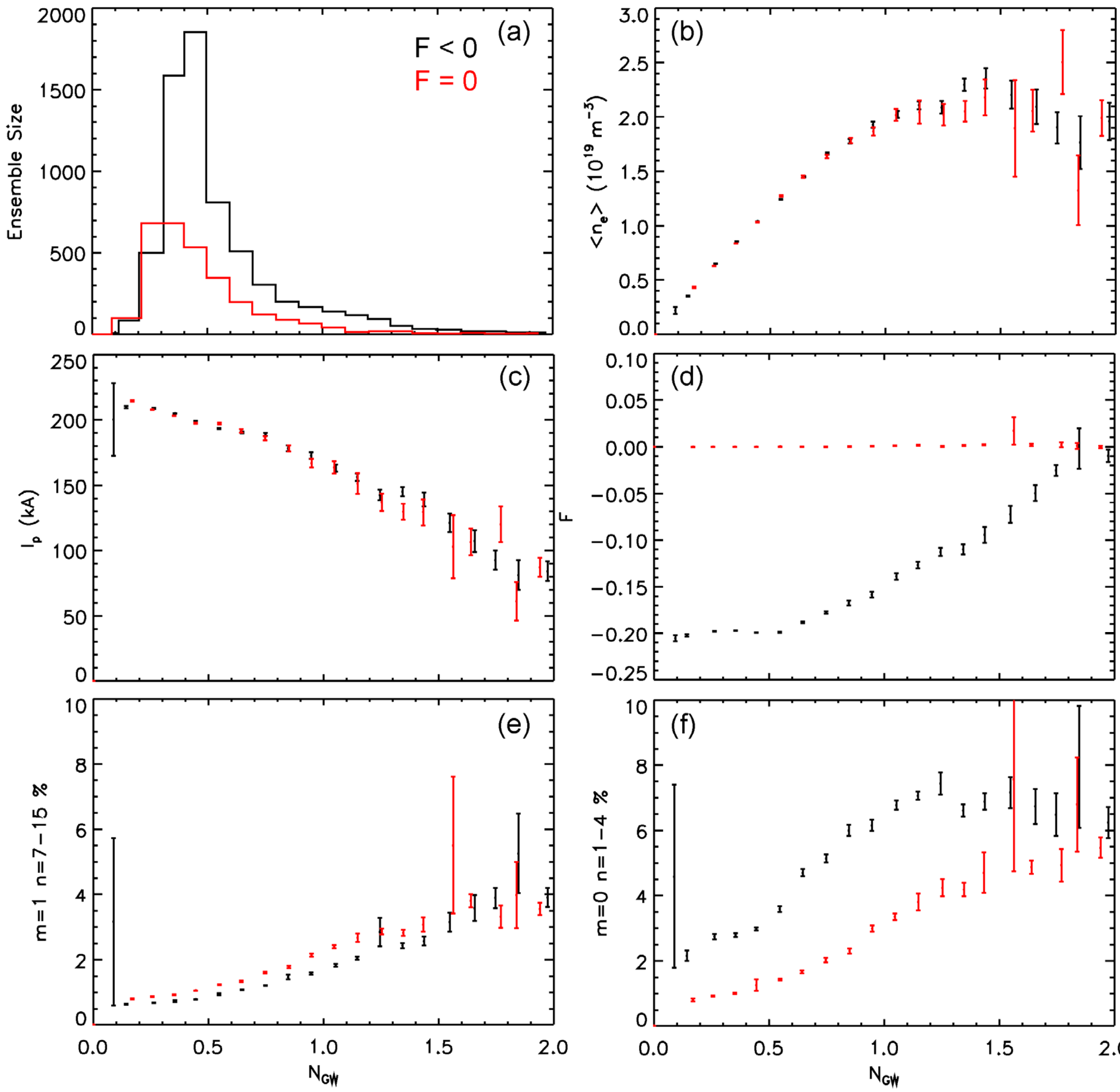

Figure 4.11: Scaling with N_{GW} for the 200 kA standard ensemble discussed in chapter 3. A series of plots represent (a) ensemble size, (b) $\langle n_e \rangle$, (c) plasma current, and (d) reversal parameter F, (e) normalized core mode activity, and (f) normalized edge mode activity. Reversed discharges are in black and non-reversed discharges are in red. Error bars are statistical.

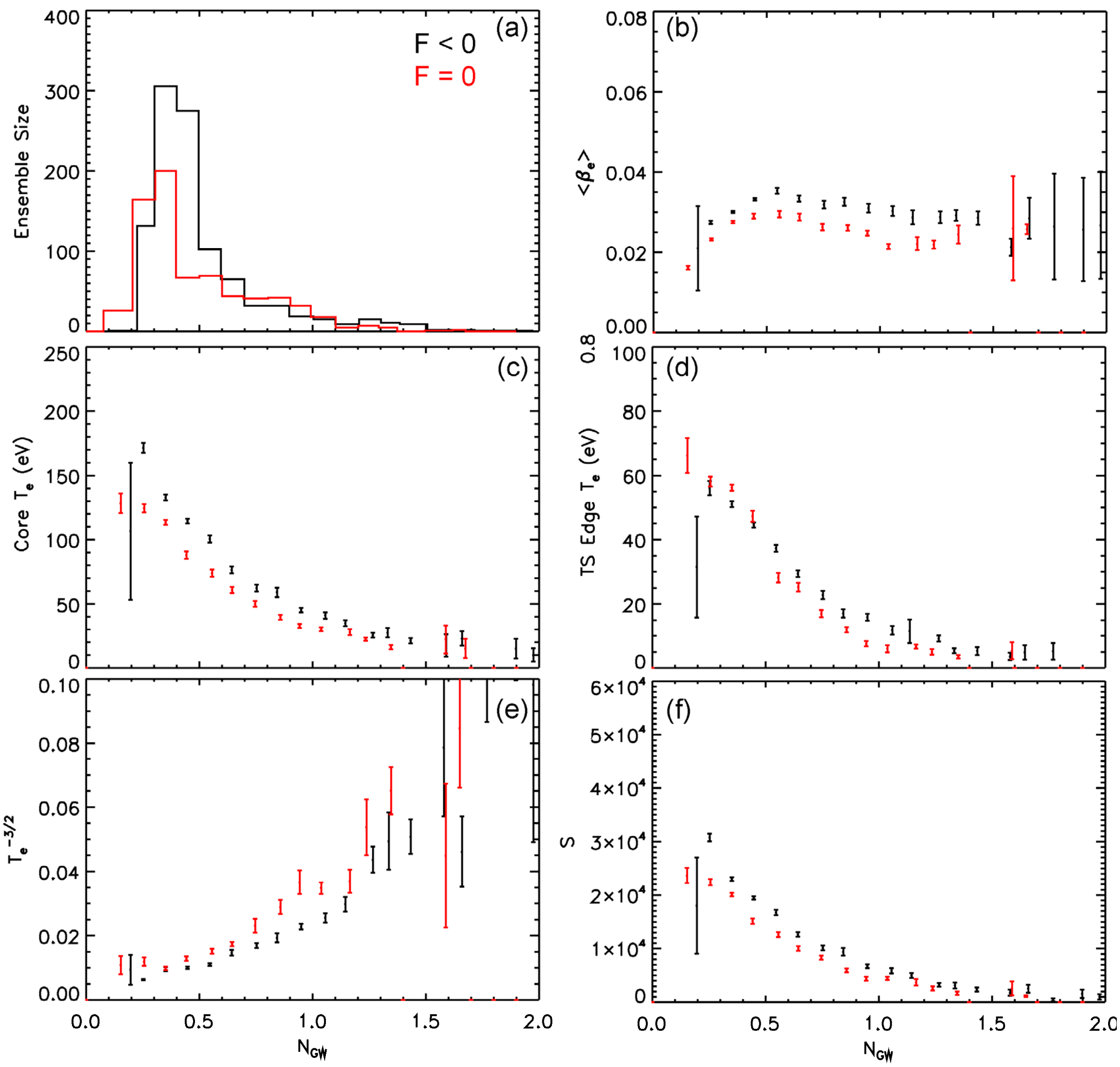

Figure 4.12: Scaling with N_{GW} for the 200 kA standard ensemble discussed in chapter 3. Plotted quantities are (a) ensemble size, (b) $\langle\beta_e\rangle$, (c) core (r/a < 0.2) Thomson scattering T_e, (d) edge (r/a = 0.7 – 0.8) Thomson scattering T_e, (e) core $T_e^{-3/2}$ and (f) S. . Error bars are statistical.

4.5 Conclusions

As we have studied the high β discharges obtained with pellet injection into PPCD discharges, we have obtained a density scan which doubles as a scan of the Ohmic heating power as the temperature decreases at higher density. What we find is an apparent saturation of β_e, the electron component of β, as the Ohmic power increases by approximately a factor of 4. In this same range, we observe an increase in fluctuations resonant in both the edge and the core. The m = 1 activity increases by a factor of 4 or more, but this is complicated by the edge resonant m = 1 modes which crop up in low density PPCD discharges. Still, if the observed limit on β_e is due to an increase in stochastic transport, a factor of 2 increase in the core resonant m = 1 modes would be sufficient to balance the additional heating power. Alternatively, the edge resonant m = 1 modes could in principle play a role, though through what mechanism is not yet clear. And of course, the m = 0 modes are known to interact nonlinearly with the core resonant m = 1 modes, and they can interact with the edge resonant m = 1 modes as well. Unfortunately, we can not ascribe a direct cause to the observed limit on β_e at this time, but it certainly appears to be confinement limited. The increase in magnetic fluctuations is a logical explanation and the increase could be a result of pressure drive, predicted to be linearly unstable in some pellet fueled PPCD discharges. As a final note, the previous record β of 26% is clearly near the maximum achievable based on this statistical look.

4.5.1 Future Work

An important piece of information would be a direct statistical measurement of β_e. We currently lack robust a density profile measurement to couple with the T_e profile measurements.

The FIR system is optimized for low density measurements, so a different wavelength system or improvements to the current system would be required to achieve the measurements required. Moving the pellet injection location might also solve the problem of signal loss. Alternatively, a direct measurement of β_e could be achieved with a calibrated Thomson Scattering measurement of the electron density to go along with the temperature measurements.

4.6 References

1) J.S. Sarff, S.A. Hokin, H. Ji, S.C. Prager, and C.R. Sovinec, Phys. Rev. Lett. **72**, 3670 (1994).

2) B.E. Chapman, J.K. Anderson, T.M. Biewer, D.L. Brower, S. Castillo, P.K. Chattopadhyay, C.-S. Chiang, D. Craig, D.J. Den Hartog, G. Fiksel, P.W. Fontana, C.B. Forest, S. Gerhardt, A.K. Hansen, D. Holly, Y. Jiang, N.E. Lanier, S.C. Prager, J.C. Reardon, and J.S. Sarff, Phys. Rev. Lett. **87**, 205001 (2001).

3) M.D. Wyman, B.E. Chapman, J.W. Ahn, A.F. Almagri, J.K. Anderson, F. Bonomo, D.L. Brower, S.K. Combs, D. Craig, D.J. Den Hartog, B.H. Deng, W.X. Ding, F. Ebrahimi, D.A. Ennis, G. Fiksel, C.R. Foust, P. Franz, S. Gangadhara, J. a. Goetz, R. O'Connell, S.P. Oliva, S.C. Prager, J.A. Reusch, J.S. Sarff, H.D. Stephens, and T. Yates, Phys. Plasmas **15**, 010701 (2008).

4) M.D. Wyman, The Physics of High-Density, High-Beta Reversed-Field Pinch Plasmas, University of Wisconsin, 2007.

5) M. Zuin, S. Spagnolo, R. Paccagnella, E. Martines, R. Cavazzana, G. Serianni, M. Spolaore, and N. Vianello, Nucl. Fusion **50**, 052001 (2010).

6) R. Paccagnella, Phys. Plasmas **20**, 012119 (2013).

7) C. Mercier, Nucl. Fusion **1**, 47 (1960).

8) M.D. Wyman, B.E. Chapman, J.W. Ahn, A.F. Almagri, J.K. Anderson, F. Bonomo, D.L. Brower, S.K. Combs, D. Craig, D.J. Den Hartog, B.H. Deng, W.X. Ding, F. Ebrahimi, D.A. Ennis, G. Fiksel, C.R. Foust, P. Franz, S. Gangadhara, J.A. Goetz, R. O'Connell,

S.P. Oliva, S.C. Prager, J.A. Reusch, J.S. Sarff, H.D. Stephens, and T. Yates, Nucl. Fusion **49**, 015003 (2009).

9) M.R. Stoneking, J.T. Chapman, D.J. Den Hartog, S.C. Prager, and J.S. Sarff, Phys. Plasmas **5**, 1004 (1998).

CHAPTER 5

Investigation of Pellet-Fast-Ion Interaction and High β Operation with NBI

5.1 Introduction and Motivation

In order to further examine the nature of a β limit in the RFP, we add NBI heating to the high β pellet fueled PPCD experiments in an attempt to increase β. To this end we first develop a simple model as a means to predict the optimal density to maximize deposited beam power. This optimal density lies in the range of 2-3*10^{19} m^{-3} and is due to several factors including slowdown of the fast ions, shinethrough due to increased beam attenuation and edge loss mechanisms. The addition of NBI heating to high β discharges shows a small impact on several parameters including T_e, and the previously discussed $\langle \beta_e \rangle$ value. The interaction of pellet fueling and NBI heating is explored further as a deflection of the pellet is observed, consistent with asymmetric ablation due to the fast ion population. Tracking the pellet deflection allows us to estimate the fast ion density with results in agreement with other estimates.

5.2 Impact of Pellet Injection on Fast Ion Population

The neutral beam on MST has a beam energy of 25 keV and can provide up to 1 MW of beam power. For the experiments with pellet fueling, a fuel mix of 95% hydrogen and 5% deuterium was used. The initial goals for the addition of NBI heating to high β plasmas was to either boost β with the additional heating power, or to establish the presence of a β limit by showing a saturation of β with added heating power. To best focus the experiments, some simple predictive modeling was done to help estimate the optimal density for maximizing the NBI heating power transferred to the pellet fueled plasma.

5.2.1 Modeling and Predictions

In order to better understand the interaction between the pellet and the NBI, first some simple modeling was done to estimate the impact of increased density on the ionization of fast neutrals. This model looks at the beam intensity I as it attenuates along the beam path length (l) to estimate the radial deposition of an idealized pencil beam traveling tangential to the plasma core, taken from [1]

$$I(l) = I(0)\exp\left[-\int_0^l n_e\left(\frac{\langle\sigma v_e\rangle}{v_b} + \sigma_i + \sigma_{cx}\right)dl\right] \tag{5.1}$$

The local electron density n_e is obtained from reconstructed data, and the cross sections for fast neutral ionization mechanisms for charge exchange (σ_{cx}), electron impact ionization ($<\sigma\, v_e>/v_b$) and ion impact ionization (σ_i) are taken from. [2] In reality, the beam is injected at a slight angle such that it passes inboard of the geometric axis, but for the purposes of this thesis a simplified view is sufficient. A comparison of the model and real beam geometry is shown in figure 5.1. The simple model allows one to rapidly change various experimental parameters for quick predictive estimates. Of note, the simple model above was compared with a more complex model of MST's NBI, discussed in [3], confirming qualitative agreement of the deposition profiles.

While the beam path is idealized, the plasma profiles are obtained from equilibrium reconstructions based on experimental measurements. The results in figure 5.2 show first, a drop in the beam shinethrough (the fraction of beam power present after the beam crosses the plasma) from 20% to 3% after doubling the density from $1*10^{19}$ to $2*10^{19}$ m^{-3}, consistent with experimental measurements from the shinethrough detector in pellet fueled discharges. Further increases in density decrease the shinethrough to a negligible amount. Second, the rapid beam attenuation which occurs as the density increases results in a shift in the fast ion deposition profile radially outward as shown in figure 5.3.

The next step for estimating the power deposition to the plasma is to consider the various loss mechanisms for fast ions. The increased deposition in the edge will lead to an increase in prompt loss of ions which are born far enough out to be within a gyroradius of the vessel, indicated by the dashed line portion of figure 5.3.

For the beam power optimization, only the largest fast ion loss mechanism will be considered here: charge exchange with background neutrals. For this we require an estimate of the neutral density profile in high density PPCD discharges. We utilize a Monte Carlo analysis code called NENE [4], which uses experimental profiles along with measurements of D_α light to fit a neutral density profile. Figure 5.4 shows the results from a set of NENE calculations of the neutral density profile for discharges with $\langle n_e \rangle$ of $1*10^{19}$ m^{-3} and $3*10^{19}$ m^{-3}. While the edge neutral density increases with the increase in $\langle n_e \rangle$, the core neutral density, where we want to maximize the deposited beam power, is smaller by more than a factor of 10. As density increases, the neutral penetration length decreases due to the increased ionization rate from increased collisions [5], resulting in the observed neutral screening. Runs for $\langle n_e \rangle$ = 7*10^{19} m^{-3} were performed and show even larger drops in the core neutral density, though these parameters actually test the limits of this analysis, despite substantially increasing the number of test particles (and in turn the calculation time). The trend is consistent though: increased electron density corresponds to an increase in edge neutral density, and also a large decrease in the core neutral density.

For the purpose of optimizing the beam power deposition, we also consider energy loss to the bulk plasma. The classical slowing down time for the fast ions is based upon classical collisions with the electrons with the energy loss governed by equation 5.2 with the key scaling for τ_{SD} of $T_e^{3/2}$ / $<n_e>$.

$$\frac{1}{E_{fi}}\frac{dE_{fi}}{dt} = \frac{-Z_{fi}^2 e^4 n_e \sqrt{m_{fi}} \ln\Lambda}{4\sqrt{2}\pi\varepsilon_0^2 m_e E_{fi}^{3/2}} \left[\frac{4}{3\sqrt{\pi}} \frac{m_e}{m_{fi}} \left(\frac{E_{fi}}{T_e} \right)^{3/2} + \sum_i \frac{m_e n_i}{m_i} \frac{Z_i^2}{n_e} \right] \tag{5.2}$$

A compilation of calculated τ_{SD} values is shown in table 5.1 with the relevant plasma conditions highlighted. In the high density, low temperature plasmas where we observe the highest β values, the τ_{SD} can be as low as 1 ms, much less than the PPCD duration of 10 ms. In contrast, the low density hot plasmas have slowdown times comparable to or greater than the PPCD duration, making those discharges poor candidates for significant NBI heating. If we only assume these two loss mechanisms, while ignoring finite thermal energy confinement, we can estimate the total fraction of power which goes to plasma heating (vs lost to charge exchange) as a function of radius. The probability of undergoing charge exchange in the plasma is given by

$$P(t) = e^{-t/\tau_{cx}} \text{ with } \tau_{cx} = \left(\sigma_{cx} n_n v_{fi}\right)^{-1} \tag{5.3}$$

We use experimental plasma parameters (T_e, n_e) to calculate the charge exchange cross section (σ_{CX}), and we use the velocity for 25 keV fast ions and the neutral density profile, obtained from the NENE analysis above, to calculate τ_{CX} for all radii. We obtain a profile of the fast ion slowing down time τ_{SD} by using experimental n_e and T_e profiles along with equation 5.2. Given the time scales for each loss mechanism, we estimate the power deposition as

$$P_{cx} = \frac{N_{fi} E_{fi}}{\tau_{cx}} \text{ and } P_{sd} = \frac{N_{fi} E_{fi}}{\tau_{sd}} \tag{5.4}$$

where N_{fi} is the radial fast ion deposition profile obtained from the model described above, and E_{fi} is the energy of the fast ions. For this work, these are the only avenues of fast ion power loss that we will consider. Under these assumptions, the ratio of the charge exchange loss to the slowing down loss is proportional to the ratio of their τ values.

$$\frac{P_{cx}}{P_{sd}} \approx \frac{\tau_{sd}}{\tau_{cx}} = R \tag{5.5}$$

If we further assume that these are the only loss mechanisms for the fast ions, (i.e. $P_{CX} + P_{SD} = 1$ MW) we can estimate the heating power to the plasma.

$$P_{cx} = \frac{R}{1+R}; P_{sd} = \frac{1}{1+R} \tag{5.6}$$

We then combine the results to estimate coarsely at what density the core deposited beam power is optimized. The available energy is capped at 80% in the core, dropping to 30% at r/a = 0.5, consistent with the findings in reference 6. In figure 5.5, for a total of six cases, we use plasma profiles from equilibrium reconstructions along with the calculated neutral density profiles to estimate the fraction of available heating power. At 200 kA we use pellet fueled cases with

$n \sim 2*10^{19}$ m^{-3} and $n \sim 3*10^{19}$ m^{-3} and a no pellet case with $n \sim 1*10^{19}$ m^{-3}. At 500 kA we use cases with $n \sim 1*10^{19}$ m^{-3}, $n \sim 3*10^{19}$ m^{-3} and $n \sim 7*10^{19}$ m^{-3}. We find that the beam deposition increases up to moderate densities ($2*10^{19}$ and $3*10^{19}$ m^{-3} for 200 and 500 kA, respectively) and subsequently decreases for the highest densities considered here. For moderate densities, we expect approximately half of the beam power to be deposited in the plasma, a significant improvement over the low density estimates obtained here. We note that the estimated heating power in the highest density cases is larger than that at low density, but is also certainly optimistic due to the lack of fast ion loss mechanisms (e.g. fast ion diffusion) and the ignored thermal energy confinement time.

An extension of this analysis only taking into account shinethrough and prompt loss was done for a variety of beam energies to estimate the optimal density to maximize deposited power as a function of beam energy and is shown in figure 5.6. The 200 kA consistently has a lower optimal density due to lower T_e resulting in a lower shinethrough, as well as larger prompt loss as deposition is pushed radially outward due to the larger gyroradius. This analysis could prove to be potentially useful should a second heating beam ever be considered on MST. For the 25 keV beam, this first estimate suggests an optimal density of $\sim 2*10^{19}$ m^{-3} for 200kA discharges and $\sim 3*10^{19}$ m^{-3} for 500 kA discharges, consistent with the results above. However, high β discharges for 200 kA can have densities of $3\text{-}4*10^{19}$ m^{-3}, which would be optimal for a 50 keV beam. The highest density 500 kA experiments can reach a density greater than 6e19 m^{-3}, which would be optimal for a neutral beam with energy above 80 keV.

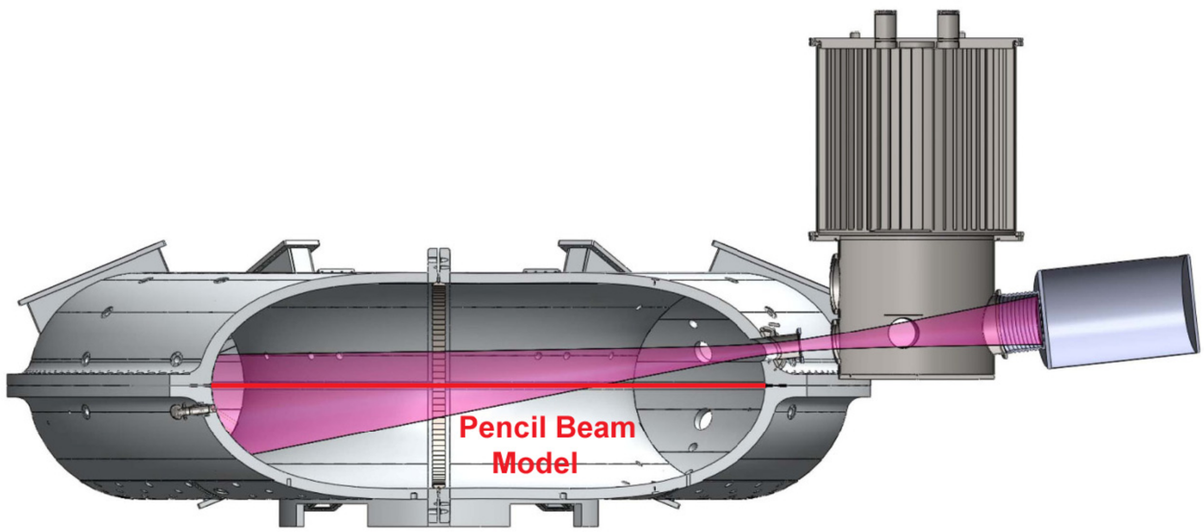

Figure 5.1: The actual NBI injection along with the geometry for the idealized pencil beam model.

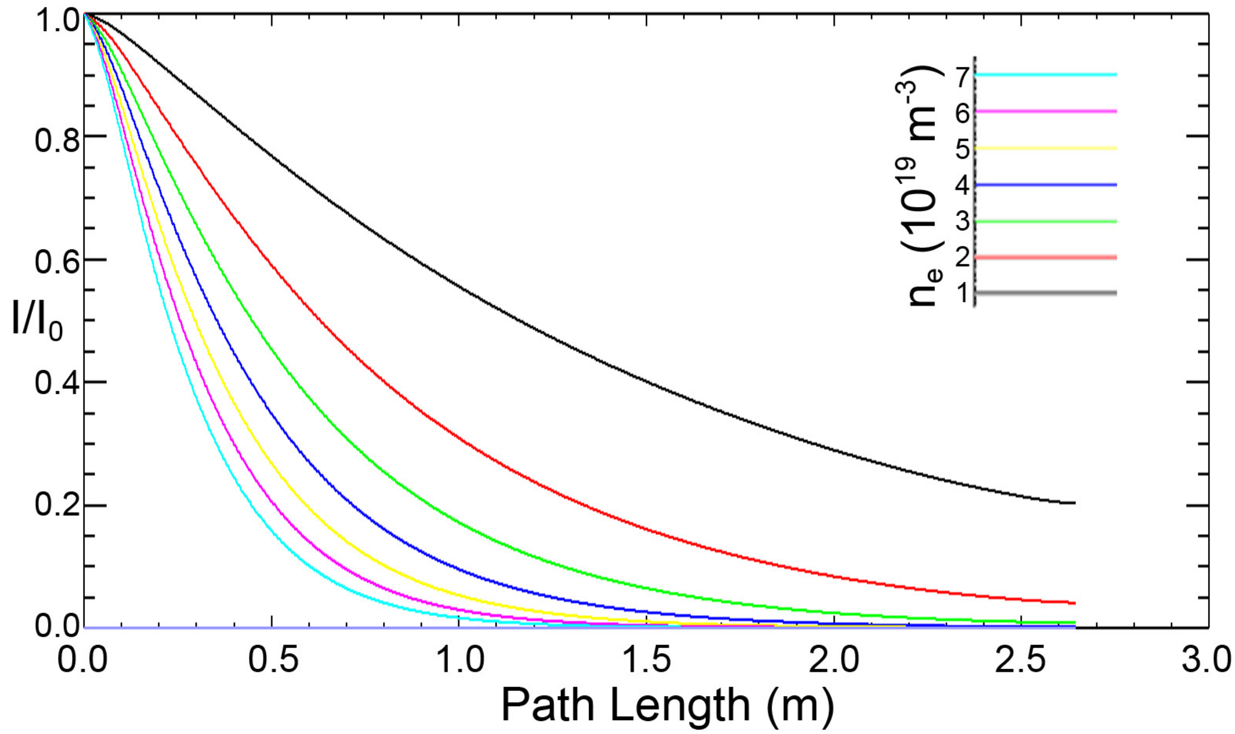

Figure 5.2: Attenuation of model beam as a function of path length for various values of line averaged density. Path length of zero corresponds to the NBI injection port, with the shine-through detector located at 2.65 m.

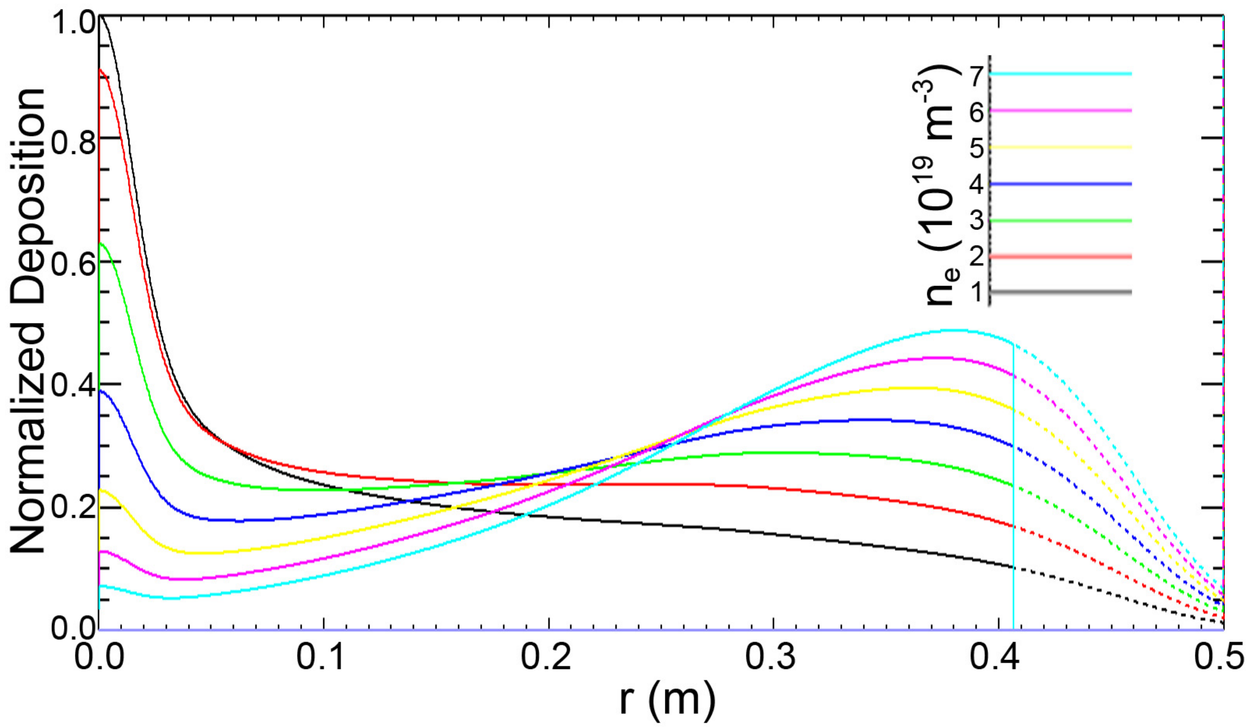

Figure 5.3: Normalized deposition profile from model beam injection into 500 kA discharge for various values of line averaged density. Dashed line corresponds to prompt loss due to deposition within a gyroradius of the wall.

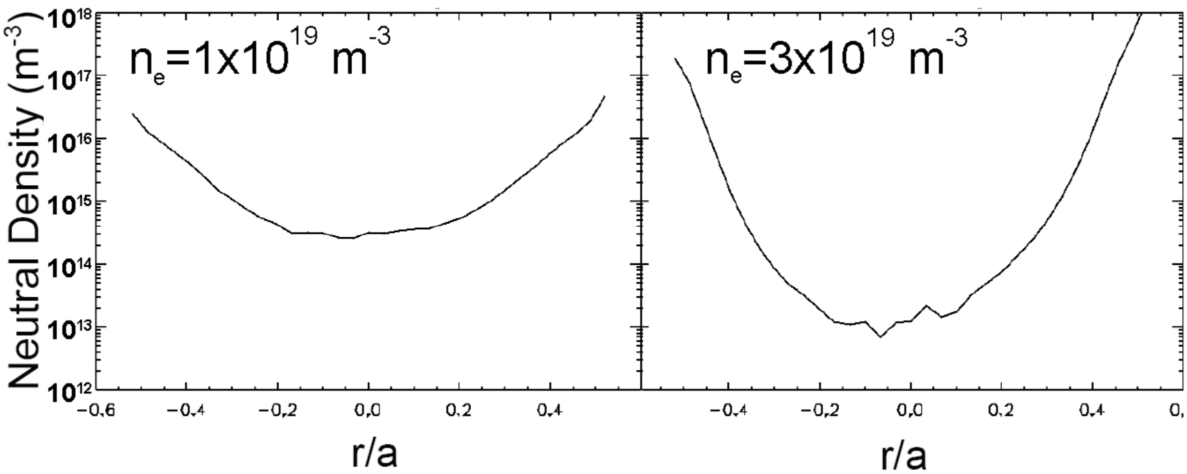

Figure 5.4: Neutral density profiles from NENE analysis for discharges with line averaged density of (a) $1*10^{19}$ m^{-3} and (b) $3*10^{19}$ m^{-3}.

τ_{fi}(ms) $\langle n_e \rangle$(10^{19} m^{-3})

T_e (eV)	1	2	3	4	5	6	7
200	5	2.5	1.7	1.3	1	0.8	0.7
400	14	7	4.6	3.5	2.8	2.3	2
600	24	12	8	6	5	4	3.5
800	36	18	12	9	7	6	5
1000	47	24	16	12	9.5	8	7
1200	59	30	20	15	12	10	8
1400	70	35	23	18	14	12	10

Pellet Fueled 500 kA PPCD

Low Density 500 kA PPCD

Pellet Fueled 200 kA PPCD

Low Density 200 kA PPCD

Table 5.1: Calculated classical fast ion slowdown times for various electron temperature and density values. The relevant experimental regimes are highlighted by the colored borders.

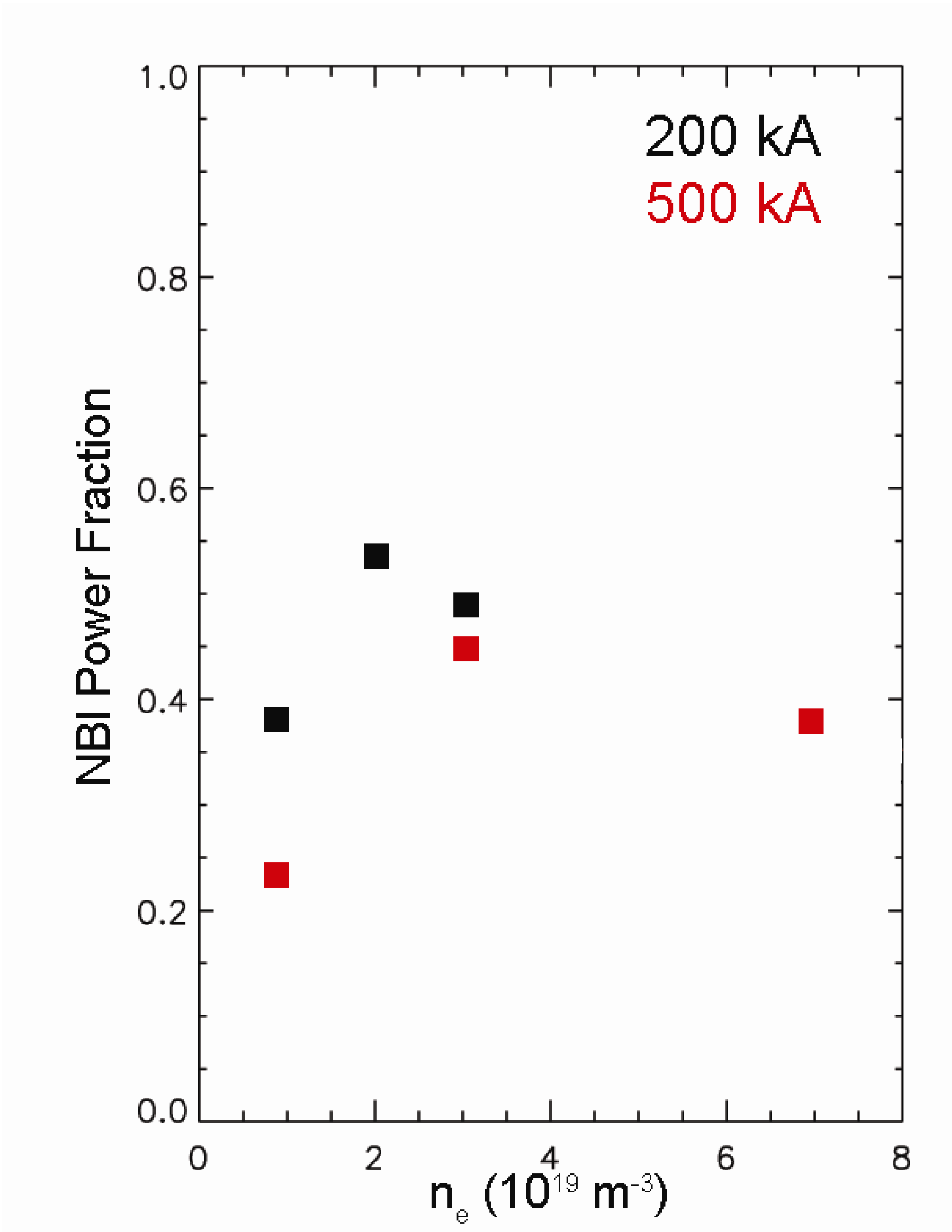

Figure 5.5: Estimated fraction of beam heating power to the plasma vs. density for 500 kA (red) and 200 kA (black) discharges. The total beam power is 1 MW making the y-axis an upper bound on the beam heating power.

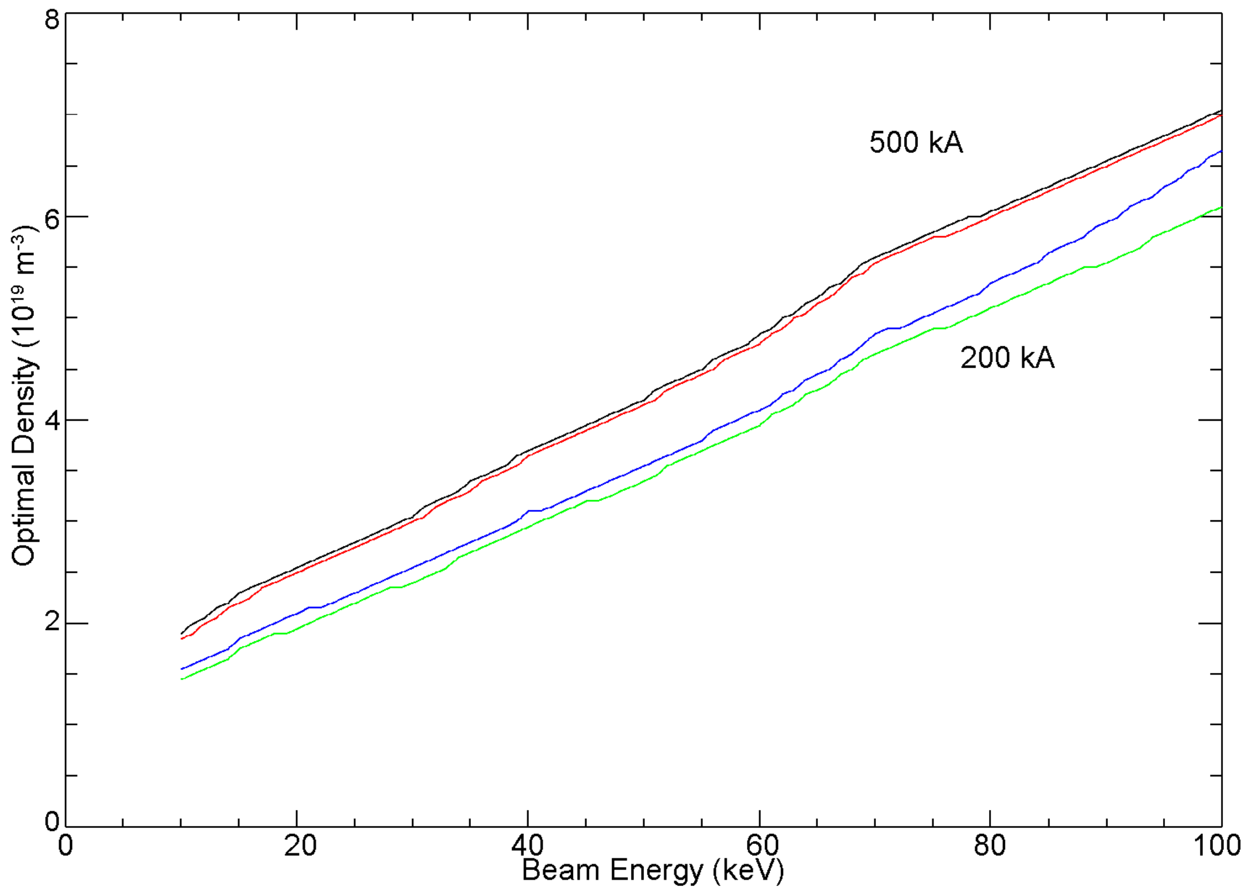

Figure 5.6: The density for optimal beam power deposition vs. beam energy for high and low current discharges for hollow and peaked density profiles. The optimal density is consistently higher for high current discharges compared to low current, and profile effects are more significant in the low current case. Each line represents a peaked (upper) or hollow (lower) density profile.

5.3 Impact of Fast Ions on Pellets

5.3.1 Pellet Deflection due to NBI heating

Not originally a dedicated experiment itself, the observation of pellet deflection in NBI heated PPCD plasmas prompted a closer look with a high speed CCD camera to better characterize the deflection. Pellet deflection and enhanced ablation have been observed elsewhere[7]. The deflection is believed to be due to rocketing from asymmetric heating caused by the fast ion population. The enhanced ablation may also help with optimizing pellet deposition in the plasma core, where the fast ion population is located on MST. In previous experiments on MST and other RFP's, a deflection of radially injected pellets in the poloidal direction has been observed and is believed to be caused by the fast election population in the edge.

The deflection of the pellet by the fast ion population was first observed in MST from the CCD camera located at 300 T, -15P. This camera has a frame rate of roughly 770 Hz, meaning a typical pellet will only be observed in a handful of frames. This field of view in figure 5.7 is normally used to determine the pellet penetration depth as well as the pellet quality. The second camera, with a larger resolution and higher frame rate (25000 Hz) was positioned directly above the pellet injection line at 240T, 90P as diagrammed in figure 5.7. The observed deflection is shown for each camera in figures 5.8 and 5.9 along with an approximate image of the camera view from a Solidworks model of the inside of the vessel. We approach the deflection of the pellet due to the NBI injected fast ion population by using camera images to estimate the pellet trajectory with and without NBI. In this case, the overhead camera gives us the best view of pellet deflection.

A model for asymmetric pellet ablation due to a fast ion population can be found in [7]. With a simplification to their approach, we will make the assumption that any deflection is due solely to the added fast ion ablation. This ignores any impact that fast ion ablation may have on the normally symmetric ablation due to the thermal electrons. The deflection is then given by

$$\frac{dv_p}{dt} = \frac{1}{N_p}\frac{dN_p}{dt} v_{jet} \tag{5.7}$$

where N_p is the pellet particle content, and v_{jet} is assumed to be approximately half the neutral gas sound speed for the neutral gas cloud surrounding an ablating pellet. As we do not have measurements of the pellet cloud characteristics during ablation, we will use a reasonable estimate of 400 m/s for v_{jet} based upon neutral cloud parameters of $n_e \sim 10^{25}$ m^{-3} and $T_e \sim .01$ eV. We can transform this to be a function of the pellet radius r_p via

$$\frac{dN_p}{dt} = 2\pi r_p^2 (2n_m)\frac{dr_p}{dt} \tag{5.8}$$

with n_m the molecular density of the solid pellet material (ρ~200 kg/m^3 for deuterium so n_m ~$3*10^{28}$ molecules/m^3). The fast ion ablation rate is given by

$$\frac{dr_p^{fi}}{dt} = C_f r_p^{-2/3} n_f^{1/3} E_b^{1.59}\left(\frac{\tilde{\Pi}\cos\theta_b}{\tilde{X}}\right) \tag{5.9}$$

with E_b the beam energy, and n_f the fast ion density. The final factor in parentheses is a geometric enhancement ~1. C_f is $4*10^{-16}$ for our pellet and beam composition and the calculation is outlined in [7]. For comparison, the Parks scaling [8] for pellet ablation from the thermal electrons goes as

$$\left(\frac{dr_p}{dt}\right)^e = C_e r_p^{-2/3} n_e^{1/3} T_e^{1.64} \tag{5.10}$$

With $C_e = 8*10^{-14}$ for hydrogen pellets.

This gives us a means of estimating the acceleration on the pellet due to the fast ion population by combining equations 5.7-5.9 above.

$$\frac{dv_p}{dt} = \frac{1}{N_p} 2\pi\, r_p^2 (2n_m) C_f r_p^{-2/3} n_f^{1/3} E_b^{1.59} v_{jet} \tag{5.11}$$

Finally, we can simplify this result slightly by assuming $2n_m = N_p/V_p$ and $V_p = 4/3\pi\, r_p^3$. This yields the pellet acceleration

$$\frac{dv_p}{dt} = C_f r_p^{-5/3} n_f^{1/3} E_b^{1.59} v_{jet} \tag{5.12}$$

For our experimental case, we fired a 2.0 mm diameter deuterium pellet into a 300 kA F=0 discharge with an estimated fast ion density of $8*10^{17}$ m^{-3} in the core. This estimate is based on transport calculations made with TRANSP/NUBEAM[9,10]. The electron temperature and density were ~300 eV and $1*10^{19}$ m^{-3}, respectively. The ablation rates for each case are calculated to be 0.4 m/s for the fast ion ablation and 0.2 m/s for electron thermal ablation from the Parks scaling.

The acceleration on the pellet is then calculated to be ~$1.3*10^5$ m/s^2. This is in fact comparable to the initial acceleration of the pellet at launch and is sufficient to achieve a deflected velocity of 100 m/s or more in a few ms, so it is no wonder the deflection is clearly visible.

The observed deflection is highlighted in a composite image of high speed video shown in figure 5.9. While no clear measurement of the enhanced ablation is made, an increase in light is clearly represented by the larger saturated pellet area in the center of the image.

5.3.2 Estimating pellet trajectory to calculate fast ion density

With a more detailed look at the pellet acceleration, we estimate the fast ion density as a function of radius to compare with the TRANSP results. The use of pellets as a diagnostic tool has been employed in a variety of settings, but this particular use could prove useful to NBI work on MST despite the less than ideal pellet tracking capabilities currently available. We start by examining the high speed video for a discharge without NBI heating. In this case, we observe no deflection and we take this as the baseline case. As we consider a discharge deflected by the fast ion population, we wish to measure the deflection from the trajectory of the no NBI case. By tracking the pellet across the camera frame with x, y corresponding to pixel coordinates, we fit a line to the pellet trajectory. The shots were chosen due to the lack of any observable poloidal deflection due to fast electrons in the edge. From here, we transform the pixel data from the camera in such a way that our new reference frame (x',y') has the non-deflected case fit well by y'=0. In this manner, the deflection of the pellet is assumed to be entirely in the y' direction.

We establish the field of view by noting the location of several landmarks observed in the camera view. This includes several portholes, an array of pumping duct holes as well as some magnetic coil arrays. This gives us an approximate map of the poloidal and toroidal locations we are observing. After transforming this map to the (x', y') system, we have an approximately linear relationship between (x', y') and (θ, φ) the poloidal and toroidal locations of the landmarks.

We can then transform our deflected pellet trajectory (x,y) $\rightarrow$ (x',y') $\rightarrow$ (θ, φ) where (θ, φ) corresponds to the machine coordinates at the vessel wall. Finally, we infer the radial location, r(t), and the deflection, z(t), of the pellet under the assumption that the pellet only deviates in the z direction from its initial flight path. This yields the deflection and radial location of the pellet in time.

By taking the time derivative of z, we can obtain both the velocity and acceleration experienced by the pellet in time. From the acceleration, it is possible to calculate, with equation 5.12, the fast ion density required to accelerate the pellet. The time evolutions of position and velocity are shown in figure 5.10, while the acceleration and fast ion density are shown in figure 5.11. In figure 5.12, we compare the fast ion density vs. radial pellet location with that of the TRANSP prediction. Two observations are made. First, the radial location of the fast ion population is consistent with TRANSP results. Second, the acceleration is greatly diminished as the pellet travels further inward, suggesting the fast ion population is quickly reduced by the ablating pellet. This means the deflection measurement will set a lower bound on the fast ion density. In that case, the deflection predicts about a twice as many fast ions.

We make one final note about the pellet-beam interaction based upon the fast ion ablation rate. As the thermal ablation rate scales as $\sim T_e^{3/2} n_e^{1/3}$, the thermal ablation will become significantly more important in discharges with higher Te. This means fast ion ablation will have a larger effect on pellet ablation, relative to thermal ablation, at lower plasma currents. The fast ion contribution at higher current will be a smaller portion of the total ablation rate.

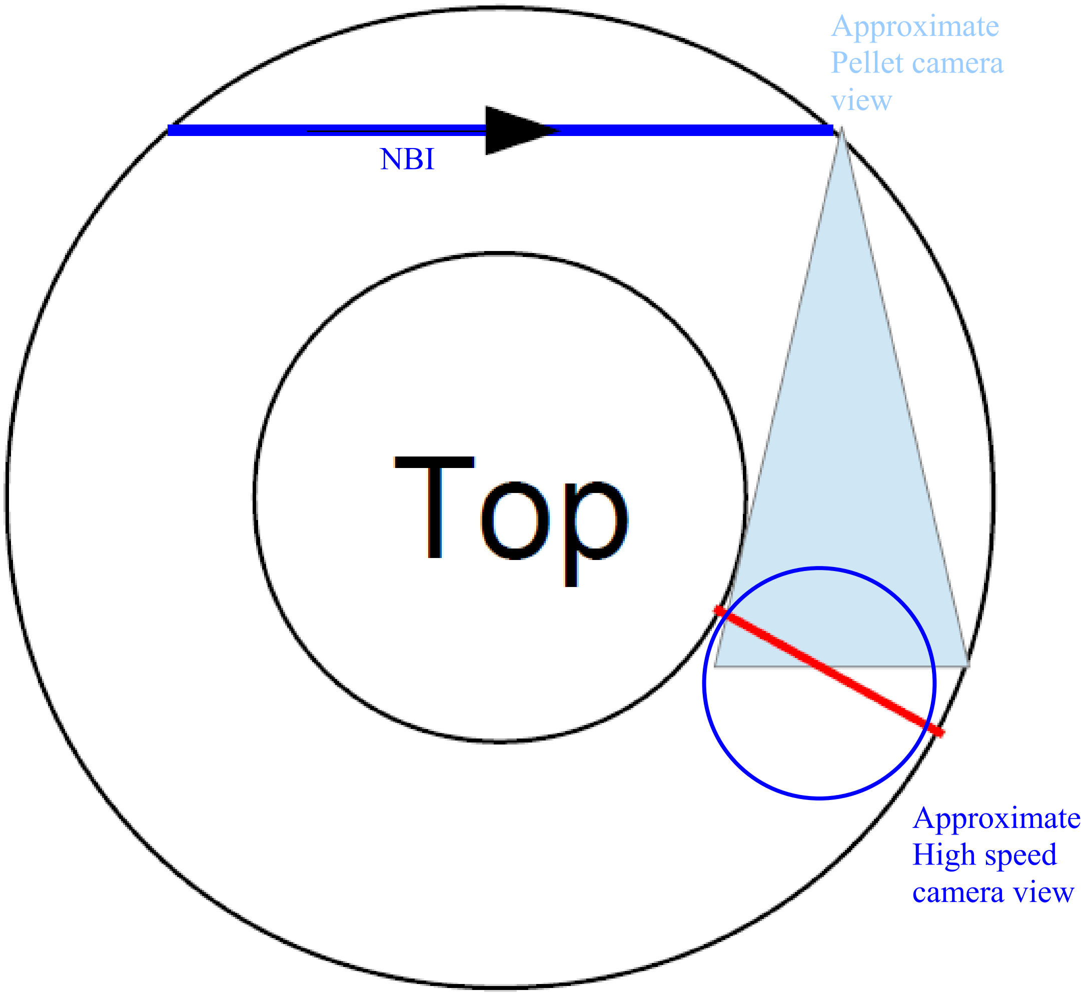

Figure 5.7: Diagram of pellet camera location and approximate camera views along with the NBI direction and pellet injection line in red.

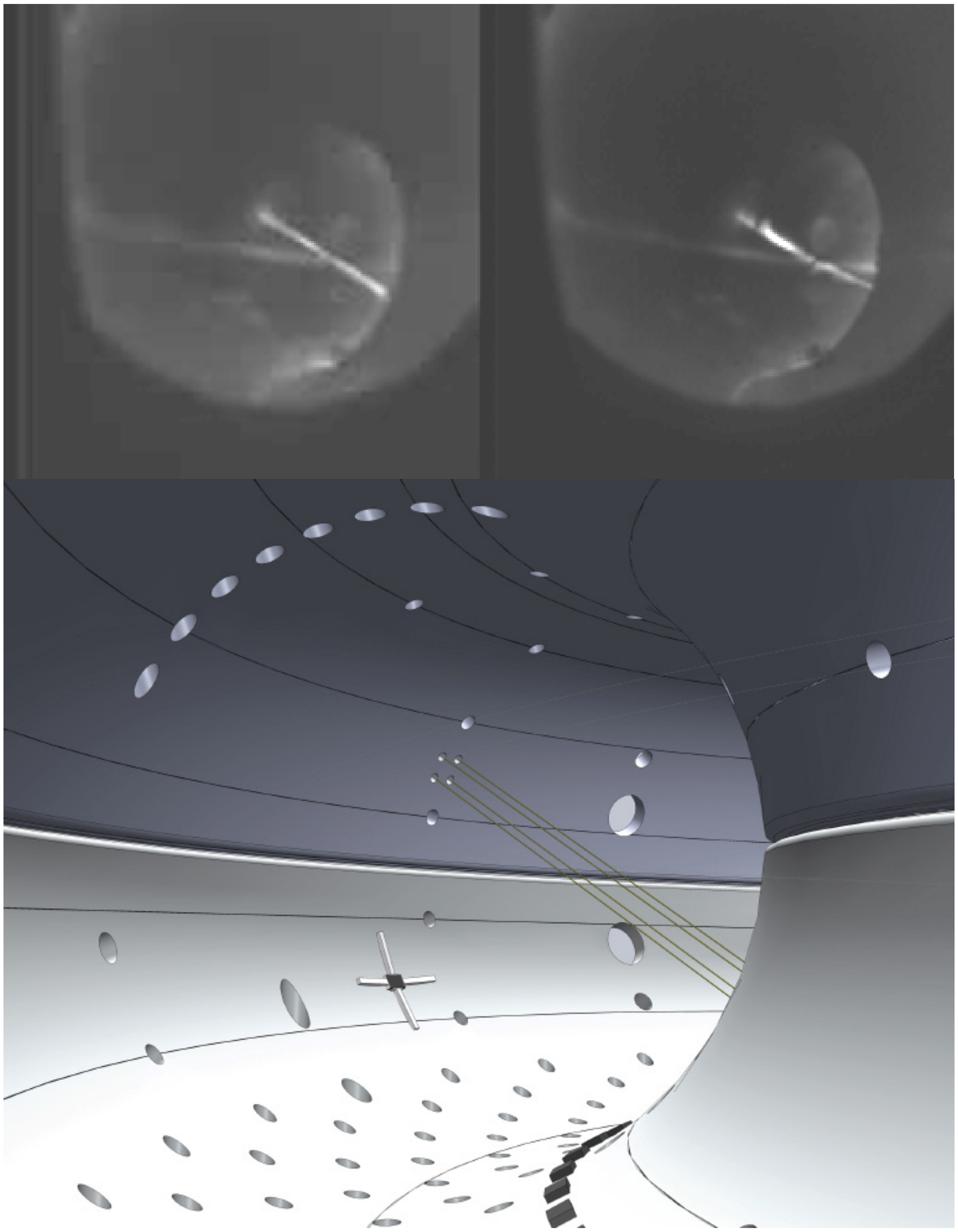

Figure 5.8: Observed deflection from the poloidal view CCD camera showing a change in pellet direction with the NBI on (right) vs the view without NBI (left). Each image is a composite of 2-3 frames of exposure. On the bottom is a Solidworks model approximating the camera view for the camera view located at 320T -15P viewing the injection line. The pellet injector ports are visible as well as the outboard toroidal limiter. Keen eyes will also not the Thomson Limiter.

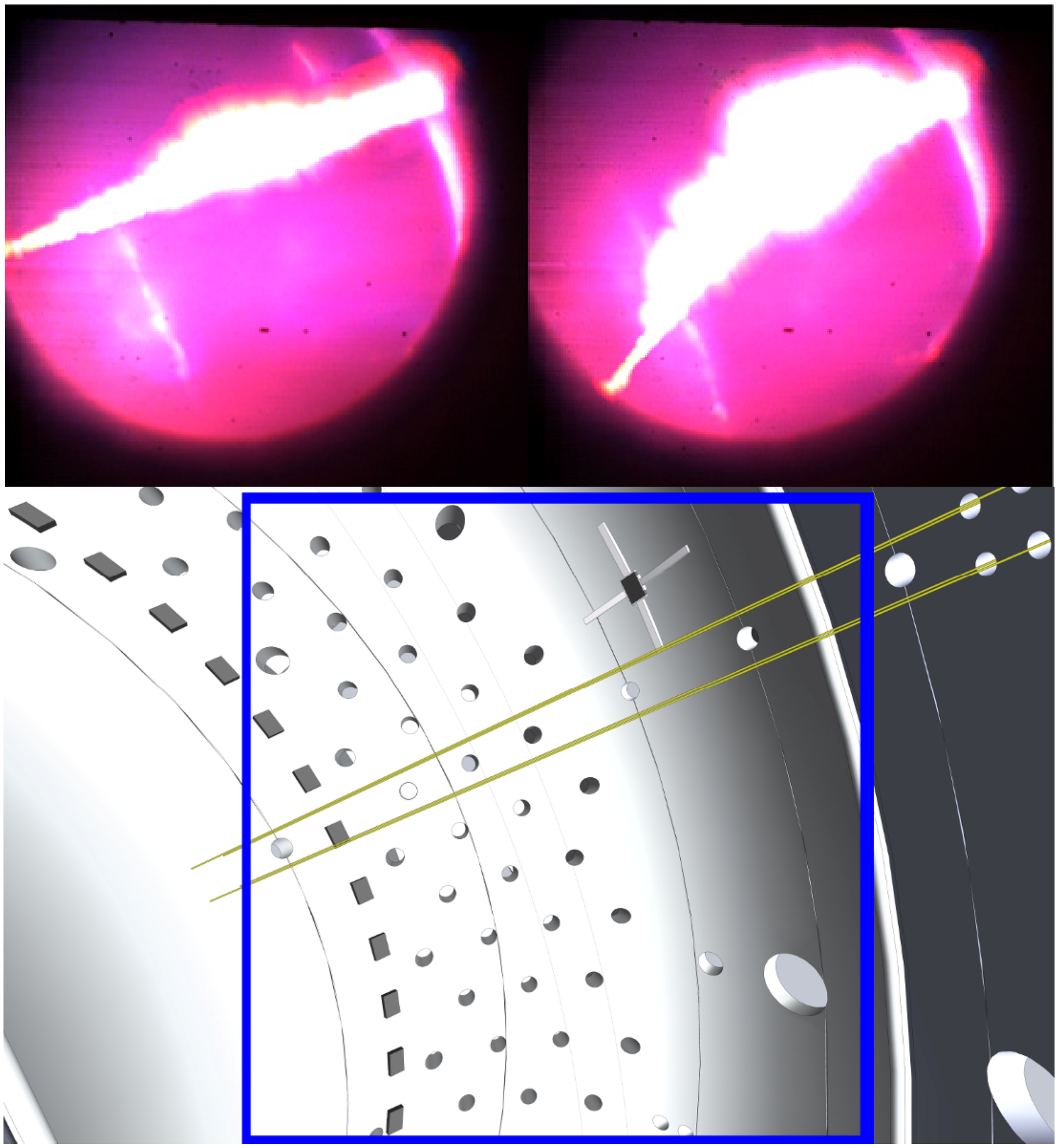

Figure 5.9: Deflection comparison for high speed camera for injection (left) into a discharge with no NBI heating and (right) into a fast ion population. Each image is a composite of frames from the high speed camera. The frame rate for the camera is 25000 Hz. On the bottom is a Solidworks model approximating the overhead camera view for the camera view located at 240T 90P viewing the injection line. The outboard limiter and the toroidal magnetic array are visible on the CCD images. Note the location of the 4 pellet ports in the Solidworks image.

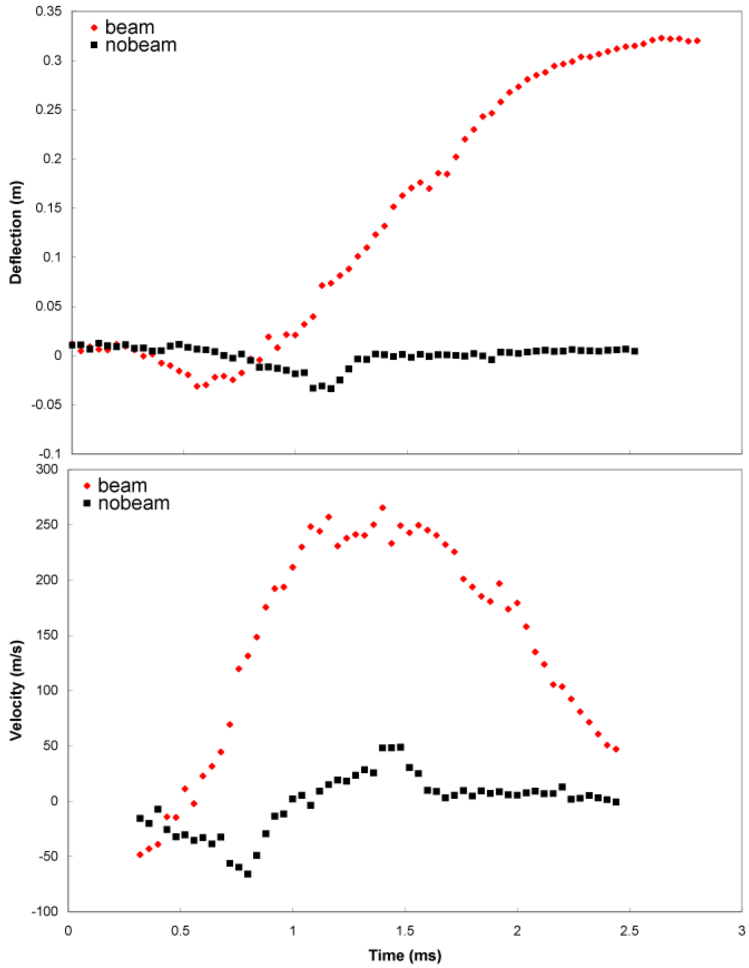

Figure 5.10: Measured (a) deflection and (b) corresponding deflected velocity vs time with and without NBI. A coarse estimate of the uncertainty is represented by the no beam deviation from zero.

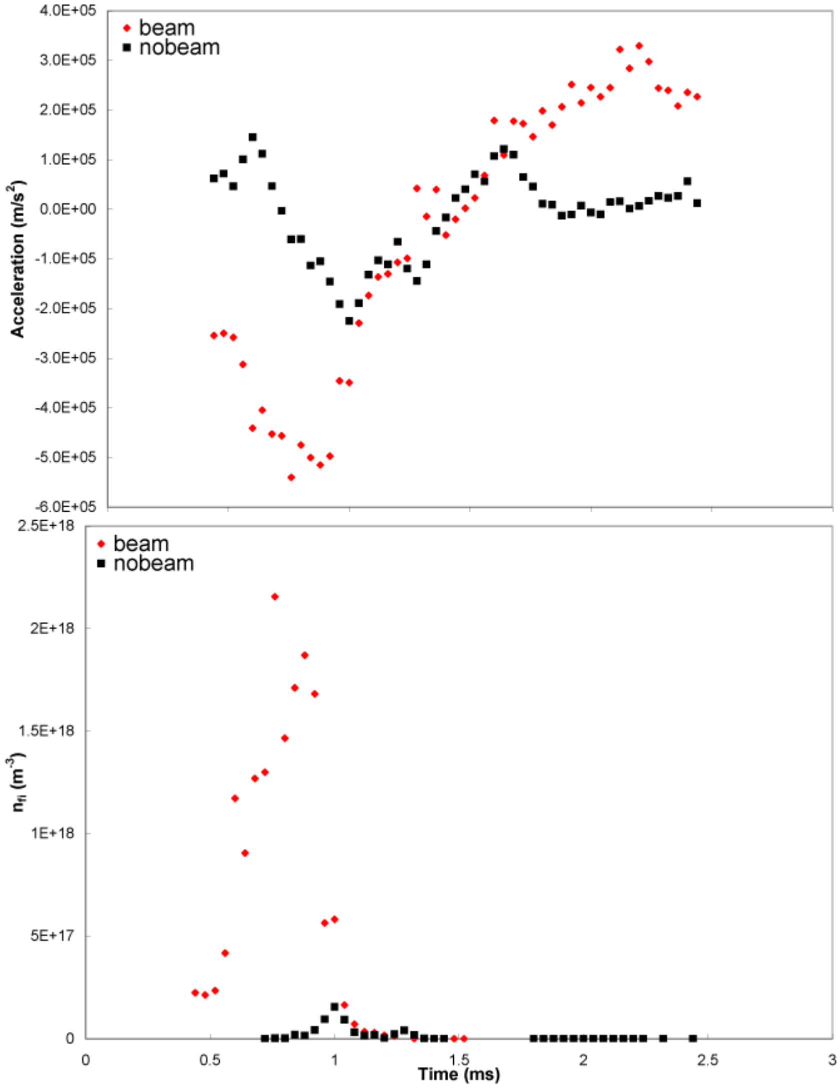

Figure 5.11: (a) acceleration and (b) corresponding fast ion density vs time with and without NBI. A coarse estimate of the uncertainty is represented by the no beam deviation from zero.

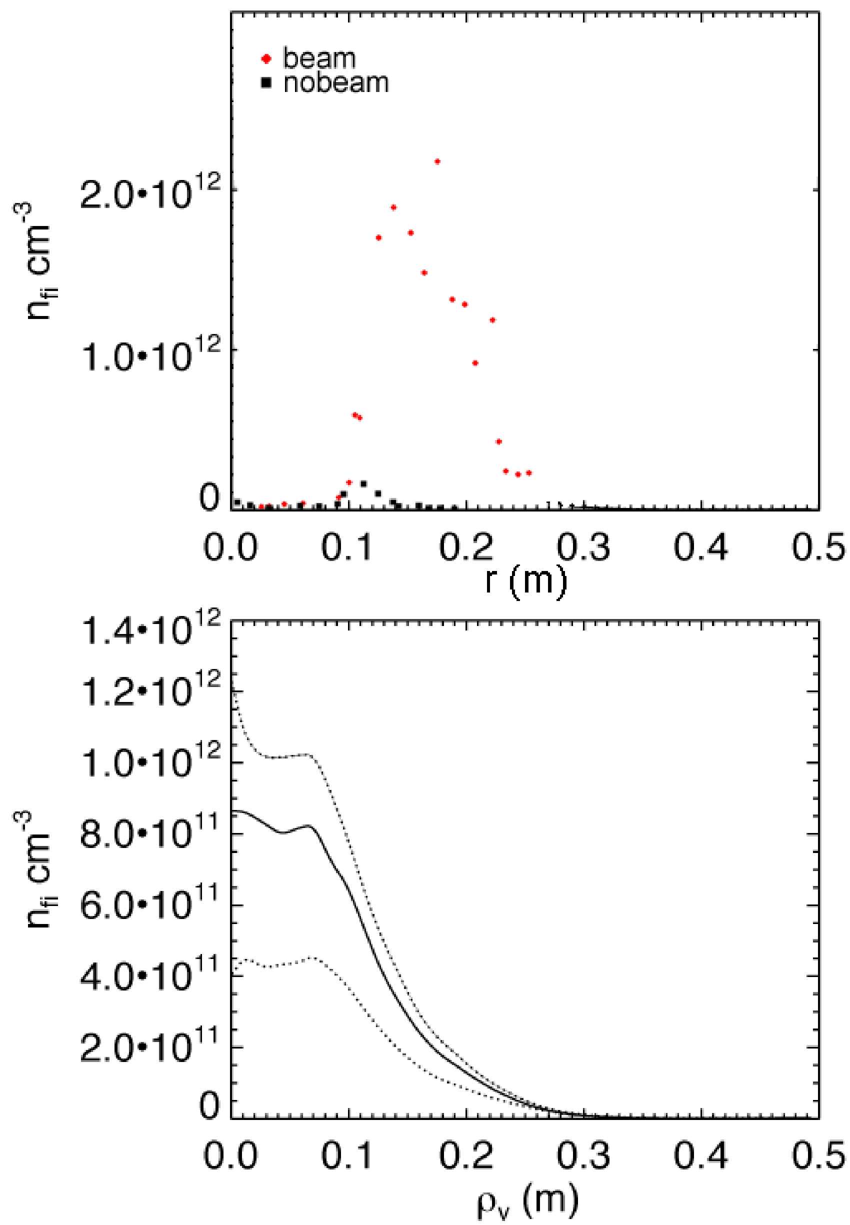

Figure 5.12: (a) Estimated fast ion density profile from pellet deflection observations. (b) TRANSP model for fast ion density. Note the difference in x-axis labels. The estimate drops in the core due to the rapid decrease in fast ion population as the pellet ablates.

5.4 High β Experiments with NBI

We now make use of the same analysis outlined in Sections 4.4 and 4.5 in order to gauge the impact of additional NBI heating in PPCD experiments. As with Chapter 4, the focus is on 200 kA PPCD experiments, and information for 500 kA experiments can be found in an appendix.

5.4.1 Impact of NBI on β and other quantities

As a means to look at the impact of NBI, we look at the $\langle\beta_e\rangle$ value for 200 kA PPCD experiments with and without NBI heating in figure 5.13. Again we observe a saturation of $\langle\beta_e\rangle$ with increasing density for cases with and without NBI; however, we now observe a small difference in $\langle\beta_e\rangle$ as we compare beam and no beam cases. We note as well, the highest β discharge with NBI heating achieves a total β of ~ 25%, corresponding to a $\langle\beta_e\rangle$ of ~11% in the scatter plot for N_{GW} ~1.2. While we do not have an estimate for the fast ion β, this could mean a new record for total β on the RFP if the fast ion contribution is substantial. Figures 5.14 and 5.15 are identical to figures 4.9 and 4.10, but with the addition of discharges with NBI heating in red.

Figure 5.14 shows dependence on the normalized density (N_{GW}) for (a) the ensemble size, (b) the measure density, (c) the plasma current, (d) reversal parameter F, (e) core mode activity, and (f) edge mode activity. There appears to be slightly smaller fluctuation amplitudes for magnetic activity in both the edge and the core, though the ensemble size is small in this region.

Figure 5.15 shows the N_{GW} dependence for (a) ensemble size, (b) $\langle\beta_e\rangle$, (c) Thomson T_e for the core (r/a < 0.2), (d) Thomson T_e for the edge (r/a = 0.7 – 0.8), (e) $T_e^{-3/2}$ scaling, and (f) S. Again we observe a mostly constant value for $\langle\beta_e\rangle$ with increasing N_{GW}; however, we also observe a slightly higher $\langle\beta_e\rangle$ value around N_{GW} = 1 in discharges with NBI heating. This corresponds to a density of $2*10^{19}$ m^{-3}. As we further compare the two sets of discharges, the temperature is higher in the edge and the core for NBI heated discharges in the range of N_{GW} ~ 0.9 – 1.3, an absolute density range of $1.9*10^{19}$ to $2.8*10^{19}$ m^{-3}, the region where $\langle\beta_e\rangle$ is larger, and also consistent with our earlier prediction of the optimal density for maximum beam power deposition. The comparison of the Spitzer like scaling of the Ohmic power suggests a slight drop in the Ohmic heating for discharges with NBI. So we either observe an increase in temperature due to additional beam heating, or due to a slight improvement in confinement from the suppression of magnetic activity.

We discuss two final thoughts on the impact of the NBI on high β discharges. First, it is possible that the NBI heating helps to achieve a more peaked density profile by aiding with the core ablation of the pellet. We see evidence of this in figure 5.13 where the highest values of N_{GW} are obtained in discharges with NBI heating. The aided fast ion pellet ablation is likely leading to increased ablation of the pellet in the core, where we seek to maximize pellet deposition.. Additionally, the fast ion β has not yet been calculated for the highest β discharge (or any pellet fueled discharges) with NBI heating, but if the fast ion population is large enough, we may have exceeded the previous mark of 26%.

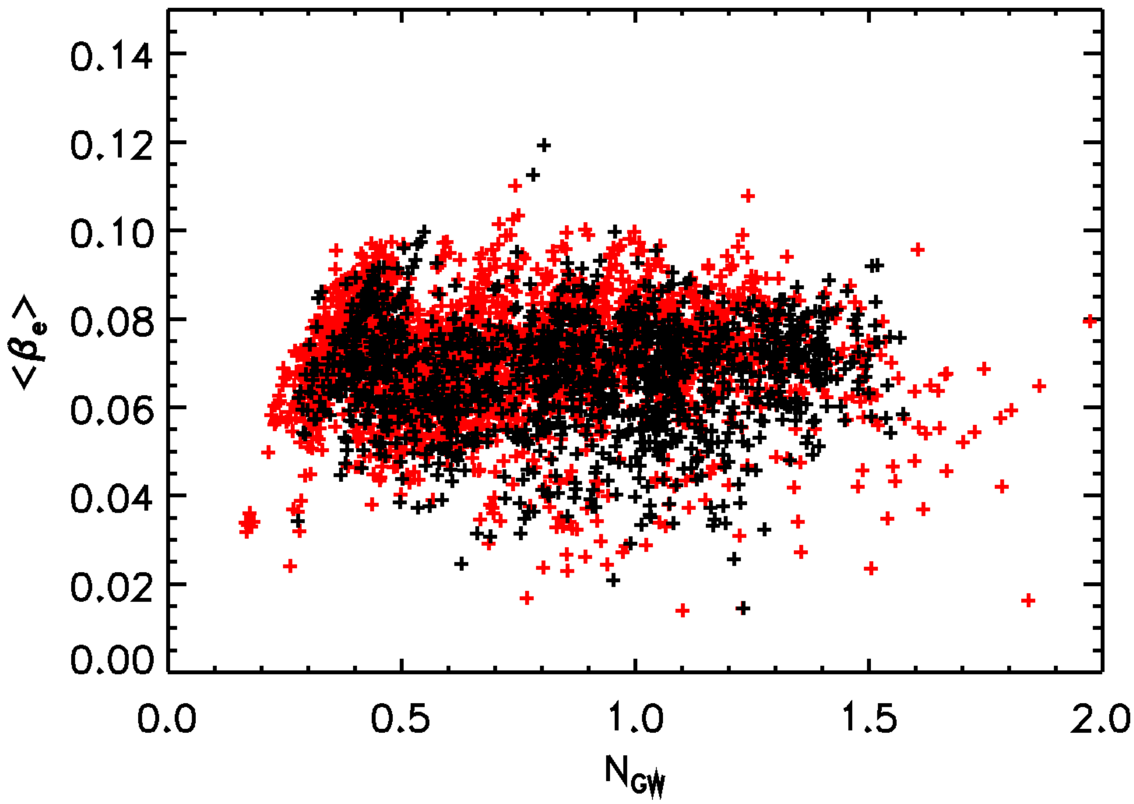

Figure 5.13: A scatter plot of $\langle \beta_e \rangle$ values for a range of N_{GW} in 200 kA PPCD discharges with and without pellet fueling. An approximately constant value of $\langle \beta_e \rangle$ is observed for discharges with (red) and without (black) NBI heating. Each point represents a single measurement of the electron temperature at 2 kHz and a 0.5 ms average of N_{GW}.

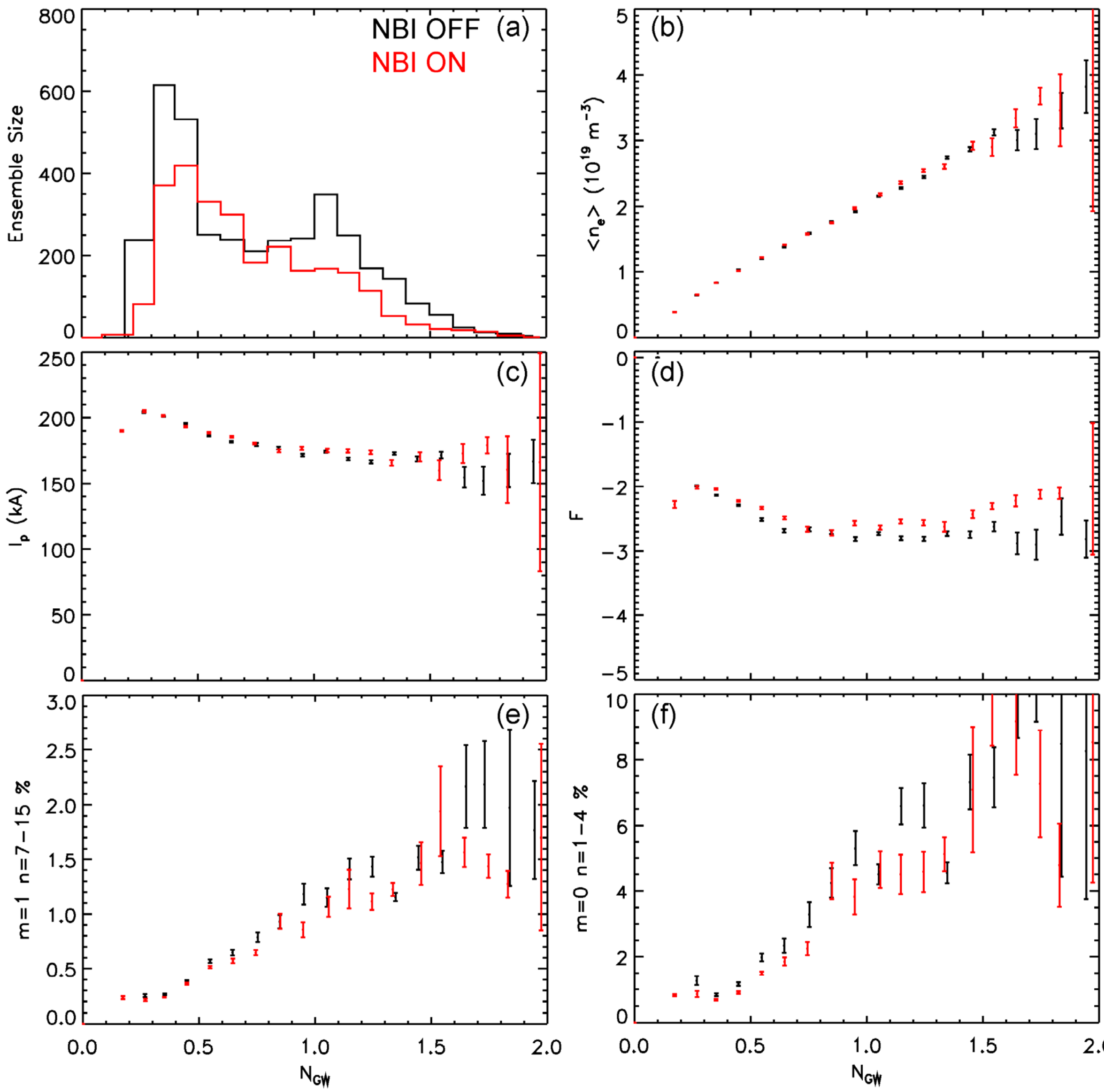

Figure 5.14: Ensemble analysis for pellet fueled 200 kA PPCD discharges with (red) and without (black) NBI heating. A series of plots represent (a) ensemble size, (b) $\langle n_e \rangle$, (c) plasma current, and (d) reversal parameter F, (e) normalized core mode activity, and (f) normalized edge mode activity. Error bars are statistical.

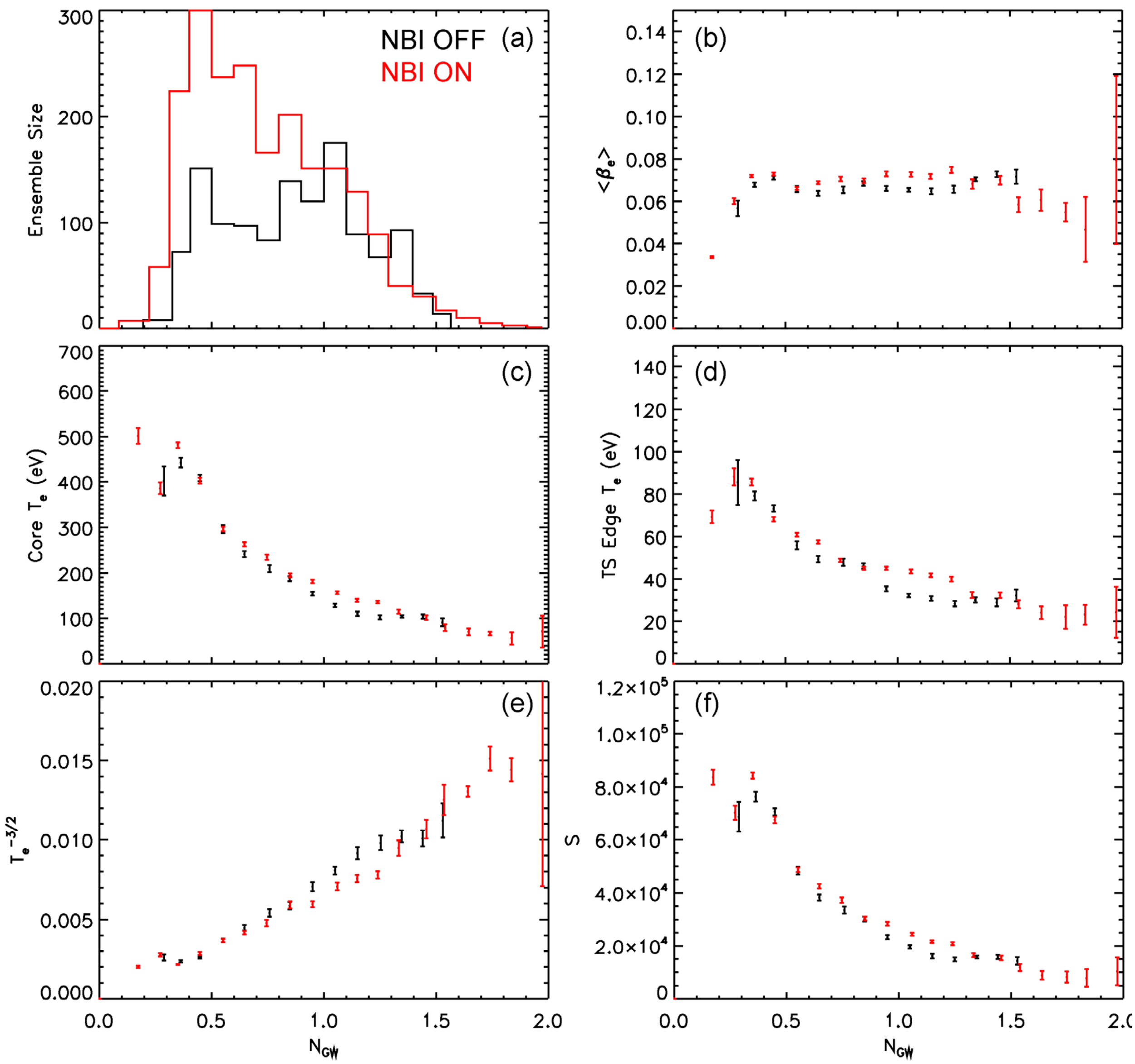

Figure 5.15: Scaling with N_{GW} for ensemble of pellet fueled 200 kA PPCD discharges with (red) and without (black) NBI heating. Plotted quantities are (a) ensemble size, (b) $\langle\beta_e\rangle$, (c) core (r/a < 0.2) Thomson scattering T_e, (d) edge (r/a = 0.7 – 0.8) Thomson scattering T_e, (e) core $T_e^{-3/2}$ and (f) S. . Error bars are statistical.

5.5 References

1) I.H. Hutchinson, Plasma Phys. Control. Fusion **44**, 2603 (2002).

2) V. Kotov, D. Reiter, and A. S. Kukushkin, "Numerical study of the ITER divertor plasma with the B2-EIRENE code package," Bericht des For-schungszentrums Jülich Jül-4257, November, 2007.

3) J. Waksman, Neutral Beam Heating of a Reversed Field Pinch in the Madison Symmetric Torus, University of Wisconsin, 2013.

4) M.H. Hughes and D.E. Post, J. Comput. Phys. **28**, 43 (1978).

5) B. Lehnert, Nucl. Fusion **8**, 173 (1968).

6) B. Hudson, Fast Ion Confinement in the Reversed Field Pinch, University of Wisconsin, 2006.

7) A. Matsuyama, B. Pégourié, R. Sakamoto, J.S. Mishra, G. Motojima, and H. Yamada, Plasma Phys. Control. Fusion **54**, 035007 (2012).

8) P.B. Parks, R.J. Turnbull, and C.A. Foster, Nucl. Fusion **17**, 539 (1977).

9) J. Crank and P. Nicolson, Math. Proc. Cambridge Philos. Soc. **43**,50 (1947).

10) R. J. Goldston, D. C. McCune, H. H. Towner, S. L. Davis, R. J. Hawryluk, and G. L. Schmidt, J. Comput. Phys. **43**, 61 (1981).

CHAPTER 6

Exploratory Experiments

6.1 What are Exploratory Experiments?

In this chapter we will highlight some of the experimental results which were more exploratory in nature, as opposed to the more focused and in depth nature of the density limit and high β experiments. Essentially, these are interesting results which for some reason or another did not necessarily merit further study, but may prove useful for future experiments with pellet fueling or otherwise. They serve to highlight some of the observations from some regimes which have not been explored fully with respect to pellet fueling as well as note some additional pellet capabilities.

6.2 Pellet Fueled SHAx Discharges

6.2.1 Introduction and Motivation

As discussed previously in Chapter 1, QSH/SHAx discharges appear to have improved particle confinement inside the helical structure which annihilates the original magnetic axis. A primary question is whether or not direct pellet fueling of this structure can take advantage of this improved confinement. In many ways, the SHAx regime shares a lot in common with PPCD. Both display a reduction in the secondary mode activity in both the edge and the core (save the innermost resonant mode in SHAx) and both appear to be limited to densities less than $1*10^{19}$ m^{-3} with edge fueling alone. Edge fueling of improved confinement tends to destabilize the m=0 modes, which ultimately degrades confinement. The low density restriction makes the SHAx discharges another attractive target for pellet fueling experiments. The main goal of experiments was be to fuel directly into the helical core structure as shown in figure 6.1. Unfortunately, the unpredictable nature of the locking location of the mode structure left much to chance. Over 100 shots were obtained over several days where pellets were fired into discharges set up to promote the growth of the n=5 mode into a QSH/SHAX state. These experiments were done before the upgrade to 4.0 mm diameter pellets. Pellet diameters of 1.0, 1.6, and 2.0 mm were utilized, with a focus on the smaller pellets for the majority of experiments. Unless otherwise noted, pellets arrived within the same 2 ms time window around 25 ms, when the n=5 dominant mode is often saturated.

6.2.2 Pellet interaction with n=5 mode

The observations during these experiments can be separated into two general categories as follows: injection into a saturated dominant mode and injection into an unsaturated dominant mode. Indeed there are several cases where injection into a QSH/SHAx plasma immediately disrupts the dominant mode as shown in figure 6.2. The relaxation of the dominant mode coincides with the observed density increase and appears to be caused by the perturbation of the ablating pellet. In other cases, the mode amplitude can survive for several ms after pellet fueling as shown in figure 6.3. The FIR system was set up for differential interferometry [1] and measured local density gradients in the time after pellet fueling, until the relaxation event. A look at the line integrated density profile in figure 6.4 shows that the density profile has an asymmetry that persists until the mode relaxes. This is similar to the trends of density profiles in pellet fueled PPCD discharges where the pellet fueled profile persists until the end of the improved confinement. There appears to be little correlation between the locking location and the plasma response. It is clear that the pellet fueling ultimately results in an early relaxation of the dominant mode, although subsequent regrowth of the mode is also observed.

For the cases where the pellet is injected into a plasma with an unsaturated n=5 mode, the pellet appears to trigger activity across all modes with the end result being a stimulation of the n=5 into full saturation, shown in figure 6.5. Often, a malformed or shattered pellet, ablating in the edge, will cause enough of a perturbation to trigger this mode growth. While no clear understanding of the mechanism was obtained, the impact was highly reproducible with a variety of injected pellets.

6.2.3 Pellet injection before mode growth

Since the SHAx regime shares many similarities with the PPCD improved confinement regime, experiments with early pellet fueling were also done to achieve QSH/SHAx discharges at higher density. A scan of pellet injection time revealed some benefit to pellet fueling early in the discharge with a few examples of pellet fueling early in the discharge leading to high density QSH/SHAX discharges shown in figure 6.6. These experiments used larger 2.0 mm pellets to achieve a density several times normal QSH/SHAx discharges. While density is higher immediately after pellet fueling, it decays as the mode grows at an almost constant rate. The density at the relaxation event is still higher than that of the highest density SHAx discharges obtained without pellet fueling.

6.2.4 Discussion and Future Work

While these results are interesting, there is yet little explanation for the observations. Why does the pellet perturbation consistently trigger growth of the dominant mode? Why do some pellet fueled shots immediately trigger a plasma relaxation while others persist for only a few ms and other still seem unaffected by the pellet perturbation?

At the time, the lack of reproducibility in both the pellets as well as the locking location of the n=5 mode made these experiments a bit unwieldy. Some recent QSH/SHAx experiments have been successful at controlling the locking location of the dominant mode. Additionally, the injector is working more reliably since the 4.0 mm upgrade. This makes a return to pellet fueled QSH/SHAx experiments an attractive prospect.

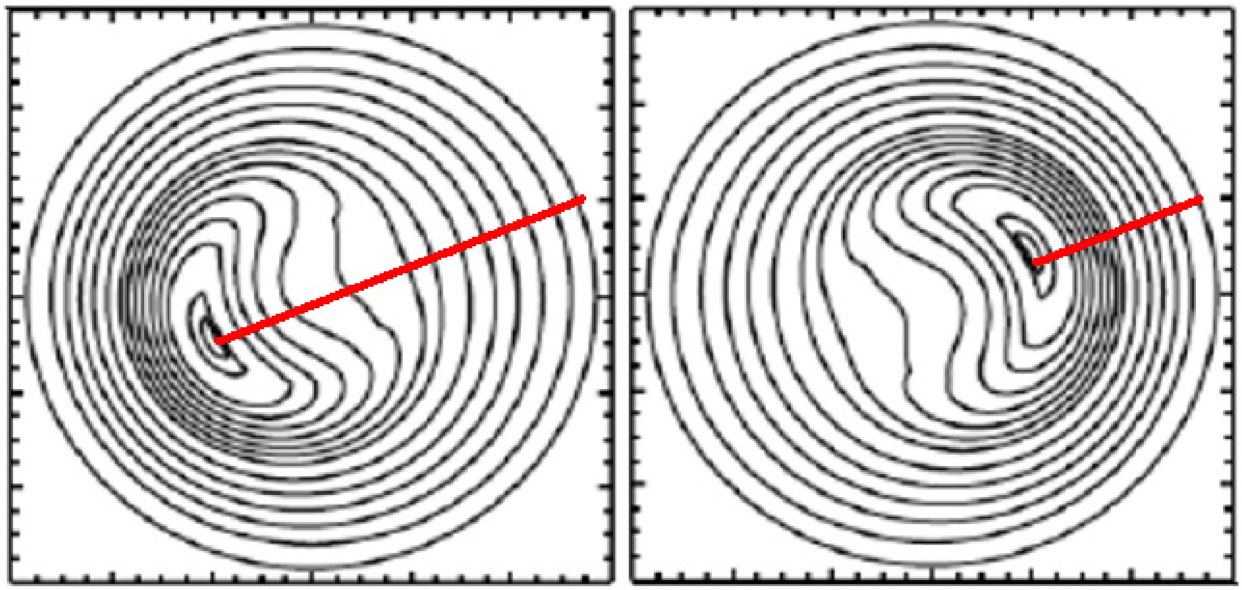

Figure 6.1: Cartoon of the optimal injection scenarios for fueling directly into the helical mode structure in a SHAx discharge.

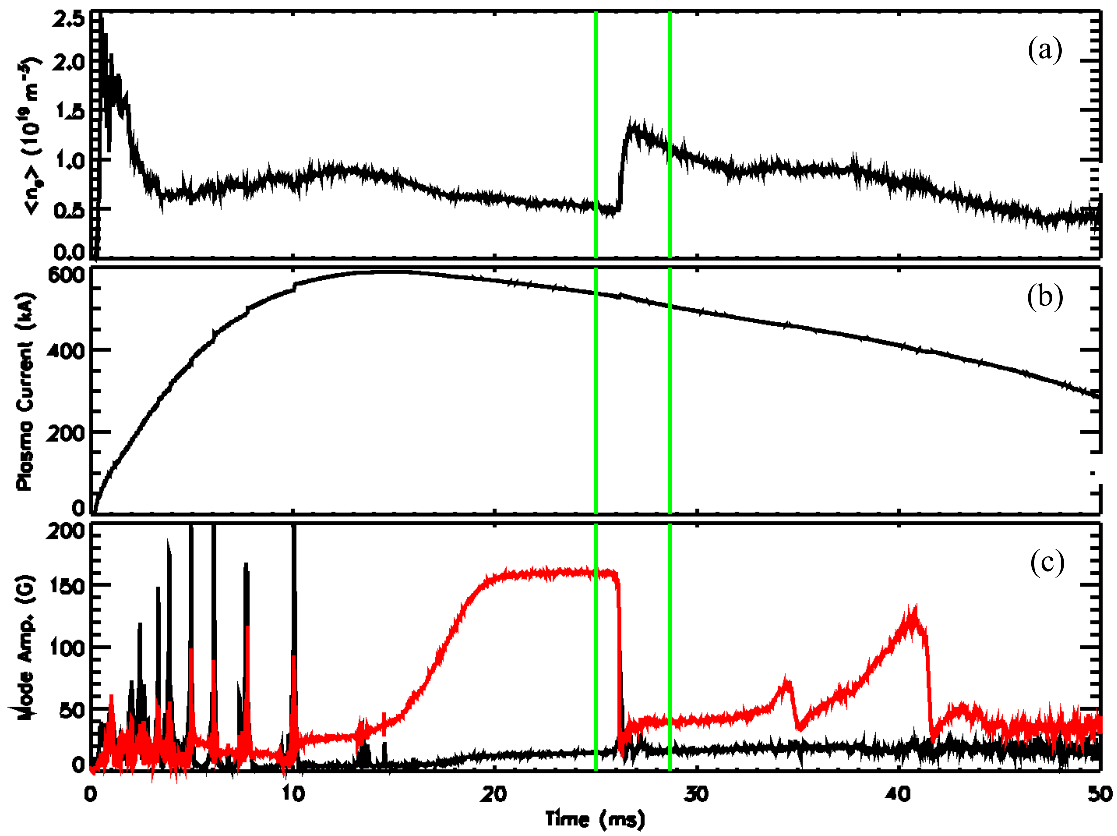

Figure 6.2: Plotted are (a) $\langle n_e \rangle$, (b) the plasma current and (c), the dominant mode (red) and the RMS value of the secondary modes (black) for a case where the dominant mode relaxes during the pellet ablation. The approximate pellet ablation duration is highlighted by vertical green lines. [Shot 1110502033]

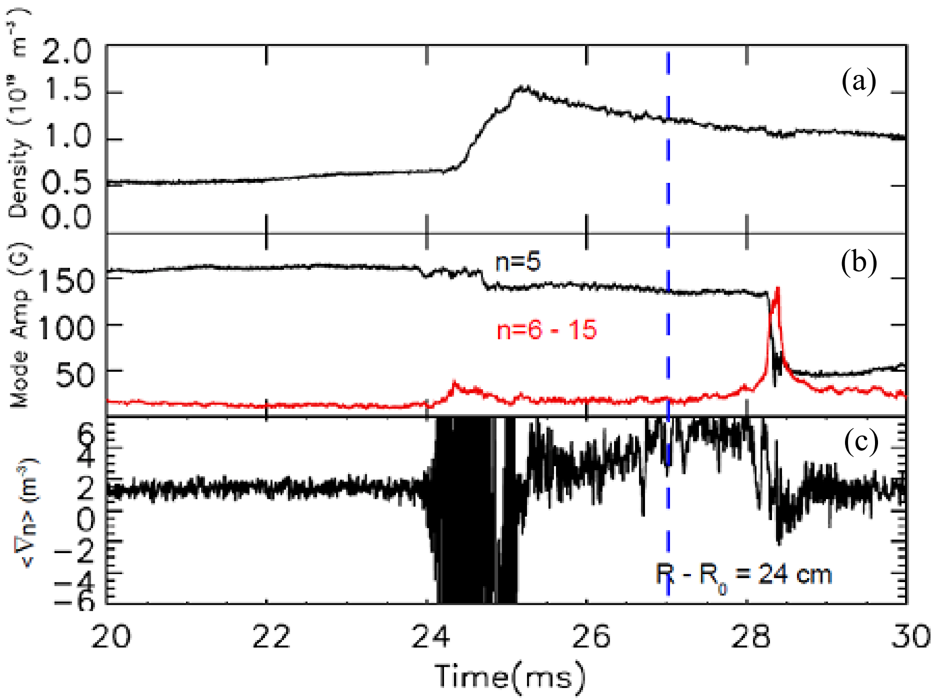

Figure 6.3: An example of a discharge where the dominant mode remains large after pellet fueling. Plotted signals are (a) $\langle n_e \rangle$, (b) the dominant mode (black) and the RMS value of the secondary modes (red) and (c) local density gradient for the FIR chord with impact parameter 24 cm. The density remains high and a locally enhanced density gradient persists until the dominant mode relaxes.

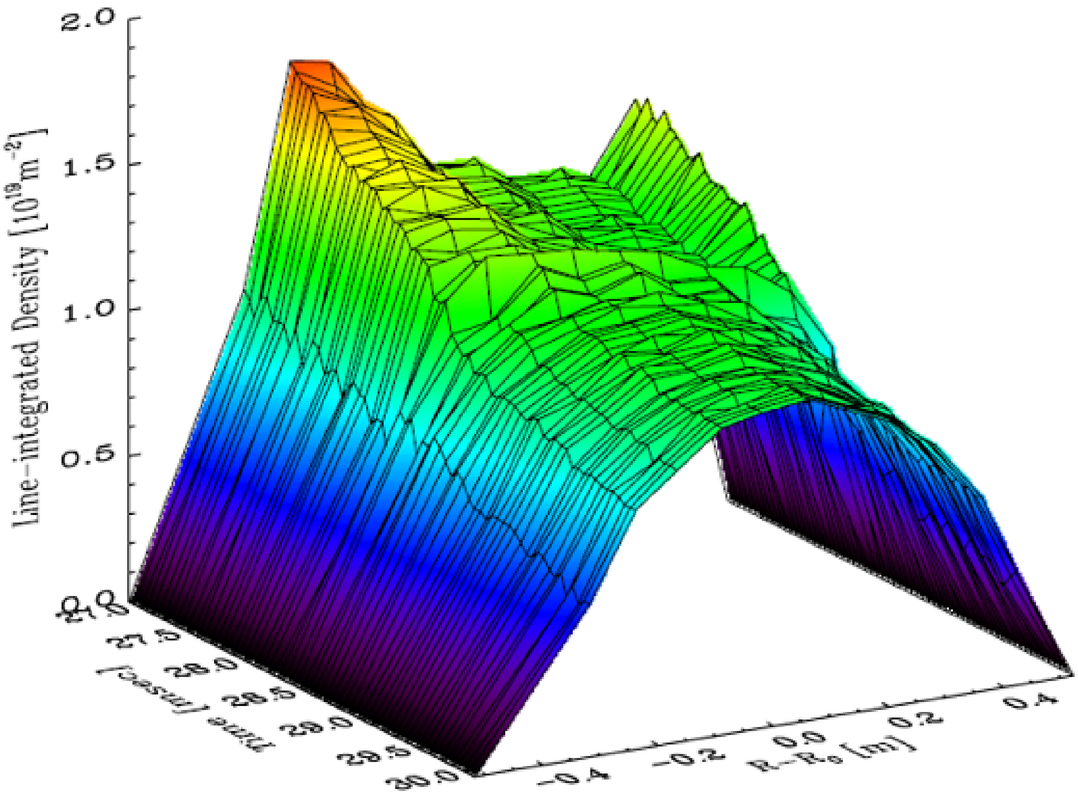

Figure 6.4: The line integrated density profile as measured by the FIR system for the period after the dashed line in figure 6.3. The asymmetry in the profile persists until the relaxation event at 28.5 ms. A standard density profile is subsequently observed.

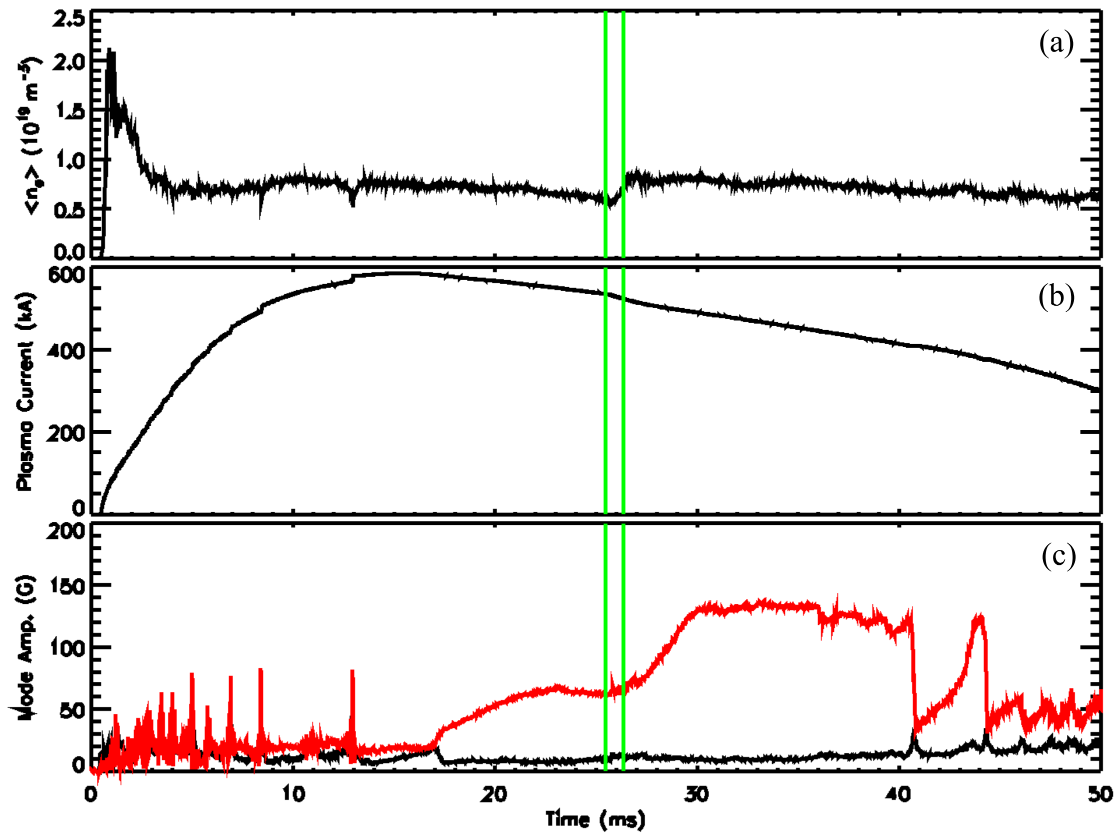

Figure 6.5: Plotted are (a) $\langle n_e \rangle$, (b) the plasma current and (c), the dominant mode (red) and the RMS value of the secondary modes (black) for a case where the dominant mode grows large immediately following the injection of a small pellet which ablates in the edge. The approximate pellet ablation duration is highlighted by vertical green lines. [Shot 1110412039]

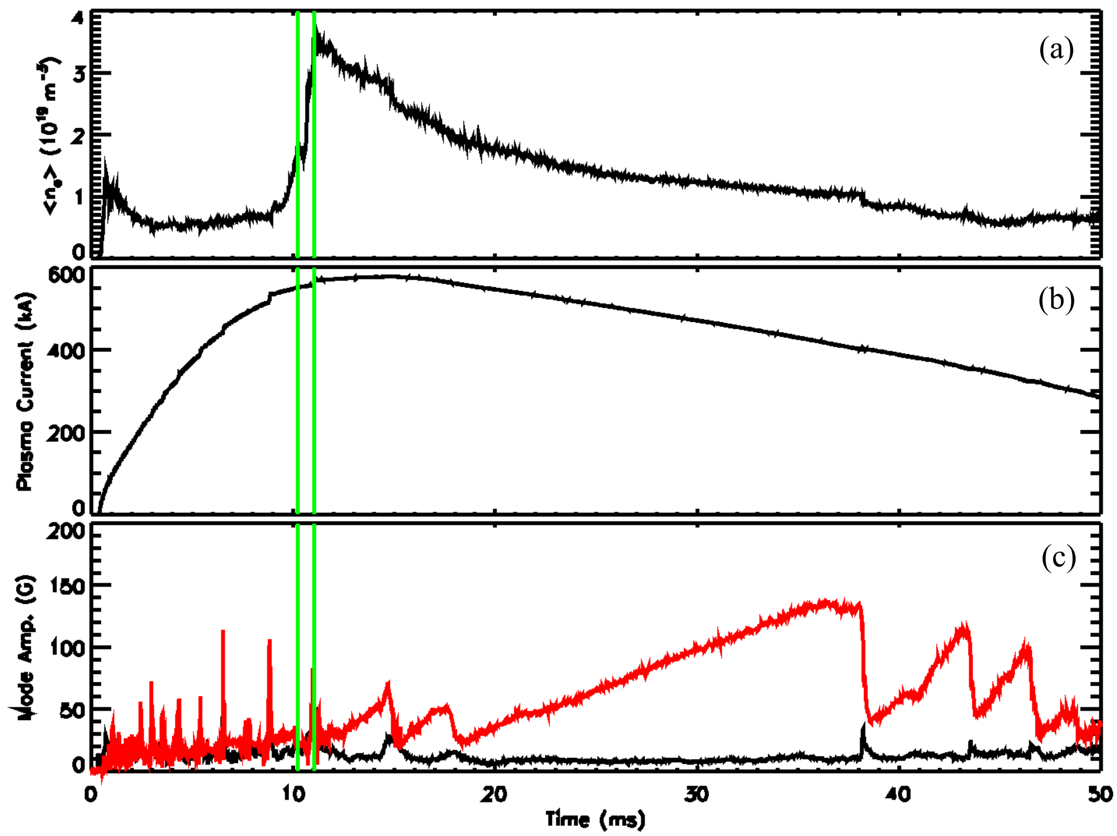

Figure 6.6: Plotted are (a) $\langle n_e \rangle$, (b) the plasma current and (c), the dominant mode (red) and the RMS value of the secondary modes (black) for a case early pellet fueling leads to a discharge with growth of the dominant mode to high value with a higher than normal density. The approximate pellet ablation duration is highlighted by vertical green lines. [Shot 1110503113]

6.3 Methane Pellet Injection

As opposed to the exploration of a new plasma regime, this section highlights the modifications made to the injector after a request was made to utilize an alternative fuel (methane/CH_4) for impurity carbon transport studies. Reprinted from Reference 2.

6.3.1 Abstract

On the Madison Symmetric Torus magnetic fusion plasma experiment, frozen pellet injection is an established method of depositing deuterium fuel into the core of the plasma. To freeze deuterium gas into pellets, the injector is cooled to 10 K with a cryogenic helium refrigerator. To exhaust residual frozen deuterium following injection of each pellet, the injector is warmed by resistive heating to > 18.7 K, the triple point of deuterium. Motivated by the desire to inject carbon-containing pellets, the injector was modified to allow the freezing and injection of methane. The triple point of methane, 90.7 K, is well beyond the capability of the resistive heating hardware. To supplement the resistive heating, a small, steady flow of room-temperature helium was introduced as a heat source. The flow rate was optimized to provide minimum and maximum injector temperatures of 24 K and 95 K, respectively, sufficient for methane pellet formation and exhaust. The flow rate can easily be optimized for other gases as well.

6.3.2 Introduction

Frozen pellet injection is a well established method of fueling the core of magnetically confined plasmas. [3, 4] On the Madison Symmetric Torus (MST) [5] deuterium pellet injection has led to as much as an eight-fold increase in the plasma density. To freeze deuterium gas into pellets, the injector is cooled to 10 K with a cryogenic helium refrigerator (Leybold Coolpower 130). Pellets are then launched with either a burst of high-pressure hydrogen gas or a solenoid-driven mechanical punch. Following the injection of each pellet, the injector must be heated to > 18.7 K, the triple point of deuterium. This allows residual frozen deuterium to be removed from the injector, a step critical to the successful formation and injection of subsequent pellets. This heating is provided resistively, temporarily overcoming the constant cooling provided by the cryogenic refrigerator.

Motivated by the desire to inject carbon into the core of MST plasmas, the capability to freeze and inject methane (CH_4) pellets was developed. Given the higher triple point of methane, 90.7 K, the operational temperature range of the injector had to be increased substantially. Without substantial modification, the existing resistive heating mechanism was unable to provide the needed temperature increase. Hence, as a simple alternative, a small, steady flow of room-temperature helium gas was introduced. When used in combination with the resistive heater, the helium provides an additional source of heat, and the helium flow rate was adjusted to raise the peak obtainable temperature to > 95 K. Without the resistive heating, the base temperature of the injector increases to 24 K, still sufficient to allow formation of frozen methane pellets. While the helium flow rate was optimized in this case for methane pellet formation, the flow rate can easily be adjusted for other target gases and triple points. In what follows, we describe in more detail the means by which deuterium pellets are formed, and we describe the means by which residual pellet material is removed after each pellet is injected. We then discuss the instrumental modification required for methane pellets, and we show an example of carbon deposition in the plasma core due to methane pellet injection.

6.3.3 Pellet Injection

The pellet injector on MST utilizes the pipe gun technique, wherein pellets are formed inside cryogenically cooled barrels and then launched with a mechanical punch or burst of high pressure hydrogen gas at 1200 psi (8.3 MPa). [6] To allow the barrels to reach a very low temperature, the barrels are housed inside a small vacuum chamber, referred to as the gun box. A schematic of the gun box for MST's pellet injector is shown in Fig. 6.7. Two of the stainless-steel injector barrels are shown. Each barrel is connected to a copper block assembly that is in turn attached to the cold head of the cryogenic refrigerator. The refrigerator runs continuously, providing a steady cooling power of ~15 W for operation at low temperature. Attached to one side of the gun box is a small (60 L/s) turbo-molecular pump, which under normal operation sustains a pressure less than 1 mTorr (0.13 Pa). The vacuum provided by this pump minimizes convective and conductive heat transfer between the room-temperature gun box and the barrels, and prevents the condensation of atmospheric gases on the super-cooled surfaces.

6.3.3.1 Deuterium Pellets

To form deuterium pellets, deuterium gas is slowly introduced to the barrels, and the gas freezes in the small region where the cooled copper block is connected to the barrels. The size of the freezing zone is determined by the placement of metal braid heat shorts connected to the room temperature gun box chamber. The 10 K freezing zone is a result of the equilibrium between the refrigerator cooling and the small ambient heat provided to the thermal load via radiation and conduction from the gun box chamber. After formation, the pellets are then propelled through the barrels toward the MST experiment. Once the pellets have been expelled, the barrels are cleared of any remaining frozen deuterium by pumping simultaneously on one end of the barrels and resistively heating them above the triple point of deuterium. Comprised simply of a 25 Ω resistance attached to the copper block, the resistive heater provides a heating power of ~ 23 W and is capable of increasing the barrel temperature to a maximum < 40 K, as shown in the < 1 mTorr case of Fig. 6.8(a), which illustrates the temporal evolution of the barrel temperature during heating.

The complex details of the dynamic thermal equilibrium in the gun box are beyond the scope of this paper, as a detailed understanding would require significant diagnostic improvements, e.g., an array of internal temperature measurements; however, some commentary is possible. The specific heat of copper increases with temperature, which results in a decrease in the rate at which the temperature increases; however, this does not explain asymptotic behavior of the temperature in Fig. 6.8(a). In order to achieve a temperature maximum as shown, the net heating power to the copper must also vary with the temperature, ultimately approaching equilibrium. Important to this equilibrium are the coupling efficiencies of both the barrel heaters and the cryogenic refrigerator, and all of the mechanisms by which heat can be gained or lost by the copper, including radiation.

6.3.3.2 Methane Pellets

To allow the formation and launch of multiple, successive methane pellets, the barrel temperature needs to be raised to > 90.7 K following each pellet launch, significantly above the temperature required for deuterium pellets. This proved to be beyond the present capability of the resistive-heating hardware. Hence a small, steady flow of room-temperature, high-purity helium was introduced into the gun box through an adjustable needle valve (Nupro/Swagelok SS-4BMG-VCR), illustrated in Fig. 6.7. The pressure upstream of the needle valve was maintained at 50 psi (345 kPa). Utilization of high-purity helium prevents contamination of the gun box by trace impurity gases, and helium will not freeze on the super-cooled injector surfaces. The impact of different helium flow rates on the injector's base temperature is illustrated in Fig. 6.8(a). The gun box pressure, measured with a convectron gauge near the helium inlet port (Fig. 6.7), is used as a rough proxy for the helium flow rate. Prior to t = 0 in Fig. 6.8(a), the time at which the barrel heater is activated, the barrel temperature reflects the change in the thermal equilibrium provided by the added helium flow. As the gun box pressure increases to 30 mTorr (4.0 Pa), the base temperature rises from 10 K to 24 K, still sufficiently below the triple point of methane for pellet freezing. At low pressure, the mean free path of the helium atoms is comparable to the dimensions of the gunbox (~0.1 m). In this low collisionality regime, the heat transferred to the copper block assembly is proportional to the pressure and the temperature difference between the copper block assembly and the gunbox walls. [7] The primary source of heat is room temperature helium atoms impacting the copper directly. As pressure increases, the mean free path decreases and a more collisional regime is approached where the heating power is governed by the thermal conductivity of the gas and the temperature difference. After the barrel heater is activated, the barrel temperature increases, approaching a maximum value. By testing a range of pressures, we determined the maximum attainable barrel temperatures. For the low pressures of < 1 mTorr and 13 mTorr, the peak barrel temperature stabilized at values well below the minimum of 90.7 K required for methane pellet exhaust. For the higher pressures of 26 mTorr (3.5 Pa) and 30 mTorr (4.0 Pa), the required 90.7 K was achieved, and the highest pressure yielded the fastest temperature rise. For cryogenic systems other than that described here, the helium flow rate required for a given elevated temperature may differ depending on specifics such as chamber pumping speed and volume, and the detailed balance of cooling and heating.

Similar results can be obtained with a static helium fill, but given the finite leak rate of the gun box, the dynamic fill results in a more stable pressure over the course of an MST run day. The continuous pumping also prevents the accumulation of atmospheric impurities in the gun box which would eventually condense on cold surfaces and interfere with injector operation. Furthermore, the dynamically achieved pressure can be controlled with a single knob and can be adjusted higher or lower at will. Adjustment to a higher pressure with a static fill would be simple, of course, but any subsequent reduction in pressure would require pumpout.

The barrel temperature range for which methane pellets form reliably is 70 - 75 K. Hence, for the injection of successive methane pellets, the injector temperature must cycle from < 75 K to > 90.7 K. Starting with the data from Fig. 6.8(a), the optimal operating helium pressure was chosen to minimize the overall temperature cycle time. The temporal evolution of the barrel temperature during a pellet injection cycle is shown in Fig. 6.8(b) for the two highest pressures in Fig. 6.8(a). The time evolution starts immediately after pellet residue is exhausted at high temperature. While barrel cooling requires less time at 26 mTorr (3.5 Pa), barrel reheating requires a substantially longer time. By choosing a helium pressure of 30 mTorr (4.0 Pa), the total cycle time is decreased while maintaining an acceptable load on the turbo-molecular pump, as reflected by the drawn current.

6.3.4 Carbon Deposition

Methane pellets were injected into MST plasmas with a toroidal plasma current of 400 kA, a central line-averaged electron density of 0.8 x 10^{19} m^{-3}, and a central electron temperature of 1 keV. Just before each pellet is injected, inductive current profile control [8, 9] is applied to reduce magnetic fluctuations and the rate of transport of particles and energy. Methane pellets provide a means of probing impurity particle transport in these plasmas. The temporal evolution of the carbon density following injection of a methane pellet is shown in Fig. 6.9 This specific pellet had a diameter of 1.0 mm and a length of about 1.5 mm and was injected shortly after 10 ms, propelled by a burst of high-pressure hydrogen gas. The resultant pellet speed was about 150 m/s, significantly slower than the typical deuterium pellet speed of 1200 m/s. This decrease in pellet speed is due to the higher mass density of the methane pellets. This speed is also significantly lower than that predicted by ideal gun theory.[3] Nevertheless, this speed was sufficient for the methane pellet to penetrate to the plasma core, resulting in a 12-fold increase in the central carbon density, measured with charge-exchange-recombination spectroscopy.[10] This increase is with respect to the background concentration of carbon that is present in all MST plasmas due to partial coverage of the plasma-facing wall with graphite tiles. The methane pellet in Fig. 6.9 is completely ablated by 14 ms. Thereafter, the central carbon density decays.

6.3.5 Summary

The addition of a steady flow of room-temperature helium allows operation of MST's pellet injector at an elevated temperature range suitable for the formation and injection of methane pellets. The flow rate can easily be adjusted to accommodate other pellet gases as well.

6.3.6 Additional Commentary

Further study of impurity transport is found in [11]. A comparison of methane and deuterium pellet fueling is shown in figure 6.10. Here we observe impact on the IMA measurements of CIII and CV for pellets of comparable size, as determined by the increase in density with pellet fueling. The increase in IMA signal is largely due to the increased carbon content, while the cooling of the plasma also plays a role in the shift in IMA signal.

6.3.6.1 Devising a Model to Explain Methane Pellet Modification

The purpose of this section is to provide a more in depth explanation of the impact of the helium flow modification on the pellet formation process. The general idea is that we have a steady source of barrel cooling provided by the cryogenic refrigerator. This particular refrigerator model (Coolpak 130) is rated for ~15 W at a temperature of 20K. To heat the barrels, a resistive heater is used. This heater consists of a 25 Ohm resistance which makes good thermal contact with the copper block located just below the coldhead as depicted in figure 6.7. This copper block is directly connected to the cooling zones on the barrels where it is clamped down on the copper discs brazed onto the barrels themselves. With a 24 V output, this means the heater can nominally provide ~23 W of heating power. The coupling efficiency of both the heating and cooling is unknown at this point without further study and direct internal measurements. We do know the resistive heating is larger than the cooling power, to what degree is not clear. Also unknown is the temperature dependence of both the heating and cooling power.

To reach higher temperatures, we augmented the resistive heating with a flow of room temperature helium into the gunbox volume. The idea was to provide a source of heat via room temperature helium atoms colliding with the copper block/barrel formation zone. In practice, this method was effective at raising both the baseline (no heaters) and maximum operating temperatures as shown in figure 6.8.

It was understood that the helium flow modification was providing substantial heat to the copper barrel contacts, but the mechanisms were not well understood initially. We start with a look at the mean free path of the helium gas inside the gunbox volume obtained from [7].

$$l = \frac{1}{\sqrt{2}\rho\sigma} \tag{6.1}$$

where ρ, the number density, and σ, the atomic cross section, are given by

$$\rho = \frac{N}{V}; \sigma = 4\pi r^2 \tag{6.2}$$

with R, the atomic radius of helium. If we make use of the ideal gas law, we obtain

$$l = \frac{kT}{4\sqrt{2}\pi R^2 P} \tag{6.3}$$

Using T = 298 K (room temperature), R = 140 pm (Van der Wahls radius) and P = 1-30 mTorr, these values give us a mean free path of .3 and 8.9 cm for pressures of 30 and 1 mTorr respectively. The dimensions of the gunbox are ~30 by 30 by 30 cm with the copper cooling zone located in the center of the chamber. So it appears we are in a region of transition where the mean free path is ~ L (the geometric space scale) and going to a region where l << L. Let us begin by investigating the case where l << L. In this case, the helium is effectively collisionless.

More often than not, the atoms will collide with the gunbox wall or the copper block before it will collide with another helium atom. We can estimate a collision frequency with the copper using

$$\upsilon = n v_{He} A_{Cu} \tag{6.4}$$

where

$$n = \frac{N}{V} = \frac{P}{kT}; v_{He} = \sqrt{\frac{8kT}{\pi m}} \tag{6.5}$$

With this collision rate, and assuming elastic collisions with the copper,

$$q = \frac{3}{2} A_{Cu} P \sqrt{\frac{8kT}{\pi m}} \left(1 - \frac{T_f}{T_i}\right) \tag{6.6}$$

$$q = \nu \Delta E = \frac{3}{2} \nu k \Delta T \tag{6.7}$$

Now again, our pressure P ranges from 1 to 30 mTorr. The temperatures will be 298 K and 10 K for the initial and final temperatures of our helium atoms. The area of the copper is ~0.01 m^2. This leads to an estimated heating power of 2.4 W up to 72.8 W for pressures of 1 to 30 mTorr respectively. The lower bound is somewhat reasonable, but the upper bound is a bit unrealistic when considering our observations. At these pressures, we don't expect our assumptions above to hold, so we'll take a look at the collisional case.

Next let us look at a simplified case as we transition to a regime where collisions become more important. In this case a temperature gradient will form from the gunbox wall to the copper formation zone. Heat will flow depending on the thermal conductivity of the transition material, helium in this case. For a very simple 1-d case with a constant temperature gradient between two points with a temperature difference ΔT, the heat flow will be

$$q = -k\frac{dT}{dr} \tag{6.8}$$

which, if we assume a constant gradient will be

$$q = -k\frac{\Delta T}{\Delta r} \tag{6.9}$$

with ΔT ranging from 200 to 288 K and Δr = 0.15 m. For estimation of heat flow for our case, we use a value of 0.142 W/mK for the thermal conductivity k.

Again we use an area of 0.01 m^2 for the copper freezing assembly. For a 200 K difference, this leads to a heating power of 1.9 W. For 288 K, we estimate 2.73 W. This result is independent of the gunbox pressure only insofar as the thermal conductivity is independent of pressure.

Obviously in practice, the heating provided by the helium is pressure dependent so neither of these models is correct, rather our real case lies somewhere in between these two models.

One key factor in the shape of the temperature curves as the barrels are heated up is the dependence of the specific heat of copper (and other metals) on temperature. As the copper warms up, its specific heat capacity also increases.

One agreement between these two extreme models is that they both depend directly on the temperature difference between the gunbox wall and the copper formation assembly. As the copper assembly warms up, the additional heat provided by the influx of helium flow will decrease. This also works to explain the asymptotic behavior of the temperature as the barrels are heated.

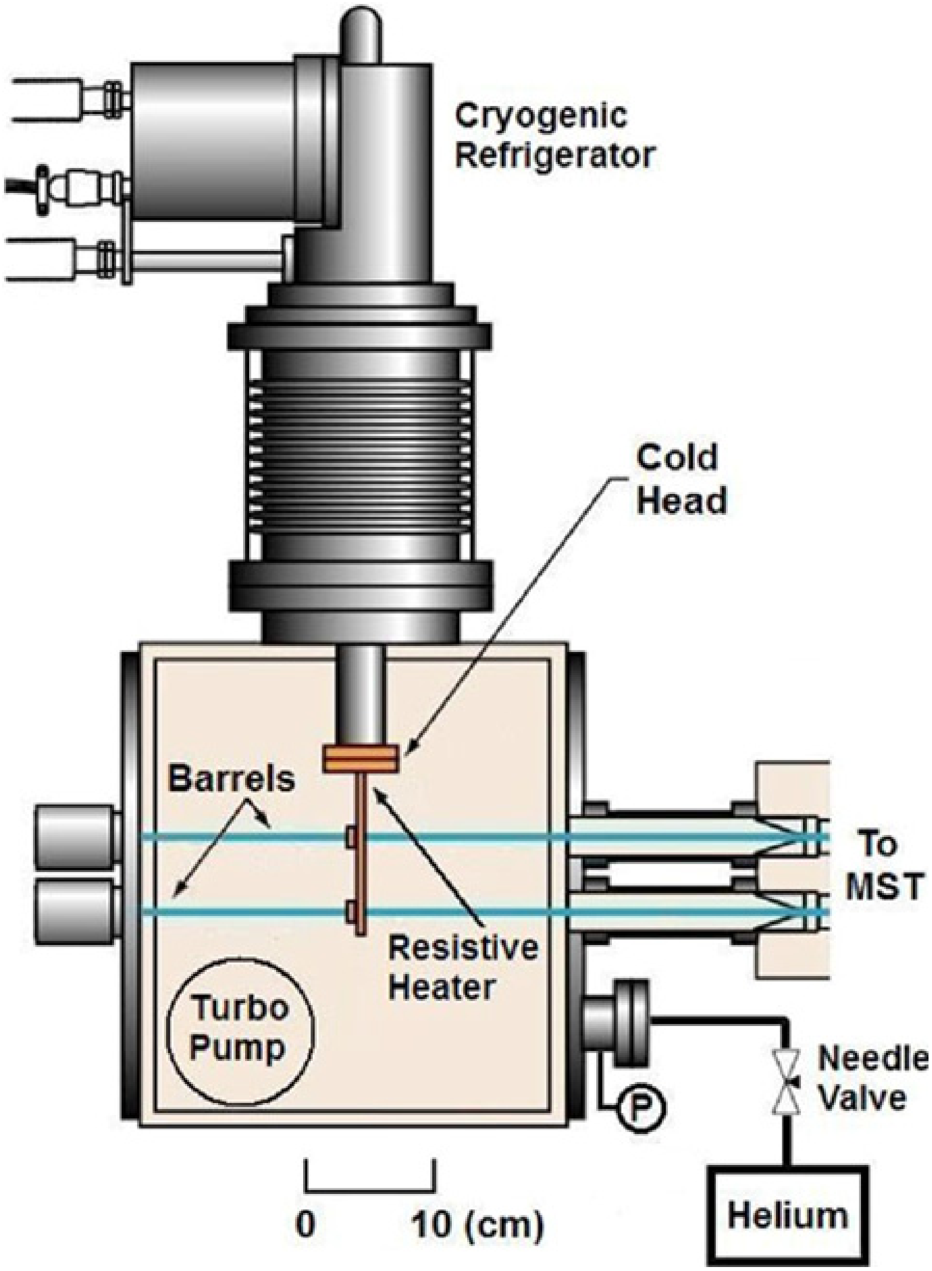

Figure 6.7: Schematic of the pellet injector barrel housing (gun box) including the newly added helium supply and needle valve. Barrel heater wire (not shown) is attached to the copper block which connects the cold head to the barrels. Temperatures are monitored at this block as well as locally on each barrel.

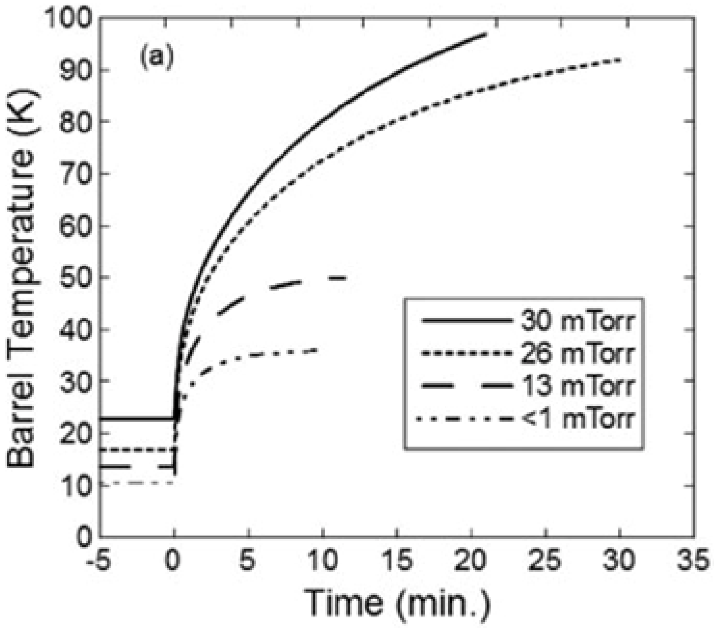

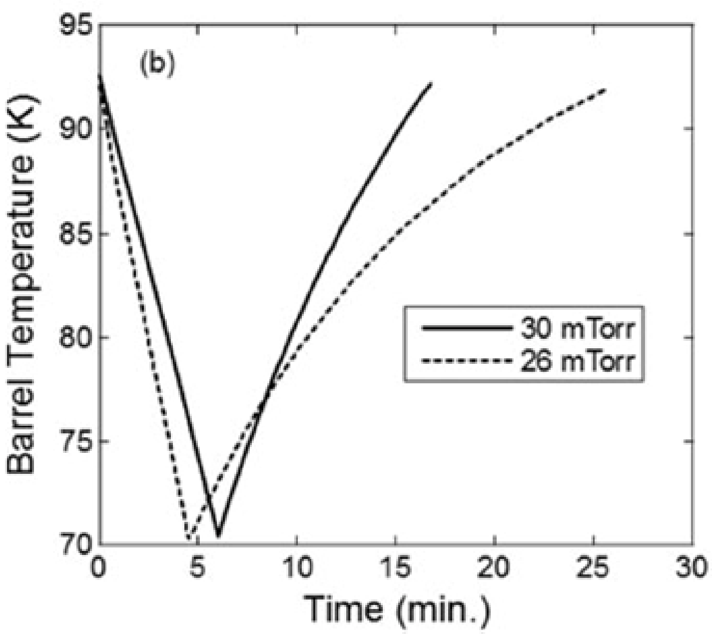

Figure 6.8: (a) Temporal evolution of barrel temperature at various helium pressures before ($t < 0$) and after ($t > 0$) the barrel heaters are activated, (b) during a cycle of pellet formation and exhaust. Pressure < 1 mTorr is below the measurement threshold for the convectron gauge and refers to operation without helium flow, suitable for deuterium pellet formation. Pressures have been re-calibrated for helium.

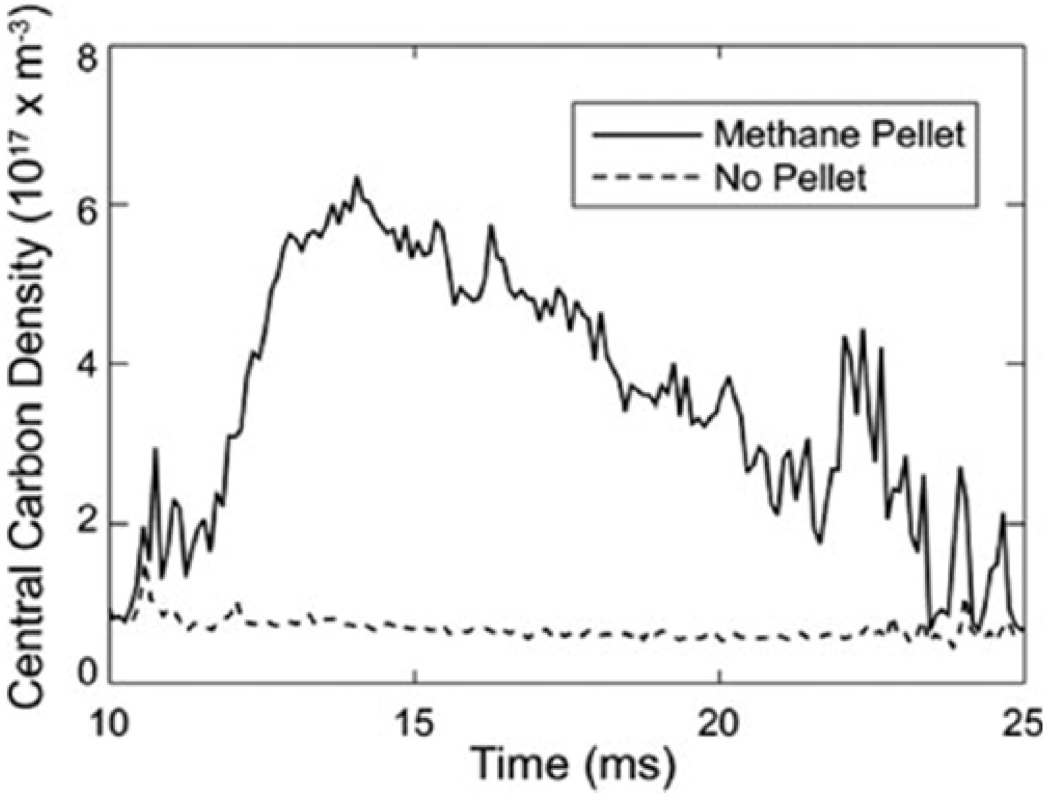

Figure 6.9: Central carbon density with and without methane pellet injection in two otherwise similar discharges. In the pellet-injected case, the pellet arrives in the plasma at about 10 ms.

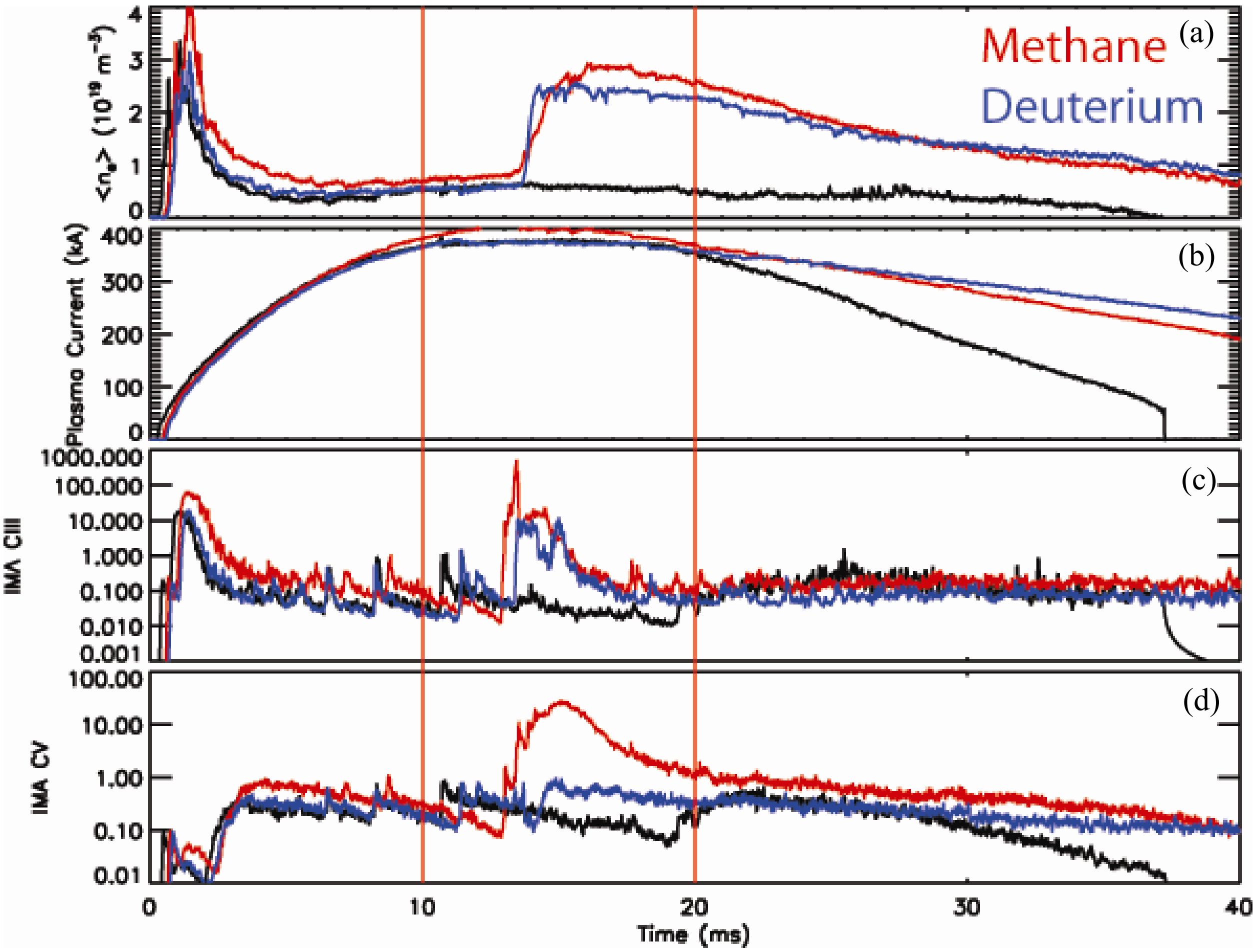

Figure 6.10: (a) $\langle n_e \rangle$, (b) plasma current (c) IMA CIII and (d) IMA C IV measurements comparing a discharge fueled with a methane pellet (red) to one fueled with a deuterium pellet (blue). A no pellet discharge is shown in black for comparison. [Shots 1100802030 (black), 1100726094 (red), 1100802030 (blue)]

6.4 Startup Fueling with Pellets

6.4.1 Introduction and Motivation

What is the impact will an ablating pellet have on the plasma startup? The motivation for this experiment was a direct result of the improved control over the pellet speed observed after the injector upgrade and installation of 4.0 mm diameter pellet barrels (Discussed in chapter 2). The control over velocity included the ability to launch extremely slow pellets with v < 100 m/s. The MST vacuum vessel is 1 m across, so a pellet with a velocity of ~100 m/s will take ~10 ms to cross the plasma. Since the plasma current ramp up lasts 10-15 ms, some attempts were made to achieve 300 kA F=0 plasmas with a pellet in the vessel at startup. While the large variation in the pellet arrival time made these pellets very unpredictable, some successful discharges were obtained with a slow traveling pellet inside the vessel during start up shown in the CCD camera images compiled in figure 6.11. The pellet is observed immediately after the startup frame and proceeds to cross the plasma and impact the far wall at ~11 ms.

6.4.2 Comparison of startup with and without pellet

Taking a closer look at the operations signals, we can see that the pellet does have an impact on the plasma startup as shown in Figures 6.12 through 6.14. Unfortunately, due to the pellet collision with the inboard wall of the vessel at ~11 ms, the plasma quality subsequently deteriorates. In the first 9 ms or so we can see a slightly slower ramp rate of the current. We also observe evidence of an overall cooler plasma in the IMA signals. The n=6 mode rotation is also observed to be slower and the magnetic activity is changed with overall higher mode amplitudes and more frequent sawtooth events. The density is however a factor of 2 higher than in the comparison case. If there was a means to fuel in this way without impacting the plasma when the pellet hits the far wall, this might be a feasible means of fueling to higher density in MST.

6.4.3 Idealized Startup fueling scenario

The uncertainty in the arrival time of the slow gas propelled pellets is far from the ideal case. One could imagine that a pellet dropper would be far preferable. A pellet dropped from the top of the MST vessel would travel a distance of 1 m to the bottom of the vessel in 0.447 s. One could then vary the drop time of the pellet to vary the position of the pellet in the plasma during startup and assuming the pellet's trajectory is not impacted by the ablation (an untested assumption), then the pellet should ablate fully in the plasma (or at least not impact the wall and disrupt the plasma). More complicated would be to launch a pellet slowly upward such that it reaches its peak height in the plasma core at the time of startup. This could be accomplished with a pellet fired with a speed of 2 m/s straight up from ~10 cm below the vessel. It would reach its peak height ~0.2 s after launch ~0.6 m above its launch point. While not feasible for a longer duration experiment, this could be an interesting high density fueling option for short pulse machines who desire a less perturbative core fueling option.

6.5 Future Work

While revisiting some of the experiments highlighted in this chapter could prove informative, there are a few regimes which have not yet been explored with pellet fueling. The first is known as Enhanced Confinement (EC) period which are obtained in plasmas with a steady but deeper than normal reversal. These plasmas show an improvement in confinement and a decrease in mode activity and are governed by rapid m=0 bursts of small amplitude. Like many other regimes which show significant heating and improved confinement the results tend to be best at low density making it yet another attractive pellet target plasma.

In addition, a recent capability on MST is the programmable power supply (PPS) for the toroidal field system. Some work has been done with this system to look at the effect of different PPCD scenarios which could be a potential regime to further explore with pellet fueling. Another option is to use the PPS to shift the onset of PPCD to better accommodate the optimized ablation for a particular plasma current.

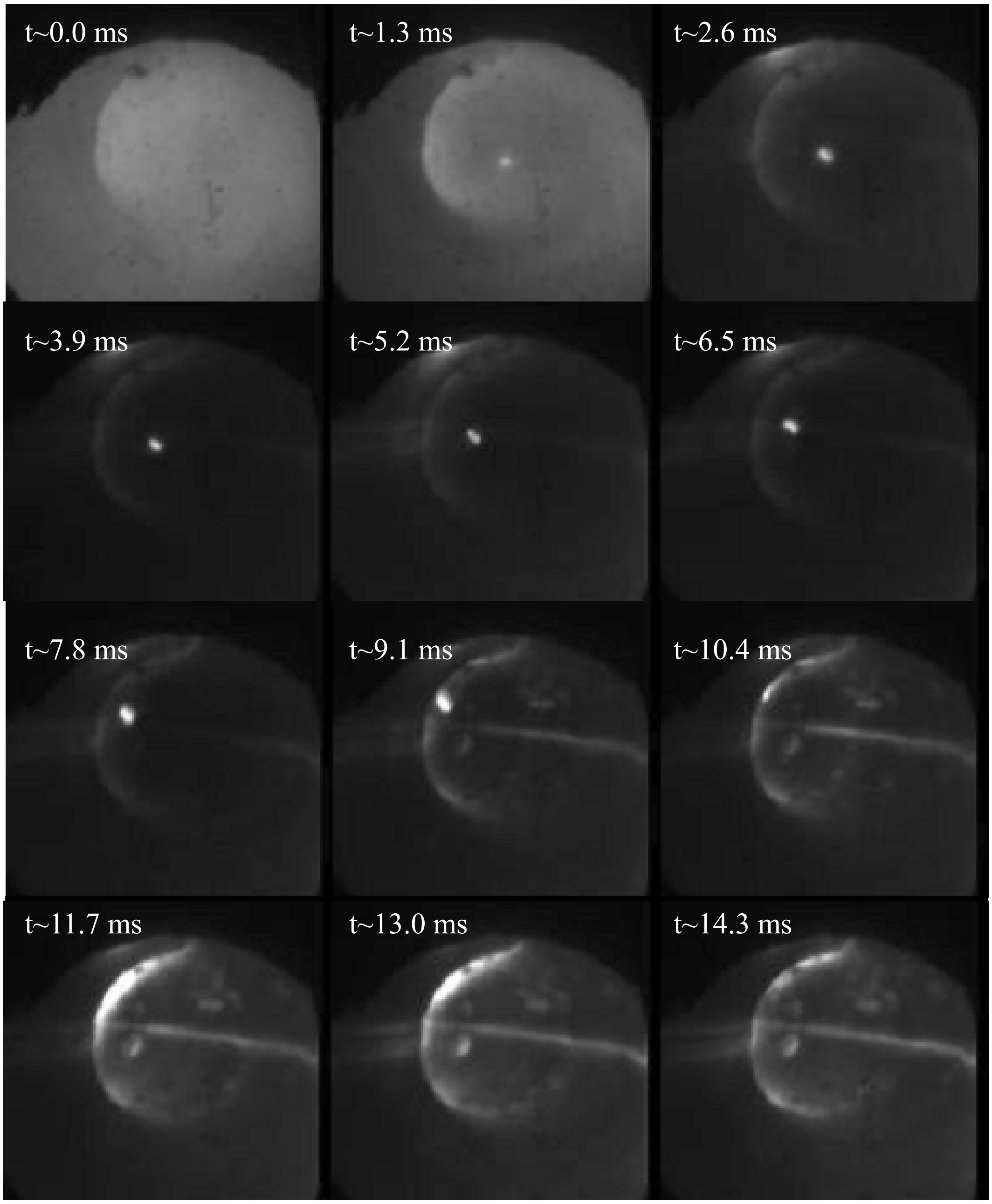

Figure 6.11: A sequence of frames for a discharge where a slow (~ 100 m/s) deuterium pellet was fired such that it is ablating during the plasma startup (plasma start is captured in frame 1 at t~0). Frame rate is ~ 770 Hz. Pellet is observed to hit the wall at ~11 ms.

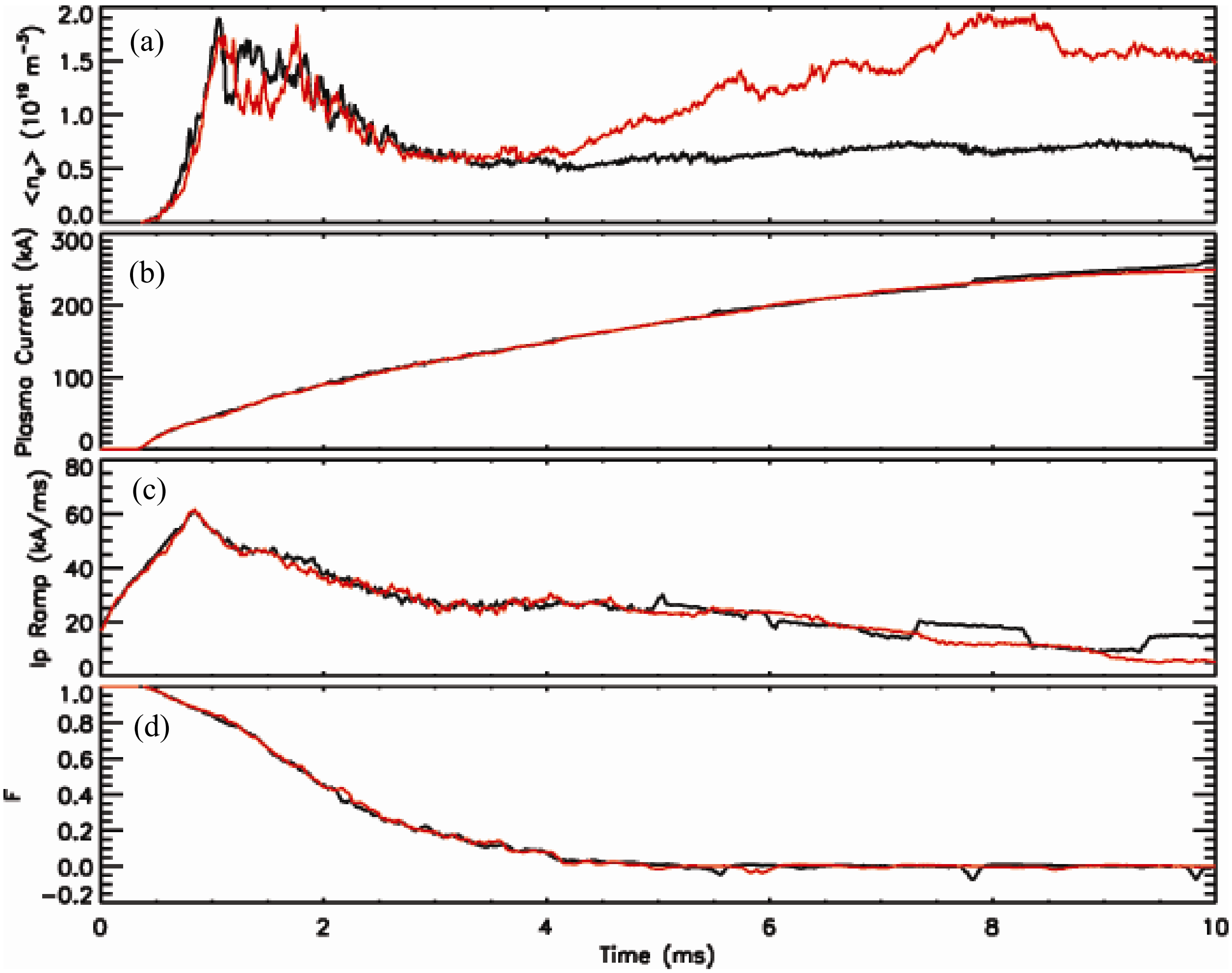

Figure 6.12: (a) $\langle n_e \rangle$, (b) plasma current, (c) dI/dt, and (d) reversal parameter F comparing discharges with (red) and without (black) a pellet ablating during startup. [Shot 1130224138(black), 1130224113(red)]

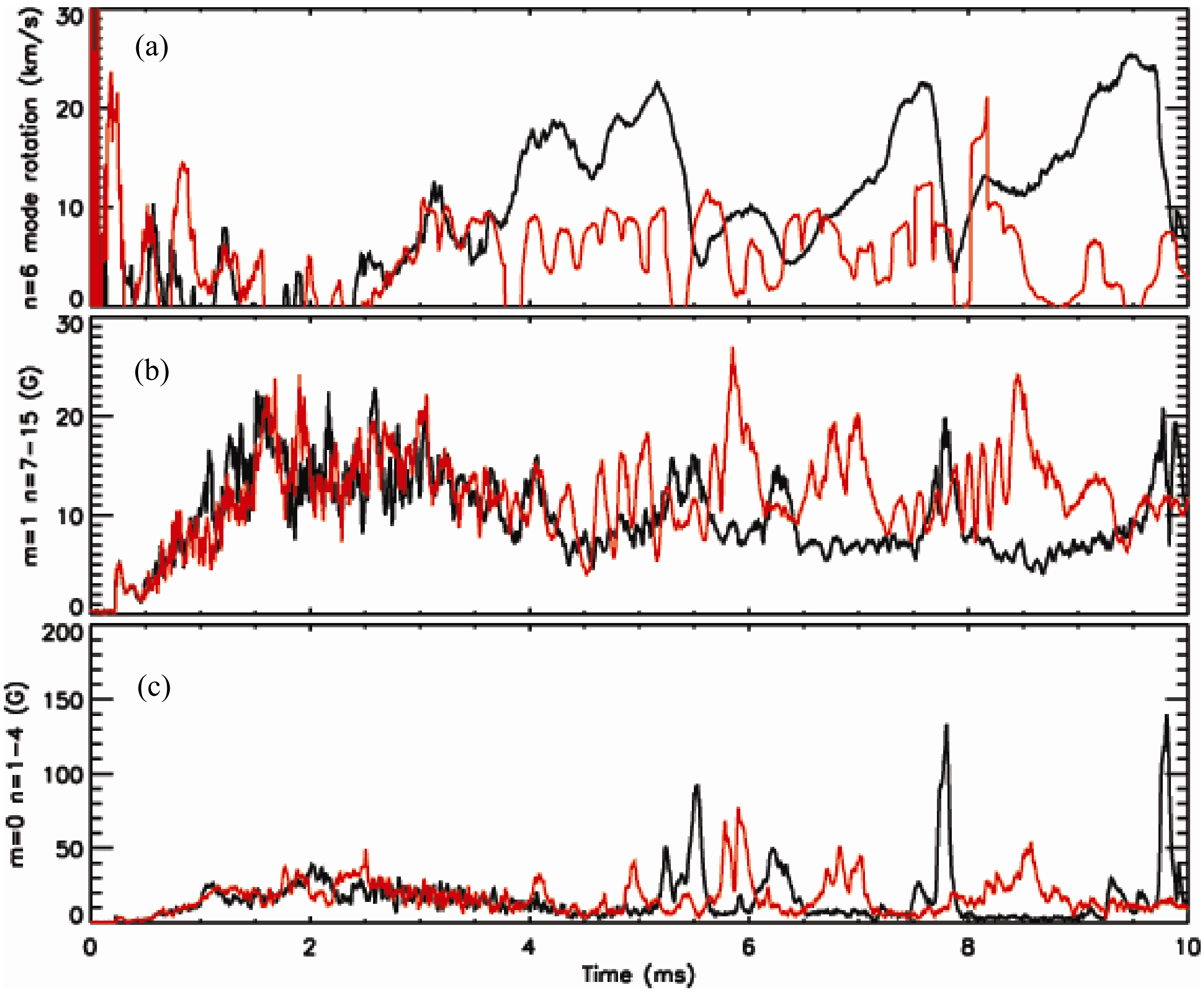

Figure 6.13: (a) n=6 mode rotation velocity, (b) core mode activity, and (c) edge mode activity comparing discharges with (red) and without (black) a pellet ablating during startup. [Shot 1130224138(black), 1130224113(red)]

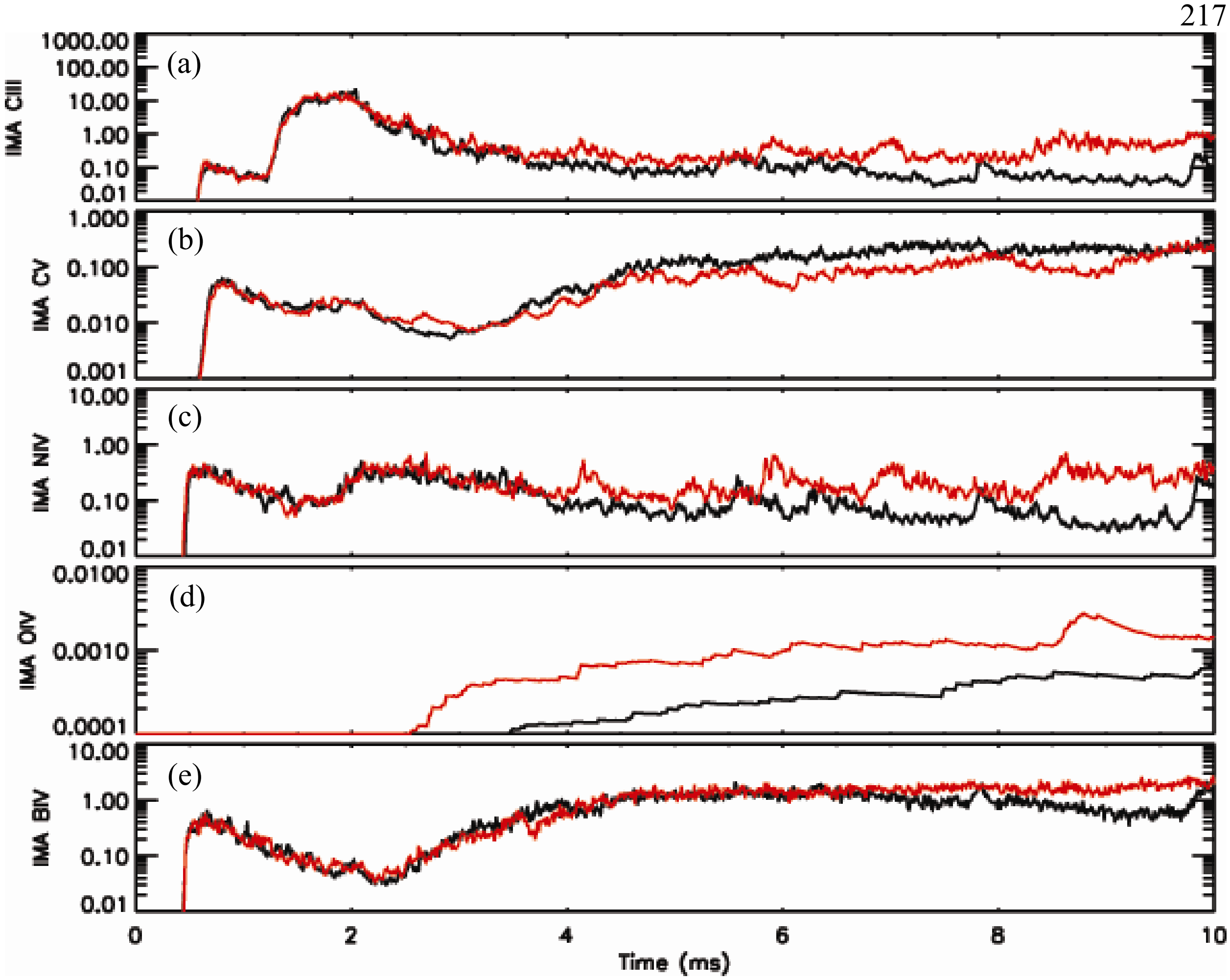

Figure 6.14: IMA radiation measurements for (a) CIII, (b) CV, (c) NIV, (d) OIV, and (e) BIV comparing discharges with (red) and without (black) a pellet ablating during startup. [Shot 1130224138(black), 1130224113(red)]

6.6 References

1) W.X. Ding, D.L. Brower, B.H. Deng, and T. Yates, Rev. Sci. Inst. **77**, 10F105 (2006)

2) K.J. Caspary, B.E. Chapman, S.P. Oliva, and S.T.A. Kumar, Fusion Sci. Technol. **62**, 375–378 (2012).

3) S. Combs, Rev. Sci. Instrum. **1679**, (1993).

4) S.L. Milora, W.A. Houlberg, L.L. Lengyel, and V. Mertens, Nucl. Fusion **35**, 657–754 (1995).

5) R.N. Dexter, D.W. Kerst, T.W. Lovell, S.C. Prager, and J.C. Sprott, Fusion Technol. **19**, 131–139 (1991).

6) S.K. Combs, L.R. Baylor, D.T. Fehling, D.L. Brower, and W.X. Ding, Fusion Sci. Technol. **44**, 513–517 (2003).

7) G.S. Springer and Thomas F. Irvine and James P. Hartnett, in ‘Advances in Heat Transfer’ (Elsevier, 1971), pp. 163–218.

8) J.S. Sarff, S.A. Hokin, H. Ji, S.C. Prager, and C.R. Sovinec, Phys. Rev. Lett. **72**, 3670–3673 (1994).

9) B.E. Chapman, J.K. Anderson, T.M. Biewer, D.L. Brower, S. Castillo, P.K. Chattopadhyay, C.-S. Chiang, D. Craig, D.J. Den Hartog, G. Fiksel, P.W. Fontana, C.B. Forest, S. Gerhardt, A.K. Hansen, D. Holly, Y. Jiang, N.E. Lanier, S.C. Prager, J.C. Reardon, and J.S. Sarff, Phys. Rev. Lett. **87**, 205001 (2001).

10) S.T.A. Kumar, D.J. Den Hartog, R.M. Magee, G. Fiksel, and D. Craig, Plasma Phys. Control. Fusion **53**, 032001 (2011).

11) S.T.A. Kumar, D.J. Den Hartog, K.J. Caspary, R.M. Magee, V. V. Mirnov, B.E. Chapman, D. Craig, G. Fiksel, and J.S. Sarff, Phys. Rev. Lett. **108**, 125006 (2012).

CHAPTER 7

Conclusions and Future Work

7.1 Density Limit Experiments

The model found in Reference 1 associates the onset of the density limit in tokamak plasmas with radiation drive of the m = 2, n = 1 tearing mode near the plasma edge. Effectively caused by the local power balance, the instability grows as the radiated power exceeds the heating power in the island. The scaling of the radiative instability matches that of the Greenwald scaling. The RFX-mod model [2] observes a similar phenomenon involving the m = 0 modes in the plasma edge. A radiation condensation instability resulting from the local power balance leads to the growth of an m = 0 island in the edge which leads to the deterioration of the plasma. The matched scaling of the density limit in the tokamak and the RFP experiment begs for a means of matching these two models.

The results on MST presented in chapter 3 bring into question the role of the m = 0 modes by effectively removing the reversal surface from the plasma. Despite this, the density limit scaling persists with a small decrease in the limiting density. However, the m =0 modes are not the only mode resonant in the edge of RFP discharges. There are an effectively infinite number of tearing instabilities which can be resonant near the reversal surface, modes with m > 0 and n > ~10 could all potentially be driven by radiation in the same way as discussed for the m = 2, n = 1 mode in tokamaks. If this radiation drive could be shown to match well the observations of the density limit on MST, it would provide the unifying explanation which governs the density limit in both tokamak and RFP devices.

Unfortunately, both of these models require measurements that are currently unavailable on MST, namely a measurement of the local power balance for the island in question. In fact, for the density limit experiments discussed in this thesis, even global measurements of the plasma radiated power were absent. Additionally, the shear number of potential culprits in the RFP edge could make the actual culprit difficult to nail down.

An experiment which should be performed is that of pellet fueled density limit experiments in discharges with a larger range of reversal parameter, including PPCD discharges. This would help to highlight how important the m = 0 modes are on the density limit by changing their location relative to the large density perturbation. The preliminary results suggest that the density limit could be higher for discharges with deeper reversal and this could be due to the location of the reversal surface relative to the wall. It could also be the result of shear stabilization for more reversed discharges. The extreme case of deep reversal would be PPCD experiments, but in addition to that, they represent a fundamentally different regime that has resulted in record plasma densities well above the limit with core fueling. Establishing the pellet edge fueled density limit in these discharges could give additional insight into the mechanism which ultimately trigger the density limit. The outermost resonant tearing mode will change as the plasma becomes more reversed. In 200kA PPCD experiments for example, the m = 1, n = -6 can come into resonance in the plasma edge. This situation might share more in common with the model in Reference 1 than to that of the RFX-mod experiment and could help to bridge the gap between the two.

7.2 β Limit Experiments

For the first time, we see strong evidence that suggests a confinement limited β in RFP plasmas and we observe no evidence of a disruptive β limit. By scanning the plasma density in PPCD discharges, we effectively scan the Ohmic heating power from approximately 1 to 3 MW. Over this range, we start to observe a continual increase in magnetic activity for both the m = 0 and m = 1 modes. Previously, pellet fueled PPCD discharges have been shown to be linearly unstable to pressure driven tearing and interchange instabilities, so these are the likely culprits. Experimentally, we have even observed pressure relaxation events in the plasma core which would be consistent with interchange instabilities, but we do not have accurate pressure profiles for all high β discharges.

The maximum achieved β is approximately 26%. Perhaps coincidently, this is consistent with Reference 3 where the β limit associated with resistive fluid turbulence is predicted to be

$$\beta \approx \left(\frac{m}{M}\right)^{1/6} \tag{7.1}$$

where m and M refer to the electron and ion mass respectively. For deuterium discharges on MST this amounts to a predicted limit of ~25%. Previously, this limit was proposed, but with only a handful of high β discharges, no strong conclusions could be drawn. After the numerous attempts to achieve a higher β, the relevance of this predicted limit has grown in importance.

We lack a reliable measurement of the ion temperature to make good measurements of the total β value. At higher density, the ions are assumed to be well coupled to the electrons.

This assumption has been previously established based on a limited subset of discharges which had ion temperature measurements.

Likewise, density profile measurements are extremely important for the measurement of total β in equilibrium reconstructions. The difficulty in inverting the FIR density profiles stems from the large local density near the pellet cloud. Perhaps the simplest solution would be to move the pellet injection location. This would require either the relocation of the injector or the installation of curved guide tubes to redirect the pellet. The degree of curvature in the guide tubes also limits the pellet speed which would preclude the launch of the fastest pellets, though these are typically not required for high β operation. Moving the pellet injection location would also open up the possibility of tangential injection which could further improve the core deposition of pellet fuel. Particularly when combined with NBI heating, tangential injection could greatly increase the core fuel deposited by an ablating pellet. Increasing the spatial distance between the pellet and the FIR system should aid the profile inversion, making it more widely available. Another possibility is the density calibration of the Thomson scattering diagnostic. This would enable a direct measurement of the electron β profile, allowing a closer look at the time evolution of electron β in PPCD discharges. By necessity, we have been forced to ignore the important profile effects in pellet fueled PPCD discharges despite knowing of their importance.

7.3 References

1) D.A. Gates, L. Delgado-Aparicio, and R.B. White, Nucl. Fusion **53**, 063008 (2013).

2) G. Spizzo, P. Scarin, M. Agostini, A. Alfier, F. Auriemma, D. Bonfiglio, S. Cappello, A. Fassina, P. Franz, L. Piron, P. Piovesan, M.E. Puiatti, M. Valisa, and N. Vianello, Plasma Phys. Control. Fusion **52**, 095011 (2010).

3) Connor, J. W., and J. B. Taylor. Plasma Phys. Control. Fusion **27**, 2676 (1984).

Appendix A

Supplemental plots for chapters 3-5

A.1 Supplemental density limit plots

We show similar plots as discussed in chapter 3 for 300 kA, 400 kA, and 500 kA density limit experiments. We will discuss the results briefly; however, the ensemble size is far less than the 200 kA case for the high density discharges. For all plasma currents, we observe a similar trend to that observed at 200 kA. Consistently, the F=0 discharges display a larger normalized current decay rate for a given value of the normalized density N_{GW}. We note again that the onset of current decay does appear at a higher N_{GW} for higher current experiments, consistent with the observations of chapter 3. Thomson scattering measurements are only available for the 500 kA case, where we also observe core T_e to drop to ~40-50 eV as N_{GW} increases. For sufficiently high N_{GW} the edge T_e also drops to 20 eV or less, even in the 500 kA case. Again we observe an increase in both m = 1 and m = 0 magnetic activity as N_{GW} increases and the m = 0 increase is observed in F = 0 discharges as well.

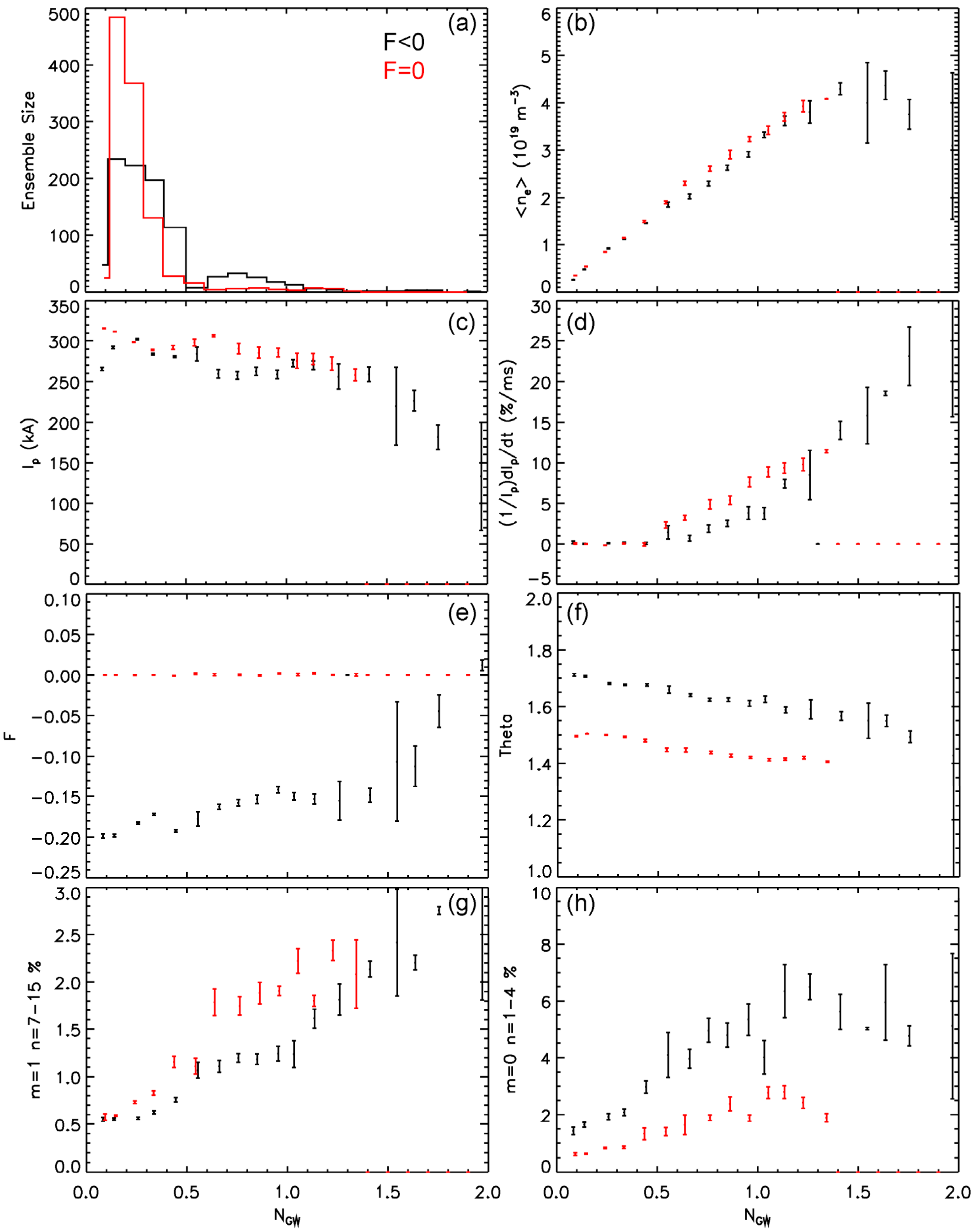

Figure A.1: (a) Ops signal ensemble size, (b) $\langle n_e \rangle$, (c) plasma current, (d) normalized current decay, (e) reversal parameter F, (f) pinch parameter Θ, (e) normalized core magnetic activity, and (f) normalized edge magnetic activity for 300 kA density limit experiments.

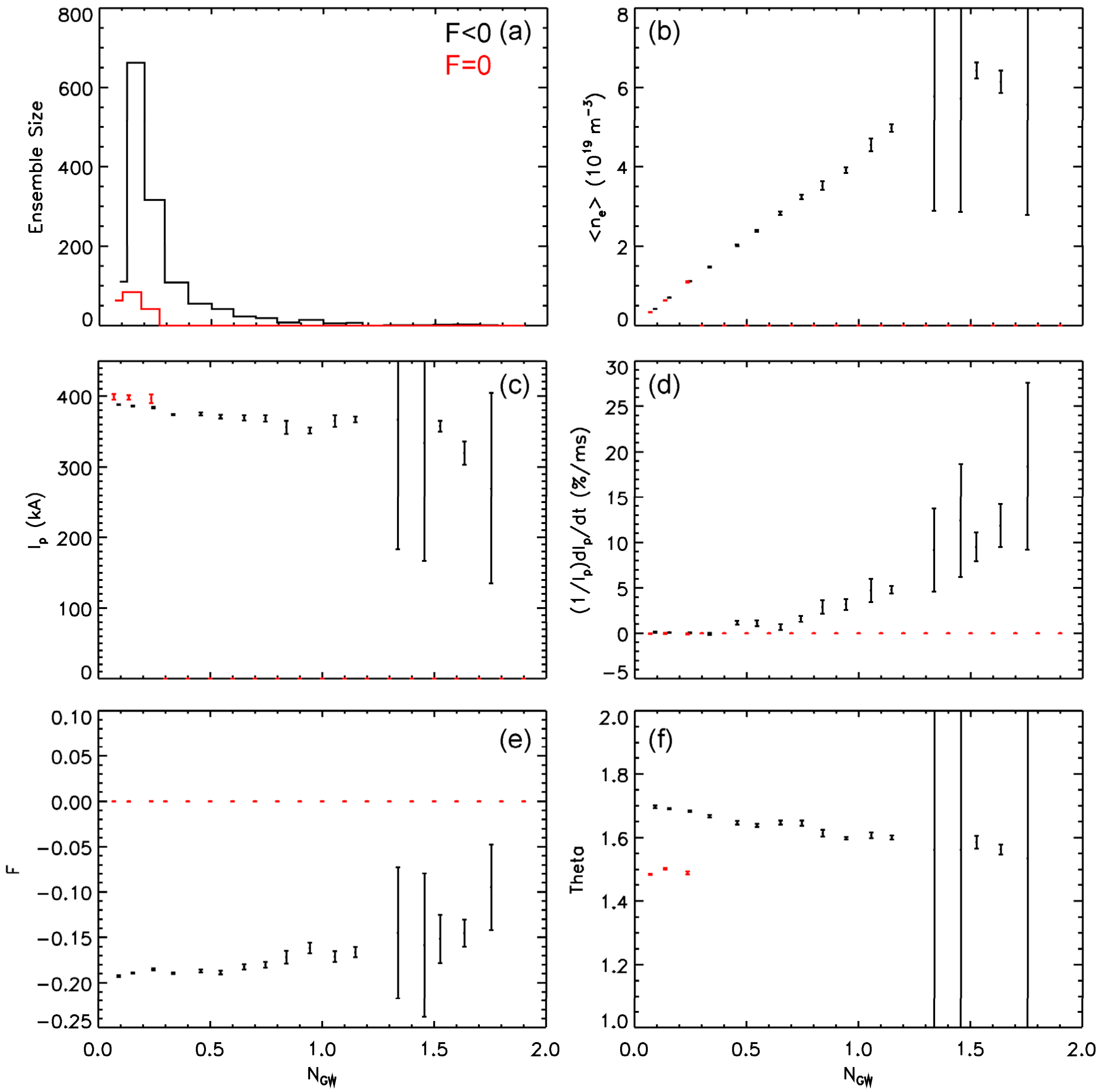

Figure A.2: (a) Ops signal ensemble size, (b) $\langle n_e \rangle$, (c) plasma current, (d) normalized current decay, (e) reversal parameter F, and (f) pinch parameter Θ for 400 kA density limit experiments.

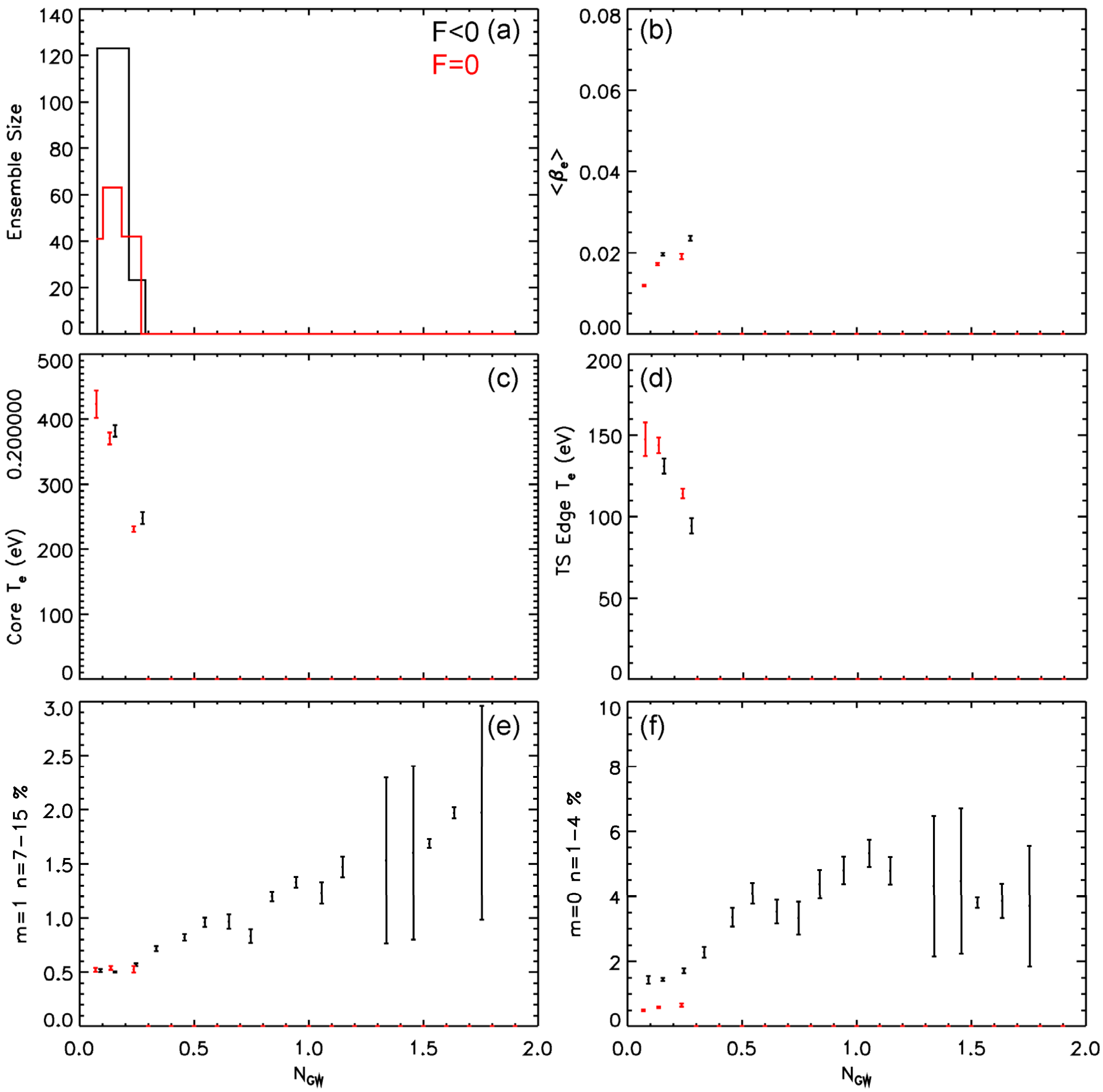

Figure A.3: (a) Temperature ensemble size, (b) $\langle \beta_e \rangle$, (c) Thomson core T_e (r/a < 0.2), (d) Thomson edge T_e (r/a = 0.7 – 0.8), (e) normalized core magnetic activity, and (f) normalized edge magnetic activity for 400 kA density limit experiments.

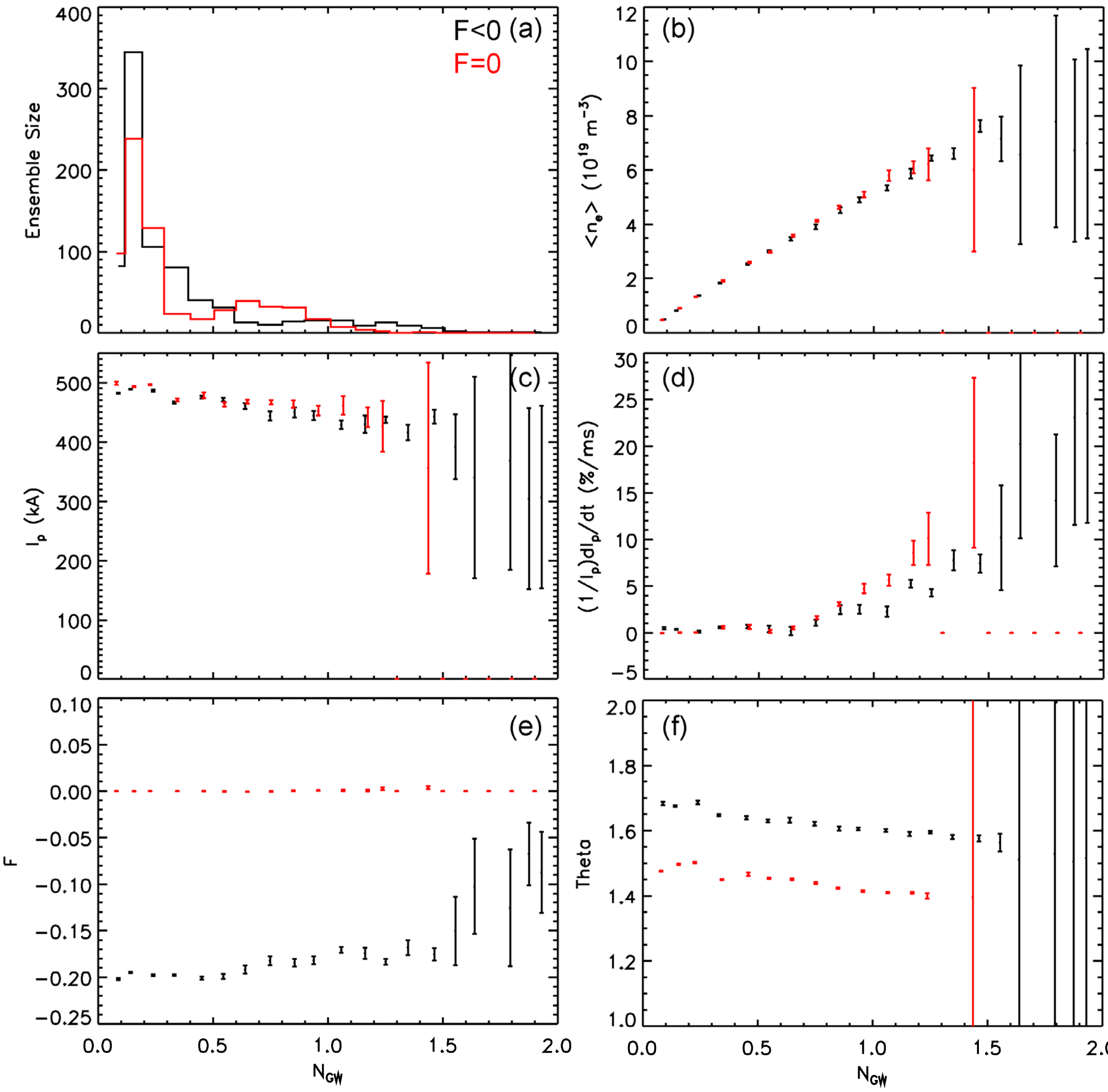

Figure A.4: (a) Ops signal ensemble size, (b) $\langle n_e \rangle$, (c) plasma current, (d) normalized current decay, (e) reversal parameter F, and (f) pinch parameter Θ for 500 kA density limit experiments.

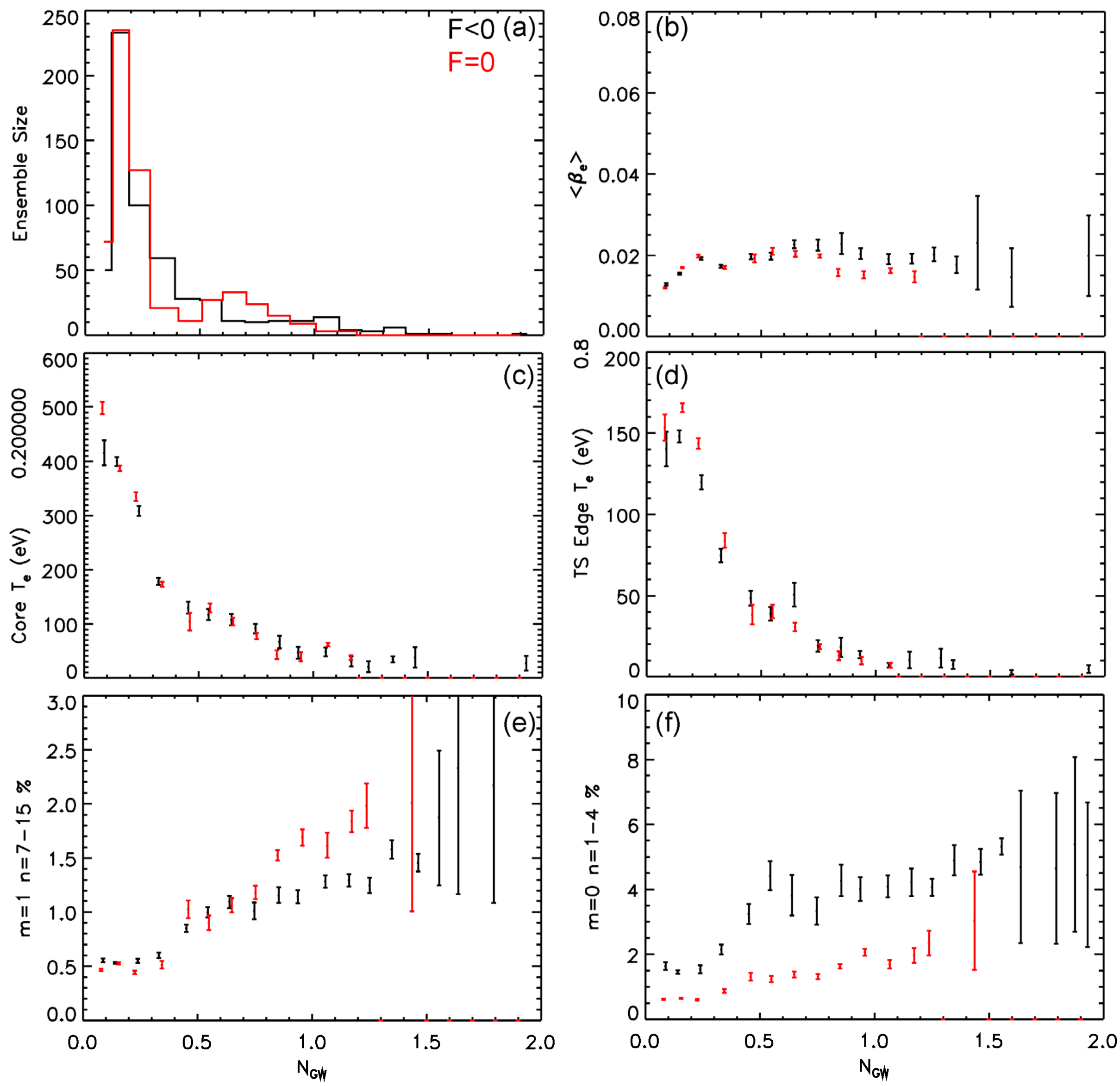

Figure A.5: (a) Temperature ensemble size, (b) $\langle \beta_e \rangle$, (c) Thomson core T_e (r/a < 0.2), (d) Thomson edge T_e (r/a = 0.7 – 0.8), (e) normalized core magnetic activity, and (f) normalized edge magnetic activity for 500 kA density limit experiments.

A.2 Supplemental high β plots

We show here the same plots as shown in chapters 4 and 5 during the discussion of a β limit and the addition of NBI heating. First, the mode and S scaling plots form chapter 4 are reprinted here with the additional NBI heated data. Little difference is observed in the scaling, but the NBI data was omitted in the original figure.

Next we discuss two other PPCD regimes where pellet fueling has resulted in an overall increase in beta; these are crash-heated and non-crash-heated 500kA PPCD. The ensemble size for both crash-heated and non-crash-heated 500 kA PPCD are significantly smaller than the 200 kA PPCD ensemble. In addition, there are some inconsistencies in the plasma parameters for comparing the NBI on and NBI off cases of 500 kA crash heated PPCD. For these reasons, the discussion of these regimes is relegated to this appendix. More work is needed, but the relevant trends will be discussed.

For 500kA non-crash heated PPCD, the ensemble size is lacking for non-NBI heated discharges. The $\langle \beta_e \rangle$ scatter plot shows a constant or slightly decreaseing $\langle \beta_e \rangle$ with increased N_{GW}. The mode and S scaling are fairly consistent with the results of the 200 kA PPCD discharges. The comparison of the NBI on and OFF data shows good agreement for the plasma parameters, but the ensemble size is fairly low for the $\langle \beta_e \rangle$ and T_e scaling with N_{GW}. We also see a slight increase in magnetic activity with added NBI, in contrast to our observations in 200 kA PPCD. This leaves a lot of open questions, but also the NBI off data is severely lacking for making a good comparison.

The 500 kA crash heated PPCD involves data taken in 2008-9 and 20013, and it shows. Specifically in the plasma parameter comparison of the NBI-on and NBI-off cases. The reversal and pinch parameters (F and Θ) are significantly different, making a direct comparison problematic. That being said, the overall nature of the scaling is somewhat similar for both the mode and S scaling. The $\langle\beta_e\rangle$ scatter plot shows for the first time a clear increase in $\langle\beta_e\rangle$ as N_{GW} increases up to N_{GW}= 0.5 – 0.7. The other standout in this region is that the m=0 activity can remain low in the best cases up to approximately this point. This is the closest thing to evidence that the m=0 is playing a role in the β limit, but this is muddled by the fact that the data from 2008-9 and 2013 do not match very well. The $\langle\beta_e\rangle$ appears to be slightly lower in the NBI heated case, though the edge T_e appears slightly higher at higher N_{GW}, possibly evidence of a larger edge deposition of beam power. This occurs above NGW = 0.5, which lies above the estimated optimal density of $3*10^{19}$ m^{-3}. The mode scaling is similar to 200kA except that the modes appear larger in NBI heated discharges.

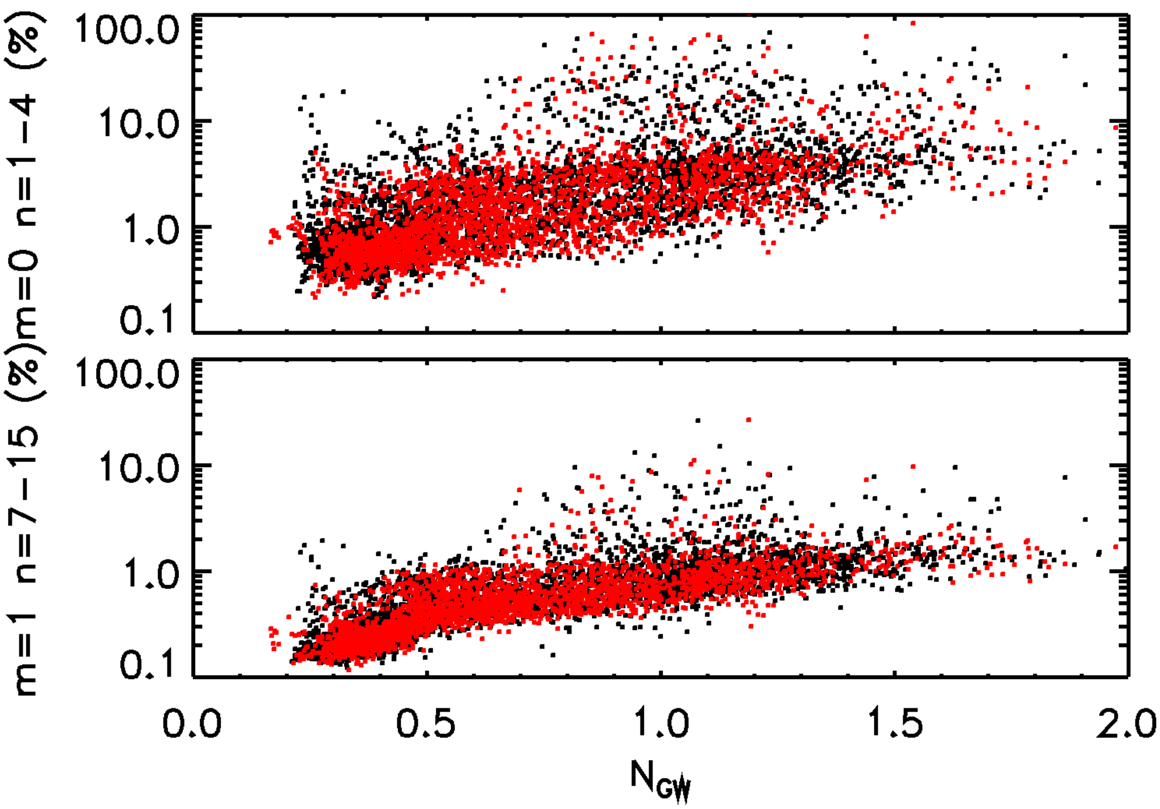

Figure A.6: Mode scaling scatter plot for 200 kA PPCD discharges with (red) and without (black) NBI heating.

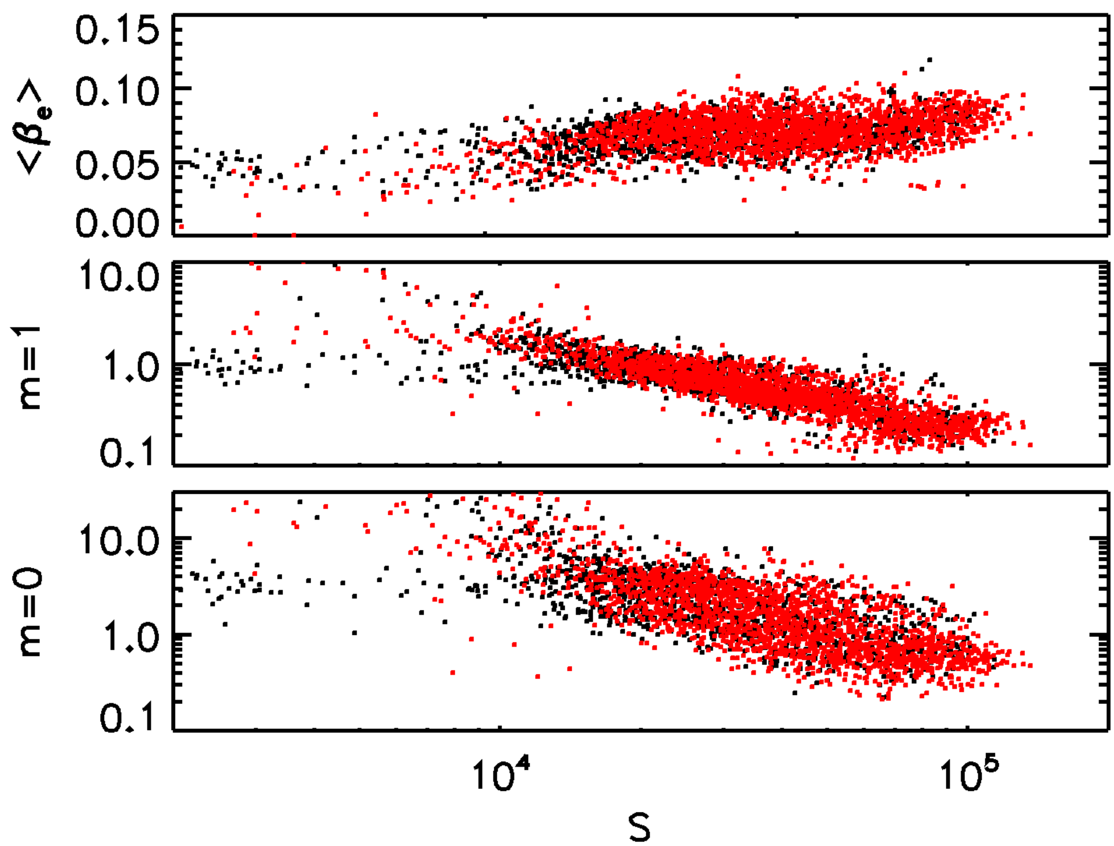

Figure A.7: S scaling scatter plot for 200 kA PPCD discharges with (red) and without (black) NBI heating.

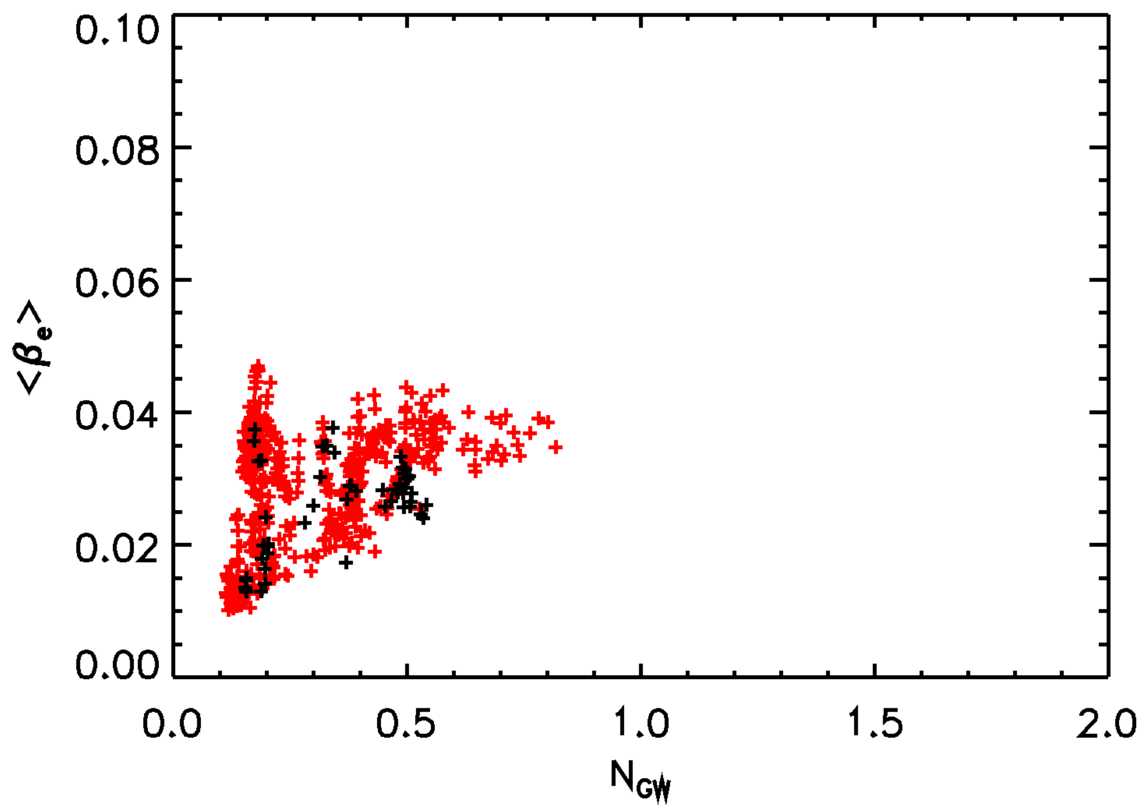

Figure A.8: $\langle \beta_e \rangle$ scaling scatter plot for 500 kA non-crash-heated PPCD discharges with (red) and without (black) NBI heating.

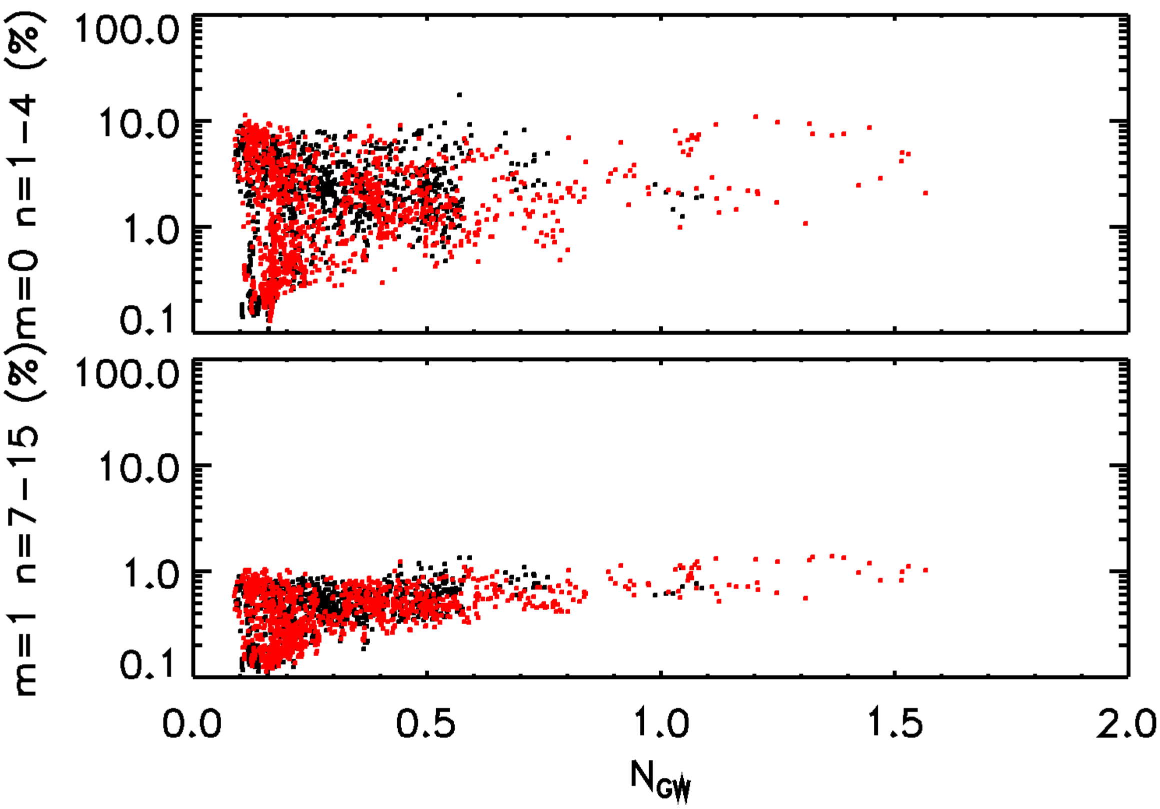

Figure A.9: Mode scaling scatter plot for 500 kA non-crash-heated PPCD discharges with (red) and without (black) NBI heating.

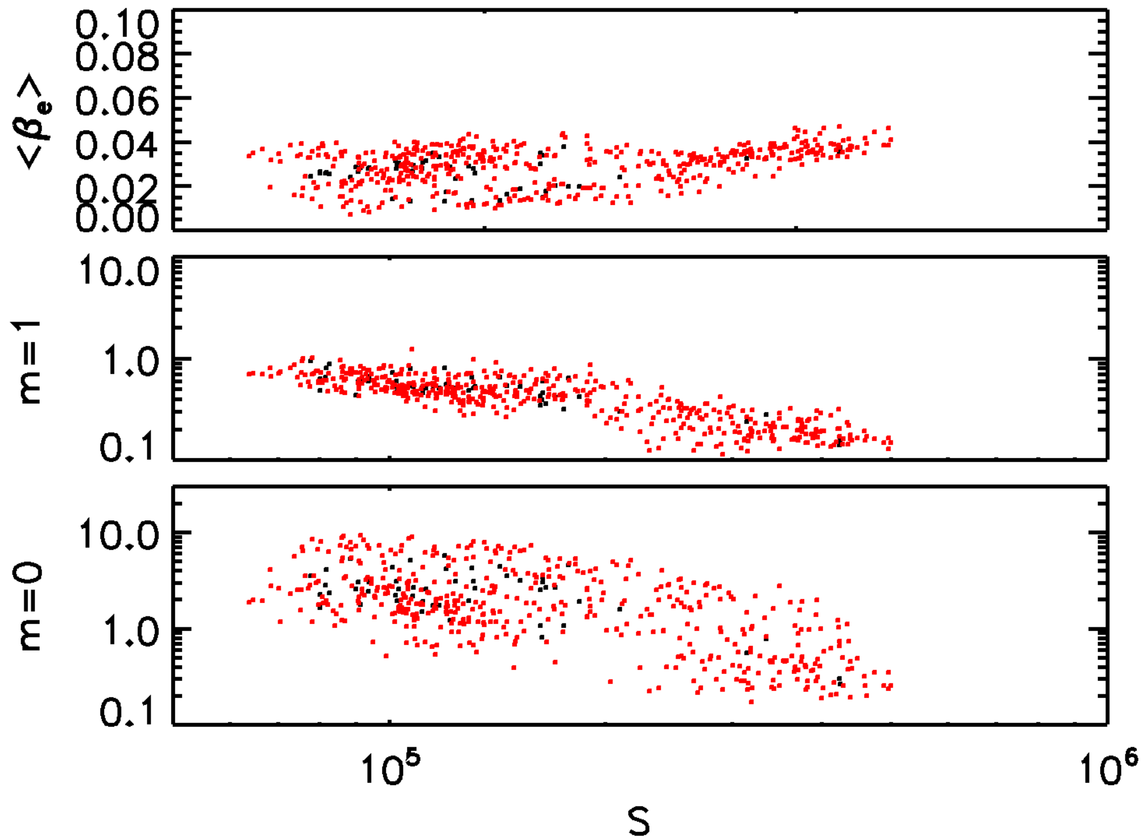

Figure A.10: S scaling scatter plot for 500 kA non-crash-heated PPCD discharges with (red) and without (black) NBI heating.

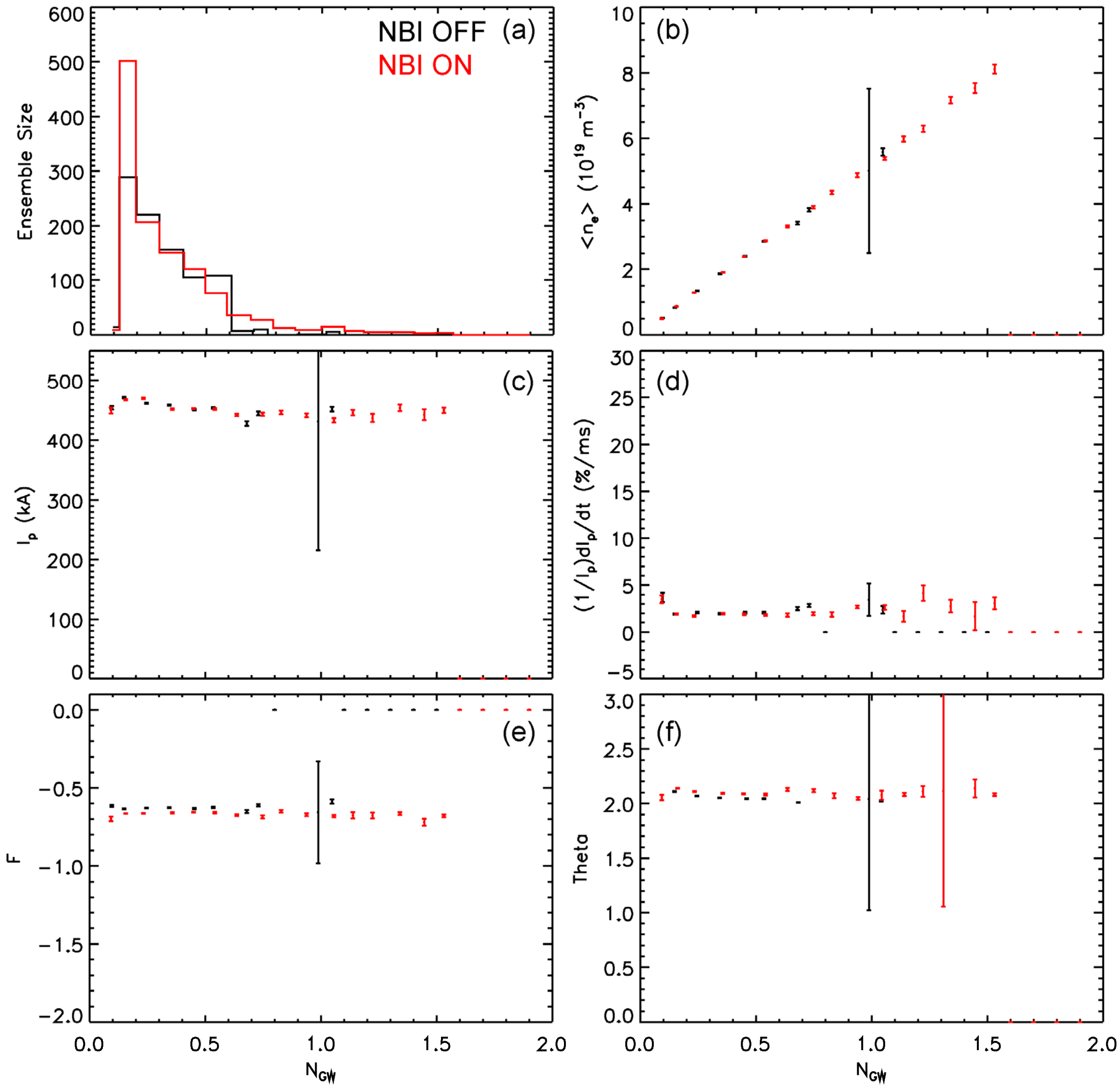

Figure A.11: (a) Ops signal ensemble size, (b) $\langle n_e \rangle$, (c) plasma current, (d) normalized current decay, (e) reversal parameter F, and (f) pinch parameter Θ for 500 kA non-crash-heated PPCD discharges with (red) and without (black) NBI heating.

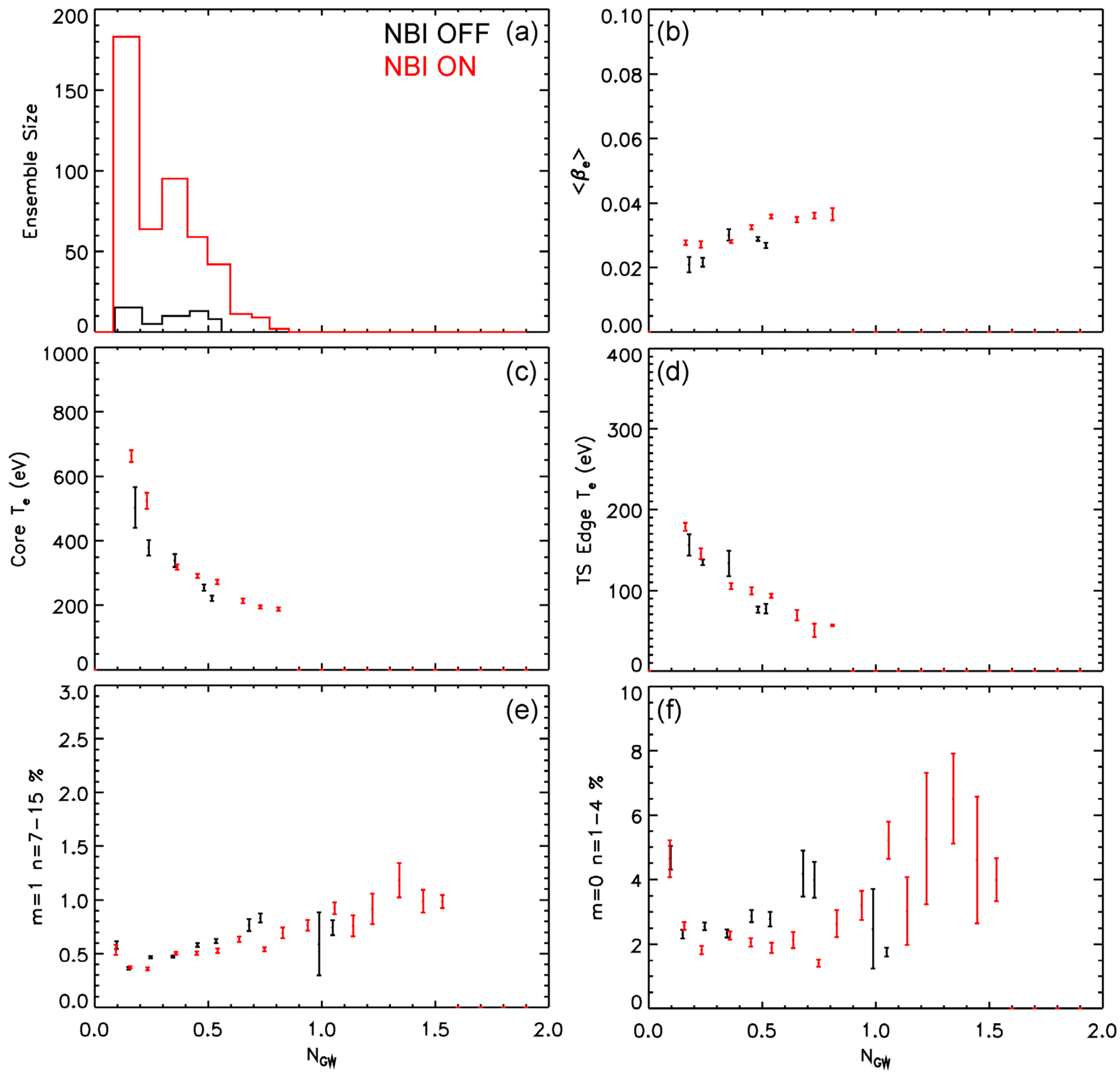

Figure A.12: (a) Temperature ensemble size, (b) $\langle \beta_e \rangle$, (c) Thomson core T_e (r/a < 0.2), (d) Thomson edge T_e (r/a = 0.7 – 0.8), (e) normalized core magnetic activity, and (f) normalized edge magnetic activity for 500 kA non-crash-heated PPCD discharges with (red) and without (black) NBI heating.

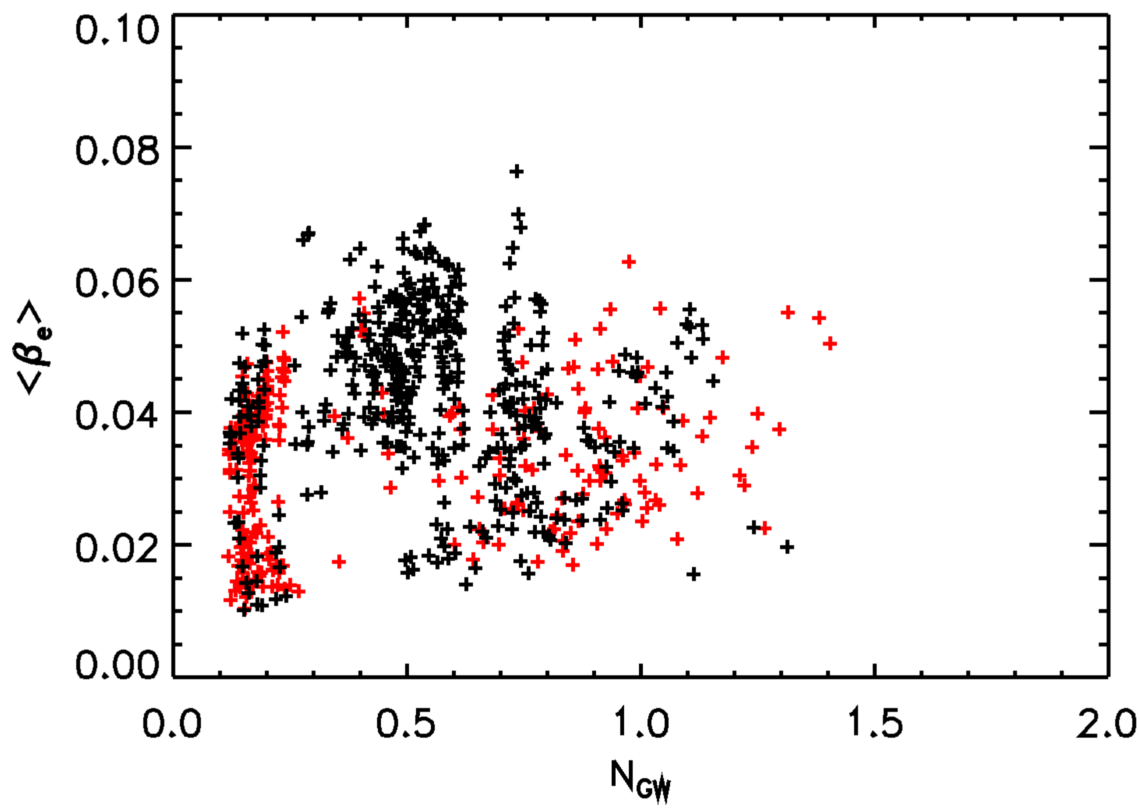

Figure A.13: $\langle \beta_e \rangle$ scaling scatter plot for 500 kA crash-heated PPCD discharges with (red) and without (black) NBI heating.

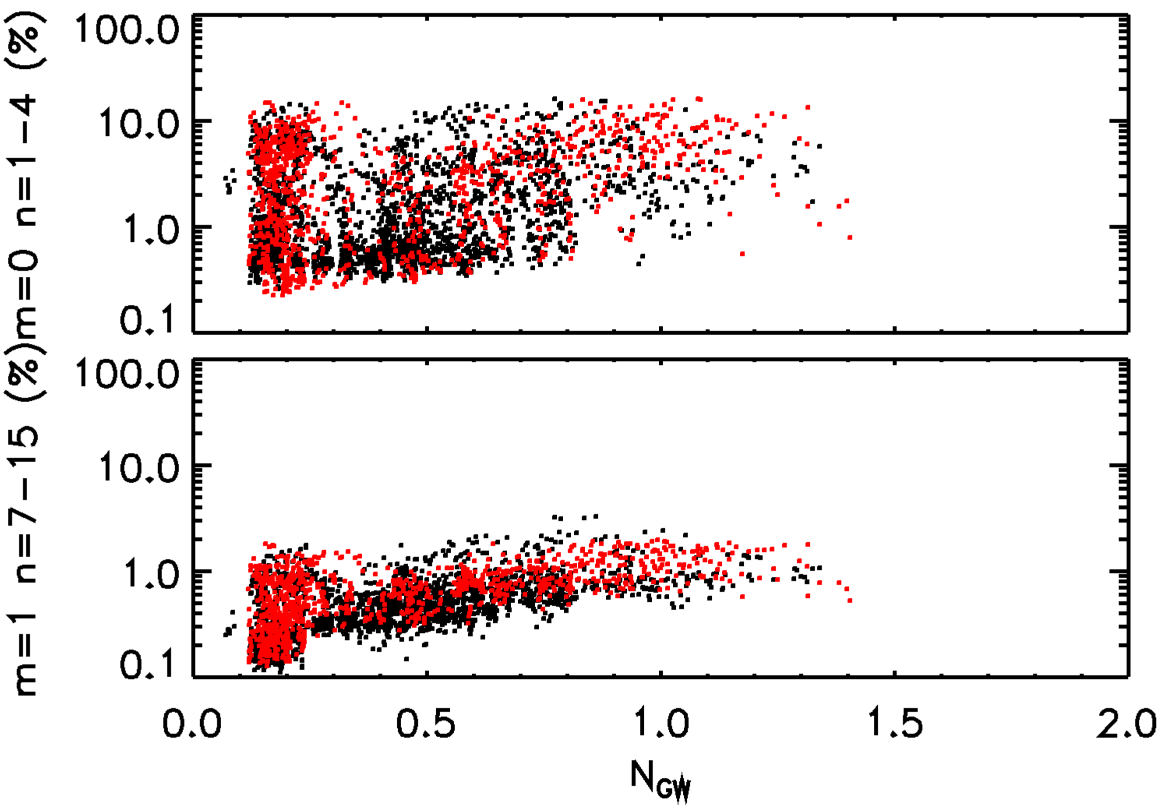

Figure A.14: Mode scaling scatter plot for 500 kA crash-heated PPCD discharges with (red) and without (black) NBI heating.

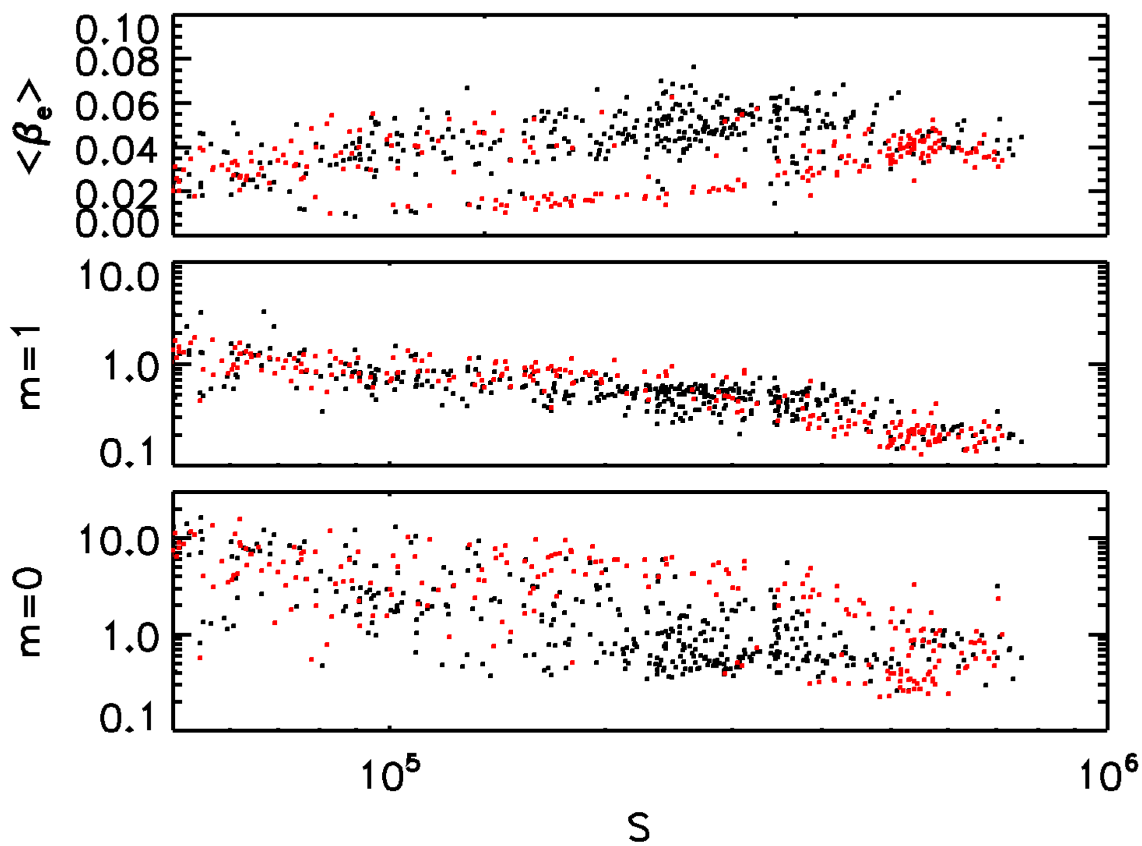

Figure A.15: S scaling scatter plot for 500 kA crash-heated PPCD discharges with (red) and without (black) NBI heating.

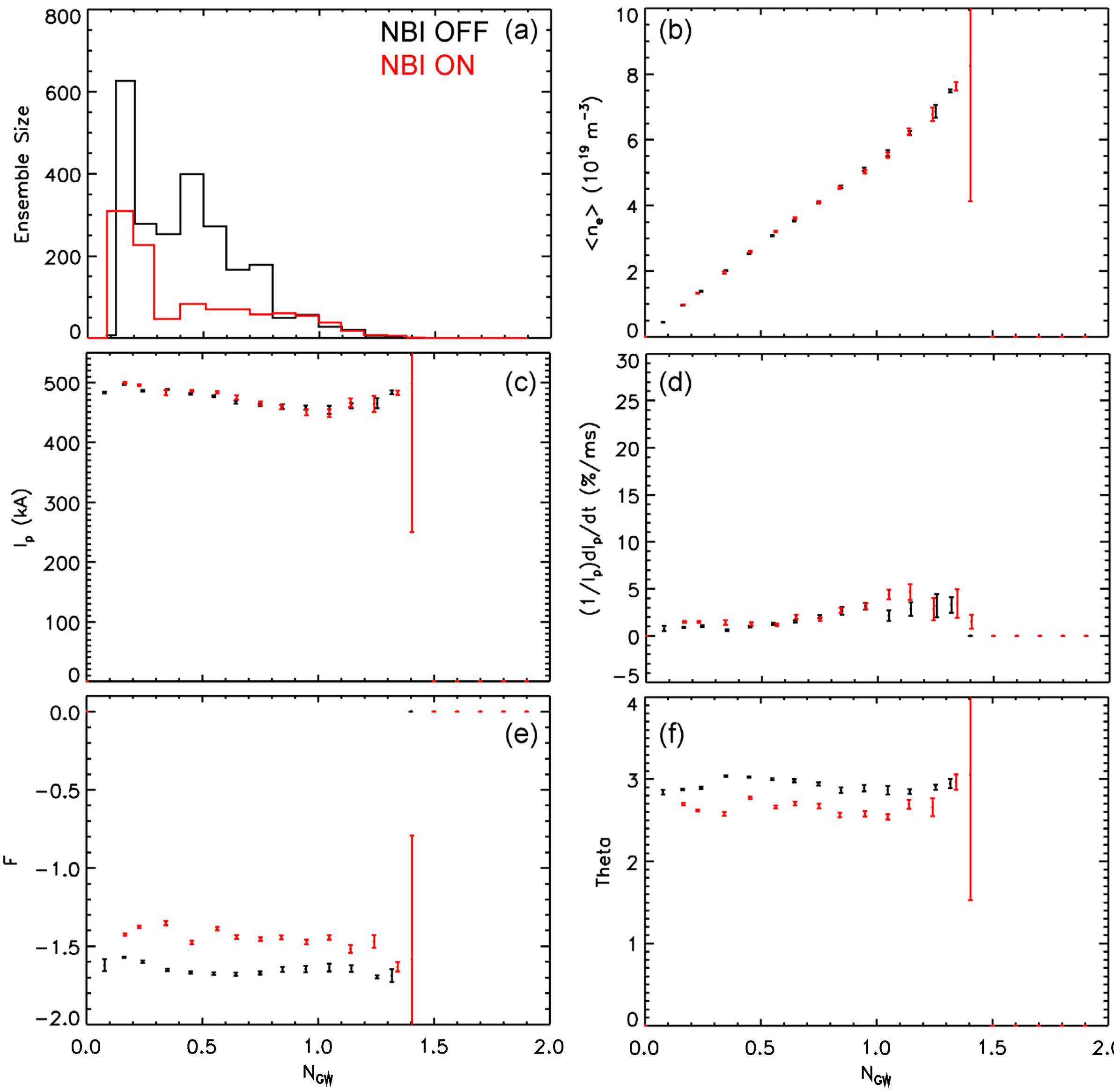

Figure A.16: (a) Ops signal ensemble size, (b) $\langle n_e \rangle$, (c) plasma current, (d) normalized current decay, (e) reversal parameter F, and (f) pinch parameter Θ for 500 kA crash-heated PPCD discharges with (red) and without (black) NBI heating.

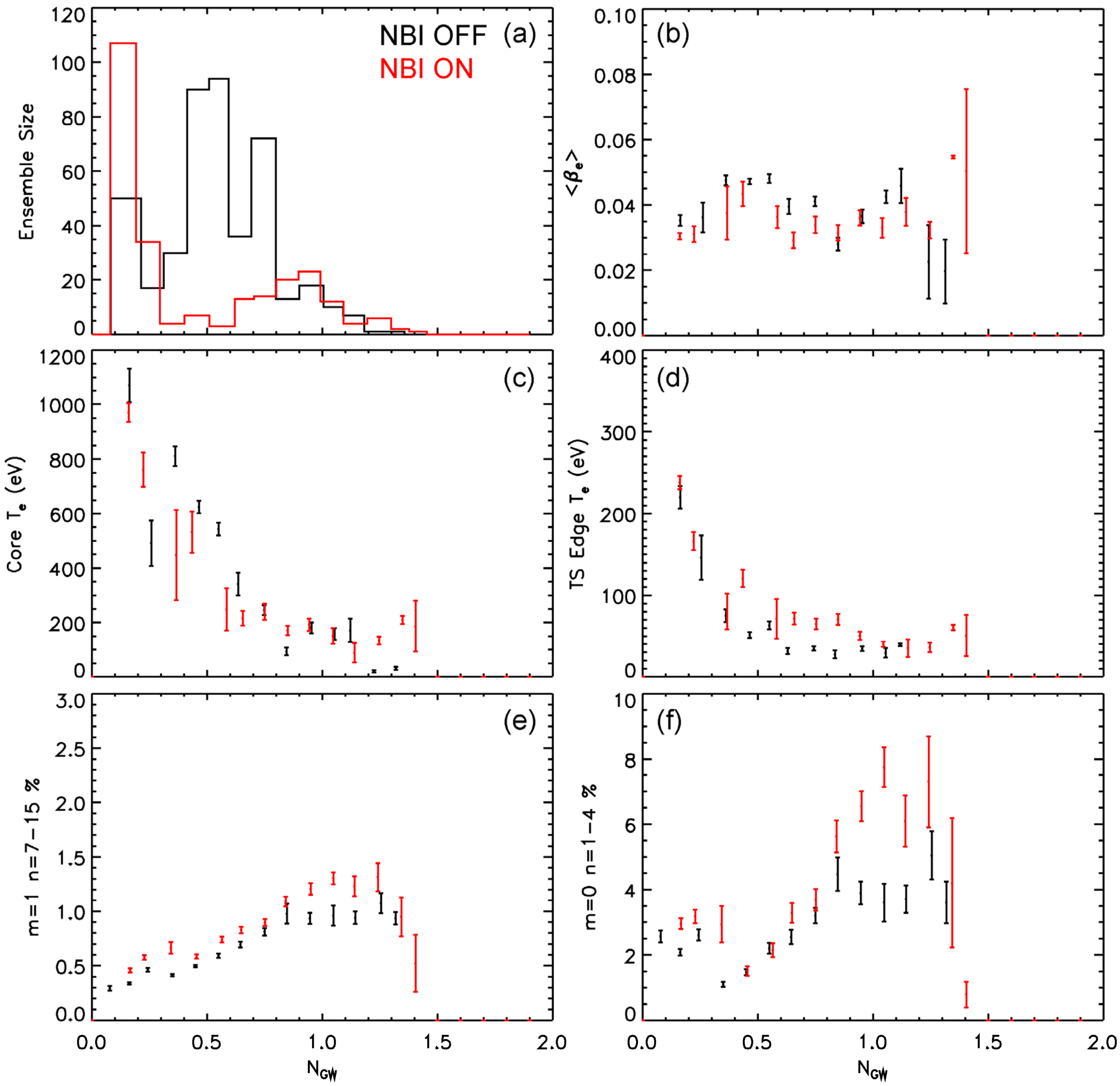

Figure A.17: (a) Temperature ensemble size, (b) $\langle\beta_e\rangle$, (c) Thomson core T_e (r/a < 0.2), (d) Thomson edge T_e (r/a = 0.7 – 0.8), (e) normalized core magnetic activity, and (f) normalized edge magnetic activity for 500 kA crash-heated PPCD discharges with (red) and without (black) NBI heating.

Appendix B

Supplemental Pellet User's Guide

B.1 Supplement to the Pellet User's Guide

Little has changed in terms of the operation of the pellet injector from that contained in the appendix of Reference 1. Instead of rehashing much of that information here, we will highlight important changes to any procedures and discuss the numerous factors which can impact the pellet formation and injection. Much of this information is qualitative in nature. It does not sound very scientific, but as you spend more time working with pellet injection, you get a 'feel' for what works and what does not. The majority of this appendix will be an attempt to transfer the knowledge that has been gained by the pelleteer. What follows is a list of the many things which impact pellet formation and the successful launch of a pellet into the plasma. Along with each item are the reasons why it matters.

B.1.1 Hardware Modifications

The fuel gas bottle was replaced with a fuel line connecting to the MST gas manifold. Reconnecting a gas bottle is still an option as was done with methane pellet experiments. MST gas manifold has purified deuterium, hydrogen, argon and helium. All but helium are viable pellet fuels.

The manifold roughing pump was replaced with a portable turbo station which currently sits on top of the helium compressor. This has resulted in a small change to the pumpout procedure which will be discussed in detail below.

After the installation of a 3.0 mm and 4.0 mm diameter barrels, the gunbox temperature increased by 2-3 K, likely due to the increased thermal load provided by the increased barrel material. This was reduced by a few Kelvin by moving (and eventually removing) the heat shorts, but the impact of increased barrel material on the barrel temperature was not previously observed.

A needle valve connected to a helium gas bottle was hooked up to the gunbox vent valve for the methane pellet experiments.

Penning gauge for FST volume was moved to the control room.

B.1.2 Procedure Changes

Pumping down the manifold is slightly different since switching to the turbo station. To protect the pump, it is manually closed off while the propellant side of the manifold is venting. Then the manifold is closed off from the vent and opened up to the vacuum line (which is no longer being pumped on actively). Then the manual valve is slowly opened to pump down the propellant side. The same method can then be done for the feed side of the manifold.

B.1.3 Known Hardware Problems

Of the four convectron gauges, 2 of them stopped working during the injector removal or during the re-installation. The manifold gauge and RST gauge are working, and the FST gauge was replaced with a similar model without a display. The pressure is still observable from the pellet control computer. The gunbox pressure was inferred based upon the current draw of the turbo pump and the RST gauge effectively measures the same pressure as the FST gauge, so the loss of two gauge measurements did not impede injector operation.

The pressure gauge for the propellant line no longer reads accurate pressures. The problem was not understood at the time. It is not a critical component for injector operation.

Despite a thorough leak checking before reinstallation, the fast fill needle valve (PV101/102) still has a through leak. It is no longer used and the pellet size criterion has been increased to make it never needed. The needle valve NV102 can be adjusted as needed, but in practice, it works for any pellet by adjusting the feed fill pressure.

There are a number of relief valves on the manifold and injector line which have not been tested.

The Penning gauge is dirty or corroded. The gauge has trouble measuring very low pressure (less than 5e-7 Torr). Knowing the exact pressure is not critical for injector operation.

The punch/valve power supplies sometime appear to behave differently, but attempts to test them have not shown any to consistently not work. Often they behave differently on different punches or valves or barrels. The suggestion is to find a good power supply valve pairing and stick with it.

The building water has gotten increasingly worse. It has reached the point where the building water filter must be changed after 3-4 days of injector operation. After that point, the water flow is insufficient to cool the helium compressor, leading to a high temperature fault of the compressor. This was repeatedly misdiagnosed as a problem with the compressor.

Discussion of moving the injector to the closed loop has begun, but as of yet, we are still on the building water.

B.2 Pellet Formation Tips, Tricks and Treats

B.2.1 Parameters Which Impact Pellet Size

These are some of the settings which impact pellet size:

Barrel diameter (1.0 to 4.0 mm)

L/D (Length/Diameter) (.2 to 3.0)

Feed Fill Pressure (30 to 150 Torr)

These quantities determine pellet size, but it is not quite that simple. The pressure in the feed reservoir is monitored as the volume is opened up to the barrel. The subsequent pressure drop corresponds to the volume of the desired pellet based on the pellet diameter and L/D ratio. The feed fill pressure primarily determines the time the barrel is opened up to the volume and typically a pellet formation time of 30 seconds or less is desired. Depending on the pellet size

During automated operation of the labview program, the feed reservoir is refilled to this setting if the pressure is sufficiently lower than the set value (lower by about 10 Torr). For smaller pellets that result in a pressure drop of less than 10 Torr, consecutive pellets can have different sizes due to the change in starting pressure. If the starting pressure is too low, the volume is opened up to the fuel supply. After the pressure reaches the set value, the volume is immediately opened up to the barrel and the pressure drops. This is slightly problematic as the maximum pressure can reach several Torr more than the setting and varies from shot to shot due to the time between pressure readings (~0.5 s). The time between pressure readings can also lead to a variation in pellet size as the time dependent readings can overshoot based on the rate of pressure drop and the time between pressure readings. This can result in larger pellets than desired and an increased variation in pellet size. The variation in pellet size can be mitigated (and even controlled to a limited extent) by manually setting the pre fill pressure.

B.2.2 Parameters Which Impact Pellet Speed

These are some of the settings which impact pellet speed:

Propulsion Method (Punch, Close Coupled Valve, Combination Punch + Valve)

The simplest control over the pellet speed is by the hardware used for propulsion. The options are close coupled gas valves which normally are limited to fast pellets with speeds up to 1200 m/s. For larger pellet barrels (such as 4.0 mm diameter pellets) a range of pellet speeds is possible with 4.0 mm pellets speeds ranging from 100 to 1200 m/s. Pellets propelled by mechanical punch are typically slow with speeds of ~100 m/s. When combined with a side mounted gas valve, a gas puff can be triggered after the punch dislodges the pellet resulting in pellets with speeds in the range of 200 – 400 m/s.

The barrel temperature has an impact on the pellet breakaway pressure. As the barrel temperature increases, the pressure required to launch the pellet decreases.

Specifically with punch driven pellets, the size of the pellet appears to impact the speed of a punch driven pellet.

For both close coupled and punch mounted gas valves, the valve pulse width can have an impact on the pellet speed.

The combination of punch and valve propulsion results in a range of speed primarily due to the separation in time of the two solenoid pulses.

B.2.3 Other Parameters of General Import

These are some of the settings which impact pellet success:

Soak Time (30 to 300 seconds)

Varying the soak time can vary the pellet size or make the pellet easier or harder to break away from the barrel. This varies widely from barrel to barrel and likely has much to do with the heat short spacing on the barrel.

Time in barrel waiting for launch (2 to ? seconds)

This might also depend on the heat short spacing, but sometimes the pellet does not last long in the barrel, requiring the pellet to be fired almost immediately. Other times, the pellet can remain in the barrel for minutes and be launched normally.

Manual vs. automatic arming

This is the primary way in which we control the amount of time the pellet remains in the barrel before being launched. By triggering the start sequence of the pellet control program with 10 – 20 seconds left in the MST charge time, the system will be waiting for a trigger when MST fires.

Phase of the Moon

The effects of the Moon's gravitational pull have not been fully explored.

Appendix C

4.0 mm pellet upgrade

C.1 Notes from Pellet Injector Disassembly

Disconnect all cabling. Take pictures and mark relevant cables to aid reassembly (Do it). After disconnecting all relevant cabling, the injector was hoisted out of the machine area. I was not present for this (Bill Zimmerman took care of this part). It was then moved to 2260 for disassembly. The final guide tube sections should be removed from the compressions fittings. There exists a customized set of valves which can be inserted into these fittings and connected to the roughing line in case of gate valve leaks. Make sure to clearly mark the pellet injector footprint before removing it. Also, put do not move signs on the pellet supports, otherwise people will use them for portable tables… I'm looking at you Rutherford guys.

The first task was opening up the gunbox and removing all of the punches, valves, barrels and other such things. Bag everything for protection and label everything for ease of reassembly.

A list of helpful items to procure beforehand:

Bags for bolts, nuts, gaskets, etc.

Tongue in groove pliers for Snout/Barrel removal

Gunbox sideplate removal kit

Wrenches 1/4" – 5/8"

Bubble wrap for barrel/punch protection

Barrel Removal kit

By removing the turbo sideplate, I was able to remove all pieces without removal of the other sideplate, but it was tight and would have been easier to remove both sideplates.

To help with reassembly, it is important to mark the tops of all pieces as they are removed. We will also document the injector as we remove components, specifically for the regions we don't currently have drawings for. To gain access to the first 3 sections of guide tubes, we start by breaking open the injector at the first cross. A ring of bolts connects the first cross to an aluminum plate contained by the shield (on the first cross side). Unfortunately the stage 2 guide tubes extend into the first cross housing enough that the piece cannot be easily removed. In the end, it was easiest to start at the bottom (Stage 6) and remove one section at a time working from the downstream side. Make sure to keep the guide tube sections fully supported. The key supports are at the gunbox and at the ST2 connection. The ST1 connection is flexible and does not offer much support. Several winch straps were connected for support of the injector guide tube sections

Next, the bolts holding the shield are removed and the shield can be taken off exposing the guide tubes, conflat valves, spacing bellows etc.

To gain access to the guide tubes, the aluminum plate is removed. There is a nut in the center holding it in place.

Next in line are some conflat valves, followed by the gate valves. Once the conflat valves are removed, the 2nd stage of guide tubes should be free. Then, once the gate valves are removed, the first stage guide tubes can be unscrewed from the lightgate assembly.

We will also need to remove the microwave cavity for replacement. This should be a bit more straightforward, but we do not have drawings of the surrounding hardware.

C.2 Overview of Modifications

Stage 1 was modified to increase the ID

Stage 2 required fabrication of 4 new pieces with larger ID

Stage 3 Newly fabricated guide tubes with larger ID were welted into the first cross housing

Stage 4 Similar to stage 3, new guide tube pieces with larger ID were welded into the housing

Stage 5 no modification

Microwave cavity was swapped with one more tuned to large pellet measurement

Stage 6 Guide tube for barrel 1 had a weld bead which was removed

Stage 7 new guide tube pieces ordered and cut with larger ID

Compression fitting on barrel gate valves had ID enlarged to match/exceed new stage 7 guide tube ID

C.3 Notes on Reassembly

Before reassembly, the squareness and alignment of all pieces was checked on the bench. After good alignment of each piece is confirmed get ready for reassembly.

List of things needed for reassembly

Cleaning supplies (cotton, ethanol, wipes, etc.)

Vacuum supplies (gaskets, o-rings, etc)

Wrenches and sockets

Camera for pictures

Winch straps for supports

Clean barrel compression fitting and barrel light gate mounts, replace o-rings and copper gaskets as needed. Can attach these back onto gunbox. Can then attach light gate mounting plate and light gate. Note light housing is very heavy, so make sure this is supported well.

Now we will first highlight the order of event which transpired during rassembly and then give some advice for the hopefully never occurring next time. The injector reassembly was done from both ends, working back from the gunbox and working upstream from the stage 6 section attached to the ST2. This turned out to be a mistake which required us to pull the lower half of the injector back in order to get the last piece (the first cross) in place. In the future, the injector should be reassembled from one end only. I think starting from stage 6 and working up would work best, but only time will tell. Anyway, here is how it went for us and everything turned out fine.

The Stage 1 guide tubes can be inserted into the light gate housing.

A few iterations of this next step were tried, but the one which ultimately worked was to attach the gate valves and stage 2 guide tubes and stage 2-3 face plate and then put the shield over the top.

Nest, the stage 6 section can be attached to surge tank 2 and can then build up from there with the microwave cavity section (with stage 5) and the stage 4 section as well as the Gate Valve 305 which separates the two halves.

It was at this point, with one piece left, the first cross, that we had a similar problem to that observed during disassembly (you might think we had learned form that mistake, but no)

The solution was to disconnect the surge tank from the pellet frame and support it with a lab jack, allowing us to retract the whole lower half of the injector a few inches, allowing enough room to reattach the first cross, then moving the entire assembly back into place. This ended up working well, and the final results were good, but as stated above, the better method would be to work from either one end or the other in entirety. There does not appear to be a clean place where a final piece can simply be inserted without some additional wiggle room. After that, the injector was crained back up into place and aligned with the pellet ports. The cableing was reconnected and luckily everything worked, for the most part.

We now present the above in terms of a picture slide show

Also included are several drawings which might be relavant for future hardware updates to the injector. In addition, all pieces have now been modeled in Solidworks by Steve Oliva. Those files are not shown here, but they exist.

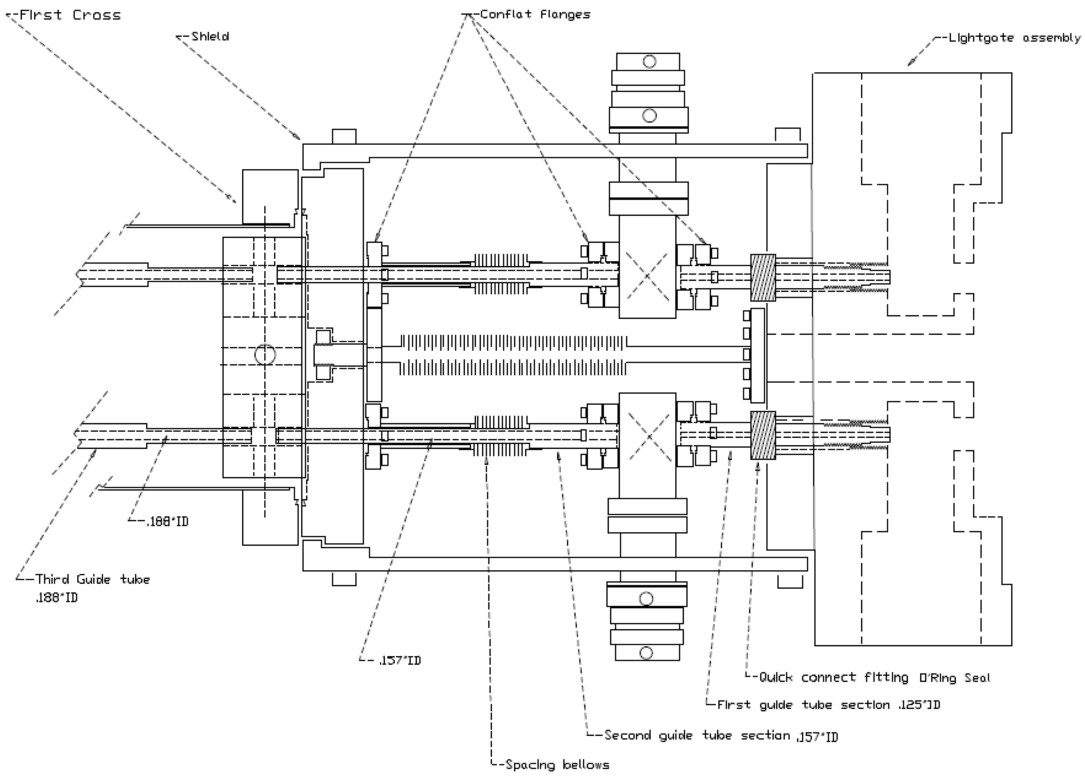

Figure C.1: The sole drawing of the injector guide tubes prior to the 4.0 mm pellet injector upgrade. The first three guide tube stages are shown along with the lightgate assembly, shield and gate valves.

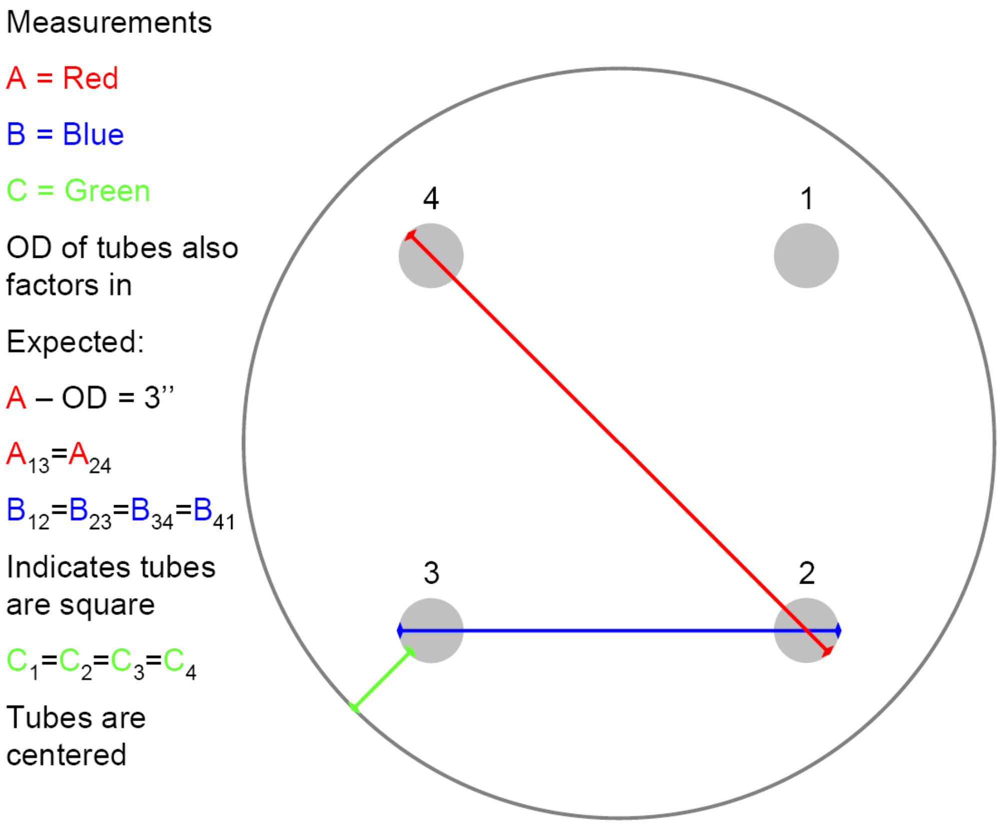

Figure C.2: Diagram of the measurements made to confirm guide tube alignment and centering after modification.

All meas. in cm	Stage 2		Stage 3	Stage 4	Microwave Cavity		Stage 5		Stage 6	
A13	11.01	8.6	8.58	8.58	8.58	8.9	8.86	8.89	8.9	8.9
A24	11.01	8.6	8.58	8.58	8.58	8.9	8.81	8.89	8.9	8.89
B12	8.78	6.35	6.33	6.34	6.35	6.66	6.62	6.63	6.66	6.66
B23	8.78	6.35	6.33	6.34	6.35	6.66	6.61	6.65	6.66	6.65
B34	8.78	6.36	6.33	6.34	6.35	6.68	6.63	6.64	6.64	6.66
B41	8.78	6.36	6.33	6.34	6.35	6.67	6.65	6.65	6.66	6.67
C1	2.06	0.47	3.28	3.28	0.55	0.39	0.5	0.5	5.65	5.6
C2	2.07	0.47	3.3	3.28	0.53	0.4	0.51	0.51	5.65	5.64
C3	2.07	0.46	3.3	3.3	0.55	0.4	0.51	0.51	5.65	5.68
C4	2.07	0.47	3.29	3.3	0.55	0.39	0.5	0.5	5.67	5.63
D1	3.38	0.96	0.96	0.96	0.95	1.25	1.25	1.26	1.26	1.27
D2	3.38	0.96	0.96	0.96	0.95	1.25	1.25	1.26	1.26	1.27
D3	3.38	0.96	0.96	0.96	0.95	1.25	1.25	1.26	1.26	1.27
D4	3.4	0.96	0.96	0.96	0.95	1.25	1.25	1.26	1.26	1.27
D =	3.385	0.96	0.96	0.96	0.95	1.25	1.25	1.26	1.26	1.27
OD	15.24	9.51	15.24	15.24	9.64	9.65	9.88	9.88	20.32	20.32
Error Checks										
A13-A24	0	0	0	0	0	0	0.05	0	0	0.01
A13 - D - 3" (7.62cm)	0.005	0.02	0	0	0.01	0.03	-0.01	0.01	0.02	0.01
A24 - 3"	0.005	0.02	0	0	0.01	0.03	-0.06	0.01	0.02	0
Max Diff in B	0	0.01	0	0	0	0.02	0.04	0.02	0.02	0.02
Max Diff in C	0.01	0.01	0.02	0.02	0.02	0.01	0.01	0.01	0.02	0.08
OD - A13 - C1 - C3	0.1	-0.02	0.08	0.08	-0.04	-0.04	0.01	-0.02	0.12	0.14
OD - A24 - C2 - C4	0.09	-0.03	0.07	0.08	-0.02	-0.04	0.06	-0.02	0.1	0.16

Table C.1: Measurements to confirm on bench alignment before reassembly.

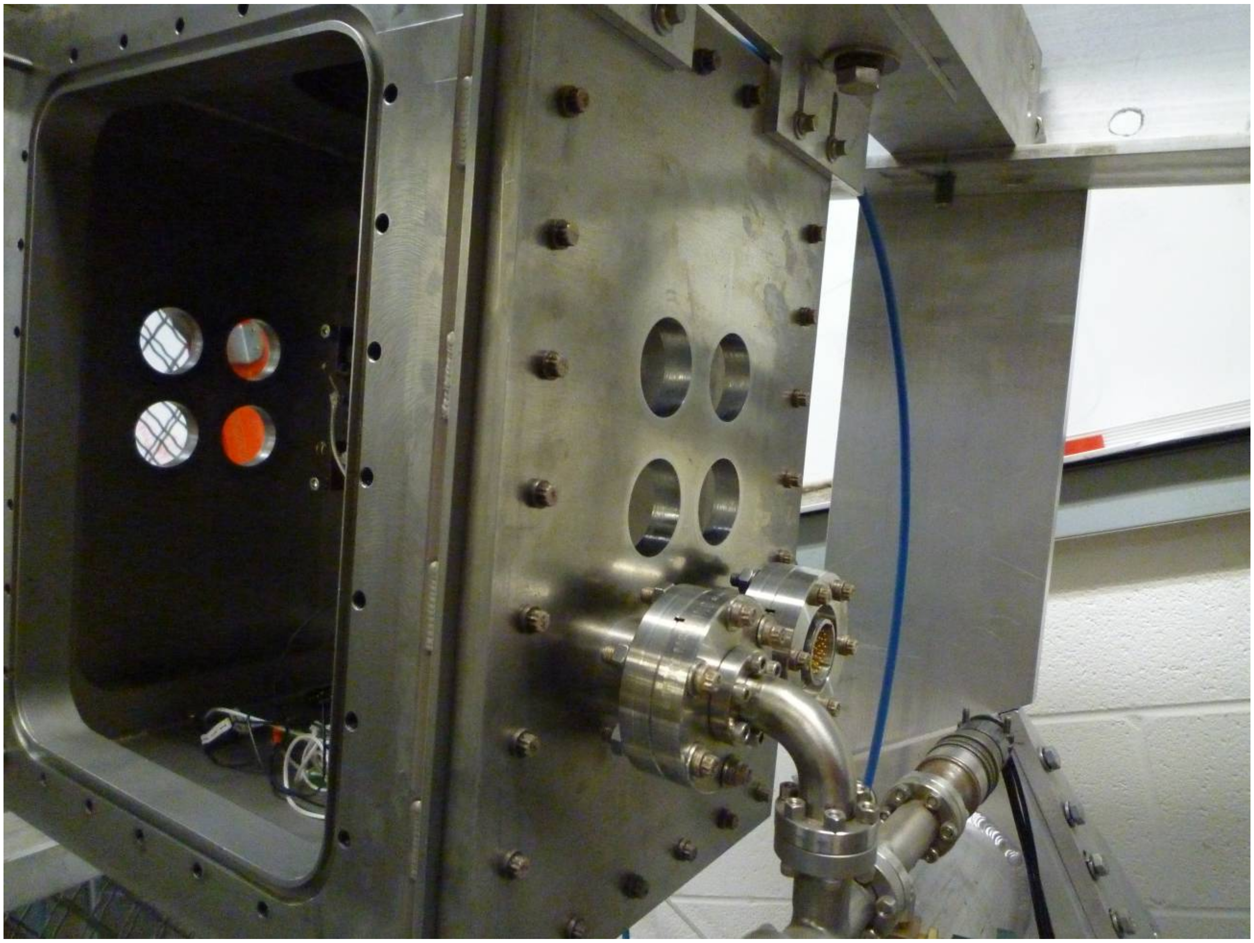

Figure C.3: Gunbox with all guide tube hardware removed. Clean surfaces are prepped for reinstallation of the barrel fitting and light gate mount.

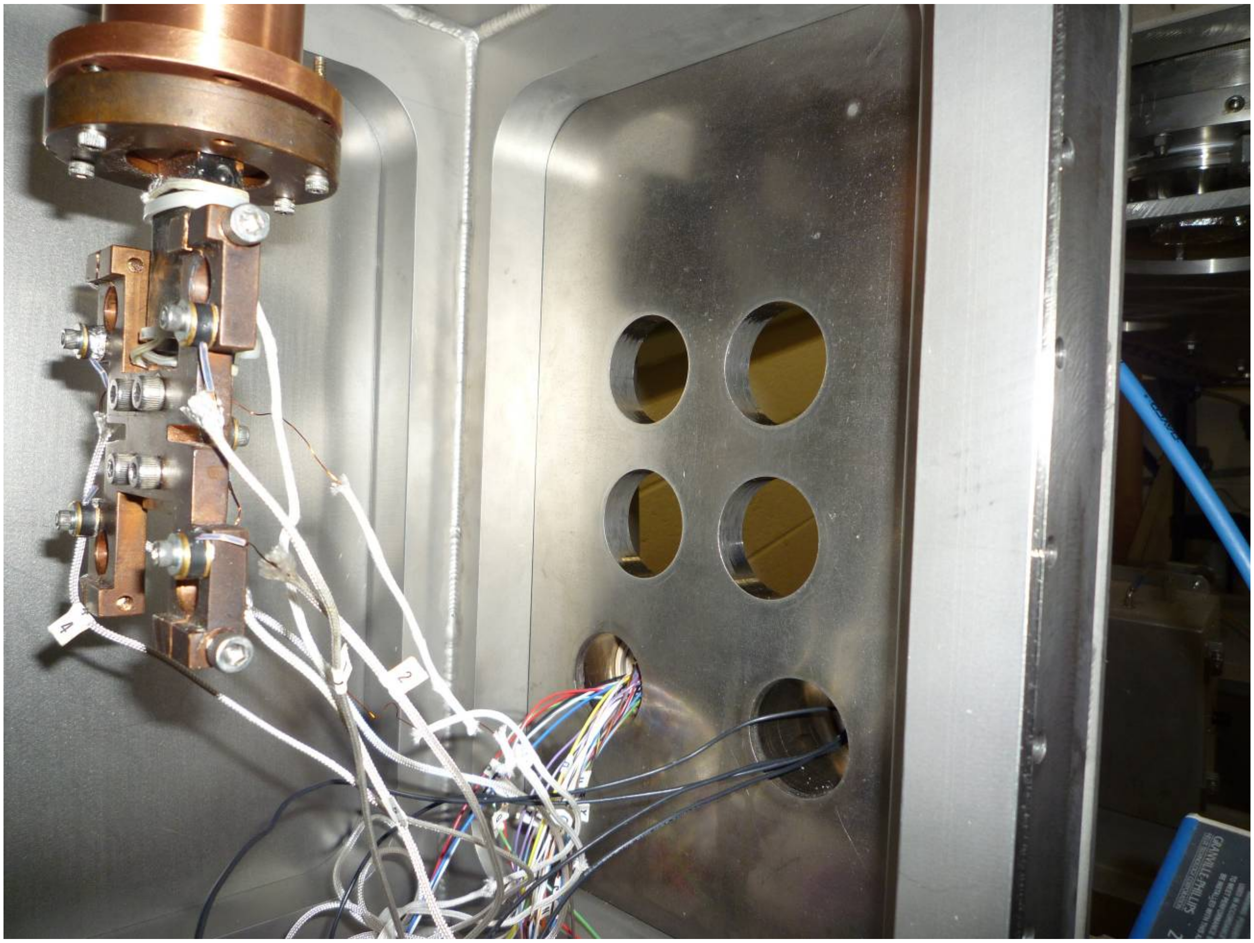

Figure C.4: Gunbox interior with all guide tube hardware removed. The copper block connection to the cold head is visible. The holes are where the barrel connections will attach.

Figure C.5: Side view of the barrel compression fitting which mounts on the inside of the gunbox.

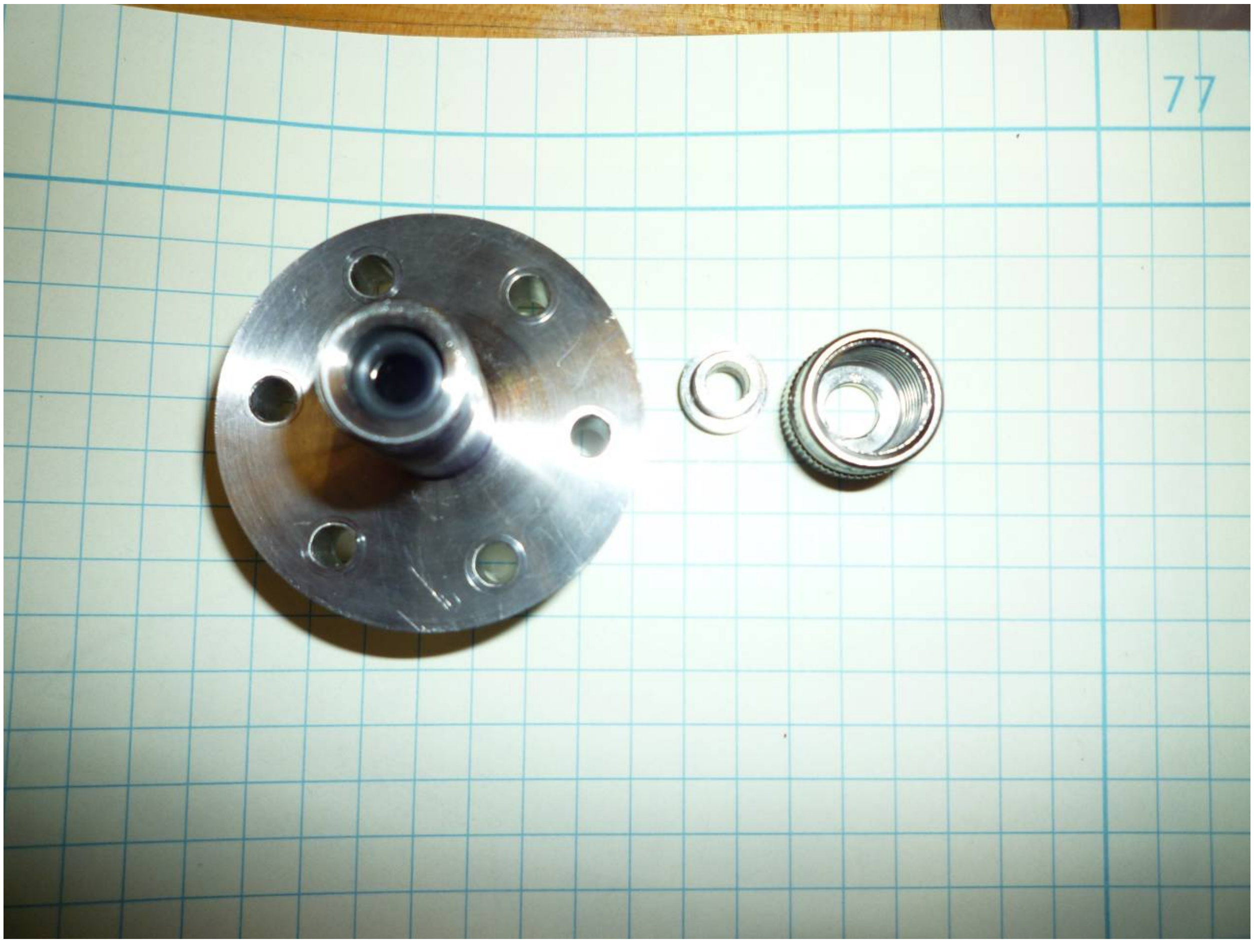

Figure C.6: Top view of the barrel compression fitting which mounts on the inside of the gunbox. The two pieces on the right are upside-down. As the rightmost piece tightens down, the middle piece compresses the O-ring, forming the seal around the barrel.

Figure C.7: Bottom view of the barrel compression fitting which goes inside the gunbox. The O-ring isolates the barrel volume from the gunbox volume. The gunbox seal is on the light gate mounting pieces on the outside of the gunbox.

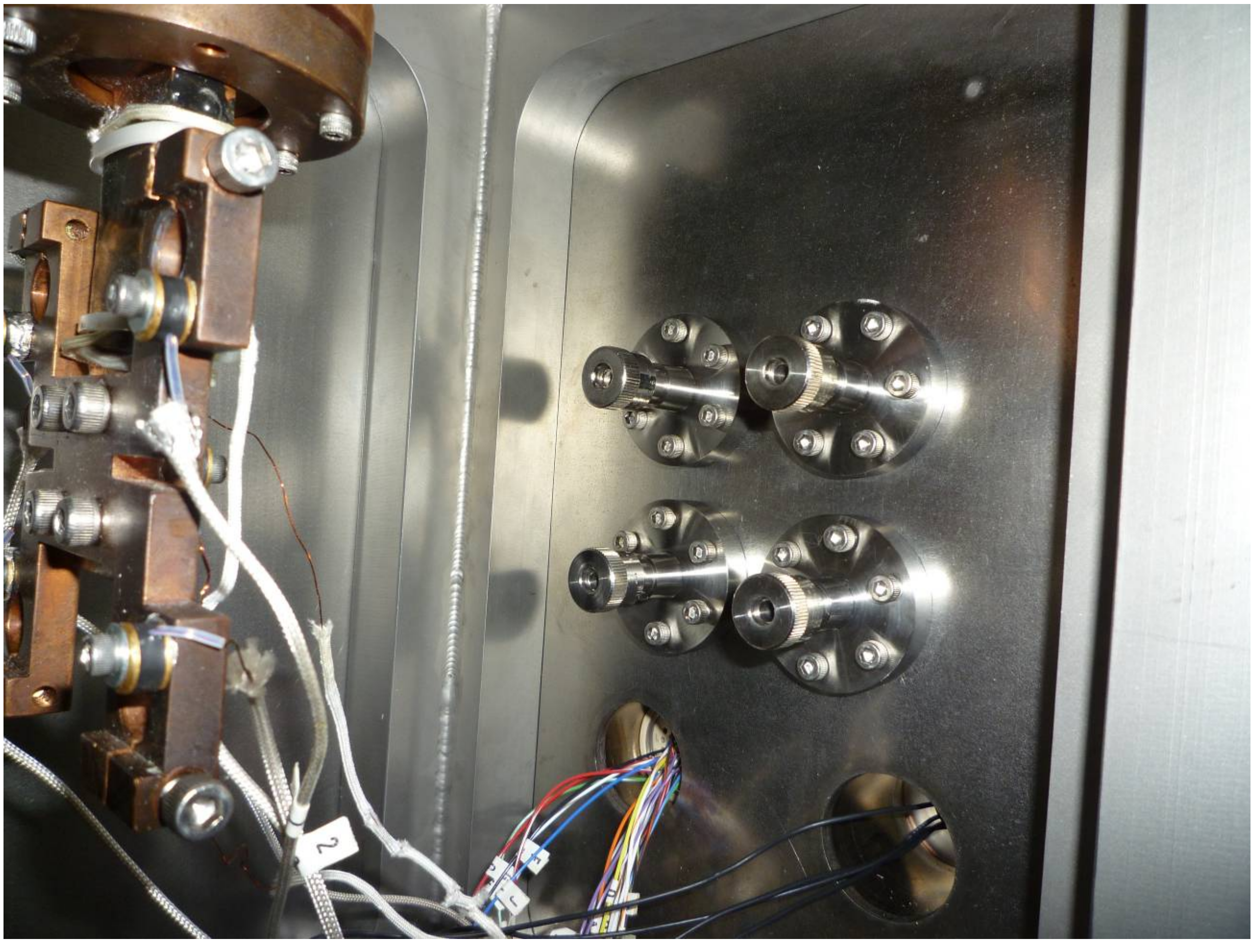

Figure C.8: Barrel compression fittings mounted on the inside of the gunbox. The bolts attach to the light gate mounting pieces.

Figure C.9: Light gate mounts which go on the outside of the gunbox along with the light gate mounting plate. All pieces are shown with downstream side up.

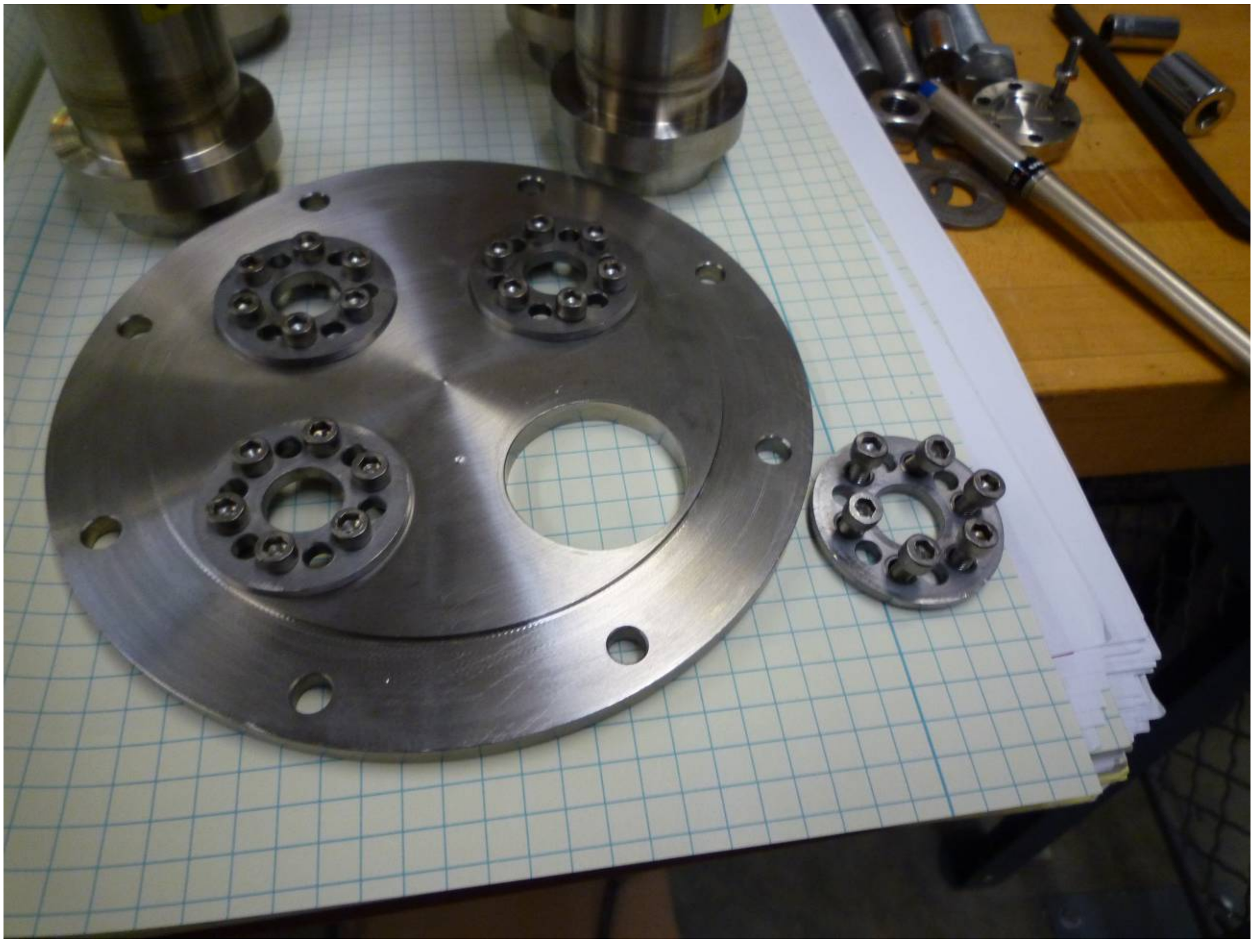

Figure C.10: Closer look at the light gate mounting plate.

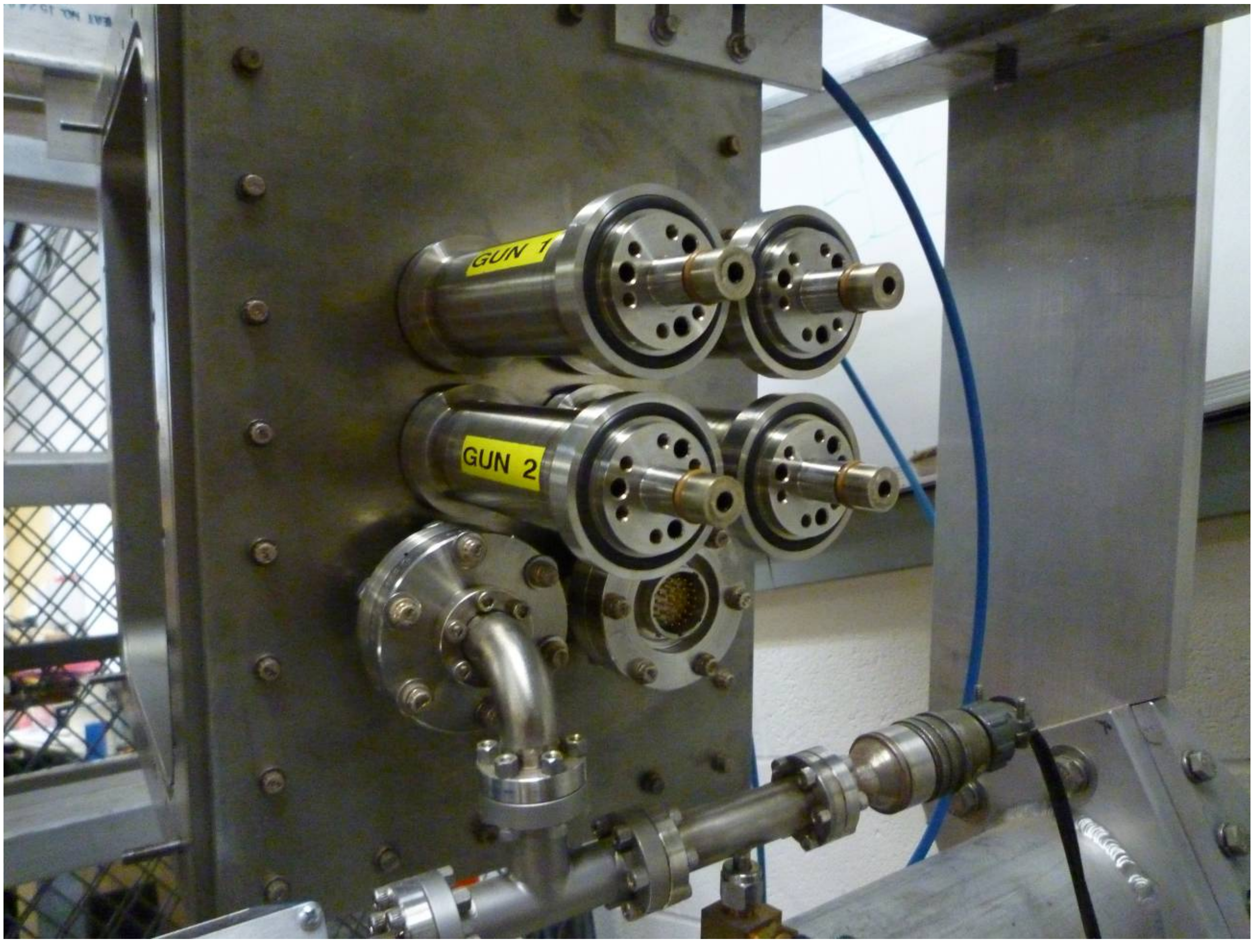

Figure C.11: The barrel connector/light gate mount attached to the gunbox.

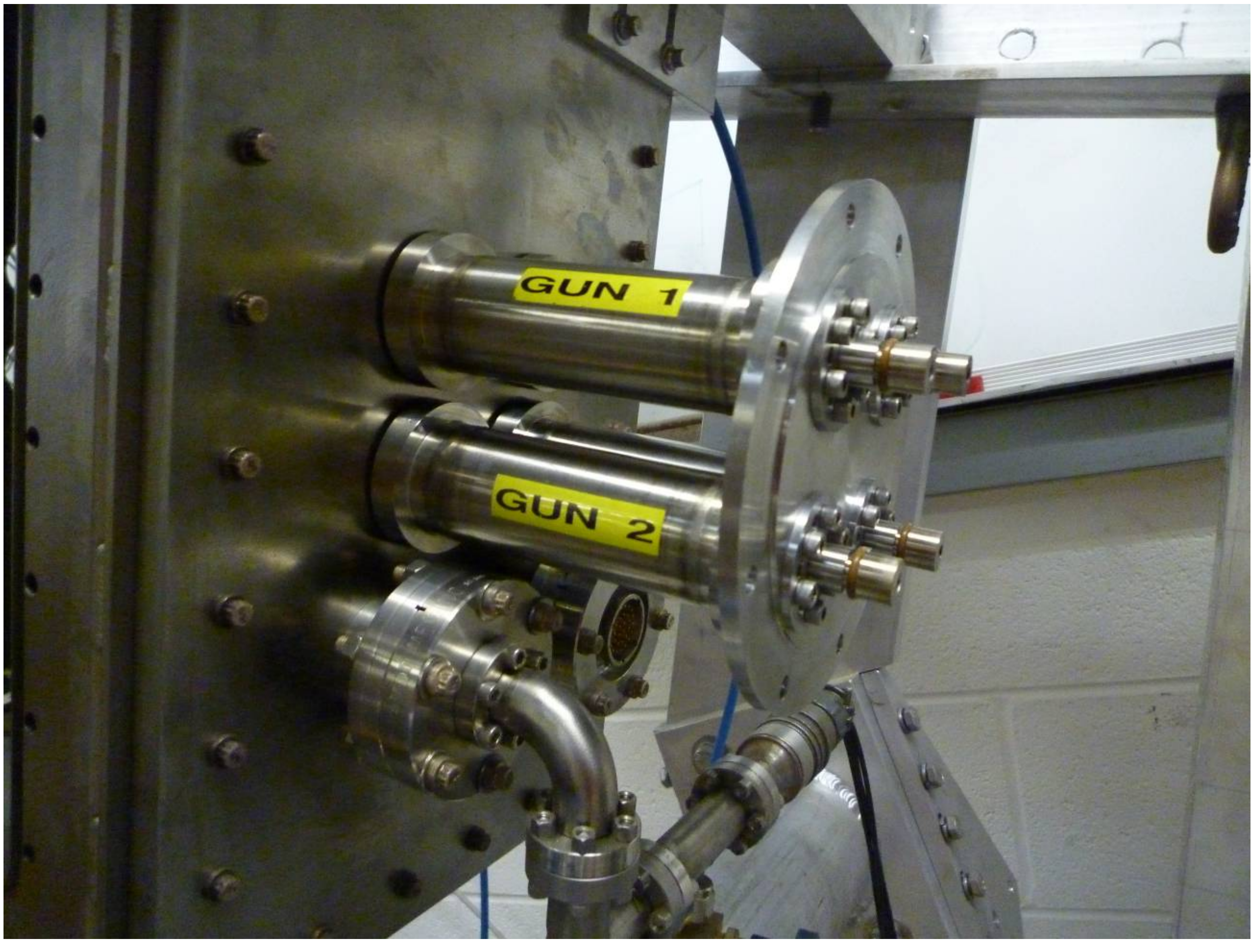

Figure C.12: Side view of the light gate mounts and the mounting plate.

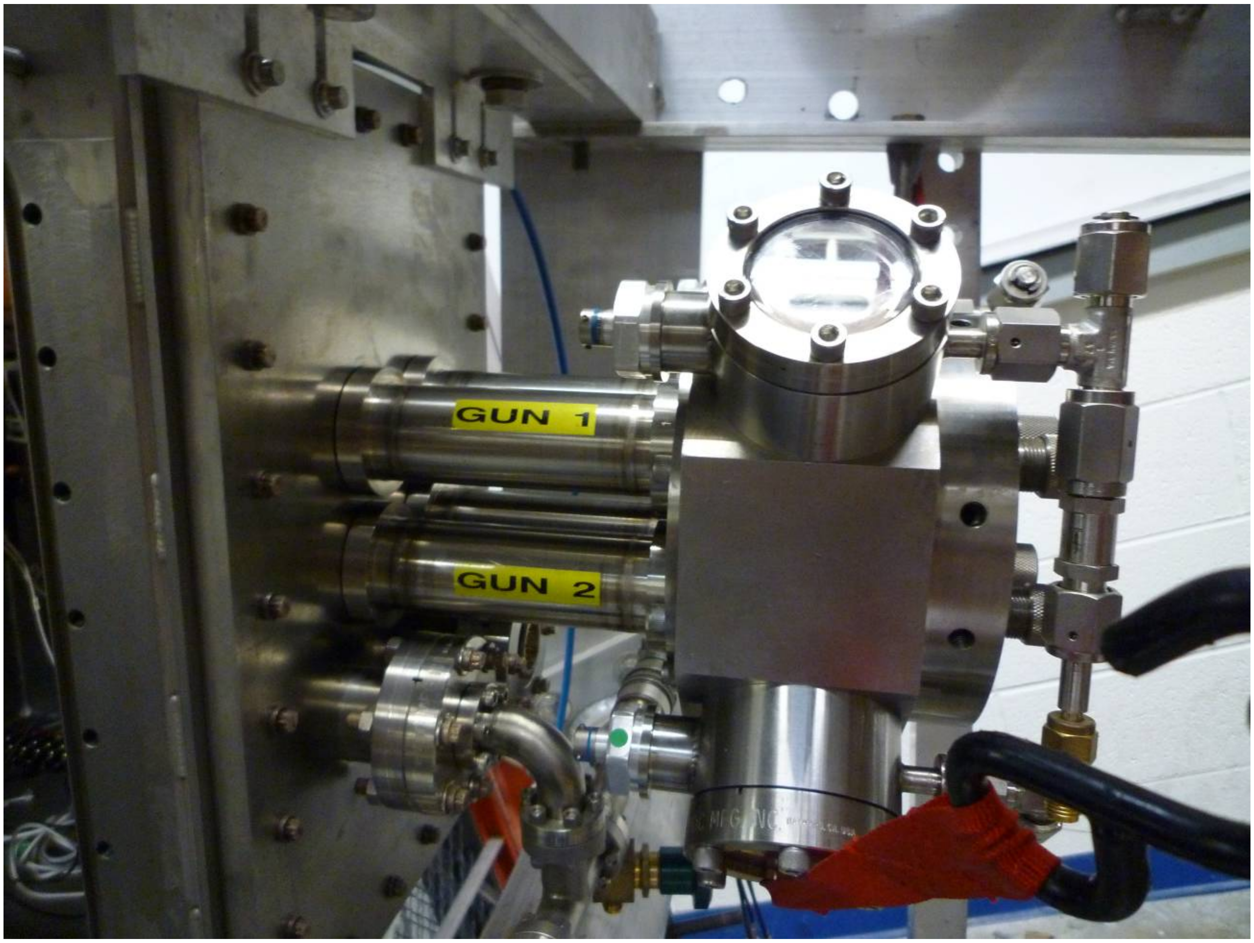

Figure C.13: Light gate attached to the mounting plate and the barrel fittings are tightened down to support the light gate.

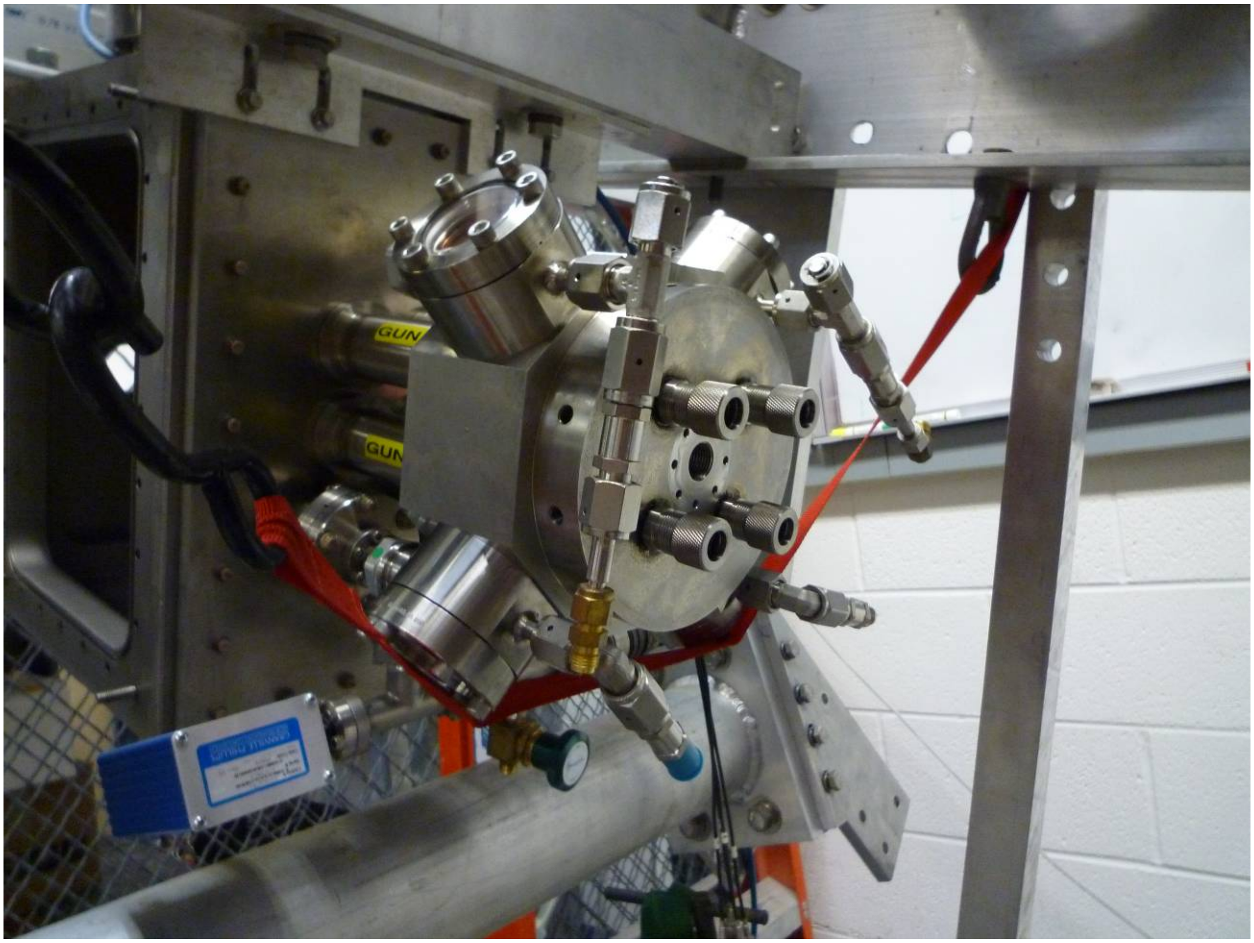

Figure C.14: Downstream end of the light gate cavity. The central bellows connects to the central hole in the light gate and the stage 1 guide tube pieces screw in to the compression fittings.

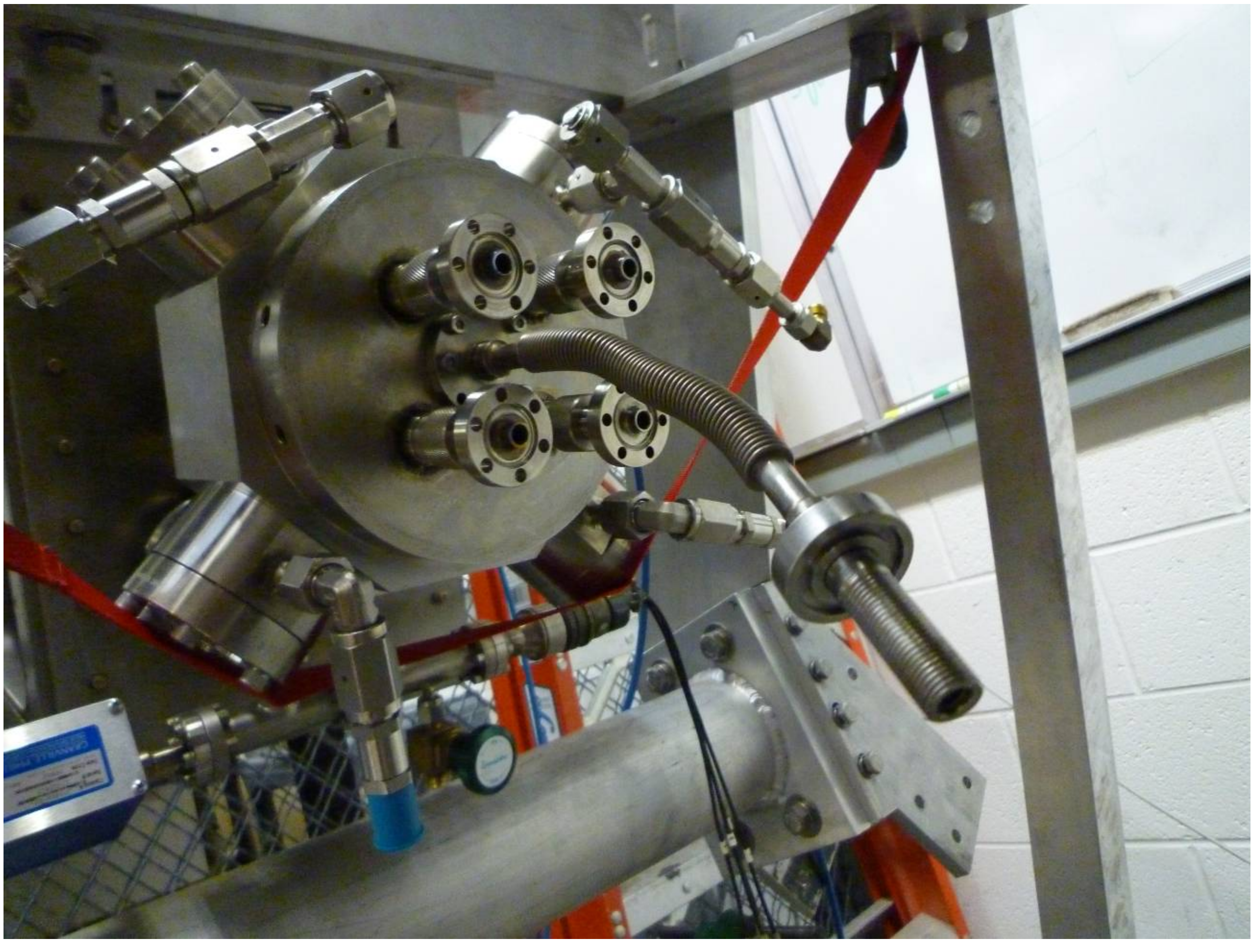

Figure C.15: Light gate with central bellows and stage 1 guide tubes attached. The gate valves and stage 2 guide tubes connect to the conflat connections and the central bellows attaches to the stage 3 plate.

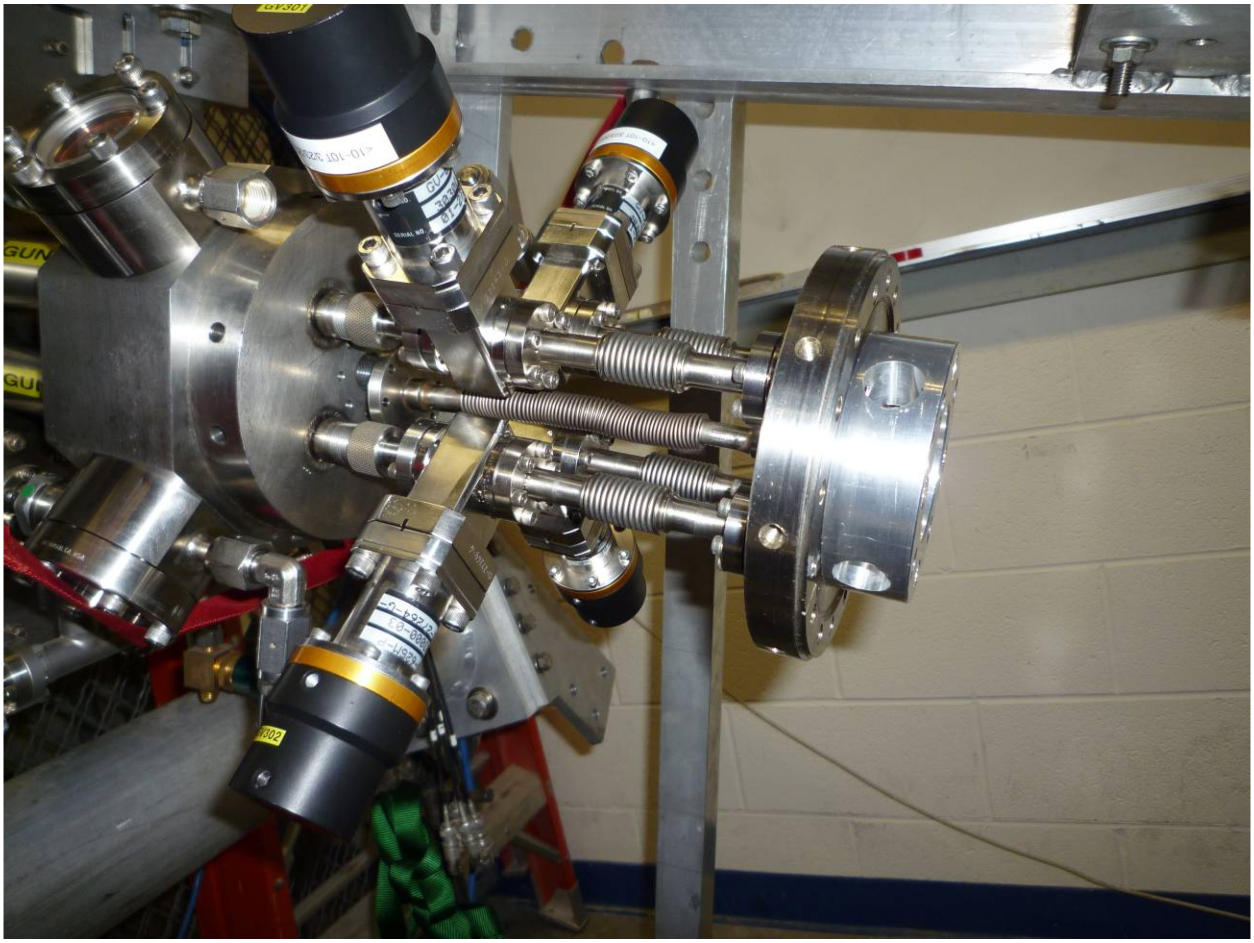

Figure C.16: Side view of the injector assembly after installing the barrel gate valves, stage 2 guide tubes and stage 3 connecting plate. The next step is to tighten down the central bellows and the gate valve conflat connections and then install the shield. This adds the needed structural support for the stage 2 guide tubes.

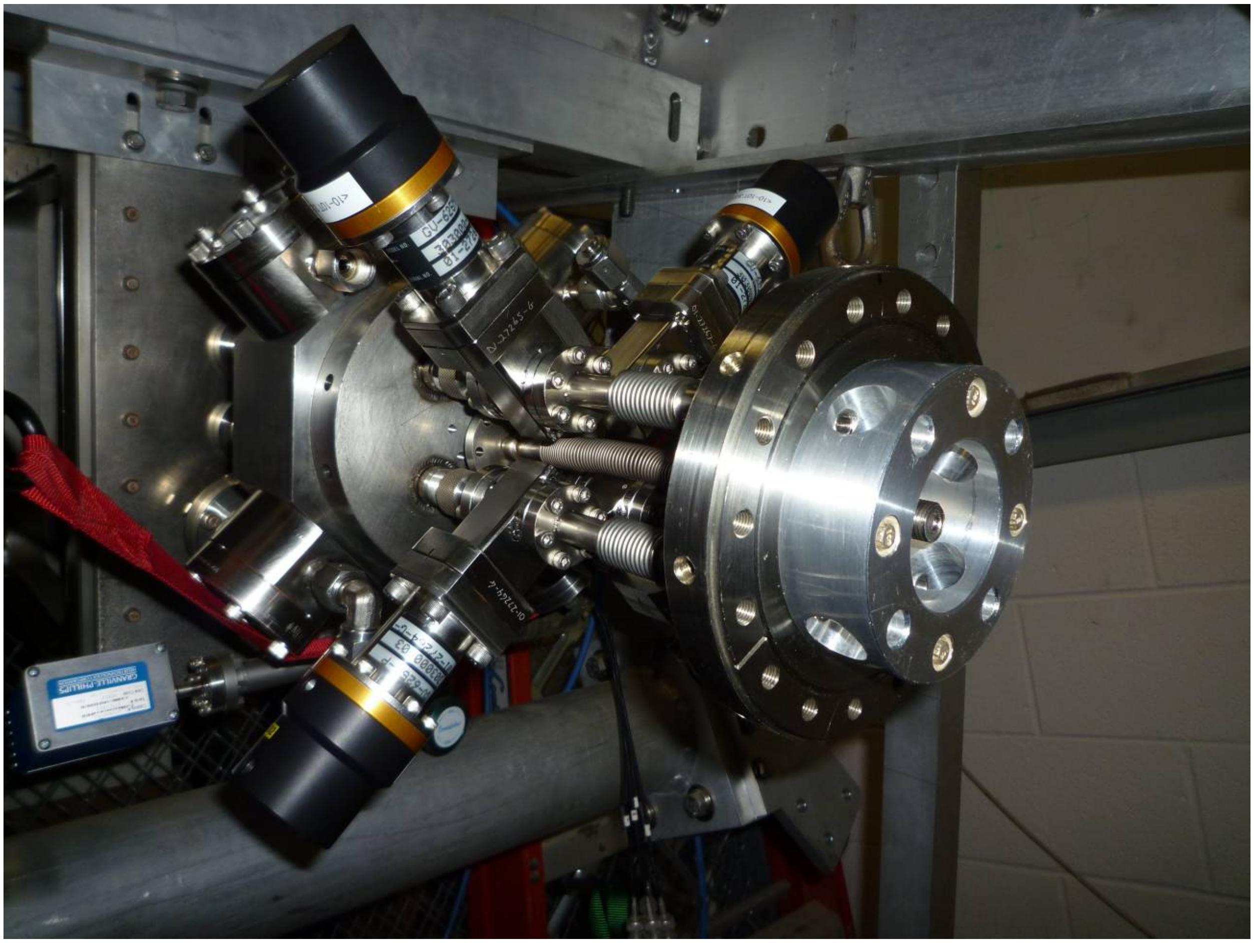

Figure C.17: Downstream view of the injector assembly prior to the installation of the shield.

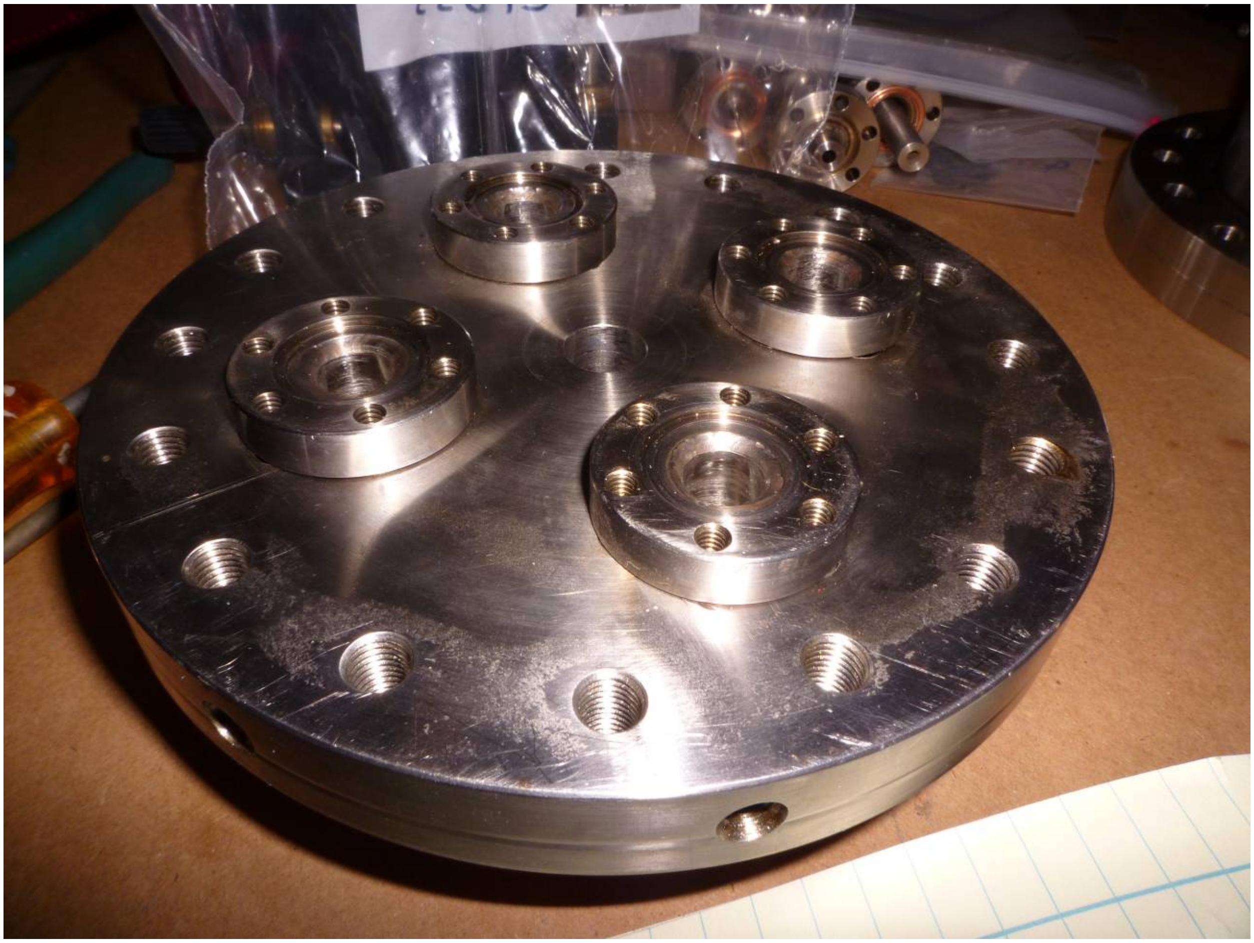

Figure C.18: Upstream view of stage 3 plate which connects to the stage 2 guide tubes.

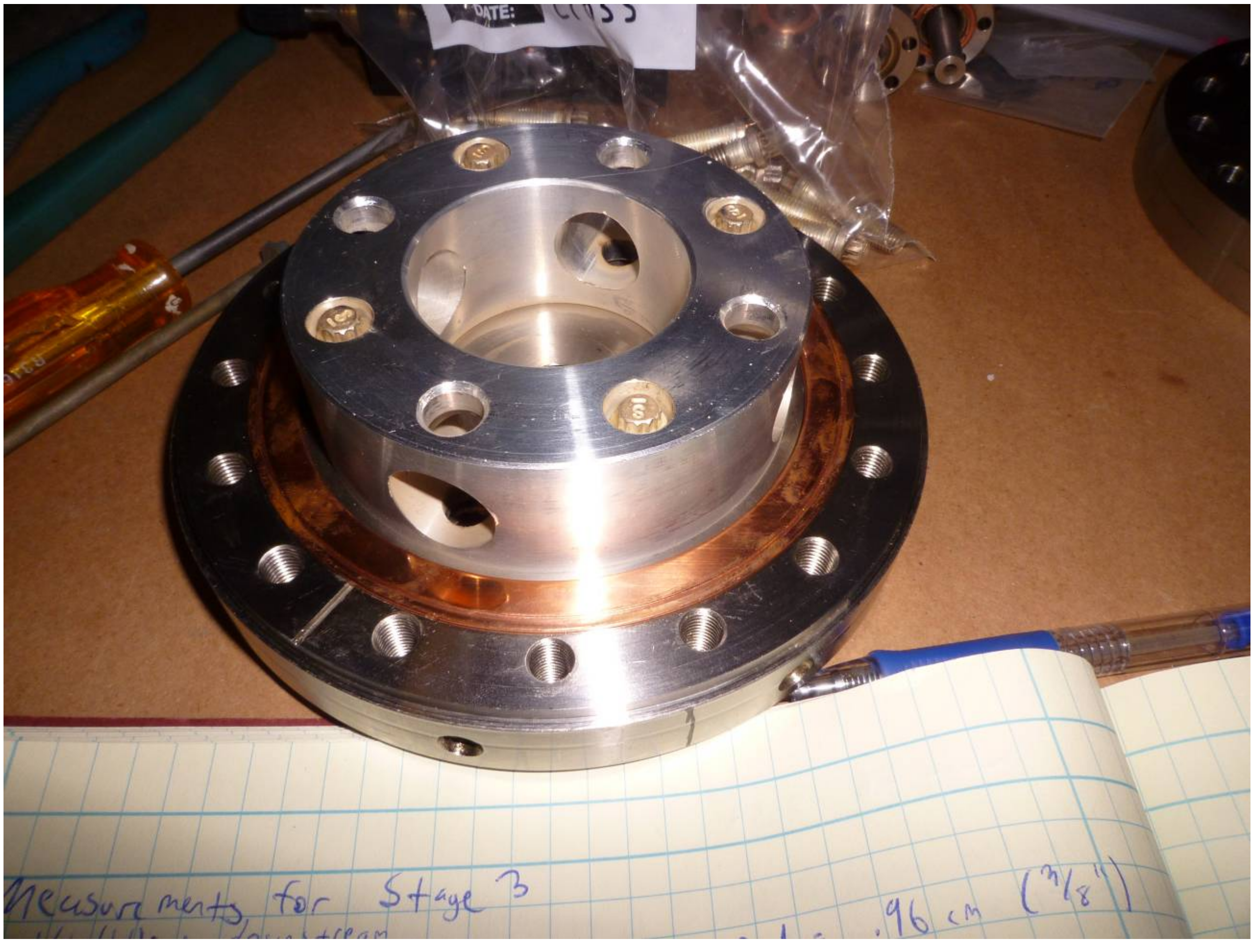

Figure C.19: Downstream view of the stage 3 plate.

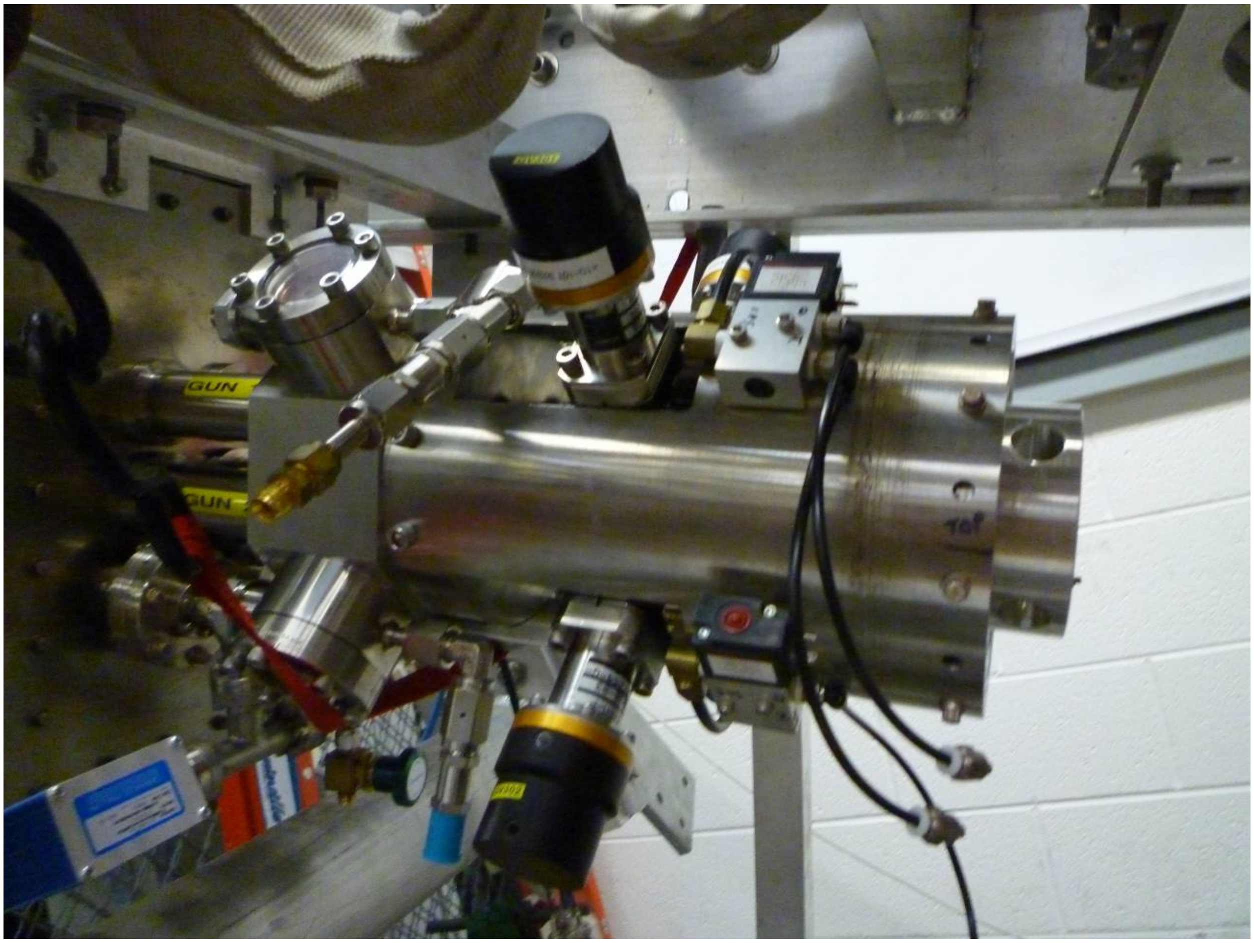

Figure C.20: Side view of the injector assembly after installation of the outer shield.

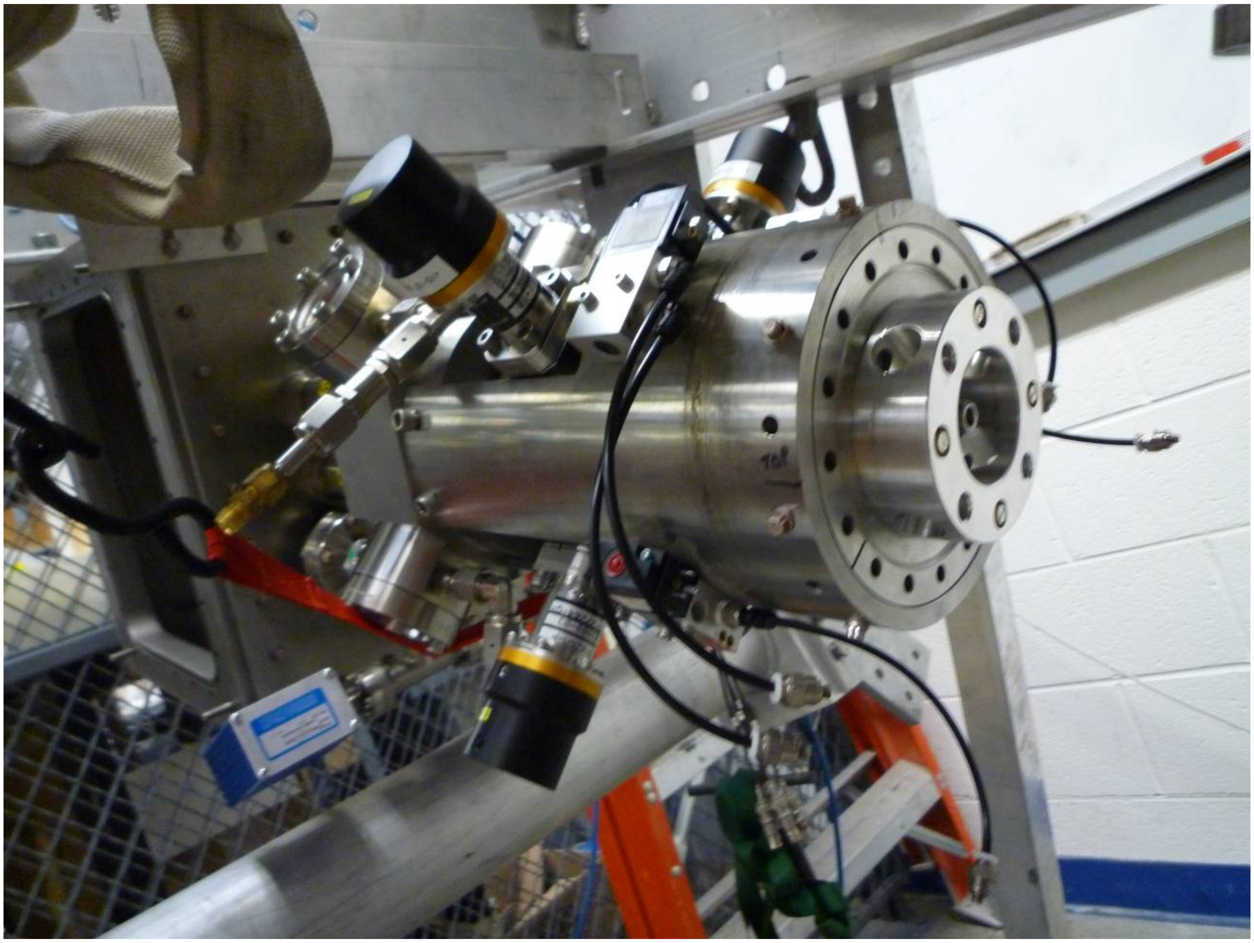

Figure C.21: Downstream view of the injector assembly after installation of the outer shield. The stage 3 guide tubes insert intot he four holes on the inner ring

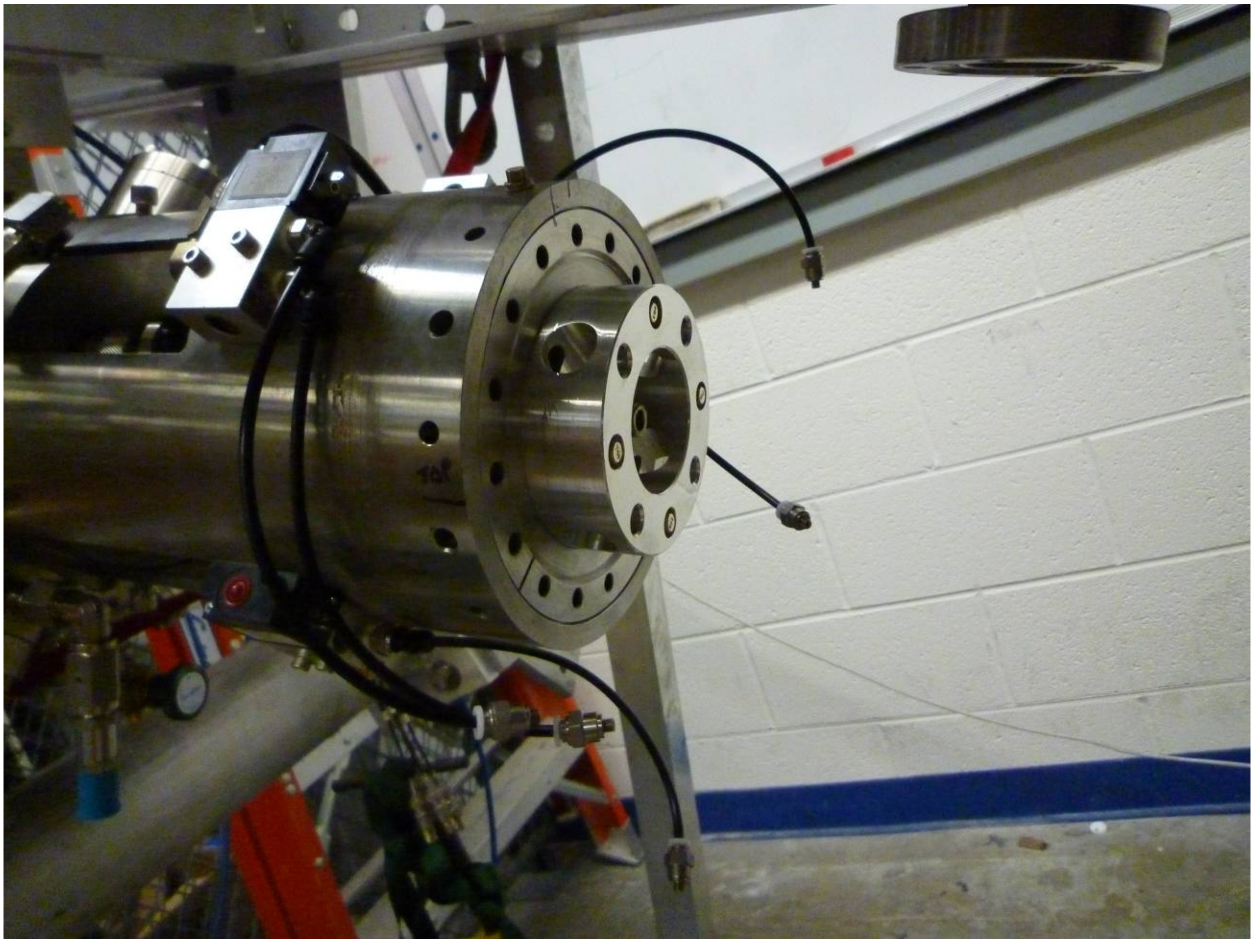

Figure C.22: The injector assembly up to the point where the stage 3 guide tube section is installed.

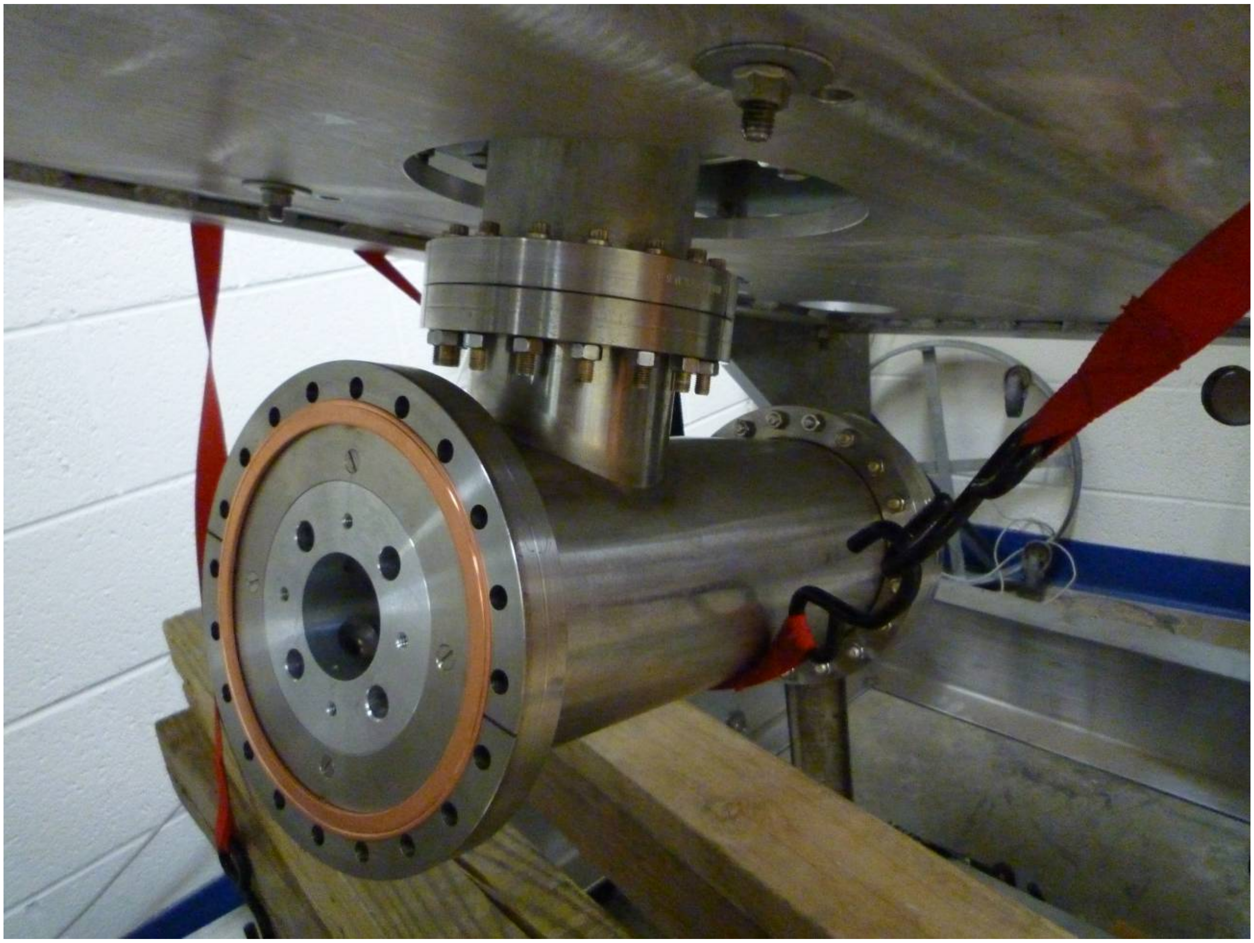

Figure C.23: Assembly from the second surge tank connection starts with the stage 6 guide tubes. The stage 5 guide tube section and microwave cavity are installed next. The surge tank connection is the primary support for the injection line.

Figure C.24: The stage 5 guide tube section with the downstream side up. The guide tubes insert into the holes of the stage 6 section.

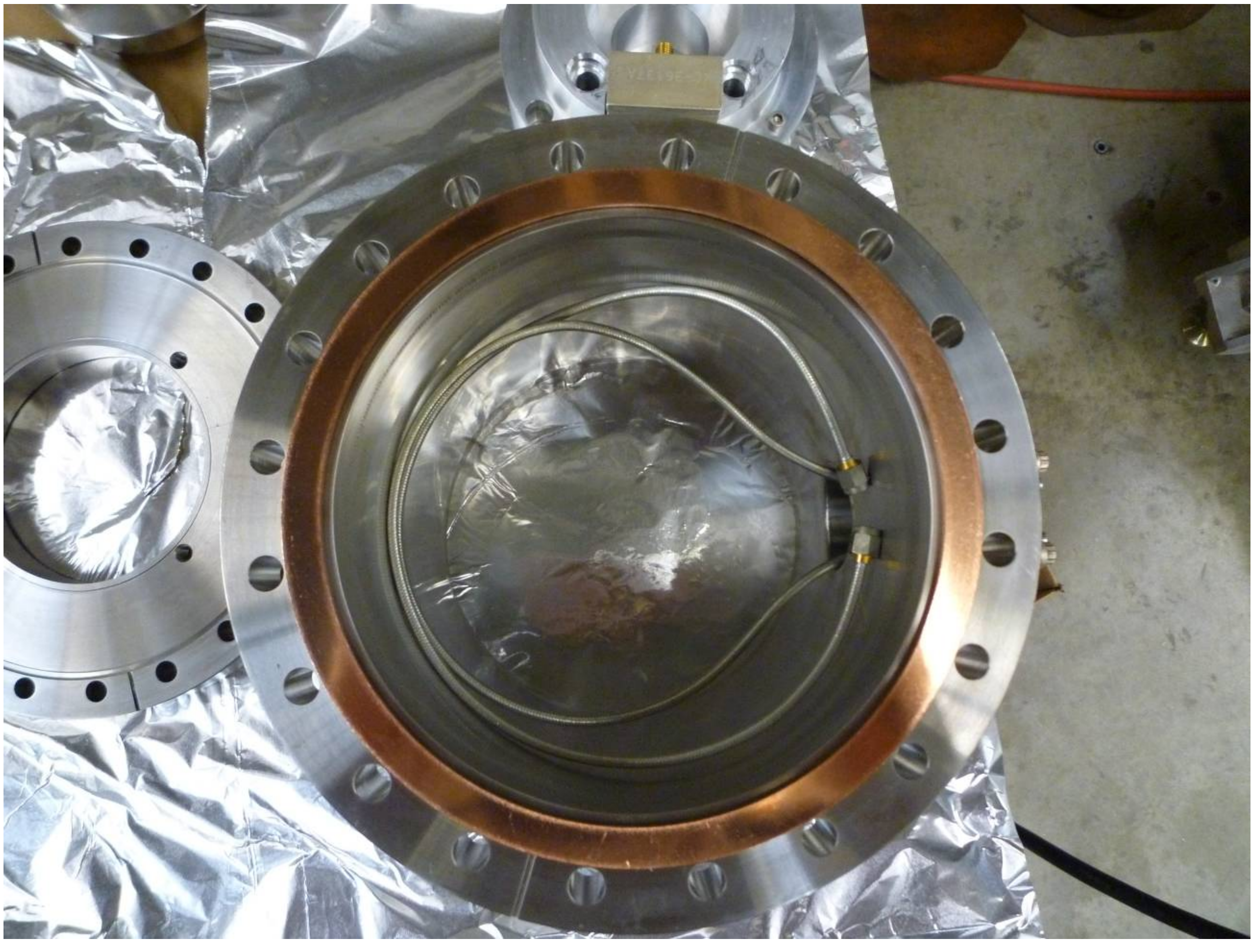

Figure C.25: The inside of the microwave housing including the microwave connections. The microwave cavity is inserted and hooked up and the stage 5 guide tube section fits into it.

Figure C.26: The microwave cavity section put together.

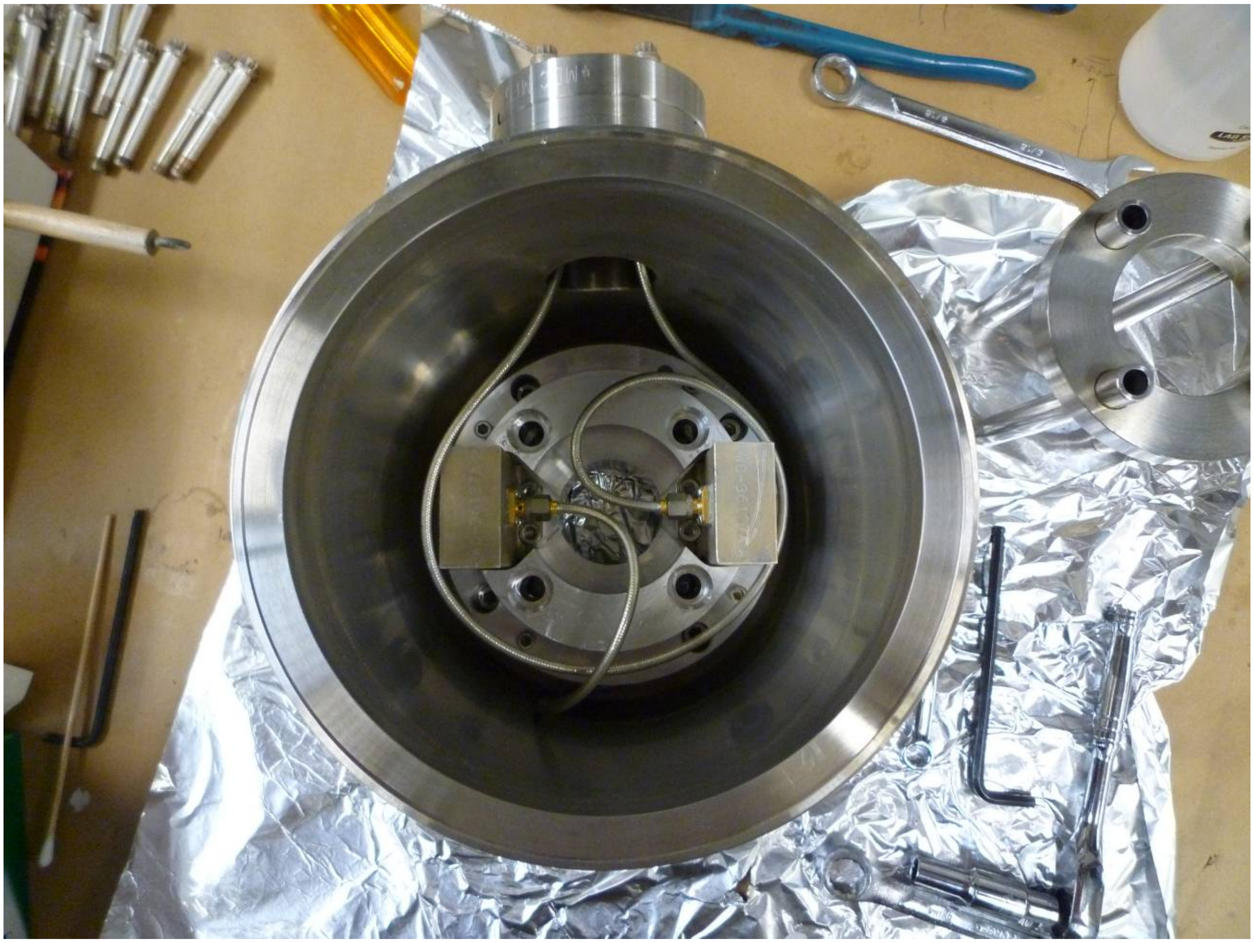

Figure C.27: Guide tube alignment measurements

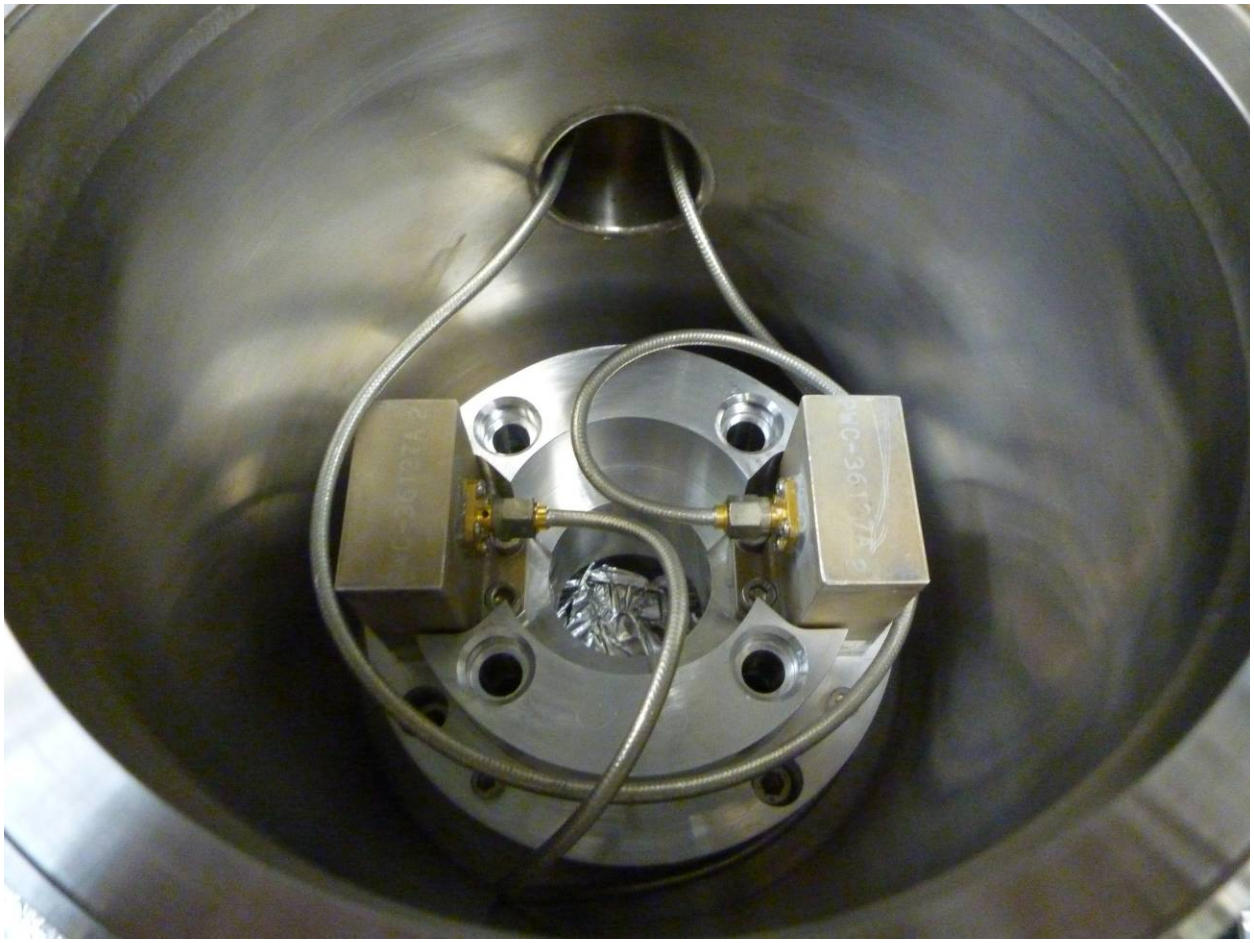

Figure C.28: Microwave cavity hookup inside the microwave cavity housing. The stage 5 guide tube section fits into the four holes.

Figure C.29: Microwave cavity housing complete with stage 5 guide tube section. This end fits into the holes of the stage 6 guide tube section.

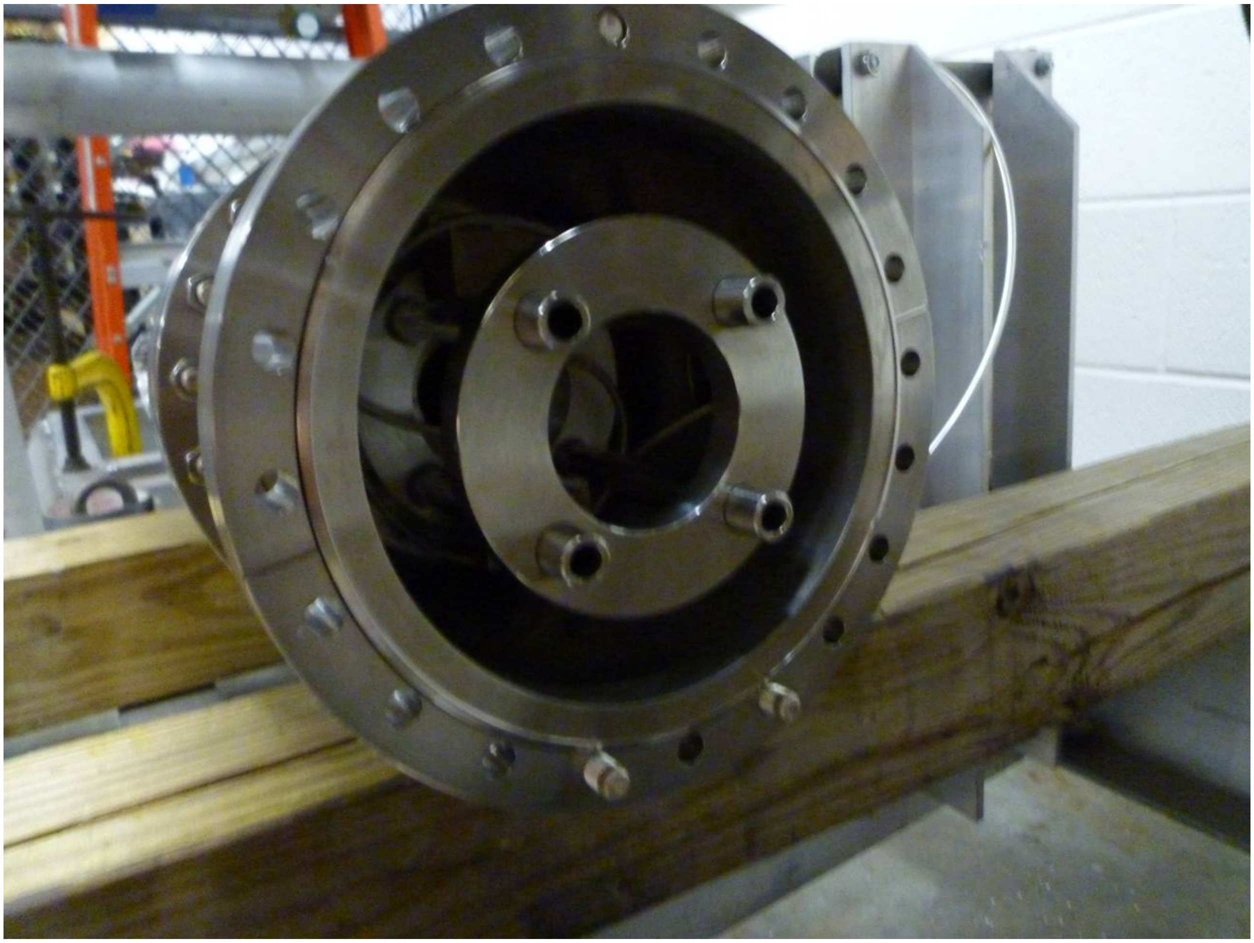

Figure C.30: The microwave cavity and stage 5 guide tube section just prior to the assembly with the stage 6 section.

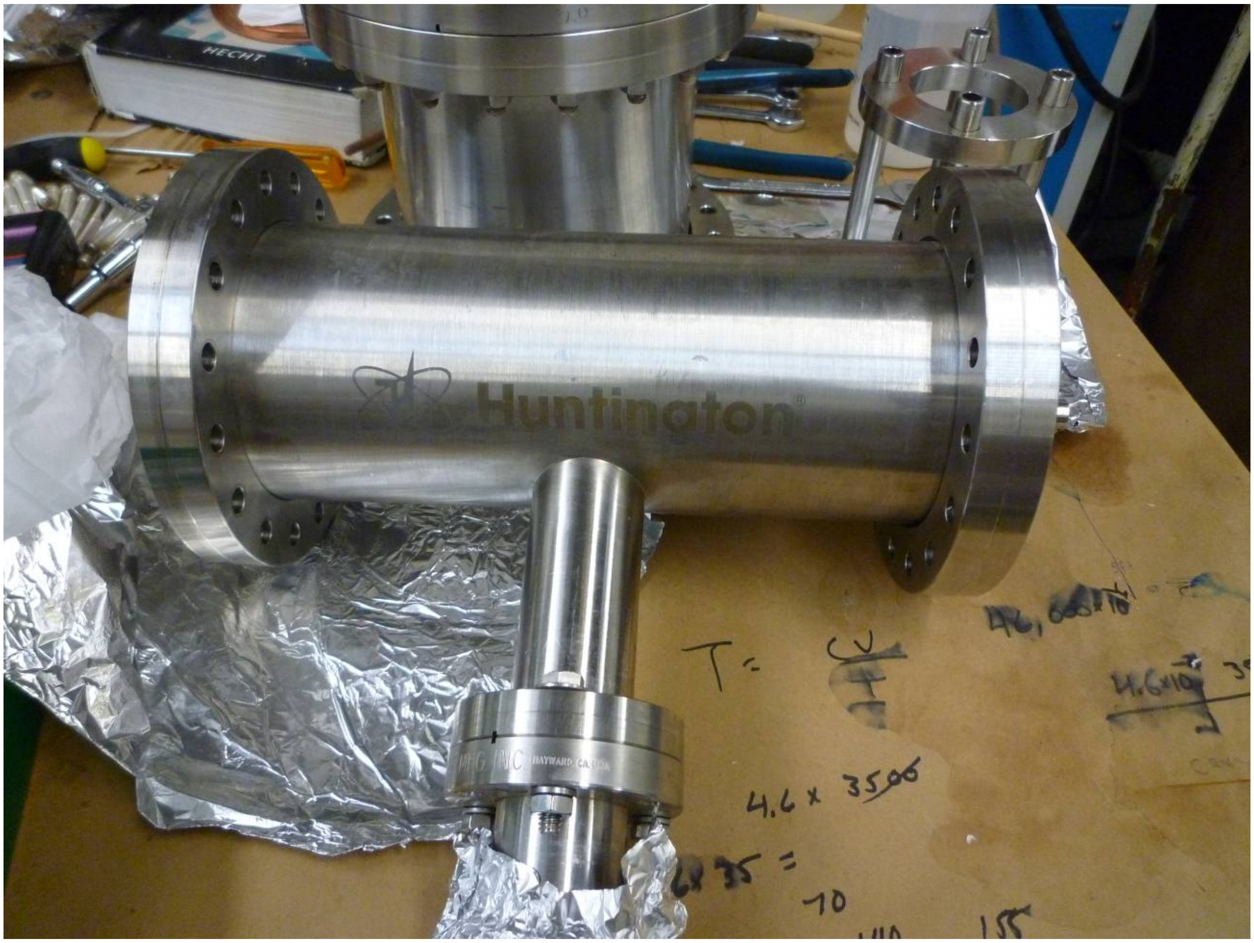

Figure C.31: Stage 4 guide tube housing on the bench. Downstream side is to the right.

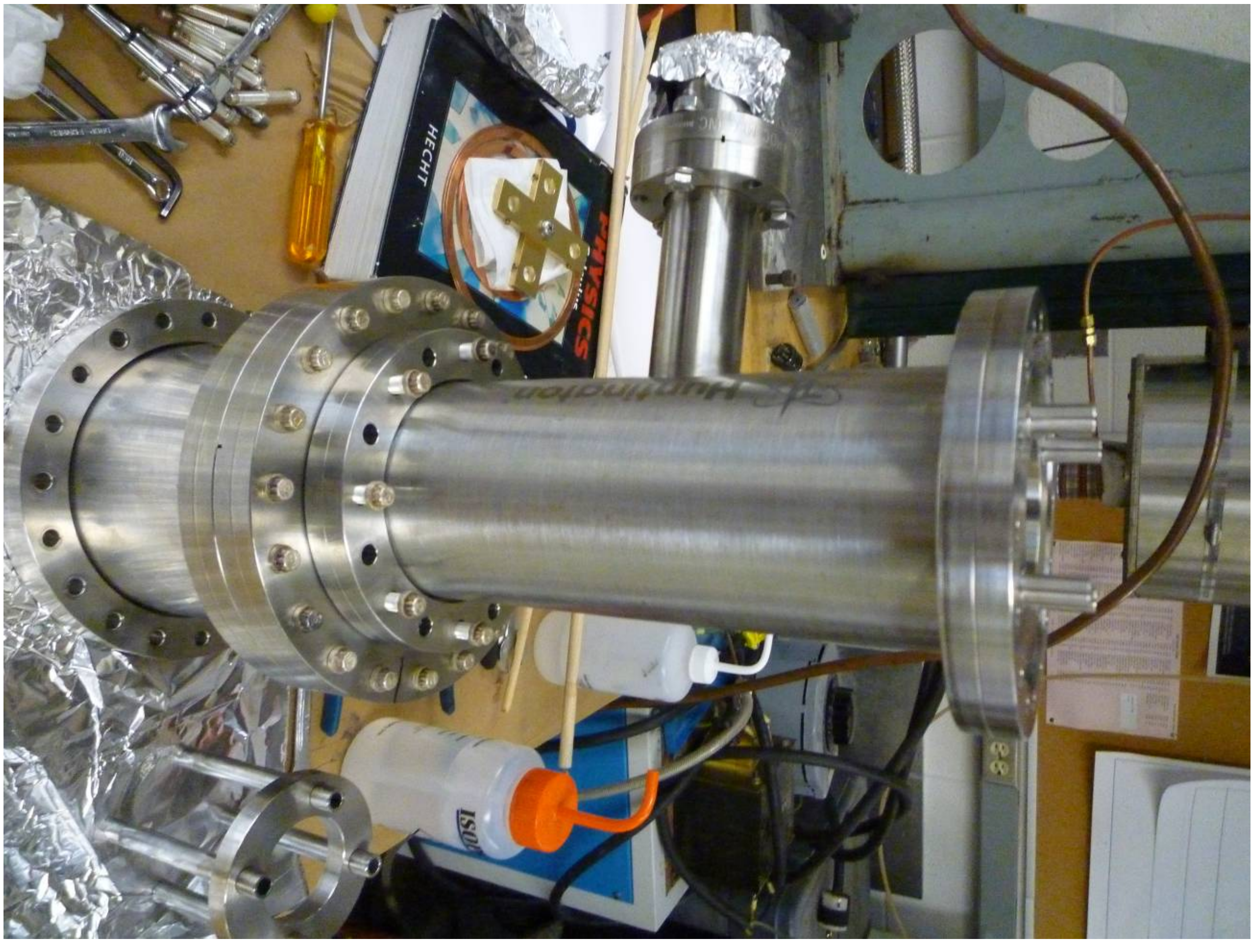

Figure C.32: The stage 4 guide tube section along with the microwave cavity housing.

Figure C.33: Assembly of the injector continues with the installation of the microwave cavity housing (with stage 5 guide tube section) as well as the stage 4 guide tube section. This leaves only the gate valve and stage 3 guide tube section left.

Figure C.34: The GV305 gate valve is installed, but the stage 3 guide tube section does not fit easily into the space.

Figure C.35: A lab jack is set up to support the lower section of the injection line. In this way, the entire injection line is retracted to make room for the final guide tube section. Then the tank is lifted back into place and secured in place.

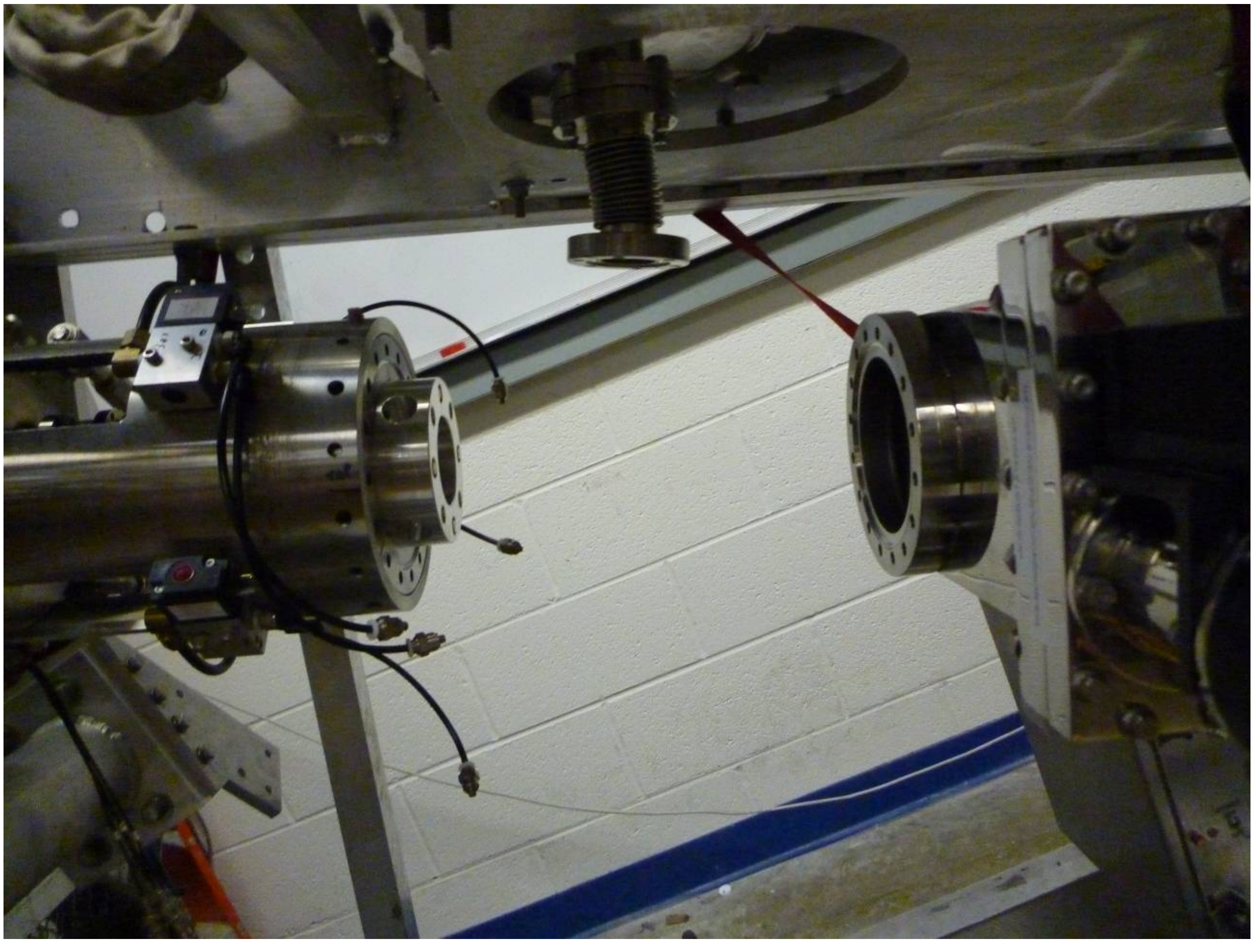

Figure C.36: The state of the injector with the stage 3 guide tube section missing. Insufficient room was available to install the final section, so the lower section of injection line (right) was retracted to make room. The stage 3 guide tube section was attached to the gate valve, and then the surge tank injection line was aligned and moved back into place before securing the stage 3 connection with the stage 3 plate/shield assembly.

Figure C.37: Upstream side of the stage 3 guide tube section.

Figure C.38: Stage 3 section attached to the gate valve, then moved back into place where it is secured to the stage 3 plate/shield assembly and to the surge tank connection.

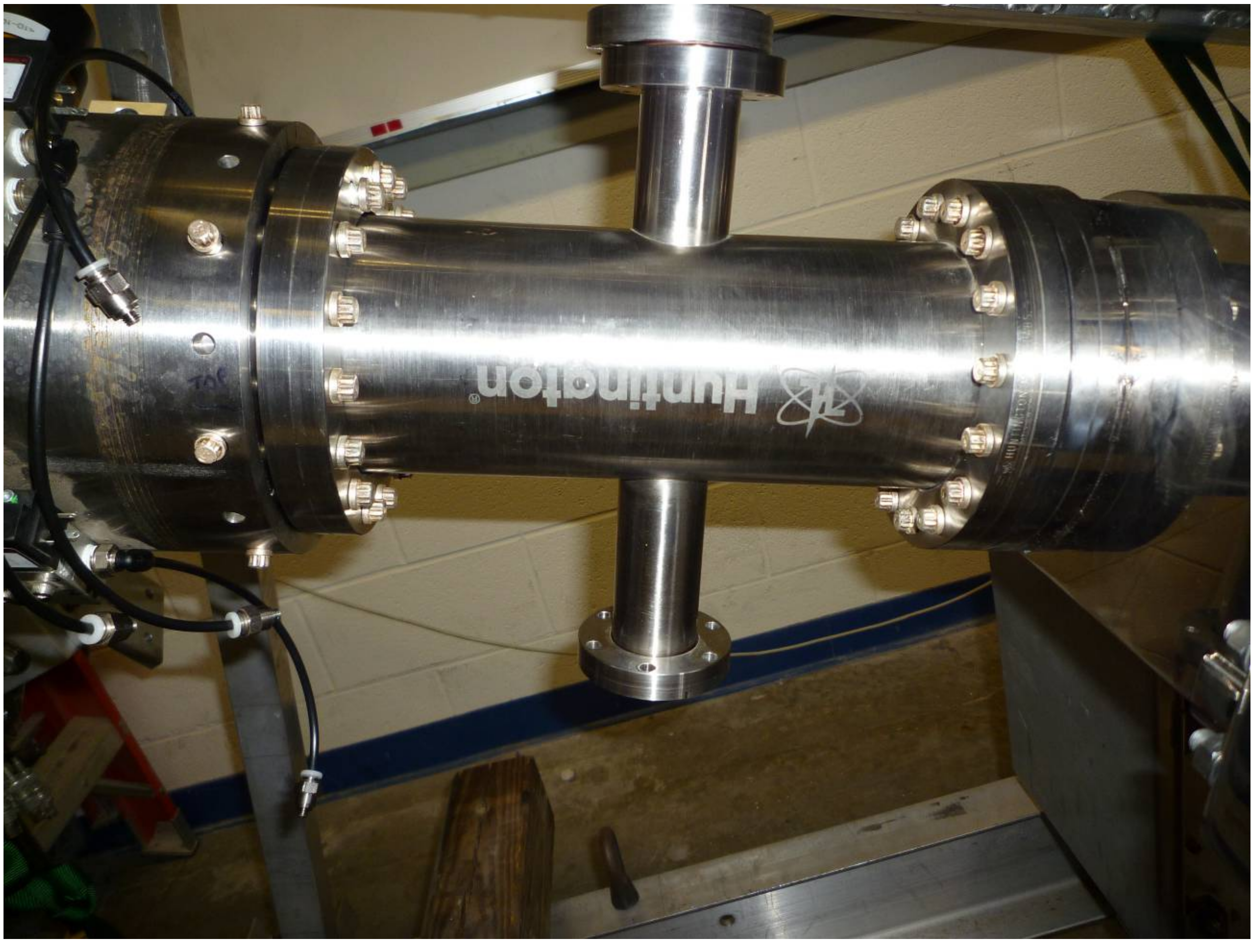

Figure C.39: Final state of assembly before all stages of the injector are tightened down.

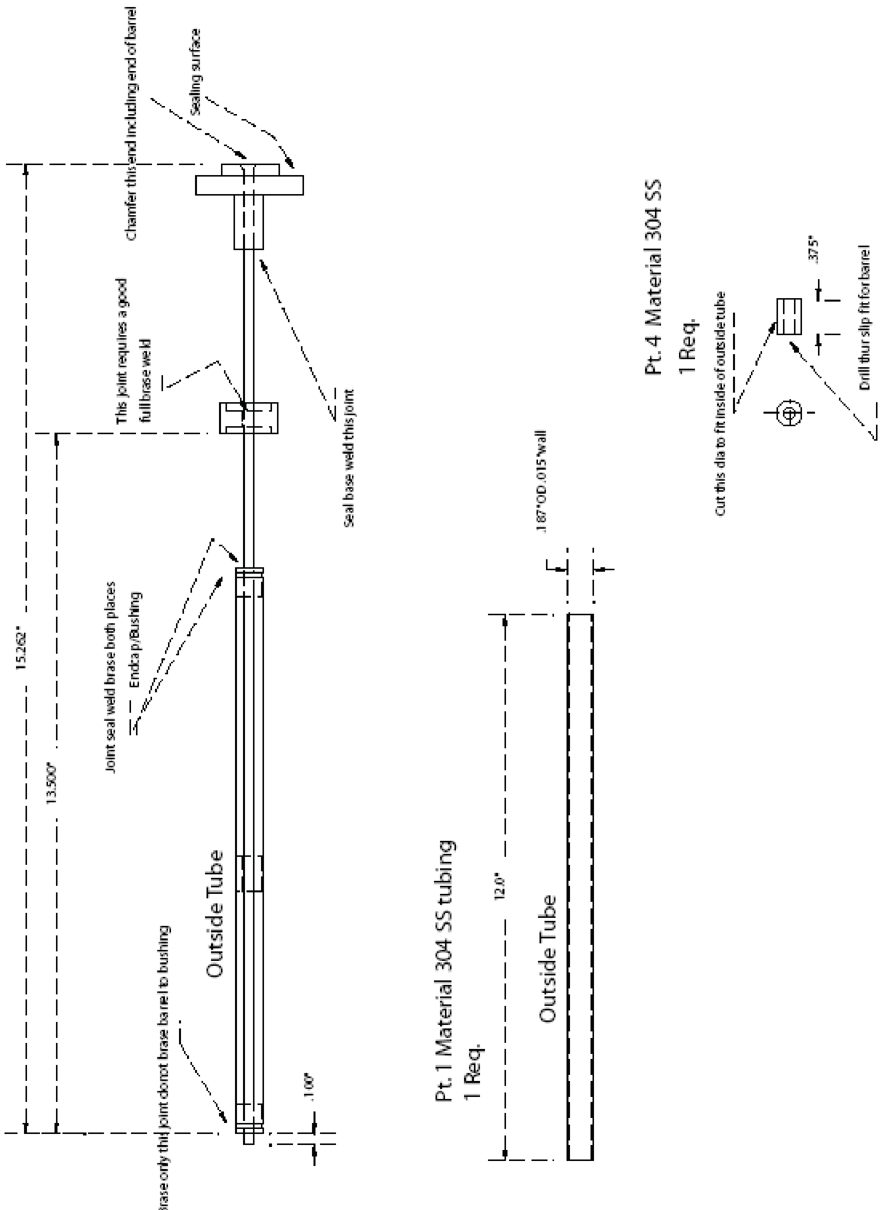

Figure C.40: Barrel drawings

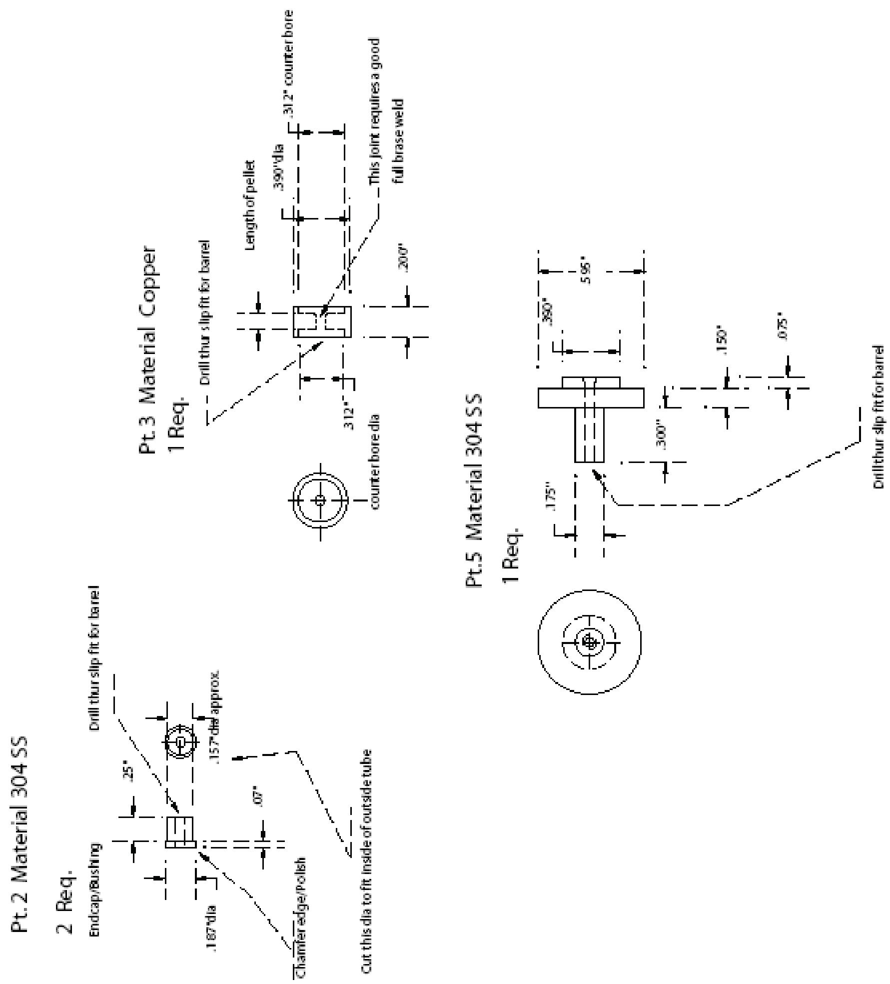

Figure C.41: Barrel drawings

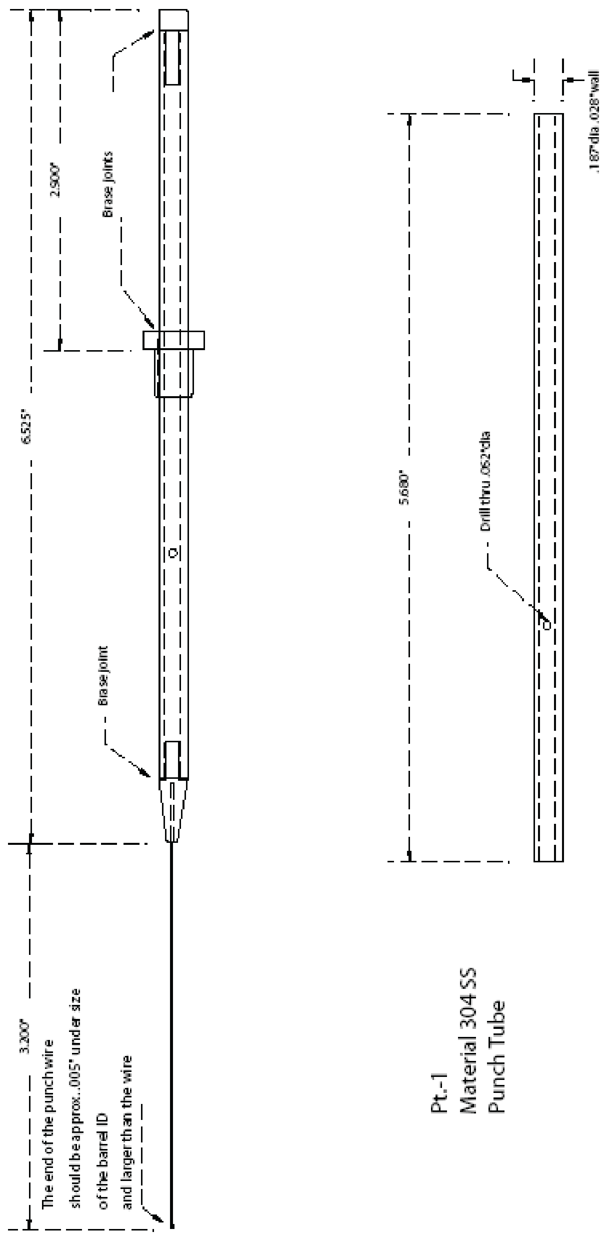

Figure C.42: Punch drawings

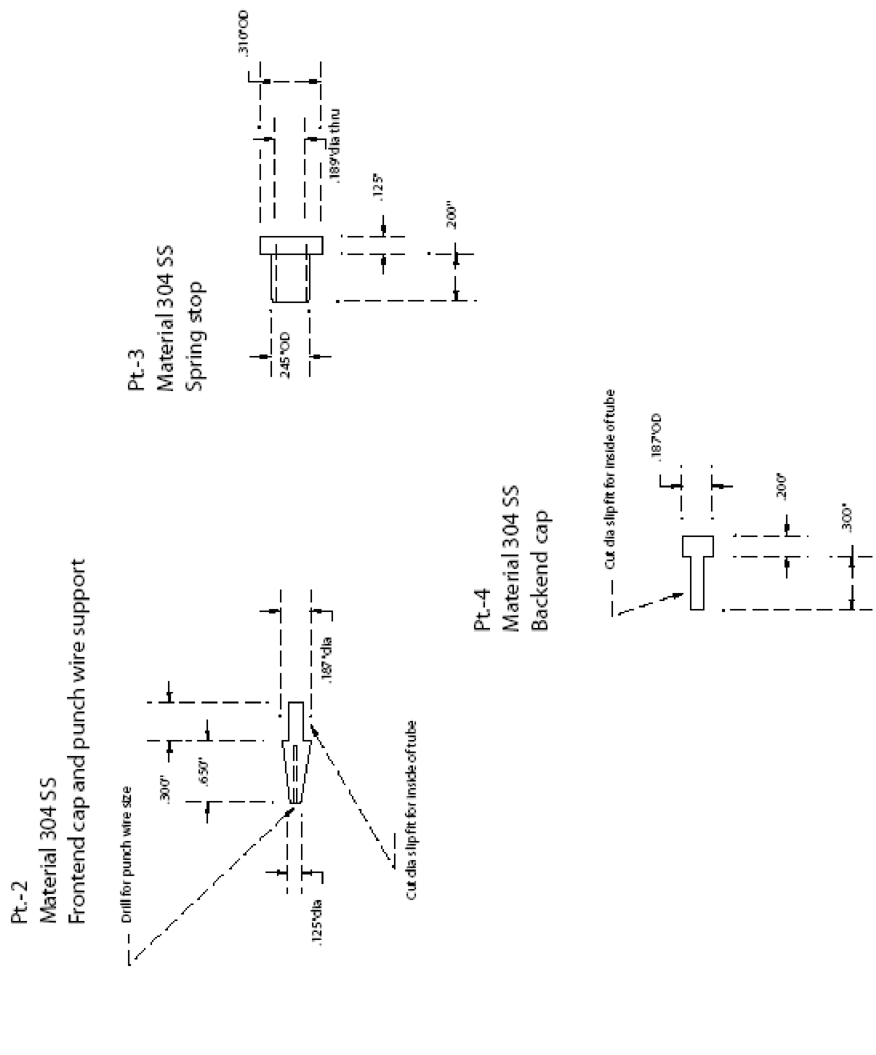

Figure C.43: Punch drawings

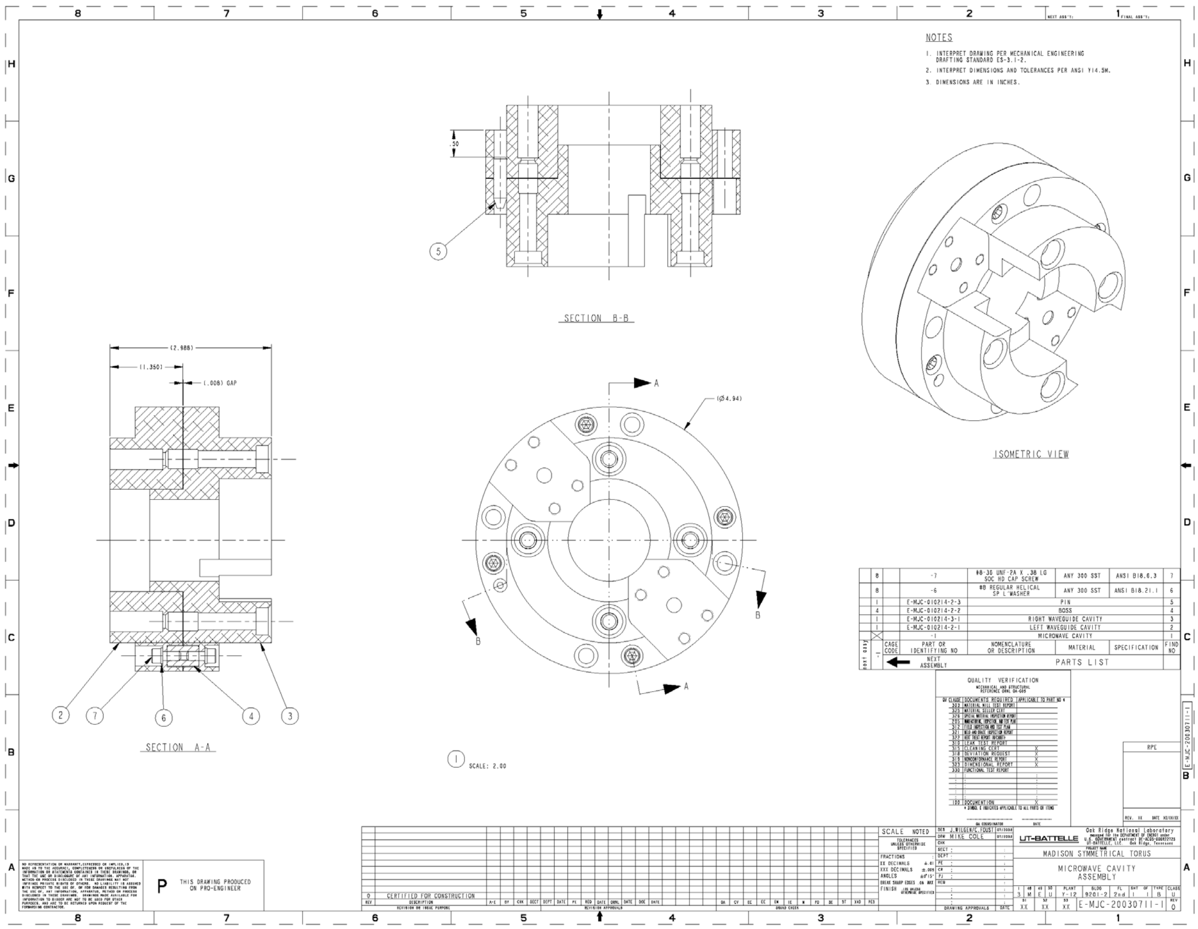

Figure C.44: Microwave cavity drawings

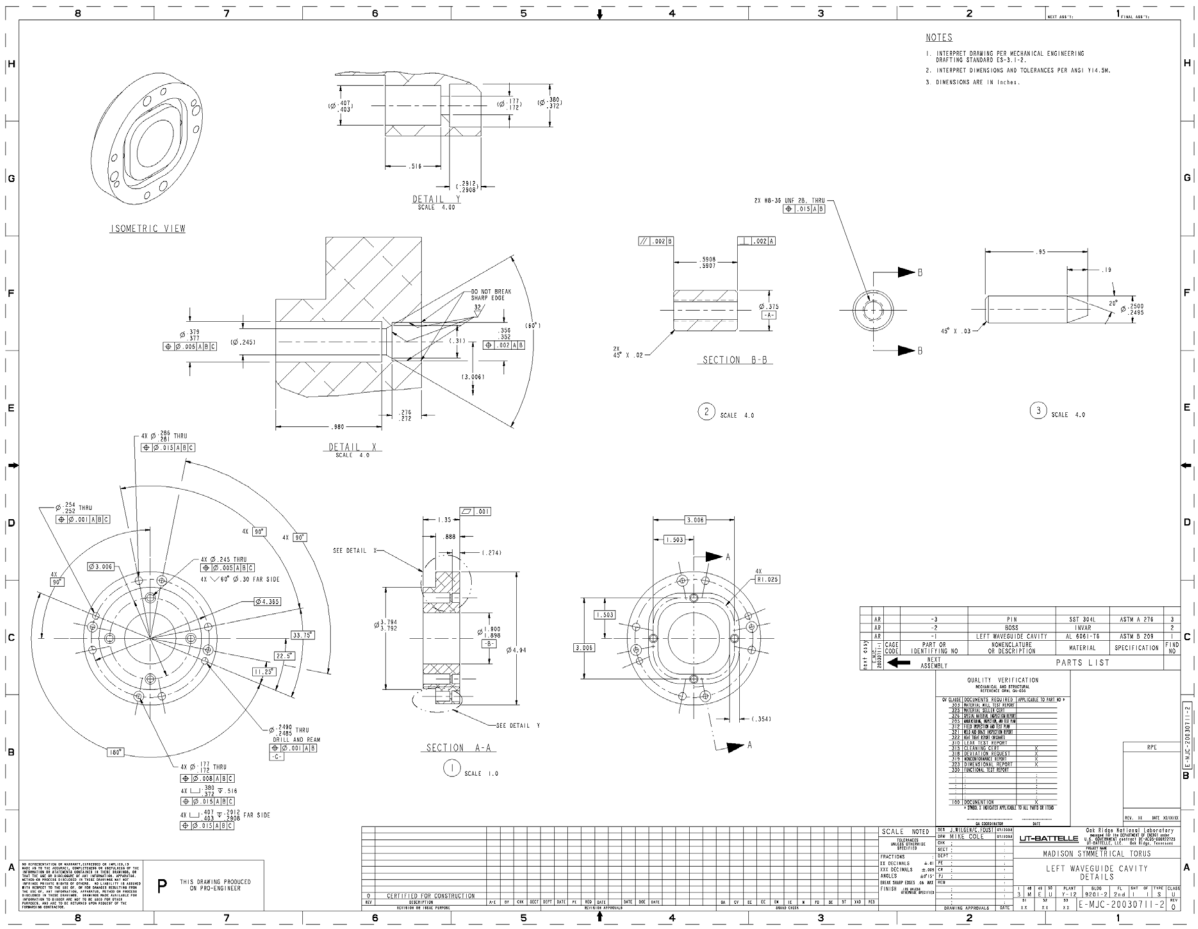

Figure C.45: Microwave cavity drawings

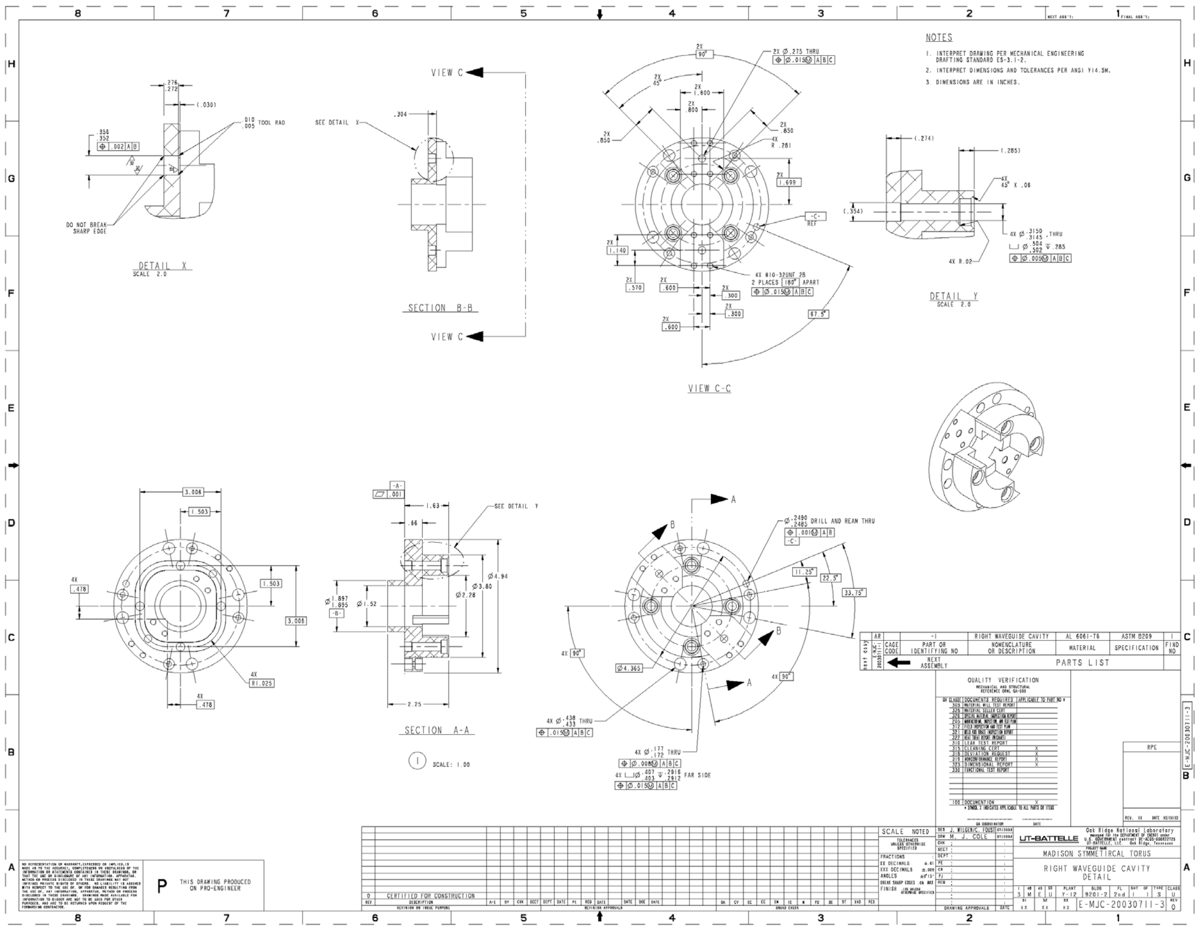

Figure C.46: Microwave cavity drawings